Surveys of Ultraluminous Activity in the Distant Universe

STUART MICHAEL STACH

Surveys of Ultraluminous Activity in the Distant Universe

Stuart Michael Stach

Abstract

In the last twenty years sub-millimetre surveys have uncovered numerous sub-millimetre bright galaxies (SMGs), sites of some of the most intense star-formation in history with rates peaking over a thousand solar masses per year. For the majority of the twenty years since their discovery, the identification and the constraints on the properties of individual SMGs has been limited by the relatively coarse resolution of single-dish sub-millimetre telescopes (typically FWHM $\sim 15''$). The more recent development of millimetre interferometers, such as the Atacama Large Millimetre/Sub-millimetre Array (ALMA), provides us with an order of magnitude increase in resolution over the single-dish surveys allowing us to precisely identify the individual SMGs. In this thesis I present an analysis of two surveys of single-dish sub-millimetre sources which have been followed up with ALMA to identify the individual SMGs. The first survey is of the 716 SCUBA-2 sources detected in the UKIDSS UDS field where our ALMA follow-up detects 708 SMGs. From the extensive multi-wavelength coverage in this field we derive photometric redshifts for each SMG, finding a median $z_{\rm phot} = 2.61 \pm 0.09$ with a high-redshift tail containing 33^{+3}_{-2} % of $z_{\rm phot} > 3$ SMGs. We find the blending of multiple galaxies into a single-dish source in 11 ± 1 % of our ALMA maps, and this rate of multiplicity increasing for brighter single-dish flux with a rate of 28 ± 2 % for $S^{\rm deb}_{850} \geq 5$ mJy. The photometric redshifts of these multiples suggest $\gtrsim 30$ % are physically associated, which potentially points to merger activity playing a role in the intense star-formation rates for a significant percentage of SMGs. I also present the results of an ALMA survey of four SCUBA-2 sources in the centre of the $z = 1.46$ cluster XCS J2215, where the high-resolution imaging shows an elevated density of SMGs with 14 detections. Detections of ^{12}CO in six of these cluster galaxies suggest they are recent accretors with larger fractions of warmer gas than comparable field galaxies suggesting ram pressure stripping is preferentially removing the cold gas content.

Surveys of Ultraluminous Activity in the Distant Universe

Stuart Michael Stach

A thesis presented in accordance with the regulations for admittance to the degree of Doctor of Philosophy

Centre for Extragalactic Astronomy
Department of Physics
University of Durham
United Kingdom

April 2019

Contents

List of Tables

List of Figures

Declaration

The work described in this thesis was undertaken between October 2015 and February 2019 while the author was a research student under the supervision of Prof. Ian Smail and Dr. Mark Swinbank in the Department of Physics at the University of Durham. No part of this thesis has been submitted for any other degree at the University of Durham or any other university.

Portions of this work have appeared in the following papers:

- *Chapter 2 and Chapter 3:* **An ALMA Survey of the SCUBA-2 Cosmology Legacy Survey UKIDSS/UDS Field: Number Counts of Submillimeter Galaxies** Stach, Stuart M.; Smail, Ian; Swinbank, A. M.; Simpson, J. M.; Geach, J. E.; An, Fang Xia; Almaini, Omar; Arumugam, Vinodiran; Blain, A. W.; Chapman, S. C.; Chen, Chian-Chou; Conselice, C. J.; Cooke, E. A.; Coppin, K. E. K.; Dunlop, J. S.; Farrah, Duncan; Gullberg, B.; Hartley, W.; Ivison, R. J.; Maltby, D. T.; Michałowski, M. J.; Scott, Douglas; Simpson, Chris; Thomson, A. P.; Wardlow, J. L.; van der Werf, P., 2018, ApJ, 860.2, 161.

- *Chapter 5:* **ALMA Pinpoints a Strong Overdensity of U/LIRGs in the Massive Cluster XCS J2215 at** $z = 1.46$ Stach, Stuart M.; Swinbank, A. M.; Smail, Ian; Hilton, Matt; Simpson, J. M.; Cooke, E. A., 2017, ApJ, 849.2, 154.

The following sections of this work appear in the following paper which has recently been submitted for peer review:

- *Chapter 2 and Chapter 4:* **An ALMA survey of the SCUBA-2 Cosmology Legacy Survey UKIDSS/UDS field: Source catalogue and properties** Stach, Stuart M.; Dudzevičiūtė, U.; Smail, Ian; Swinbank, A. M.; Geach, J. E.; Simpson, J. M.; An, Fang Xia; Almaini, Omar; Arumugam, Vinodiran; Blain, A. W.; Chapman, S. C.; Chen, Chian-Chou; Conselice, C. J.; Cooke, E. A.; Coppin, K. E. K.; da Cunha, E.; Dunlop, J. S.; Farrah, Duncan; Gullberg, B.; Hodge, J. A.; Ivison, R. J., Kocevski, Dale D.; Michałowski, M. J., Miyaji, Takamitsu; Scott, Douglas; Thomson, A. P.; Wardlow, J. L.; van der Werf, P., 2019, MNRAS (Submitted).

The author carried out the work in this thesis with the following exceptions: (1) the AS2UDS data was taken from ALMA proposals led by Ian Smail, with the exception of the 'blank map' follow-up which was written by the author, and the XCS J2215 ALMA proposal was written by C.J. Ma, (2) the deblended *Herschel*/SPIRE fluxes used in chapters 2 and 3 were calculated by Mark Swinbank, (3) the MAGPHYS SED fitting and IRAC flux derivations in chapter 4 were carried out by Ugne Dudzevičiūtė, (4) the MUSE data reduction in chapter 5 was carried out by Mark Swinbank.

In addition to the work presented in this thesis, the author has also worked on, or been involved in, the following work during the period of their PhD:

- **Dark matter dynamics in Abell 3827: new data consistent with standard cold dark matter** Massey, Richard; Harvey, David; Liesenborgs, Jori; Richard, Johan; **Stach, Stuart**; Swinbank, Mark; Taylor, Peter; Williams, Liliya; Clowe, Douglas; Courbin, Frdric; Edge, Alastair; Israel, Holger; Jauzac, Mathilde; Joseph, Rmy; Jullo, Eric; Kitching, Thomas D.; Leonard, Adrienne; Merten, Julian; Nagai, Daisuke; Nightingale, James; Robertson, Andrew; Romualdez, Luis Javier; Saha, Prasenjit; Smit, Renske; Tam, Sut-Ieng; Tittley, Eric, 2018, MNRAS, 477.1, 669-677.

- **The Dust and [CII] Morphologies of Redshift $\sim$4.5 Sub-millimeter Galaxies at $\sim$200 pc Resolution: The Absence of Large Clumps in the Interstellar Medium at High-redshift** Gullberg, B.; Swinbank, A. M.; Smail, I.; Biggs, A. D.; Bertoldi, F.; De Breuck, C.; Chapman, S. C.; Chen, C.-C.; Cooke, E. A.; Coppin, K. E. K.; Cox, P.; Dannerbauer, H.; Dunlop, J. S.; Edge, A. C.; Farrah, D.; Geach, J. E.; Greve, T. R.; Hodge, J.; Ibar, E.; Ivison, R. J.; Karim, A.; Schinnerer, E.; Scott, D.; Simpson, J. M.; **Stach, S. M.**; Thomson, A. P.; van der Werf, P.; Walter, F.; Wardlow, J. L.; Weiss, A., 2018, ApJ, 859.1, 12.

- **An ALMA Survey of the SCUBA-2 Cosmology Legacy Survey UKIDSS/UDS Field: Identifying Candidate z$\sim$4.5 [CII] Emitters** Cooke, E. A.; Smail, Ian; Swinbank, A. M.; **Stach, S. M.**; An, Fang Xia; Gullberg, B.; Almaini, O.; Simpson, C. J.; Wardlow, J. L.; Blain, A. W.; Chapman, S. C.; Chen, Chian-Chou; Conselice, C. J.; Coppin, K. E. K.; Farrah, D.; Maltby, D. T.; Michaowski, M. J.; Scott, D.; Simpson, J. M.; Thomson, A. P.; van der Werf, P., 2018, ApJ, 861.2., 100.

- **A Machine-learning Method for Identifying Multiwavelength Counterparts of Submillimeter Galaxies: Training and Testing Using AS2UDS and ALESS** An, Fang Xia; **Stach, S. M.**; Smail, Ian; Swinbank, A. M.; Almaini, O.; Simpson, C.; Hartley, W.; Maltby, D. T.; Ivison, R. J.; Arumugam, V.; Wardlow, J. L.; Cooke, E. A.; Gullberg, B.; Thomson, A. P.; Chen, Chian-Chou; Simpson, J. M.; Geach, J. E.; Scott, D.; Dunlop, J. S.; Farrah, D.; van der Werf, P.; Blain, A. W.; Conselice, C.; Michaowski, M.; Chapman, S. C.; Coppin, K. E. K., 2018, ApJ, 862.2, 101.

- **The submillimetre view of massive clusters at** $z \sim 0.8-1.6$ Cooke, E. A.; Smail, Ian; **Stach, S. M.**; Swinbank, A. M.; Bower, R. G.; Chen, Chian-Chou; Koyama, Y.; Thomson, A. P., 2019, MNRAS, submitted

Acknowledgements

The only section, outside of examiners and supervisors, that anybody will ever read, so...Hi. I need to thank Ian and Mark for taking me on as a student, scribbling in red over everything I write, never giving up sending e-mails that I'd probably not reply to, and reminding me I need to finish writing a thesis. Any failing of this thesis is due to my poor abilities and not poor supervision. I was also fortunate enough to spend my PhD in the presence of a number of other, vastly more talented people than me, within our sub-millimetre group, whose skills I had hoped to assimilate through osmosis (although the next 150 pages suggest that might have failed): Julie W., Bitten G., Lizzie C., T.C., Alasdair T.

Throughout my time in Durham, through the multiple office moves, I have been blessed with great office-mates: Andrew 'Voted for Brexit so not that great' G., Helen J., Flora S., Anna G., FangXia A., Ugne D., Steve G., Will C., Sut Ieng T., Piotr O., Dan K. I have equally been fortunate to be in the year group that has consistently supplied much needed levity, you've definitely improved PhD life: Stefan A., Oliver N., Jan S., Behzad A.

Big thanks to housemates for all the food supplied, drunk chatting, general entertainment: Zhen L., Joanna Y., Bonnie L., Martin T., Daisy W., I would have got more work done without you guys but it's better to drink with friends.

I owe a debt to Kathryn and Richard, I may be the least communicative brother/brother-in-law you can get but I literally wouldn't be here without you guys, I mean...you've got a car. Finally, Esther T., becoming friends with the person who turns up to every physics lecture and writes notes with multiple coloured pens was definitely a fortunate turn of events. I probably wouldn't have made it through undergrad without your excellent work-ethics and note-taking (the baking didn't hurt either).

Dedicated to

the Laphroaig distillery

CHAPTER 1

Introduction

1.1 Overview

Almost thirty years ago the *Cosmic Background Explorer* (COBE) measured the energy spectrum of the Universe at far-infrared wavelengths. Puget et al. (1996) identified an isotropic emission which was not capable of being explained by galactic sources and therefore represents the first detection of the cosmic infrared background. This energy density at infrared and sub-millimetre wavelengths is found to be comparable to that in the optical and ultraviolet (UV), therefore the traditional surveys of galaxy evolution at optical and ultraviolet are only probing approximately half of the true star formation activity in the Universe, with the origin of this optically-obscured emission being the reprocessed light from stars absorbed by the dust content of the host galaxy. In the intervening 23 years our ability to resolve this emission has improved immensely due to improvements in detectors and the commissioning of the first sub-millimetre interferometers, which have allowed us to probe deeper and at higher resolutions so that now we are capable of resolving the contributions to the cosmic infrared background from the individual high redshift galaxies contributing to the emission. These surveys find a population of extremely bright galaxies in the far-infrared wavelengths, almost completely obscured in the optical, with star-formation rates amongst the highest in the Universe.

In this thesis I present the results of two surveys of the sub-millimetre bright population; one in the Ultra Deep Survey (UDS) field and the other one in the centre of a high redshift cluster. The aim of both studies is to accurately identify the galaxies re-

sponsible for the sub-millimetre bright emission so that they can be matched robustly to emission across multiple photometric bands. From this information we can understand at what epoch of the Universe these sources are most commonly found and how they evolve. From the cluster observations, the key question is understanding what mechanism is responsible for quenching the star-formation in the dense cores of clusters such that lower redshift clusters have centres devoid of actively star-forming galaxies.

1.2 Galaxies

The field of extragalactic astronomy was 'somewhat hampered' until fairly recently in history because until nearly 100 years ago we were not certain that objects beyond our galaxy existed. The ancient Greeks as early as a few hundred BC recognised the Milky Way as a collection of distant stars with a geocentric model placing the Earth at the centre of the Universe. Approximately 2000 years later Copernicus established the heliocentric model placing the Sun at the centre of our solar system. A few years later, largely regarded as the first 'observational astronomer', Galileo Galilei built one of the first telescopes to observe the night sky and becomes convinced of this heliocentric model. As the development of telescopes improves, a major debate breaks out over the origins of the increasing number of extended, 'nebulous objects' being discovered (Messier, 1781). Immanuel Kant had speculated that our Milky Way was just one 'Island Universe' of many (Kant, 1755) and Thomas Wright of Durham suggested these nebulous objects could be galaxies of their own, outside of the Milky Way. The first spectroscopy of these 'nebulae' found they were indeed large groups of stars with radial velocities far in excess of other astronomical objects at the time (Slipher, 1915). The debate ended when Edwin Hubble inferred distances of Cepheid variables, pulsating stars with a tight luminosity–period relation, firmly placing the 'nebulae' outside of the Milky Way (Hubble, 1925).

Having established that the Milky Way is just one galaxy of many (with current estimations from deep *Hubble Space Telescope* (*HST*) imaging suggesting over 100 billion), Hubble created a classification scheme (Hubble, 1926) for these 'nebulae' based on their morphology (Figure 1.1). This 'tuning fork' classifies the galaxies into three categories.

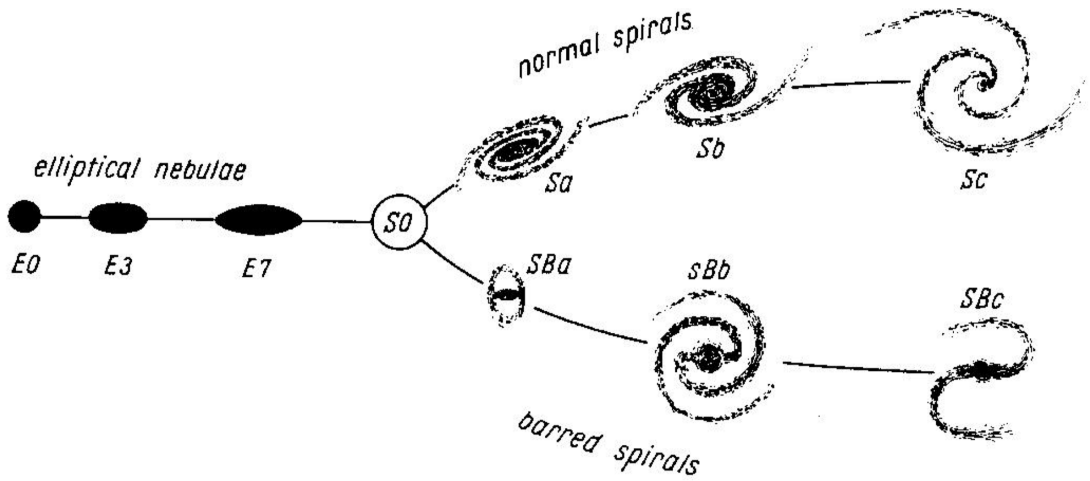

Figure 1.1: The Hubble 'Tuning fork', the morphological classification scheme for galaxies, as presented in Hubble & Rosseland (1936).

First the ellipticals (called 'early-type' galaxies) which show a roughly spherical distribution of stars and are further subdivided by their axis ratio ranging from a spherical (E0) to flat (E7). Then there are the Spiral galaxies ('late-type' galaxies) which show a central bulge of stars in addition to a disc of stars in spiral 'arms'. The spiral galaxies are subdivided into two, those with a 'bar' in the centre and those without and these are further subdivided from Sa/SBa for tightly wound spirals around the bulge to Sbc/SBc for the least tightly round spirals. Finally there are the lenticulars (SO) which are morphologically between the two groups, which have a central bulge but also poorly-defined spiral arms.

The labelling of ellipticals as 'early type' and spirals as 'late type' is somewhat of a misnomer and the tuning fork is not intended as an evolutionary path for galaxies. In reality we have since found that the early-type galaxies are primarily high mass galaxies with little to no active star formation. The elliptical galaxies have older stellar populations, with the higher mass stars having evolved off the main sequence leaving the smaller mass stars which are cooler and therefore redder in colour giving rise to the 'red and dead' appearance of the elliptical galaxies. In contrast, spectroscopy of spiral galaxies shows galaxies rich in cold gas, a necessary ingredient for star formation, with a large number of young, high-mass stars which are by their nature bluer in colour. Therefore a key question in extragalactic astronomy is what are the physical processes responsible for

galaxies evolving into the classifications that we observe them at today.

1.3 Star-Formation Rate Density

In the cold dark matter model of the Universe we can understand the origins of galaxy formation as sites of tiny fluctuations in the dark matter density field in the early Universe. These fluctuations in the non-baryonic dark matter cause instabilities that inevitable collapse due to gravity forming dark matter haloes which grow through 'hierarchical assembly' i.e. mergers of smaller haloes into larger haloes. It is in these haloes that galaxies are seeded as the gas in these haloes cools and collapses creating the first sites of star formation (see: White & Rees, 1978; Komatsu et al., 2009). Whilst the majority of a galaxy's mass is accounted for by this dark matter, as observers we only directly measure radiation from a galaxy which comes from its luminous baryonic matter. This matter comes in the form of the stars, and the dust and gas of the interstellar medium (ISM), which are all intrinsically linked to the star formation in the galaxy. Therefore one of the most effective means to probe galaxy evolution is through examining the rate at which galaxies are forming stars as a function of galaxy age, i.e. tracing their stellar mass growth.

The first such estimations of the star-formation rate density with redshift relied on UV/optical surveys to trace the star-formation activity of galaxies (Lilly et al., 1996; Madau et al., 1996). The UV emission traces the instantaneous star-formation rate of a galaxy, as its emission is generated from the most massive and thus most short lived stellar population in the galaxies. These earliest surveys found that the star-formation rate density of the Universe was increasing with 'lookback' time and suggested a peak in the star-formation rate density at $z \sim 1$, however UV emission alone does not paint the complete picture.

The inter-stellar medium of galaxies is comprised of a mix of gas and tiny particles, called dust, of varying sizes. The exact composition of these dust grains is still poorly understood however the make-up of them can be inferred from the behaviour of the extinction of light at varying wavelengths (see for review: Franceschini, 2003). The models predict silicates (largely from supernovae), graphite or amorphous carbon grains of vary-

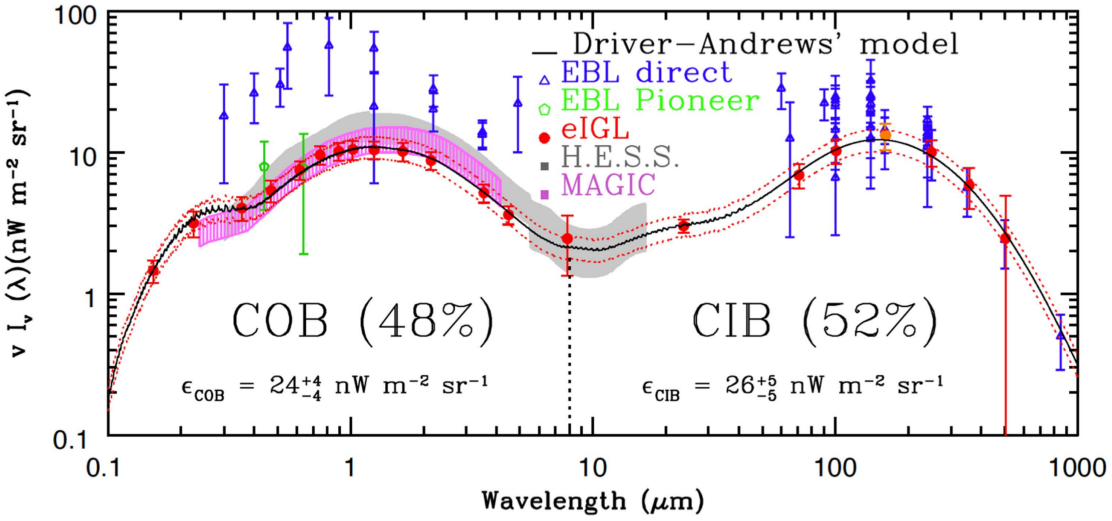

Figure 1.2: Extrapolated extragalactic background light estimations from the optical to the far-infrared. The references for the surveys plotted and the figure are taken from Driver et al. (2016). The cosmic infrared background is shown to constitute ∼52 % of the total energy density, which highlights the importance of infrared emission as a significant indicator of stellar emission.

ing sizes. For the grain sizes that match the wavelength of incoming light they become very effective at either scattering the photons or absorbing them and thus heating up. For the UV light incident on these dust grains the former effect results in a 'reddening' of the galaxy colours as preferentially bluer photons are scattered from the line of sight whilst the latter effect results in a thermal re-emission of the energy. As a dust grain absorbs the photon it will then re-emit the energy as a modified black body at a variety of characteristic temperatures dependent on the nature of the dust grain e.g. its size and environment. As they are heated to temperature of ∼15-50 K (well below their sublimation temperatures of ∼2000 K) their black body radiation peaks in the infrared, at wavelengths ∼60-200 μm.

The importance of this dust emission is made apparent from measurements of the extragalactic background light at these two wavelength regimes (Blain & Phillips, 2002; Lagache et al., 2005; Driver et al., 2016), which find that the energy density at infrared wavelengths is comparable to that of the UV/optical wavelengths suggesting roughly half of the stellar emission is missed in purely UV/optical surveys (Figure 1.2)

Incorporating subsequent surveys, including those targeting the infrared emission, into the star-formation rate density measurements results in a shifting of the peak of star-

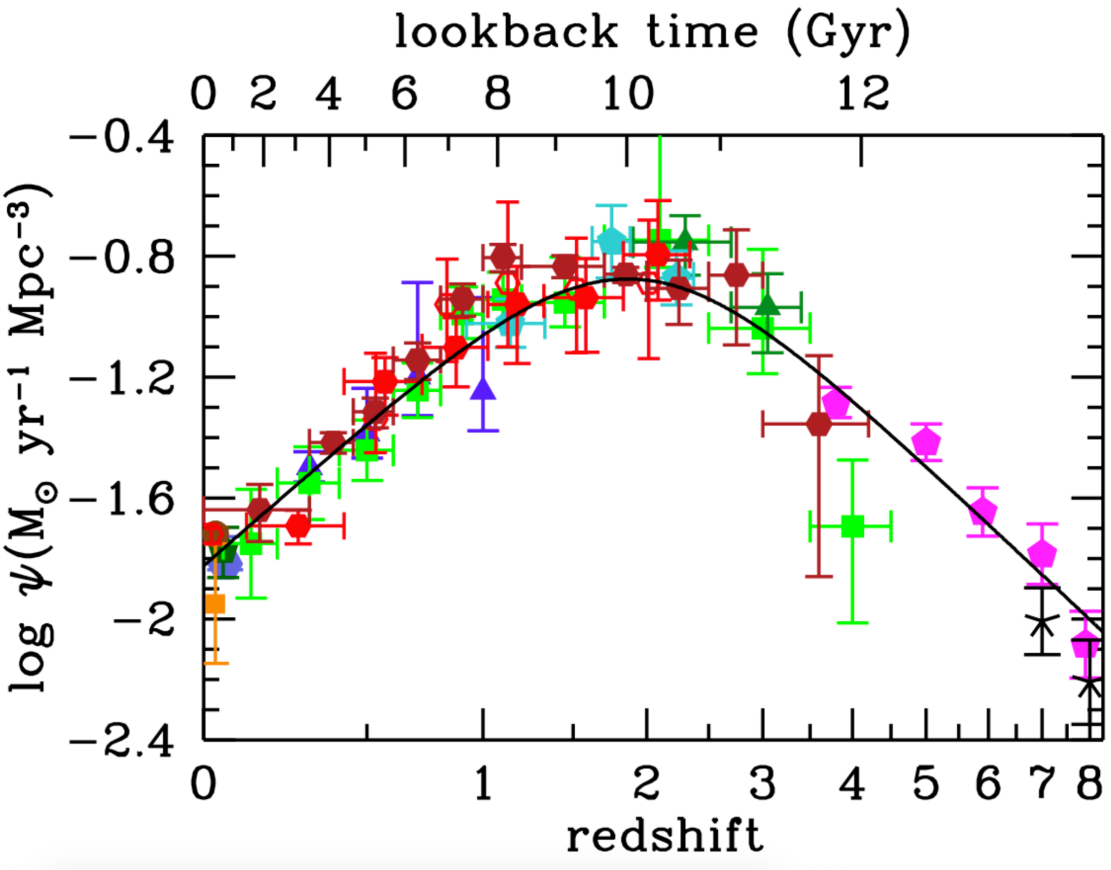

Figure 1.3: The star-formation rate density as a function of redshift from surveys in both the UV/optical and infrared, taken from Madau & Dickinson (2014). The best fit curve for the various surveys listed in Madau & Dickinson (2014) puts the peak star formation activity for the Universe at a $z \sim 1.9$, or roughly 3.5 Gyrs after the Big Bang.

formation activity in the Universe to $z \sim 1.9$ (∼3.5 Gyr after the Big Bang, Figure 1.3). Figures 1.2 and 1.3, combined, suggesting that the Universe was considerably more active in the past with a significant amount of the Universe's stellar mass being already assembled over 10 Gyrs ago (25 % of present-day stellar mass formed by $z = 2$ Madau & Dickinson, 2014) and that to reliably estimate this activity, at the epoch of peak star formation, surveys at the far-infrared wavelengths are required.

1.4 Sub-Millimetre Galaxies

It follows from the evolution of the star-formation rate density that to understand what caused this peak in the assembly of stellar mass in the Universe, and its subsequent decline, requires observations of the individual galaxies which contribute to the cosmic in-

frared background and an understanding of their evolution. Observations at these wavelengths, however, come with their own set of strengths and weaknesses. The major difficulty with sub-millimetre wavelength observations at the ground level comes from the heavy potential attenuation at this wavelengths from water vapour in the atmosphere. Thus whilst the ideal wavelengths to observe galaxies contributing to the CIB would be at the peak of their thermal dust emission, which is found at $\sim$100 μm, from our ground telescopes we are constrained to set atmospheric windows, i.e. bands of wavelength ranges where the atmospheric water vapour does not make observations impossible: $\sim$350 μm, 450 μm, 770 μm, and 850 μm in the sub-millimetre.

1.4.1 *K*-Correction

Whilst ground-based sub-millimetre imaging is limited to certain wavelength bands there is a boon to observing the thermal emission at these bands, the very negative *K*-correction. The *K*-correction is the correction to the magnitude or flux of a source to convert it from an observed-frame to rest-frame, thus the strength of this correction is dependant on the shape of the spectral energy distribution (SED) for the galaxy. The *K*-correction is defined as positive if it results in an increase in magnitude (reduction in flux) and negative for a decrease in magnitude (increase in flux). Galaxies observed in the sub-millimetre have a strong *negative K*-correction such that galaxies at very high redshift detected in the sub-millimetre can have roughly constant flux across a very large range of redshifts, e.g. $z = 1 - 8$, Figure 1.4.

As mentioned above, the cause of this negative *K*-correction is the shape of the SED of the galaxies. As the thermal dust emission, which is roughly black-body like in shape, peaks at $\sim$100 μm then sub-millimetre observations are probing the Rayleigh-Jeans tail. In this tail the flux density is scaling with frequency as $S_\nu \propto \nu^{2+\beta}$, where β is the dust emissivity spectral index. The precise value of β is a matter of debate, but a typical value used for dusty galaxies is $\beta = 2$ (Dunne & Eales, 2001; Magnelli et al., 2012). For a fixed luminosity source the flux density will dim with redshift $S_\nu \propto (1+z)^{-4}$ because $S_\nu = L_\nu / 4\pi D_L^2$ and $D_L \propto (1+z)^2$ and the frequency will shift $\nu_{rest} = \nu_{obs}(1+z)$. Combining these we derive a shift in the flux density as $S_\nu \propto \nu_{rest}^{2+\beta} / 4\pi D_L^2 \propto \nu_{obs}^{2+\beta}(1+z)^{2+\beta}/(1+z)^4 \propto$

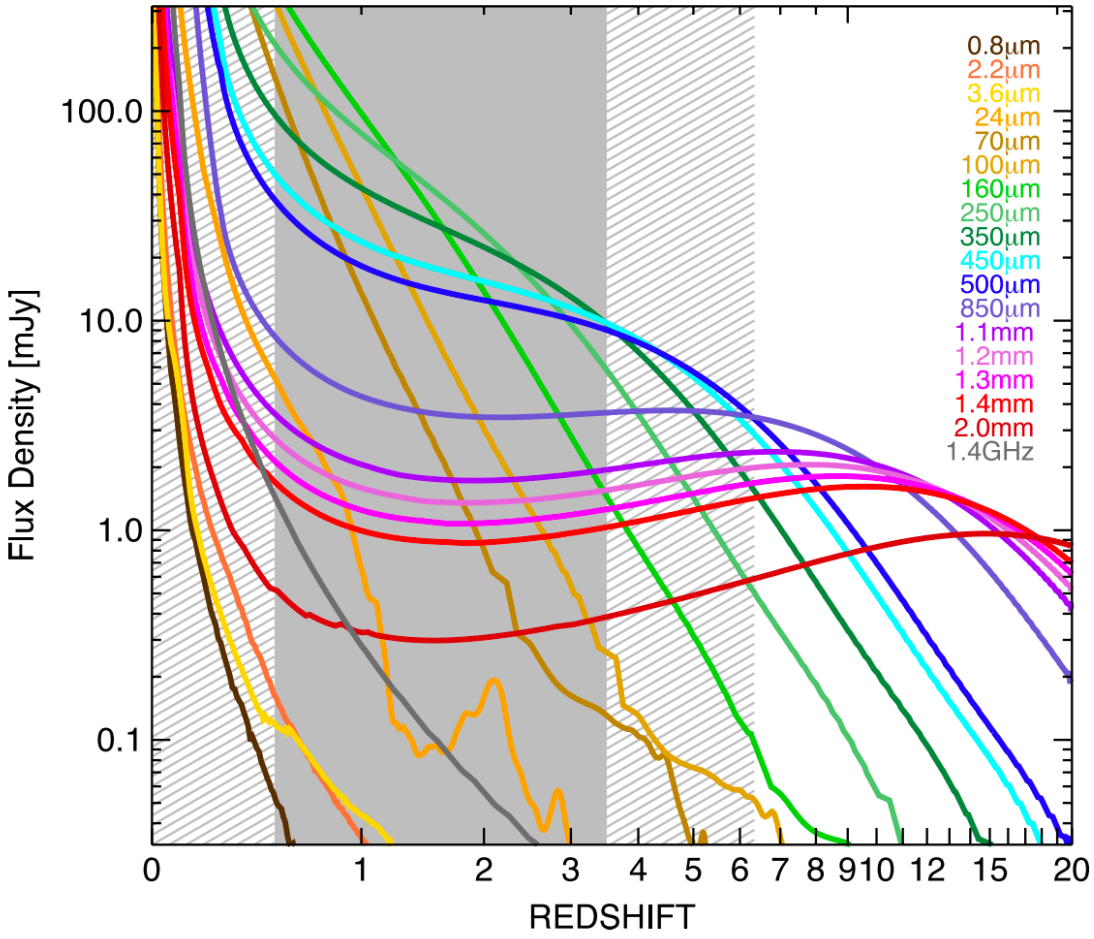

Figure 1.4: Illustration of the various K-corrections for differing wavelength observations, taken from Casey et al. (2014). Each line is the observed flux densities for a typical $10^{12.5}\,L_{\odot}$ infra-red luminosity galaxy using the SMG composite SED from Pope et al. (2008) for the K-correction of observations at 24 μm and above and an Arp220 SED for 0.8 μm, 2.2 μm, and 3.6 μm. The strength of sub-millimetre emission is made apparent by the plateaus/positive gradients of the flux-densities with redshifts at these wavelengths from $z \approx$1–8.

$(1+z)^{\beta-2}$ which for $\beta \approx 2$ is a constant. Therefore these galaxies will not fade but could possibly get *brighter* at the observed wavelength, hence the negative *K*-correction, and this is a major advantage of sub-millimetre observations. As shown in Figure 1.4 this negative *K*-correction is found at other wavelengths, however, for 850 μm surveys the very negative *K*-correction gives the potential to probe the very highest redshift galaxies as they are potentially even brighter than similar luminosity lower redshift analogues, and this was a strong motivator for the original 850 μm surveys.

1.4.2 First Detections and Single-Dish Surveys

The first sub-millimetre surveys to detect these expected high-redshift, sub-millimetre bright sources were made possible in 1997 through the commissioning of the Sub-millimetre Common User Bolometer Array (SCUBA) instrument on the James Clerk Maxwell Telescope (JCMT). This instrument simultaneously observed in the 450 μm and 850 μm windows and could reach 1 σ depths of $\sim$2 mJy in the 850 μm band (the 450 μm sensitivity was significantly shallower) in $\sim$5 arcmin^2 area within six hours of integration. The results from the first SCUBA maps of two galaxy clusters found the first six sub-millimetre sources (Smail et al., 1997). These were gravitationally lensed sources found at a significantly higher surface density than expected from local ultra-luminous infrared galaxies confirming the need for a strong evolution in the cosmic star formation rate density out to the high redshifts of these newly discovered sub-millimetre sources. Further blank field maps confirmed this result (Barger et al., 1998; Hughes et al., 1998).

From these early surveys on several sources the number of sub-millimetre sources would increase from large surveys undertaken from ground-based observations, in particular from the continued use of SCUBA (e.g. SCUBA HAlf DEgree Extragalactic Survey (SHADES): Coppin et al., 2006), 1.2 mm detections with the MAx-planck Millimetre BOlometer (MAMBO) camera at the Institut de RadioAstronomie Millimetrique (IRAM) (Greve et al., 2004; Bertoldi et al., 2007; Greve et al., 2008; Lindner et al., 2011), for a full review of the early history of sub-millimetre sources see: Casey et al. (2014).

The next big leap in the detection of sub-millimetre selected sources came with the launch of the *Herschel* Space Observatory in May 2009. Multiple deep surveys target-

ing the rest-frame far-infrared emission of galaxies were performed using a couple of the instruments on the *Herschel* telescope. These instruments were the Spectral and Photometric Imaging REceiver (SPIRE) which was a spectrometer and imaging photometer which simultaneously imaged at three wavebands: 250 μm, 360 μm, and 520 μm and the the Photodetector Array Camera and Spectrometer (PACS) instrument which can simultaneously image two wavebands out the three available: 70 μm, 100 μm, and 160 μm. The space-based observations opened up wavebands impractical for the ground-based telescopes and thus improved the sampling of the infrared peak, however the relatively small mirror size (3.5 m diameter) resulted in significant source blending owing to beamsizes of 18″, 26″, and 36″ for the three SPIRE wavebands respectively. The largest surveys of sub-millimetre sources using SPIRE were the *Herschel* Multi-tiered Extragalactic Survey (HerMES; Oliver et al., 2012) which imaged $\sim$380 deg^2 to detect hundreds of thousands of far-infrared bright galaxies in all the main extragalactic fields. Another example was the *Herschel*-Astrophysical Terahertz Large Area Survey (H-ATLAS Eales et al., 2010) which mapped $\sim$550 deg^2 and with PACS: the PACS Evolution Probe (PEP; Lutz et al., 2011) and GOODS-*Herschel* (Elbaz et al., 2011). In the four years of operation *Herschel* dramatically increased the sample size of far-infrared bright galaxies from the 100's discovered by SCUBA to 10,000's, discovered the brightest and most dramatically star-forming examples of them to date (Riechers et al., 2013) and helped to constrain the measurements of the CIB (Berta et al., 2011).

More recently the second generation bolometer array, SCUBA-2, was installed at the JCMT (2011), providing a $>$ 100 times mapping speed in comparison to the first generation SCUBA. The largest and deepest 850 μm survey of sub-millimetre sources has been carried out recently with SCUBA-2, the 'SCUBA-2 Cosmology Legacy Survey' (S2CLS) (Geach et al., 2017). This survey covered $\sim$5 deg^2 across seven extra-galactic fields with close to 3000 sub-millimetre sources, providing an order of magnitude increase in 850 μm catalogued sources. The legacy value of this survey is made abundantly clear by the body of work which utilises this catalogue, for which I discuss some of the results below, (e.g. Geach et al., 2013; Smail et al., 2014; Coppin et al., 2015; Chen et al., 2016; Wilkinson et al., 2017; Bourne et al., 2017), and in addition the bulk of this thesis is dependent on

the S2CLS survey.

1.4.3 Multiwavelength Identification

To put meaningful constraints on the properties of the sub-millimetre galaxy (SMG) population, the sub-millimetre sources have to be matched to the individual galaxies in other wavebands. At the redshifts where we expect to see the peak of sub-millimetre activity $z \sim 1-2$ that requires sub-arcsecond positional accuracy which is an order of magnitude finer than even the largest single dishes can provide at 850 μm (JCMT 15 m dish: $\sim$15$''$resolution). This issue is exacerbated by the dusty nature of these galaxies which causes a number of the galaxies responsible for the sub-millimetre source to not even being detectable at optical wavelengths (Smail et al., 2002; Wang et al., 2016). Therefore to match the ever increasing number of sub-millimetre sources to the individual galaxies responsible a number of statistical association techniques had to be created.

One of the earliest methods was to match the sub-millimetre sources to radio bright detections. In the local Universe there is an observed correlation between infrared and radio emission (Helou et al., 1985; Condon, 1992; Xu et al., 1992; Sargent et al., 2010), with the proposed origin due to both wavelengths tracing recent star formation, as the centimetre wavelength radio emission is thought to be produced from the relativistic electrons accelerated by the supernova remnants of former OB stars which have main-sequence lifetimes of $\sim$30 Myrs. Studies into this relation towards higher redshifts, relevant to SMGs, have found no evidence for an evolution in this relation (Murphy, 2009; Ivison et al., 2010a,b; Thomson et al., 2014) and therefore we would expect a significant percentage of sub-millimetre galaxies to be radio bright.

There are a number of advantages in observing in the radio waveband that make it particularly suitable for finding candidate counterparts. Firstly the atmospheric transmission at radio wavelengths is higher than at the sub-millimetre, so the extragalactic fields can be mapped by radio interferometers comparatively quickly. In addition radio was first considered due to the high-resolution made possible by the use of interferometers. As an interferometer resolution does not scale with the dish size, as single-dish observations do, they instead scale with the separation of the individual antennae (the baseline lengths). For

the Jansky Very Large Array (VLA) the baseline lengths can be up to $\sim$30 km which more than compensates for the longer wavelengths being observed in the λ/D scaling, resulting in arcsecond scale imaging. Finally, any statistical association method for matching galaxies to the sub-millimetre galaxies is more reliable if the number of potential candidates is reduced. A common technique for matching likely candidates galaxies at different wavelengths is to calculate the Poissonian probabilities for counterpart alignments. The p-values for this is calculated as:

$$p = 1 - \exp\left(-\pi n \theta^2\right) \tag{1.4.1}$$

where n is the source density for the type of galaxy you are matching (e.g. radio bright) and θ is the angular offset from the sub-millimetre source and the counterpart you are calculating the p value for. As a reliable match is considered when $p < 0.05$, this method finds more reliable matches for types of galaxies with low source density. Radio bright galaxies are comparatively rare in comparison to galaxies in the optical wavelengths, a sub-millimetre beam will rarely contain more than one radio bright galaxy whereas it can contain over 10 optically-bright galaxies (Smail et al., 2002; Ivison et al., 2007), and thus the low source density of radio bright galaxies makes them particularly suitable for Poisson-probability matching.

Radio detection matching is a frequently used tool (Ivison et al., 2002; Bertoldi et al., 2007; Biggs et al., 2011) with some of the first redshift surveys targeted from those with bright detected radio emission (Chapman et al., 2005), however there are potentially significant biases with the radio-selected samples. Most obviously this method breaks down when there are no radio counterparts within the sub-millimetre beam which, even in the deepest radio imaging, has been found to occur in roughly a third of $S_{850} > 5$ mJy sources (Chapman et al., 2003). A likely cause for this can be seen in Figure 1.4 where at 1.4 GHz the radio observations do not benefit from a negative K-correction and so we might expect the highest redshift sources to drop-out from radio imaging and therefore bias our samples to lower redshifts.

Whilst p-statistics are not ideal for matching to shorter wavelength, likelihood analysis matching (Sutherland & Saunders, 1992) of optical and near-infrared galaxies has

been used (Chapin et al., 2009; Smith et al., 2011; Bond et al., 2012). Reliable optical and near-infrared matching is particularly desirable because of the extensive coverage in the extra-galactic fields already available, however as mentioned above they do not benefit from the negative K-correction and the optical bands also suffer from drop-outs due to the dusty nature of the galaxies. Another key issue with these probabilistic methods is their assumption of a single counterpart for each sub-millimetre source. Before high-resolution sub-millimetre imaging was possible it was still understood that this was unlikely. The negative K-correction makes sub-millimetre maps sensitive to bright sources across a huge range in redshifts which increases the chances of detections of similar flux density sources lying in chance projection which the above methods do not account for. The only way to robustly identify counterparts is from high-resolution imaging in the sub-millimetre and, due to the λ/D scaling, this is only possible with interferometry.

1.4.4 Interferometric Surveys of SMGs

Interferometry overcomes the angular resolution issue of single-dish observations by 'synthesising' a large aperture by combining the signals detected by multiple dishes in an 'array'. The resulting images produced will have resolutions that scale not with the individual dish sizes, but instead from the maximum distances between the individual dishes. Whilst this enables interferometers to scale their synthesised dish sizes onto the scales of kilometres (c.f. 15 m JCMT dish) the primary beam size (effectively the field-of-view, set by the sensitivity of the instrument) *is* set by the individual dish sizes and the wavelength of the observations and independent of the configuration of the array of dishes. The end result of this is that sub-millimetre interferometers provide the highest resolution images currently possible at these wavelengths but their field of views are so narrow that surveying large areas of the sky are prohibitively expensive.

The first sub-millimetre interferometer was the Submillimeter Array (SMA) (Ho et al., 2004), this array consists of 8 6 m diameter dishes with maximum baselines of 509 m that can observe at wavelengths 710–1670 μm (180–420 GHz). The SMA is therefore capable of the order of magnitude increase in resolution over single-dish telescopes, however the poor sensitivity has confined SMA observations to mostly observing the brightest sources

in single-dish surveys (Iono et al., 2006; Younger et al., 2007; Wang et al., 2011; Hill et al., 2018). Whilst the observed SMGs were biased to the brightest sources, studies with the SMA did confirm that these brightest single-dish sources were resolving into multiple galaxies. In Wang et al. (2011) the first examples of this 'multiplicity' were found with two sub-millimetre sources resolving into 2 and 3 galaxies, each with fluxes of 3–5 mJy, that were physically unassociated based off their spectroscopic redshifts. This highlighted the necessity of sub-millimetre interferometry for reliable identifications of SMGs.

The most recent, generational leap in sub-millimetre astronomy has come from the Atacama Large Millimetre/Sub-millimetre Array (ALMA). A significant improvement over the SMA, it consists of 54 12 m diameter dishes and 12 7 m dishes with maximum baselines of 16 km. ALMA is orders of magnitude more sensitive and can reach milliarcsecond resolution and is therefore capable of imaging even the faintest SMGs from single-dish surveys in minutes. With ALMA in full operation we now have the opportunity to follow-up the thousands of sub-millimetre sources discovered in single-dish surveys such as S2CLS at sub-arcsecond resolutions to accurately identify all counterpart galaxies.

During Cycle 0, 126 sub-millimeter sources detected in the Extended *Chandra* Deep Field South (ECDFS) by LABOCA were followed up at 870 μm with ALMA (ALESS) which doubled the total number of interferometrically observed sub-millimetre sources (Hodge et al., 2013). ALESS found robust detections of 99 SMGs which formed the basis of a sample for a significant body of work (e.g. Swinbank et al., 2012; Karim et al., 2013; Wang et al., 2013; Simpson et al., 2014; da Cunha et al., 2015; Chen et al., 2015; Danielson et al., 2017). Since Cycle 0 there has been a number of 'blank field' surveys at millimetre wavelengths, which can exploit the larger field-of-view, primarily in the GOODS-S field (Walter et al., 2016; Dunlop et al., 2016; Franco et al., 2018; Cowie et al., 2018; Hatsukade et al., 2018) however being blank field surveys they return small samples of SMGs ($n \sim 20$) that make deriving physical properties of the population as a whole at their selection wavelengths difficult. Now that ALMA is fully operational it is an opportune time to follow-up single-dish surveys of larger cosmological volumes than the ECDFS to provide more statistically robust samples of SMGs.

1.4.5 SMG Properties

Photometric and spectroscopic redshift surveys place the median SMG redshift at $z \sim 2-3$. The first samples of SMGs identified and spectroscopic follow-up taken were the radio bright samples of Chapman et al. (2005) which found a median redshift of $z = 2.2 \pm 0.1$ for 73 radio bright SMGs. However we know this sample to be biased both due to the lack of *K*-correction in the radio waveband, and also limitations in the use of the Low Resolution Imaging Spectrograph (LRIS) used on the Keck telescope to obtain these redshift. The emission lines used to retrieve redshifts (Ly-α, [OII], [OIII], and Hα) are outside of the wavelength coverage of LRIS at redshifts of z =1.2–1.8, this is indicative of the problems with retrieving spectroscopic redshifts for SMGs in the optical/near-infrared. In Danielson et al. (2017) spectroscopic redshifts for 52 of the ALESS SMGs had a median redshift of $z = 2.40 \pm 0.10$, but again these are biased to SMGs which were optically or near-infrared bright. As spectroscopic redshifts prove difficult to obtain we can still use photometric redshifts to constrain the general properties of SMGs for example using MAGPHYS SED fitting da Cunha et al. (2015) found a median redshift of $z = 2.7 \pm 0.1$ for the ALESS SMGs.

These redshift distributions place SMGs at high-redshifts, with far-infrared luminosities in excess of $10^{12}\,L_{\odot}$ which classifies them as ultra-luminous infrared galaxies (ULIRGs). However in comparison to the local space density of ULIRGs, the SMGs at $z \sim$2 are found to be 1000 times higher (Daddi et al., 2007). The star-formation rates required to drive this far-infrared luminosity resulted in Swinbank et al. (2014) estimating that SMGs with $S_{870} > 1$ mJy account for 30-40 % of the total stellar mass density at $z \sim 2$. To understand what is triggering this intense star-formation, when we look to the local analogue ULIRGs they appear to be major mergers which are triggering starbursts (Sanders & Mirabel, 1996). Kinematics of SMGs and optical morphologies suggest these high redshift analogues also undergo merger driven starbursts, however not conclusive, with varying fractions of disturbed systems (Blain et al., 2002; Swinbank et al., 2006; Engel et al., 2010; Chen et al., 2015) and simulations suggesting that it is secular, disk instabilities that are the primary driver for the starburst (Cowley et al., 2015a). Whatever the trigger, the intense star-formation that results ($\sim$1000 $\mathrm{M}_{\odot}$ yr^{-1}) is intense enough that

the typical mass of a local elliptical galaxy ($10^{11}\,M_{\odot}$) can be amassed in $\sim$100 Myr. In addition the star-formation histories of massive elliptical galaxies show formation ages that broadly match the photometric distribution of SMGs (Whitaker et al., 2012; Estrada-Carpenter et al., 2019) and stellar populations which must have formed in a short duration burst (Thomas et al., 2005) which points to SMGs as likely candidate progenitors for the most massive elliptical galaxies in the local Universe.

1.4.6 The Progenitors of Local Ellipticals

For local ULIRGs, based on the high star-formation and major merger rates, Sanders et al. (1988) proposed the following evolutionary path (schematic shown in Figure 1.5). The ULIRG is triggered by the major merger of two gas rich galaxies compressing and cooling gas. The intense star-formation results in increased production of dust which then absorbs the UV emission from the OB stars and re-emits it in the infrared. The two galaxies cores coalesce and from the merging of the two super massive black holes an active galactic nuclei (AGN) is formed. The feedback winds from the AGN will expel the gas and dust from the galaxy and now the galaxy will be detected as potentially a quasar. As the galaxy lacks cool gas to form stars it transitions into a 'dead' elliptical galaxy.

Whilst SMGs are found in significantly higher densities than local ULIRGs and the dominance of mergers being the trigger for the starburst is less conclusive for SMGs than for local ULIRGs there is still a significant amount of evidence in agreement with the Sanders et al. (1988) model for SMGs. As noted above there are indicators that the local elliptical population has stellar populations that formed at the redshifts we find for SMGs (e.g. Nelan et al., 2005). In reverse, by assuming 100 Myr star-formation burst and then passively evolving the ALESS SMGs, Simpson et al. (2014) found the resulting H-band magnitudes and densities matched those of local ellipticals. Estimations of the dark matter halo masses from clustering strength measurements also suggest a link between the two populations (Hickox et al., 2012; Wilkinson et al., 2017) however there are significant uncertainties in these values due to a lack of robust SMG identification from sub-millimetre interferometry and the use of photometric redshifts.

There is mounting evidence of a link between SMGs and quasars too. The discovery

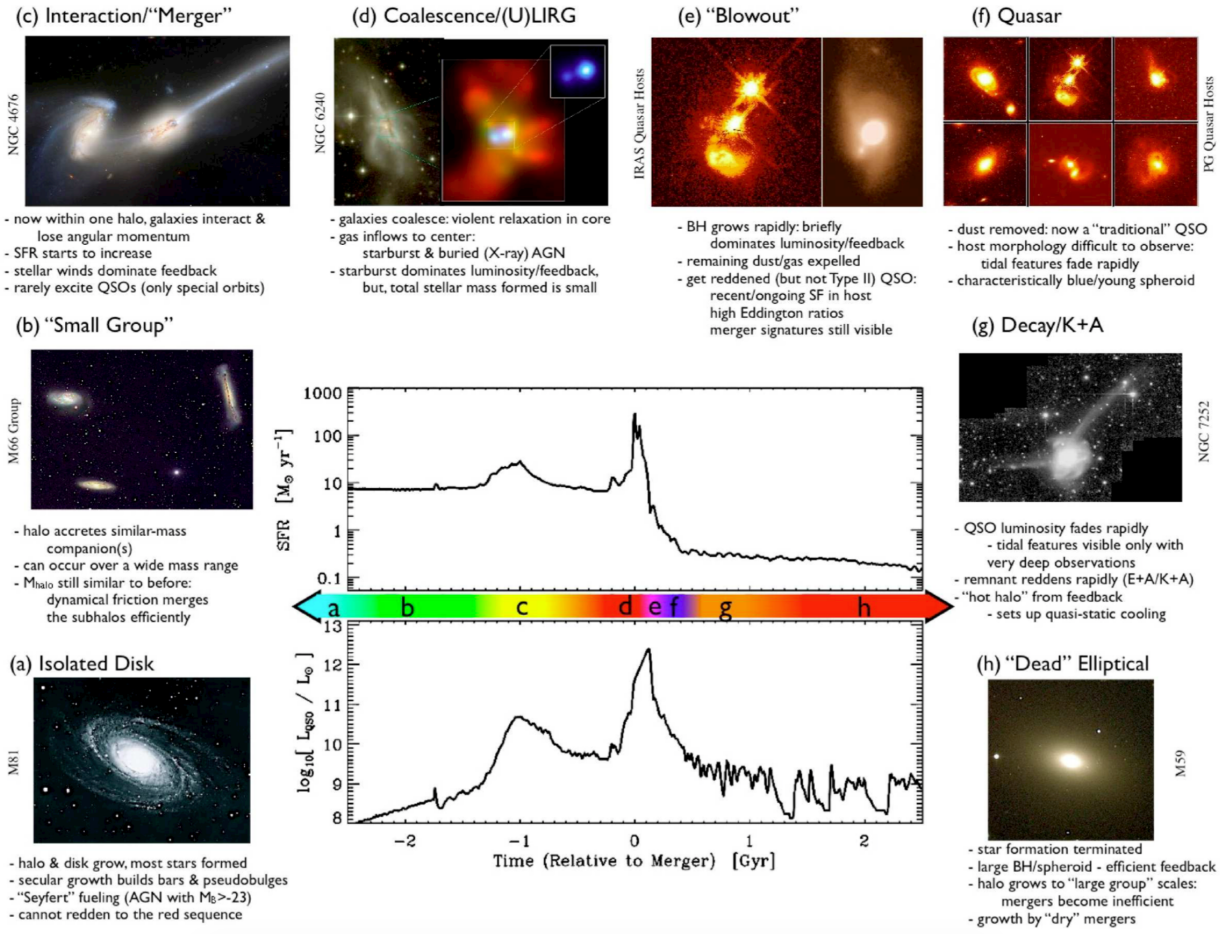

Figure 1.5: Schematic of the Sanders et al. (1988) model taken from Hopkins et al. (2008) which describes the proposed evolution path for local ULIRGs which is also applied to their SMG high-redshift cousins. Briefly, a merger triggers the starburst and as the two SMBH coalescse an AGN is formed which expels the gas and dust until the galaxy ceases star-formation and becomes an elliptical galaxy. The central plot demonstrates the brightness of the resulting quasar approximately matches the ensuing star-formation rate burst from the merger.

of a relation between a galaxies supermassive black hole mass and the stellar mass of the bulge ('Magorrian relation': Magorrian et al., 1998) suggests a co-evolutionary growth between the supermassive black hole and the host which is accounted for in the Sanders et al. (1988) model. The clustering analysis that suggested a link between SMGs and local ellipticals also suggests a link between SMGs and quasars, however the above mentioned caveats still hold true (Hickox et al., 2012). Further potential evidence came from the supermassive black hole masses for a sample of SMGs, measured from Hα, and Hβ emission lines, in Alexander et al. (2008) which were significantly lower than that expected from the 'Magorrian relation'. This suggests that subsequent to their SMG phase there must be a period of rapid black hole growth which is potentially the quasar phase suggested by the evolutionary model. Finally, using CO detections for a sample of far-infrared bright quasars, Coppin et al. (2008) (see also: Simpson et al., 2012) found for their fainter quasars they had black hole masses consistent with estimated SMG masses when accounting for Eddington-limited growth on time-scales equal to the gas depletion time-scales from the CO measurements. These black hole masses were also consistent with the local 'Magorrian relation' and thus potential 'transition' quasars between SMGs and local ellipticals as predicted in the model.

1.5 Thesis Overview

This thesis presents the high-resolution imaging of sub-millimetre bright galaxies found in both the UDS field and a detailed study of the far-infrared luminous population within the dense environment of a $z = 1.46$ cluster centre. Both samples are ALMA interferometric follow-up observations of SCUBA-2 selected sub-millimetre sources, with the aim to accurately identify the counterpart galaxies responsible for the sub-millimetre emission seen in the coarse SCUBA-2 imaging and derive a number of the galaxies properties. Chapters 2, 3, and 5 consist of published work (Stach et al., 2017, 2018), Chapter 4 is presented in work that has been submitted for review, and Chapter 6 summarises the conclusion of the previous chapters and introduces the future projects that are currently being worked on to take the work presented forward.

- **Chapter 2:** In chapter 2 I cover the sample selection, data reduction, and source extraction for the AS2UDS survey. This was an ALMA survey of 716 SCUBA-2 sources in the UDS field that were observed over four ALMA cycles, and this forms the basis for the following two chapters. The source extractions finds a final sample of 708 SMGs from the 716 maps and the second half of the chapter calculates the completeness fractions, flux deboosting values, ALMA SMG position offsets relative to the SCUBA-2 positions, and the single-dish flux recovery fractions and briefly discusses the implications of these values.

- **Chapter 3:** This chapter introduces the first results of the AS2UDS survey, the cumulative and differential 870 μm number counts and their comparison to the parent SCUBA-2 counts. In addition I investigate the multiplicity fraction, the rates at which single-dish source split into multiple SMGs in the high resolution imaging and how this fraction varies with single dish flux. Finally, from the photometric redshifts of these multiples I estimate constraints on the percentage of the multiples which are physically associated and not just chance projections along our line of sight.

- **Chapter 4:** Following on from chapter 3, this chapter presents more results from the AS2UDS survey, including the first results from our MAGPHYS SED fitting, namely the photometric redshift distributions. I combine these photometric redshifts with the multi-wavelength coverage of the field to select AGN dominated systems in our catalogue and investigate the potential evolution path of SMGs by comparing their formation redshift and number densities to those of lower redshift quiescent galaxies.

- **Chapter 5:** In this chapter I cover the ALMA follow-up of the central four sources, detected in SCUBA-2, at the centre of the cluster XCS J2215. This cluster shows an elevated density of sub-millimetre bright sources in this high density region in comparison to other clusters at a similar redshift range and the ALMA follow-up found an extremely high rate of multiplicity with the 4 sources resolving into 14 galaxies. In addition to the dust measurements this chapter covers the CO gas detections for

six of the galaxies and we compare the gas and dust properties to galaxies in the field at a similar redshift.

- **Chapter 6:** I end with Chapter 6, which recaps the previous chapters and introduces a number of ongoing projects and future projects that we have been allocated telescope time for.

- **Appendices:** In Appendix A I present the locations and fluxes for all 708 AS2UDS SMGs.

CHAPTER 2

An ALMA Survey of the SCUBA-2 Cosmology Legacy Survey UKIDSS/UDS field: Data Reduction and Catalogue Creation

2.1 Motivation

In the previous chapter I outlined how the high-redshift SMG population are some of the brightest galaxies in the Universe and galaxies with amongst the higher star-formation rates in the Universe and thus a vital component in the understanding of galaxy formation and evolution (Smail et al., 1997; Blain et al., 2002; Casey et al., 2014). This population was originally detected through single-dish observations, e.g. using SCUBA (Smail et al., 1997; Barger et al., 1998), and more recently the largest 850 μm survey of these sources is the SCUBA-2 Cosmology Legacy Survey (S2CLS) which detects over 3000 sources across seven extragalactic fields (Geach et al., 2017). As the single-dish surveys suffer from coarse angular resolution (FWHM $\sim$15$''$) this makes identifying the galaxies responsible for the sub-millimetre emission difficult. Attempts to identify the counterparts through statistical associations at wavelengths with higher spatial resolutions are incomplete and biased (Ivison et al., 2007; Biggs et al., 2011). With the advent of ALMA, precise identification of galaxy counterparts selected at the same wavelengths as the single-dish surveys is now possible. The previously largest such ALMA follow-up survey, the ALMA follow-up of LABOCA selected sources (Weiß et al., 2009) in the Ex-

tended *Chandra* Deep-Field South (ECDFS) (ALESS) (Hodge et al., 2013), demonstrated the extent of the limitations of the probabilistic identification techniques, finding that radio and mid-infrared associations were only correctly identifying the source galaxies $\sim$55 % of the time (Hodge et al., 2013).

ALESS highlighted the requirement of interferometric follow-up observations of the larger single-dish surveys for accurate counterpart identification. Whilst ALESS was a significant leap in robustly identified SMGs it was still limited by the relatively small volume probed in the ECDFS. With the completion of the S2CLS survey (Geach et al., 2017), significantly larger degree-scale extragalactic fields covered by 850 μm single-dish observations that are ALMA observable are available for high-resolution interferometric follow-up. The UDS field was chosen as it was the degree-scale field of the S2CLS survey which had the deepest, most uniform ($\sigma_{850} = 0.9\,\mathrm{mJy\,beam^{-1}}$) observations. The S2CLS UDS map contained 716 sources detected with signal-to-noise ratios $>$4.0 and these formed the sample for our ALMA follow-up survey (AS2UDS). The UDS field provides a $\sim$4$\times$ increase in survey area than the ECDFS and $\sim$7$\times$ larger sample with a smaller parent beam size. Combined with the extensive multi-wavelength coverage available, from radio to X-ray and including very deep near-infrared imaging from UKIDSS UDS (Almaini et al. in prep.), the UDS field provided the best opportunity for ALMA studies on SMGs.

In this chapter I cover the data reduction and source extraction for the 716 maps in the ALMA survey of the SCUBA-2 sources in the UDS field from the S2CLS survey. This chapter contains content taken from both Stach et al. (2018) and Stach et al. (2019, submitted), which are covered in Chapters 3 and 4.

2.2 Interferometry and ALMA

As mentioned above, ALMA provides an order of magnitude increase in resolution in comparison to single-dish observations and this is made possible through 'synthesis imaging', i.e. the process of combining observations from a system of telescopes to produce images with angular resolutions set by the scale of the physical separations of the tele-

scopes and not their individual dish sizes. A full description of the principles of interferometry can be found at Thompson et al. (1986) however here is a brief description of the technique.

The λ/D scaling relation for image resolution means that at the sub-millimetre wavelengths it is not feasible to create single dishes which produce images at arcsecond resolutions. However, due to the nature of measuring electromagnetic power at antennas, there is no need for measurements to be made at *physically* connected parts of a parabolic dish, rather just pairs of voltage readings at any arbitrary separation. Interferometry is the process of measuring the interference patterns created by these pairs of physically separated antenna, thus the sky brightness is sampled discretely based on the projected separation distances (baselines) of the individual antenna. The 'magic' of interferometry comes from the van Cittert-Zernike theorem which states the inverse Fourier transform of the measured complex visibilites derived from the interference patterns measured by the antennae in an array returns the intrinsic sky brightness distribution. The major complication however is that the complex visibilities are sampled at discrete baselines set by the antenna placement and therefore the true sky brightness becomes an inverse Fourier transform of the convolution of the measured integrated complex visibilities with a point spread function, sometimes called the *dirty beam*.

For the closest, true sky brightness pattern to be recovered the Fourier transform requires complete information at all angular scales from the complex visibilities. This is impractical, e.g. minimum baselines might be set by physical constraints on the separation of telescopes (i.e. the ALMA telescopes cannot be placed so close together such that they block line-of-sight of neighbouring telescopes), and with a lack of coverage in the angular scales of the complex visibilities (*uv*-plane) comes a lack of sensitivity in the interferometer for emission at the corresponding angular scales and through the inverse Fourier transform process will result in noise artifacts that complicate the data reduction process. Thus any observer wishing to apply for observing time with an interferometer needs to consider not just the integration time required to return a detection, but also the configuration of the array of telescopes and whether it will return the image at the resolution and sensitivity at the emission scales required e.g. long baselines return superior

angular resolution whilst short baselines are more sensitive to extended emission.

For sub-millimetre imaging the Atacama Large Millimetre/Sub-millimetre Array (ALMA) is the best (and most in demand) interferometer to date. Situated in one of the driest climates in the World at the Chajnantor Plateau in the Atacama Desert in Chile results in minimal water vapour, a requirement for sub-millimetre observations. ALMA minimises the impact of the poor sampling of the *uv*-plane mentioned above by consisting of 54 12 m diameter dishes and 12 7 m dishes which can be moved to differing array placement configurations throughout the year. For the 12 m dishes the minimum baselines length is 15 m and maximum baselines set at 16 km. The smaller 7 m dishes form part of the Atacama Compact Array (ACA) which, due to their smaller size, can be placed closer together to minimum baselines of 9 m and maximum 30 m and thus they sample the more extended angular scales in comparison to the 12 m array. In addition four of the 12 m telescopes can act as single-dish telescopes, the Total Power array (TP), and thus fill in the baselines smaller than that of the ACA array (0-12 m) and therefore between the 12 m, ACA, and TP arrays baselines up to 16 km can be covered. Each of these telescopes are equipped with receivers that currently measure signals in 8 possible wavelength bands ranging from 0.3–3.6 mm with planned further expansion into two more wavelength bands at 3.3–8.6 mm. ALMA therefore is the optimum instrument for follow-up observations of S2CLS sources, with resolution and depth improvements over the Sub-millimeter Array (SMA) with shorter integration times with fields of view at the matched single-dish wavelengths which match the resolution of the SCUBA-2 beam.

2.3 Sample Selection

The AS2UDS survey, is a high-resolution, sub-millimetre interferometric follow-up survey of the SCUBA-2 850 μm sources selected from the S2CLS map of the UDS field (Geach et al., 2017) (Fig 2.1). The parent single-dish survey covers an area of 0.96 deg^2, with noise levels below 1.3 mJy and a median depth of $\sigma_{850} = 0.88$ mJy beam^{-1} with 80% of sources identified in regions of the map with $\sigma_{850} = 0.86$–1.02 mJy beam^{-1} (Geach et al., 2017). Across four ALMA cycles (1, 3, 4 and 5) we observed all $716 > 4\sigma$ sources

from the S2CLS map (corresponding to observed flux densities $S_{850} \geq 3.4$ mJy) (see: Figure 2.1).

In Cycle 1 (Project ID: 2012.1.00090.S), 30 of the brightest sources from an early version of the SCUBA-2 UDS map (data taken before 2013 February) were observed in ALMA Band 7 (Simpson et al., 2015b,a, 2017). This early version of the SCUBA-2 map had a depth of only $\sigma_{850} \sim 2.0\,\mathrm{mJy\,beam^{-1}}$ and subsequent integration time in the S2CLS survey scattered three of these sources below our final sample selection criteria ($> 4\sigma$), leaving 27 of these original single-dish detected sources in our final sample. The remaining 689 single-dish sources in the final S2CLS catalogue were observed across ALMA Cycles 3 and 4 (Project ID: 2015.1.01528.S and 2016.1.00434.S, respectively). To cross calibrate the data, a fraction of these sources were observed twice, once in Cycle 3 *and* 4. In addition, in Cycle 5 ten of the brightest SCUBA-2 sources which returned 'blank' maps from the Cycle 3 and 4 ALMA observations were re-observed at greater depth (Project ID: 2017.1.01492.S), these maps will be discussed further in §4.4.3.

2.4 Data Reduction

Our ALMA targets were observed in Band 7 (central frequency 344 GHz equivalent to $\sim 870\,\mu$m). This was chosen to match the earlier ALESS study (Hodge et al., 2013) and closely matched the central frequency of the SCUBA-2 850 μm filter (Figure 2.2). At this frequency the FWHM of the ALMA primary beam ($17\farcs3$) covers the FWHM of the SCUBA-2 beam ($14\farcs7$). Cycle 1 observations were carried out on 2013 November 1 (Simpson et al., 2017), Cycle 3 between 2016 July 23 and August 11, Cycle 4 between 2016 November 9 and 17 and 2017 May 6, and Cycle 5 on 2018 August 24.

These ALMA Band 7 continuum observations were 150 second integrations in Cycle 1 using 26 dishes, 40 second integrations in Cycle 3 and 4 (with 45–50 dishes), and 285 second integrations using 44 dishes in Cycle 5, with the 7.5 GHz bandwidth of the four spectral windows centred at 344.00 GHz. The array configurations for Cycle 1 observations yielded a median synthesised beam size of $0\farcs35 \times 0\farcs25$. With Cycle 3 and 4 observations we aimed to match this resolution, however our Cycle 3 observations were

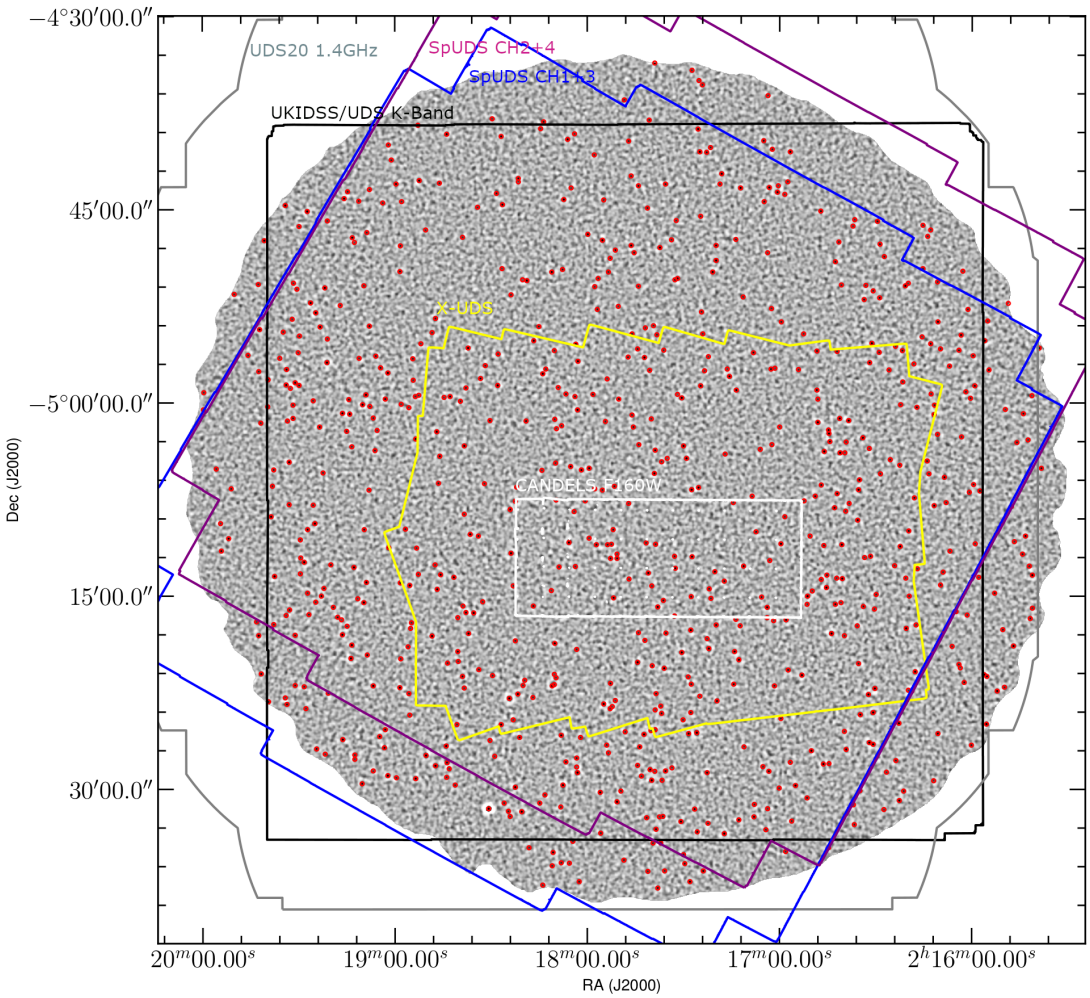

Figure 2.1: A sample of the multi-wavelength coverage of the AS2UDS sample which motivates this extra-galactic field being chosen for high resolution ALMA follow-up. The background shows the S2CLS 850 μm UDS map from which the parent sample is extracted (Geach et al., 2017). The red circles are the primary beams for AS2UDS targetting the 4 σ detections in the S2CLS map. The black outline shows the *K*-band coverage that forms the footprint for the UKIDSS UDS catalogue (O. Almaini et al. in prep.). The *Spitzer*/IRAC CH1/3 and CH2/4 coverage is shown in blue/purple respectively, the *HST* CANDELS F160W in white, VLA 1.4 GHz in grey, and the X-UDS *Chandra* coverage in yellow (Kocevski et al., 2018).

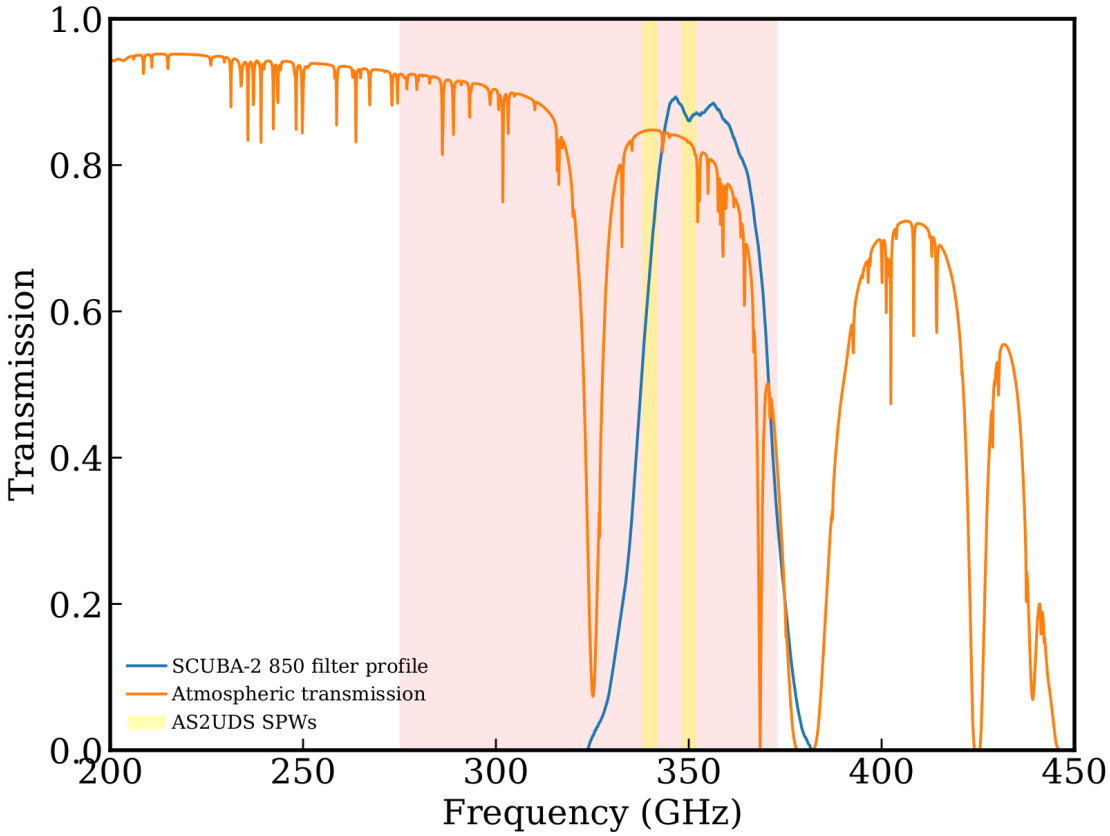

Figure 2.2: The AS2UDS frequency coverage, shown in the yellow bands, was chosen to match the central frequency of the SCUBA-2 850 μm filter which is shown in blue. This frequency, by design, matches a peak in the atmospheric transmission in ALMA Band 7, which I show for a precipitable water vapour value of 1.0 mm in orange. The spectral windows (SPWs) for AS2UDS are plotted as the yellow bars.

taken with a more extended array configurations resulting in median synthesised beam sizes of $0\farcs19\times0\farcs18$ ('natural' weighting). Our Cycle 5 observations were intended to test whether the lack of detected counterparts in the ALMA observations of ten SCUBA-2 sources observed in previous cycles was not a result of flux being resolved out, and therefore were taken with a median synthesised beam size of $0\farcs81\times0\farcs54$.

The observing strategy for the bulk of the targets, which were observed in Cycles 3 and 4, was to split the sources into multiple scheduling blocks with sources allocated randomly to ensure any observing incompleteness would not result in a sample biased to any SCUBA-2 (and potentially ALMA) flux range. Phase centres for each observation were set to the SCUBA-2 positions of the S2CLS catalogue at the time of ALMA proposal submissions. For the 689 SCUBA-2 sources followed up in Cycle 3, 4, and 5 this results in phase centres coincident to the SCUBA-2 positions from the S2CLS DR1 sub-millimetre source catalogue (Geach et al., 2017), however for Cycle 1 the 27 SCUBA-2 source positions were not corrected for a systematic astrometric offset in the interim map and an offset exists between the final S2CLS DR1 source position and ALMA phase centres, with a median offset of $3.2^{+0.1}_{-0.6}$ arcsec. The ALMA primary beam size is large enough that this offset still results in the majority ($\sim95\%$) of the SCUBA-2 beam falling within the primary beam of in our 30 Cycle 1 observations and, as discussed in §2.7, these are observations which were targeting the brighter SCUBA-2 sources and thus we expect detections closer to the offset phase centres and thus still well within the ALMA primary beams.

Figure 2.3 shows the basic work flow for producing ALMA images with CASA. Before imaging of interferometric data can be performed the calibration of the raw data (called 'measurement sets') needs to be completed. This involves a number of steps, explained below, which correct the raw data for a number of atmospheric and instrumental effects on the measurement sets and identifies potential problematic sections of the data (e.g. measurements taken from a temporarily faulty telescope) and flags those data so they are not included in the imaging, as they may be responsible for artifacts in the final imaging. For the calibration, COMMON ASTRONOMY SOFTWARE APPLICATION (CASA McMullin et al., 2007) v4.1, v4.5.3, v4.7.2, v5.3.0 was used for data from Cycle

1, 3, 4, and 5 respectively.

The standard calibration scripts supplied with each observing block were used to create initial measurement sets with the Water Vapour Radiometry calibrations (WVR), which corrects antennae phase variations with time as a result of the atmospheric water lines, and the T_{sys} corrections which corrects for receiver noise and atmospheric attenuation with time and frequency pre-applied using the CASA task APPLYCAL. No intervention in this stage of the calibration was required as the supplied default calibration scripts correctly identified problematic WVR measurements and where flagged they automatically interpolated WVR measurements from neighbouring antennas and applied this to the faulty antennas.

After these instrumental calibrators a series of calibrations are applied to the measurement sets based off observations of a number of quasars. These calibrator observations are taken regularly during ALMA observations with the aim of correcting phase and amplitude errors in the visibilities for each baseline of the science targets. Since the quasars are well studied sources with known flux densities and model visibilities the corrections required to the phase and amplitude of the observed visibilities to return the true visibilities can be derived. For each calibrator field (quasar pointing) a series of diagnostic plots are made such as the *uv*-amplitude as a function of spectral window channel, amplitude against time, etc and unexpected behaviour such as discontinuities or abnormally low amplitude from single antenna are checked with problematic regions in these plots flagged. Finally the bandpass and gain calibration tables are calculated using the CASA BANDPASS and GAINCAL tasks on the calibrator fields (J0006−0623, J0423−0120, J0238+1636, J0241−0815, and J0006−0623) and absolute flux scaling using the SETJY task on one of the flux calibrator fields: J0217−0820 and J0238+1636. These calibrations are then applied to the raw measurement set using APPLYCAL creating a 'corrected' data column that was ready for the imaging in the data reduction process.

For the imaging CASA v 4.7.2 was used, with the CONCAT task to combine the visibilities of the 125 maps that were observed in both Cycle 3 and Cycle 4. To create the continuum maps we used the CLEAN task in multi-frequency synthesis mode. Previous studies on the sizes of sub-millimetre galaxies suggests their sub-millimetre intrinsic sizes

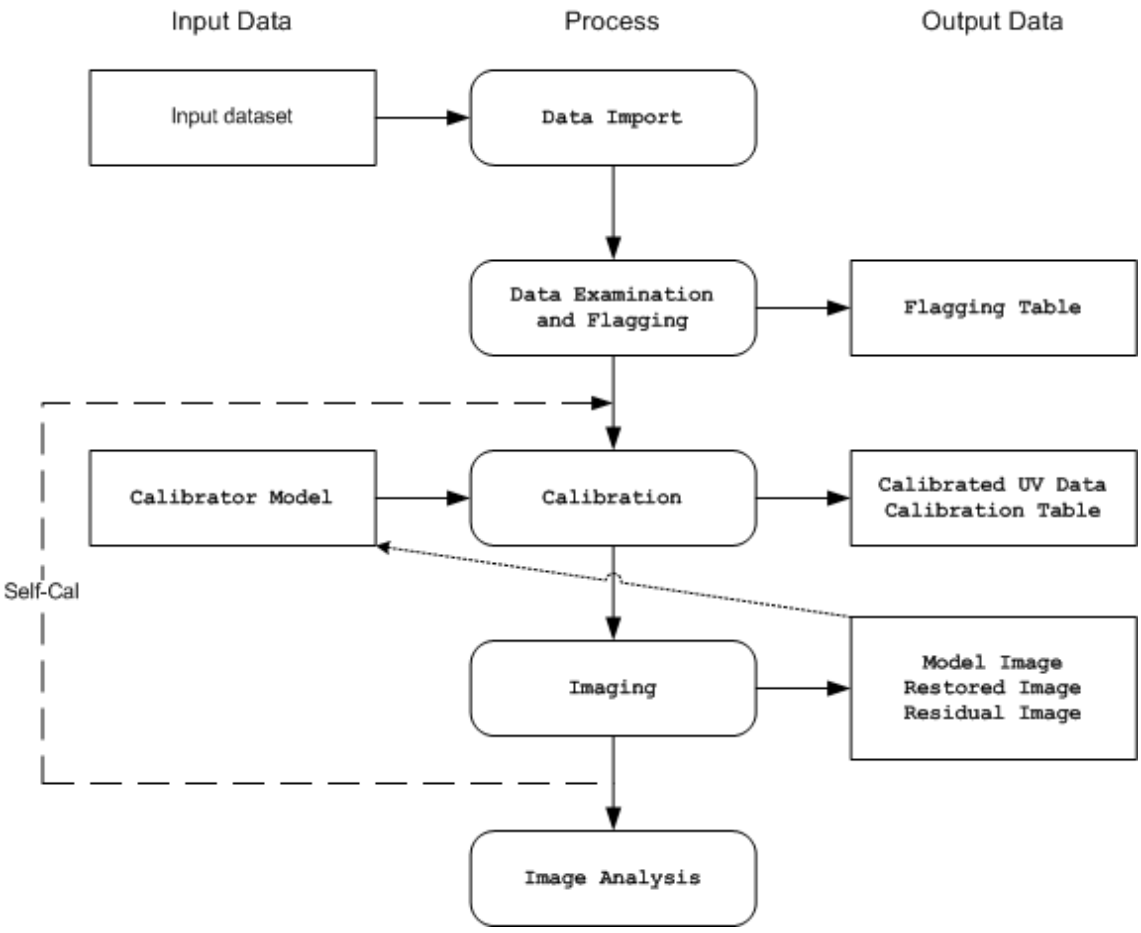

Figure 2.3: Flow chart (taken from the CASA User Reference & Cookbook) of the CASA data-reduction process from the delivered raw input data to the output images.

Table 2.1: Representative 'detection' map parameters per Cycle for AS2UDS.

Cycle	Number of Sources	Restoring Beam Shape	Median RMS Depth
1	27	$0\farcs73 \times 0\farcs59$	$0.25\,\mathrm{mJy\,beam^{-1}}$
3	533	$0\farcs56 \times 0\farcs50$	$0.34\,\mathrm{mJy\,beam^{-1}}$
4	281	$0\farcs58 \times 0\farcs55$	$0.23\,\mathrm{mJy\,beam^{-1}}$
5	10	$0\farcs79 \times 0\farcs52$	$0.085\,\mathrm{mJy\,beam^{-1}}$

are $0\farcs3 \pm 0\farcs1$ (e.g. Simpson et al., 2015a; Hodge et al., 2016; Ikarashi et al., 2017) therefore we expect the majority of our detections to be marginally resolved. To ensure we are not biased against selecting extended sources, by remaining sensitive to extended flux from our SMGs, we employed a $0\farcs5$ FWHM Gaussian taper in the *uv*-plane using the *uvtaper* parameter in CLEAN for the Cycle 1,3, and 4 data. This effectively down-weights the visibilities from the longer baselines thus enhancing the sensitivity to extended emission at the expense of overall reduced sensitivity in the maps (see Figure 2.4). Combined with natural weighting this resulted in 'detection' maps with median synthesized beam sizes of $0\farcs73 \times 0\farcs59$ for Cycle 1, $0\farcs56 \times 0\farcs50$ for Cycle 3 and $0\farcs58 \times 0\farcs55$ for Cycle 4 (the untapered Cycle 5 maps has beam sizes $0\farcs79 \times 0\farcs52$), see Table 2.1.

For the ALMA map cleaning, the first step was creating 'dirty' maps, 512×512 pixels in size with a pixel scale of $0\farcs06$ ($30\farcs7$ square), by combining the spectral windows with no cleaning cycles applied. We calculated the average root mean square (rms) flux density for each of these 'dirty' maps by first removing pixels associated with potential sources in the maps by applying an iterative sigma-clipping routine to the map, and then finding the rms value of the unclipped values (σ). Each map was then initially cleaned to $3\,\sigma$, and islands of pixels with flux densities above $4\,\sigma$ were convolved with the reconstructed beam to create cleaning masks. If no islands were detected then the initially-cleaned map was taken as the final map however if any sources were detected then the clean mask was applied and sources cleaned to $1.5\,\sigma$. This resulted in final cleaned 'detection' maps which have mean depths of $\sigma_{870} = 0.25\,\mathrm{mJy\,beam^{-1}}$ for Cycle 1, $\sigma_{870} = 0.34\,\mathrm{mJy\,beam^{-1}}$ for Cycle 3, $\sigma_{870} = 0.23\,\mathrm{mJy\,beam^{-1}}$ for Cycle 4, and $\sigma_{870} = 0.085\,\mathrm{mJy\,beam^{-1}}$ for Cycle 5. Figure 2.5 shows the histogram of the depths for each of the 716 images with the median

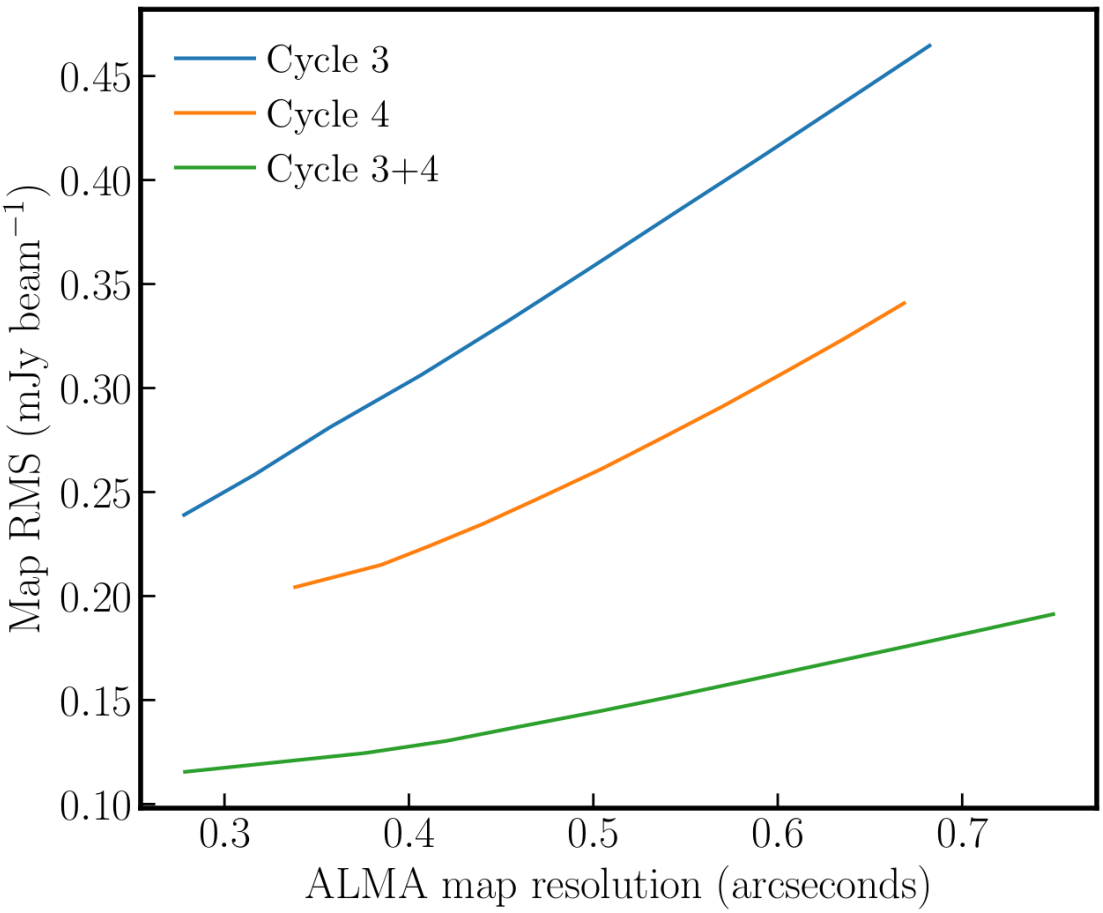

Figure 2.4: The ALMA map rms values as a function of the map resolution after *uv*-tapering for a random AS2UDS map taken from Cycle 3, 4 and a map observed both in Cycle 3 and 4 and subsequently having its visibilities concatenated. The finest resolution for each cycle is the untapered map, and then progressively increasing uv-tapers are applied, downweighting more information from the longest baselines thus reducing the resolution of the maps and increasing the noise/reducing sensitivity. This highlights the compromise with *uv*-tapering, for our 'detection' maps in Cycle 3, where a tapering to a $\sim$0.″5 resolution results in an 50 % increase in the rms noise of the maps. In comparison for the maps that were imaged in Cycle 3 *and* 4 this same level of tapering results in only a $\sim$25 % increase in the rms noise as these maps benefit from the shorter baseline observations taken in Cycle 4.

depth across the survey of $0.3^{+0.1}_{-0.2}$ mJy beam^{-1}, which is $\sim 3\times$ deeper than the original single-dish SCUBA-2 survey but with a beam $\sim 600\times$ smaller in area – allowing us to precisely locate the source(s) of the sub-millimetre emission seen by SCUBA-2.

2.5 Source Extraction

A variety of source extraction methods were tested across the 716 maps. The first method was using the source extraction software written specifically for radio interferometric images, AEGEAN Hancock et al. (2012). This uses a flood-fill algorithm where groups of adjacent pixels above a user-specified significance are grouped into islands and then these islands are split into a number of Gaussian components determined by the 'curvature' of the map (for details see: Hancock et al., 2012, 2018).

The second method was to replicate the process performed in Simpson et al. (2015b) for the AS2UDS Cycle 1 data, which was extracting sources based off the SNR of the peak flux density pixel values associated with each potential source being greater than four sigma. As the Cycle 1 maps were observed at a lower resolution to the Cycle 3 and 4 maps, the 'detection' maps in Simpson et al. (2015b,a) were *uv*-tapered to $\sim 0\farcs8$ resolution and thus every source detected in these low resolution maps would be expected to be unresolved and thus the peak source brightness should correspond to the true flux density of the source. The Cycle 3 and 4 data was observed at a higher resolution and thus could not be *uv*-tapered to the same low resolution and thus we expect a number of the detected sources to be at least partially resolved and thus a peak brightness would underestimate the true source flux density and would be a less reliable SNR indicator for our sources. For this reason a third method tested was *aperture* SNRs.

We calculated aperture SNRs by first using SEXTRACTOR to find $> 2\,\sigma$ peaks within the 'detection' maps. Noise estimates were then calculated from the standard deviation in the integrated fluxes in 100 randomly placed $0\farcs5$ diameter apertures in each map. These were then used, along with the $0\farcs5$ diameter flux measured for each detection, to determine the signal-to-noise ratio (SNR) of the sources. As we used an aperture smaller than the beam size the mean $0\farcs5$ aperture depths in the detection maps are approximately a

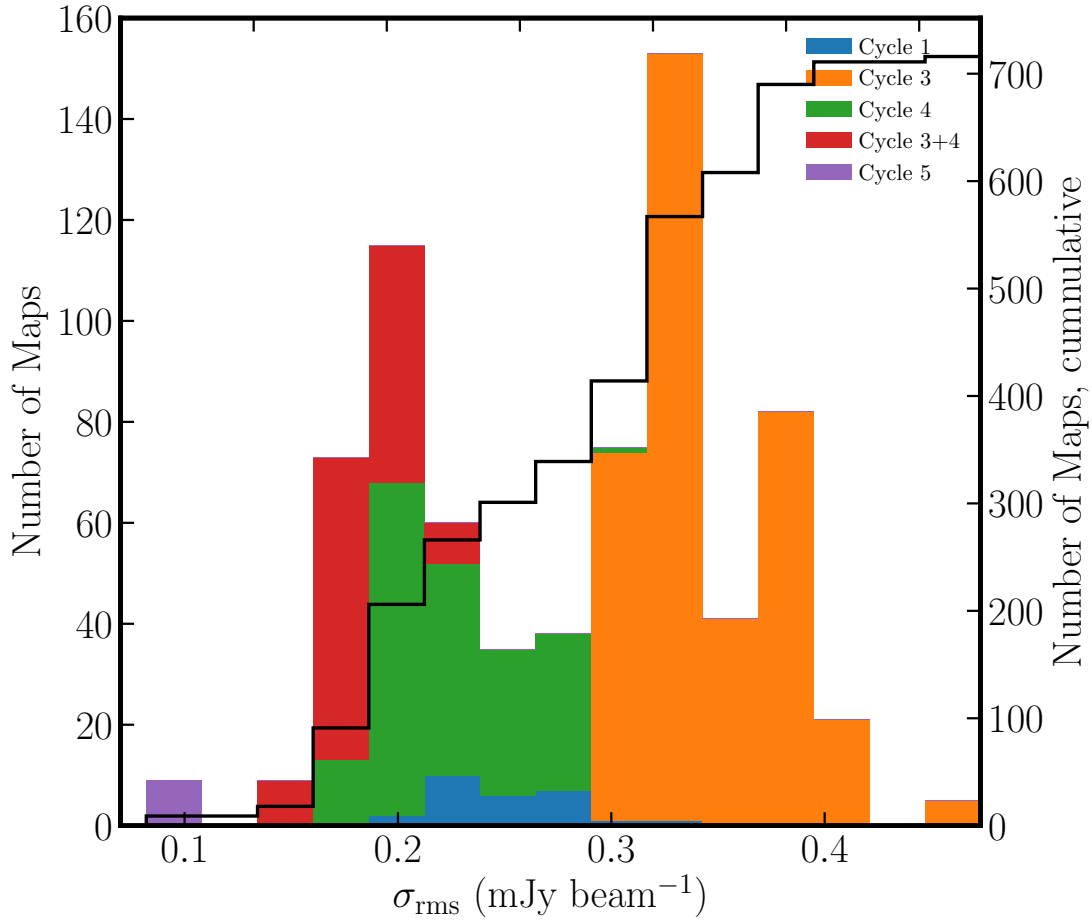

Figure 2.5: The distribution of the rms noise estimates from the 0.″5 *uv*-tapered detection maps for the different cycles used in AS2UDS. Adopting similar reconstructed beam sizes across all our maps results in the final rms noise varying inversely with their original observed resolution, with the exception of the purposefully much deeper 'blank' field repeat observations in Cycle 5. Deviations in rms across the same cycle are a result of different observing conditions. Overlaid is the cumulative distribution of the rms which shows after tapering the median rms of the full survey is $0.3^{+0.1}_{-0.2}$ mJy beam^{-1}.

factor of two deeper than the noise per beams quoted above (with the caveat of a corresponding aperture correction).

Our choice of detection method was made by finding the method which returned the greatest number of detected galaxies yet still returning a 98 % purity rate, $P_{\rm r}$ (2 % contamination), calculated as follows:

$$P_{\rm r} = \frac{N_p - N_n}{N_p}, \tag{2.5.1}$$

where N_p is the number of positive sources detected above the chosen SNR limit (i.e. 708) and N_n is the number of sources detected above the same limit in the inverted detection maps (made by multiplying the detection maps by -1).

For each detection method we varied the threshold SNR for detection and found the number of detected galaxies as a function of the resulting purity rate and we show this in Figure 2.6. The aperture SNR method returned the most detected galaxies (708), at the 98 % purity, this corresponded to sources detected at a 4.3 SNR with this method (Figure 2.7). Therefore the final catalogue consists of the 708[1] ALMA-detected SMGs in the maps of 716 SCUBA-2 sources that have a $0\farcs5$ aperture SNR ≥ 4.3 and fall within the primary beam of the ALMA maps.

We confirm the behaviour of the noise in our maps by comparing our number of 'negative' sources from the inverted maps at our selected SNR threshold against that expected from a simple Gaussian distribution of independent synthesised beams (Dunlop et al., 2016). In AS2UDS, for our average restored beam size, there are roughly $\sim$450,000 independent beams across the 716 ALMA pointings. For Gaussian statistics we would then expect ~ 8 'negative' sources at $4.3\,\sigma$. However, as noted by Dunlop et al. (2016), based on Condon (1997); Condon et al. (1998), there are effectively twice as many statistically independent noise samples as one would expect from a naive Gaussian approach due to the non-independence of pixel values in synthesised imaging. This would result in an expected ~ 16 "negative" sources or 2.3 ± 0.5 %, which is consistent with the number we detect.

[1]We detect the strongly lensed SMG 'Orochi' (Ikarashi et al., 2011) but remove this from our analysis.

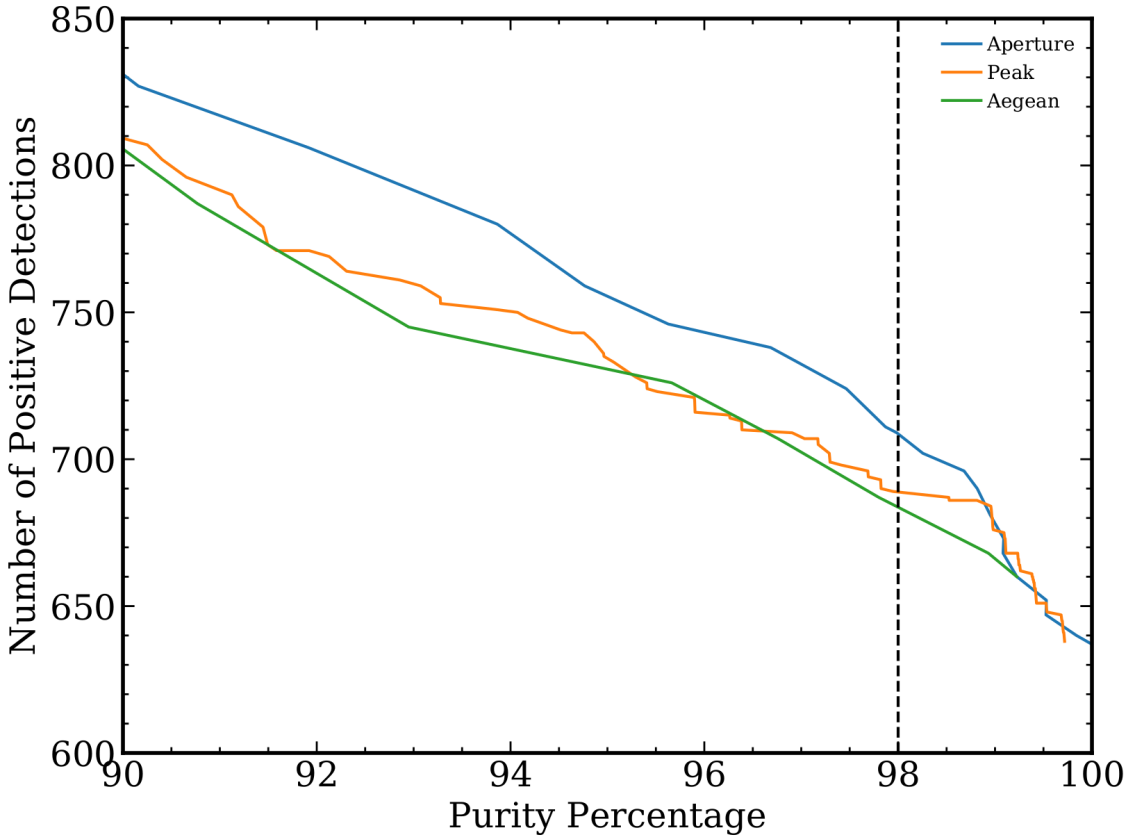

Figure 2.6: The number of detected galaxies as a function of the Purity Percentage derived from the ratio of positive source and 'negative' sources from the inverted source detection maps for the three source extraction methods. The purity corresponds to differing SNR threshold for each method, with ultimately the $0\farcs5$ aperture SNR method returning the most galaxies detected at the 98 % purity cut with 708 detections.

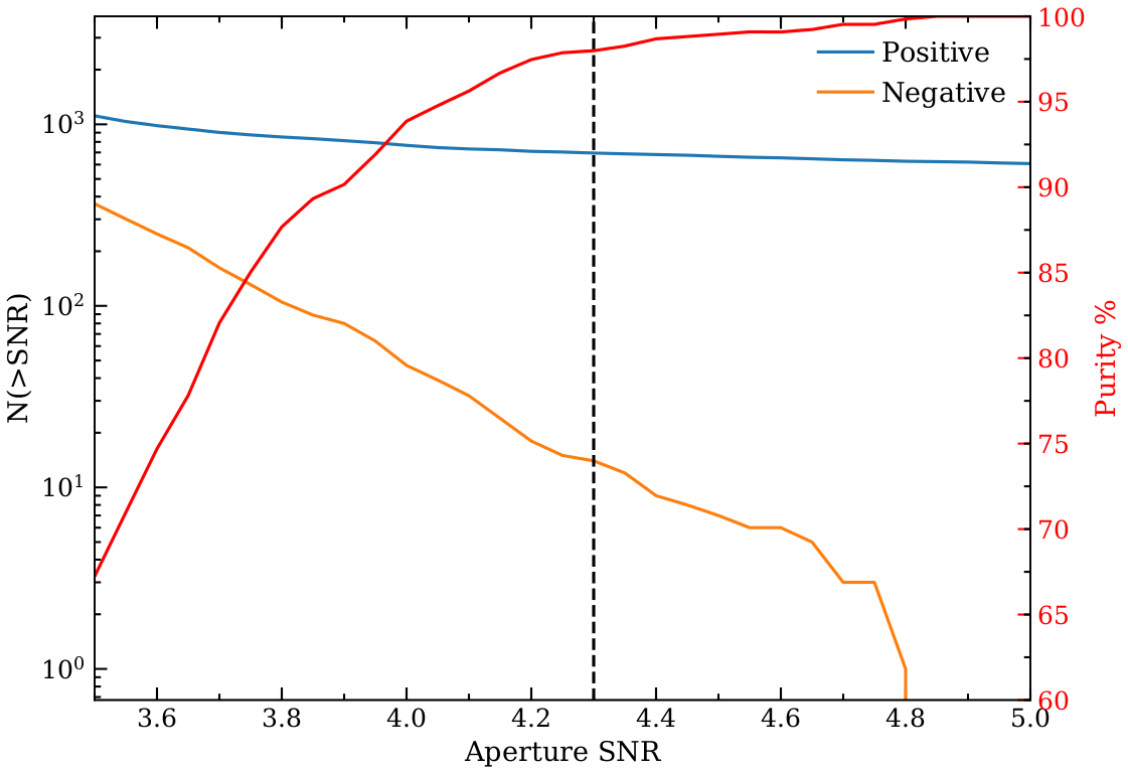

Figure 2.7: The cumulative numbers of sources detected in our 716 ALMA maps above a given signal-to-noise ratio in both the tapered detection maps (Positive) and the inverted detection maps (Negative). We select a SNR threshold for the final AS2UDS catalogue which minimises the contamination from spurious detections, as estimated from the number of equivalent SNR negative sources. We show the corresponding 'purity' as a function of SNR threshold and mark our adopted 4.3 σ threshold (dashed line), which yields a 98 % purity, equivalent to 14 false sources in a final catalogue of 695 SMGs.

To measure the flux density of our sources, 1.″0 diameter aperture fluxes were extracted for the 708 sources from the primary beam corrected maps. A 20 % aperture correction is applied to the fluxes. This correction is derived from aperture fluxes taken from the flux calibrator maps imaged in the same manner as the science targets. We note that our typical sources are not expected to be well-resolved in these 0.″5-tapered maps. The fluxes were additionally flux deboosted using the same methodology as Simpson et al. (2015a), which is briefly described below.

2.6 Completeness and Flux Deboosting

To calculate the completeness and flux deboosting factors for our ALMA catalogue we inserted model sources into simulated ALMA maps and determined the properties of those which were recovered. We start with simulated noise maps, to make these as realistic as possible we used ten residual maps output from CASA (i.e. an observed ALMA map where the source flux from any detected sources has been removed). The maps were selected to match the distribution in observed σ_{870} for all 716 AS2UDS pointings. Model sources with flux densities drawn from a steeply declining power-law distribution with an index of -2, consistent with Karim et al. (2013); Simpson et al. (2015a), and intrinsic FWHM sizes drawn uniformly from a range 0–0.″9, were convolved with ALMA synthesized beams and inserted into 60,000 simulated noise maps, with one simulated source injected into each of these noise maps to avoid the possibility of multiple injected sources being injected into the same beam location. Then we applied our source detection algorithm and measured recovered fluxes as detailed above, with a successful recovery claimed for detections within the size of a synthesized beam, i.e. 0.″6, from the injected model source position.

The intrinsic sizes of the injected sources has a noticeable effect on the recovered completeness fractions, particularly at lower signal-to-noise (see also: Franco et al., 2018). In Figure 2.8 we show completeness fractions for the recovered sources in Cycle 3, Cycle 4, and Cycle 3+4 for the complete simulated sample in the solid lines and the completeness fractions when cutting simulated sources with intrinsic FWHM$>$0.″6 (dashed lines).

At the highest signal-to-noise, and at the original SCUBA-2 flux limit of $S_{850} \geq 4.0$ mJy, AS2UDS is 98 ± 1 % complete for all simulated sources with only the most extended sources suffering some more significant incompleteness (see: Stach et al., 2018). The difference in completeness ratios at the fainter end however becomes more pronounced with a 1.5 mJy source having a median 52±4% chance of detection with an intrinsic source size $<0\farcs3$, 25±2% for sizes $0\farcs3$–$0\farcs6$, and 7±1% for sizes $>0\farcs6$. We note that our simulated sources had sizes which were uniformly distributed up to $0\farcs9$, whereas previous studies suggest median sub-millimeter sizes of $\sim 0\farcs3$ (Tacconi et al., 2006; Simpson et al., 2015b) therefore the 98±1 % completeness for $S_{870} \geq 4.0$ mJy is probably conservative.

Next, we estimate the effect of flux boosting. The flux boosting is a potential statistical bias in the catalogue source fluxes due to the non-uniform flux distribution of the intrinsic sources. The noise fluctuations in the maps results in a measured source flux being possibly scattered up and thus being detected in our signal-to-noise ratio cut catalogue. Due to the shape of sub-millimetre number counts there are many more potential SMGs that will be scattered up in our catalogue at faint fluxes than catalogue sources at higher fluxes being scattered down, i.e. a kind of Eddington bias. We estimate the magnitude of this effect by taking the median ratios of the recovered flux density for each of the detected simulated sources with the known input flux density as a function of the signal-to-noise ratio as shown in Figure 2.9. As with the completeness we show that the intrinsic source size distribution can have a noticeable effect on the flux deboosting. In Figure 2.9 we show the flux recovery as a function of intrinsic source FWHM which indicates that the recovered flux of extended sources is systematically low therefore bringing the flux deboosting values down. As previous studies suggest median sub-millimetre emission sizes of $\sim 0\farcs3$ (Tacconi et al., 2006; Simpson et al., 2015b) we follow Simpson et al. (2015b) and limit our simulated sources to FWHM$<0\farcs6$. This results in flux deboosting factors of 32 % for sources at our $4.3\,\sigma$ detection threshold, reducing to 10 % at $7.8\,\sigma$ and $\sim$0 % at $12\,\sigma$. A running median is calculated from this ratio as a function of SNR in a $0\farcs5$ diameter aperture, shown in Figure. 2.9, and this median value is used to correct the boosted fluxes to derive our final aperture corrected, flux deboosted, flux densities.

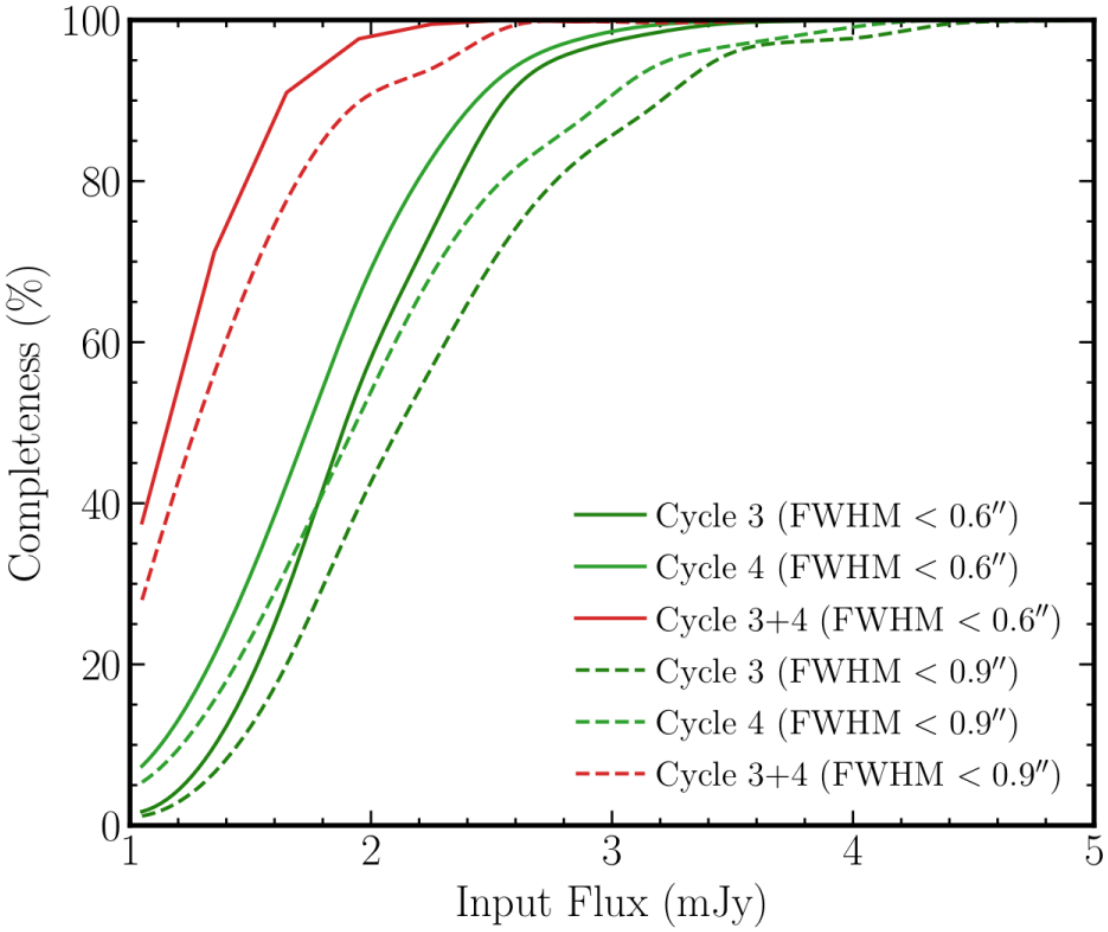

Figure 2.8: Completeness fractions as a function of the input total flux for each simulated galaxy estimated from 60,000 simulated ALMA observations. As described in Stach et al. (2018) our catalogue is complete for sources above $S_{850} \geq 4$ mJy. However, below this flux limit the completeness declines, reaching 50 % at 1.3 mJy for the ALMA maps that were observed twice. The solid lines show the completeness fractions for simulated sources with intrinsic FWHM $<0.''6$ whilst the dashed line shows a more conservative estimate including all simulated sources (with sizes up to $0.''9$).

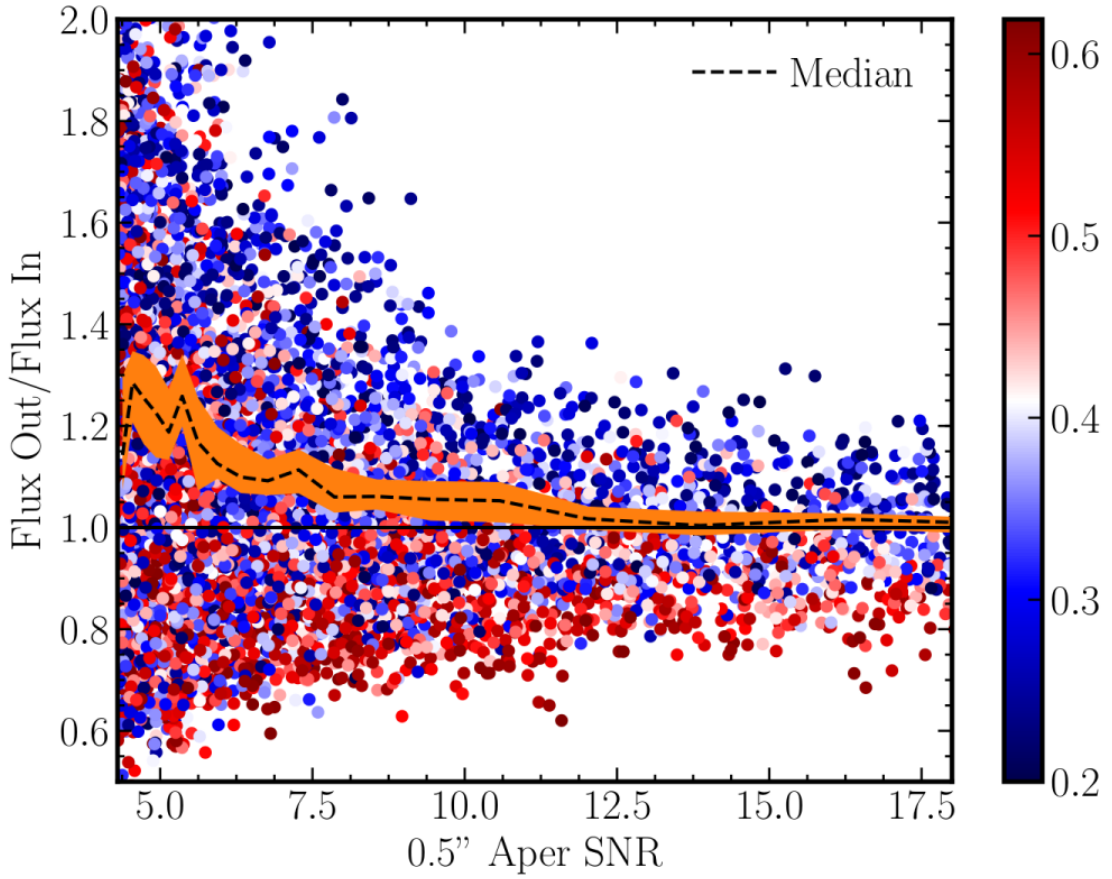

Figure 2.9: The ratio of the recovered to injected fluxes for our simulated galaxies showing the influence of flux boosting, where the lower signal-to-noise sources have measured fluxes boosted relatively higher by noise fluctuations. To correct for this we calculate the median boosting (dashed line) with the shaded region showing the 1 σ bootstrap error. Using the power-law distribution of simulated sources we find a boosting factor of 32 % for sources at our 4.3 σ threshold. The colour coding of the points is based on the intrinsic FWHM size of the simulated sources using the colour bar on the right (scale in arcseconds). As the extended sources have systematically lower recovered fluxes this tends to reduce the flux deboosting factors.

2.7 SCUBA-2 Positional Offsets

Surveys such as AS2UDS and ALESS (Hodge et al., 2013) have been motivated by the need to identify large samples of sub-millimetre galaxies to bright single-dish sub-millimetre sources. In the absence of sub-millimetre interferometry, this requires statistical associations between the single-dish sources and sources identified in higher-resolution multiwavelength observations. These statistical associations are complicated by the significant uncertainties in the single-dish source positions. It is expected that these positional uncertainties are dependant on the SNR of the single-dish detection and in Ivison et al. (2007) the ideal theoretical expression for this dependence was given as:

$$\Delta\alpha = \Delta\delta = 0.6[(\mathrm{SNR})^2 - (2\beta + 4)]^{-1/2}\mathrm{FWHM}, \tag{2.7.2}$$

where $\Delta\alpha$ and $\Delta\delta$ are the rms positional errors in R.A. and Dec., SNR is the signal to noise ratio of the SCUBA-2 detection, FWHM is the full-width-half-maximum of the single-dish beam, and β is the slope of the power law number counts which is required to correct for the Malmquist bias ($\beta \sim -2$).

With our ALMA survey we can empirically test this relation by checking the positional offsets of the AS2UDS sources relative to their corresponding SCUBA-2 source position. We check for a systematic astrometric offset between the parent SCUBA-2 S2CLS position and the detected ALMA sources (the offset corrections for the Cycle 1 sources, mentioned in §2.4, were pre-applied) by calculating median offsets in Right Ascension and Declination. We find a significant median offset of $-1\farcs6 \pm 0\farcs1$ in R.A. and $+0\farcs6 \pm 0\farcs1$ in Dec. (Figure 2.10), a result of a rounding error in the assigning of phase centres to ALMA and we subsequently apply these corrections to the ALMA phase centres when calculating the radial separations between SCUBA-2 positions and ALMA source detections. We note that this error in phase centre pointings could result in a modest reduction in the number of ALMA counterparts detected at the very edge of the ALMA primary beam, as a shift of this magnitude results in a region with an area corresponding to 12 % of the primary beam $\sim 8''$ from the intended phase centre falling outside the actual primary beam. We estimate a constraint of ~ 11 potentially missed galaxies due to this

offset, calculated by assuming a rotationally symmetric distribution of galaxies around the phase centres and counting the number of galaxies in our catalogue detected at the very edges of our primary beams.

In Figure 2.11 we show the radial offsets as a function of the SNR of the parent single-dish source and overlay the predicted uncertainties on the single-dish positions from Ivison et al. (2007). In agreement with the predicted uncertainties, 63 ± 3 % of the brightest detected sources are within the 1-σ uncertainty and 92 ± 4 % within the 2-σ uncertainty. However, the actual functional form of the uncertainty in position with signal-to-noise ratio has previously been used to determine the search radius for counterparts (e.g. Biggs et al., 2011) and therefore we look in more detail at how the trend of median offsets varies as a function of signal-to-noise in Figure 2.11. The median offsets shows a much flatter trend in comparison to the theoretical expectation, with the faintest SCUBA-2 sources (SNR < 5) median offsets lying significantly below the 1-σ theoretical prediction of Ivison et al. (2007), whilst the median for the brighter (SNR > 6) sources lies above. This trend suggests that altering the search radius to identify counterparts based on signal-to-noise could result in a failure to correctly identify the correct counterparts in high significance SCUBA-2 detections. This failure to follow the expected behaviour is likely due to the presence of more than one sub-millimetre galaxy in a map of a single-dish source, which is not accounted for by the model, such 'multiplicity' is particularly prevalent in brighter sources (e.g. Simpson et al., 2015a, and see Chapter 3.).

2.8 Flux Recovery

To determine the reliability of our flux measurements we next compare the total flux recovered from all sources detected in an ALMA map against the corresponding deboosted SCUBA-2 fluxes from Geach et al. (2017). To do this we correct the SCUBA-2 850 μm fluxes to the ALMA wavelength using a $S_{870}/S_{850} = 0.95$ factor derived from the ALESS survey composite spectral energy distribution (SED) (Swinbank et al., 2014) redshifted to $z = 2.5$ (Figure. 2.12). For SCUBA-2 sources brighter than $S_{850} \geq 4\,\mathrm{mJy\,beam^{-1}}$ we have a median recovery rate of 97^{+1}_{-2} % of the flux in the ALMA pointings, which

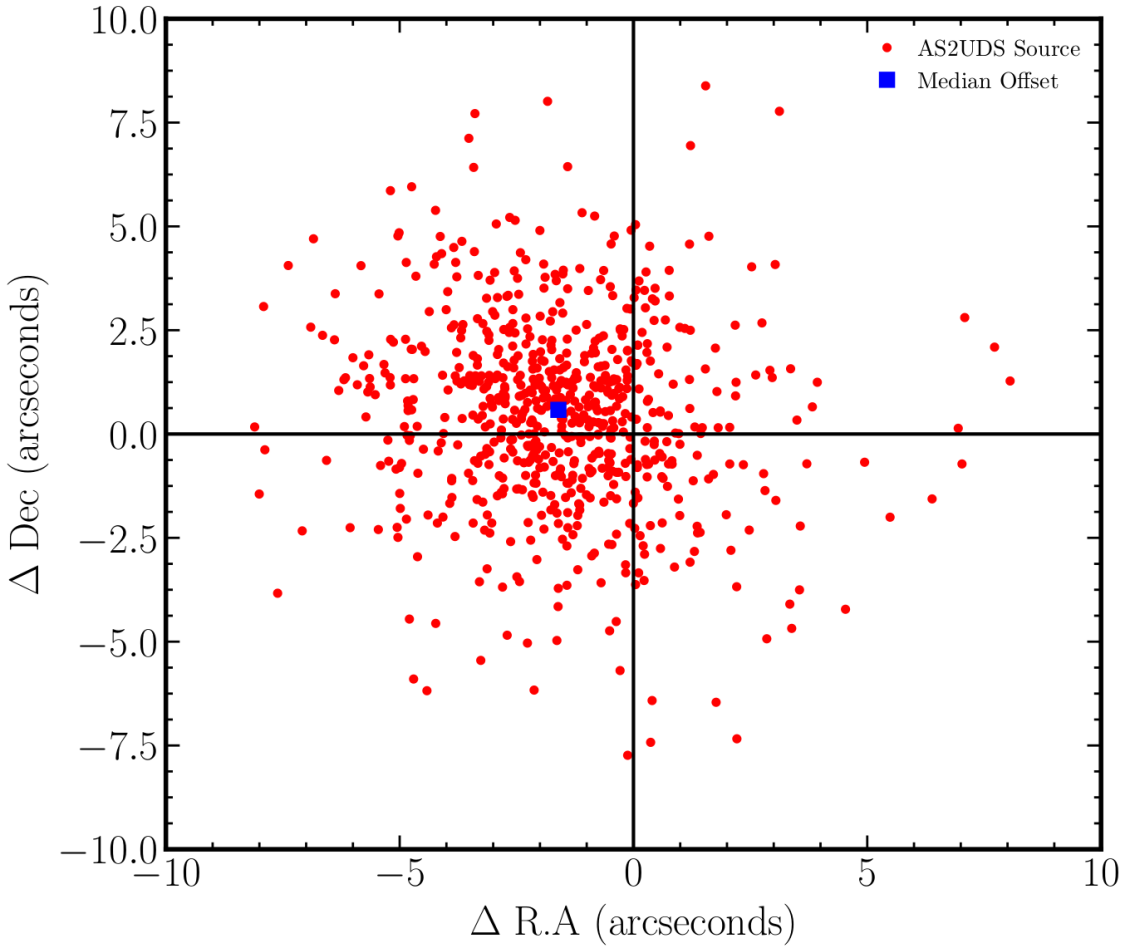

Figure 2.10: The positional offsets of the AS2UDS SMGs from the phase centres of the maps, which correspond to the SCUBA-2 positions in the S2CLS catalogue (Geach et al., 2017). One would expect the AS2UDS galaxies to be positioned randomly around the phase centre at 0 ΔR.A and Dec however as can be seen the distribution is off-centre, a result of a rounding error in assigning phase centres in the original ALMA proposal. This median offset of $-1\farcs6 \pm 0\farcs1$ in R.A. and $+0\farcs6 \pm 0\farcs1$ in Dec. is corrected for when calculated radial separations in Figure 2.11

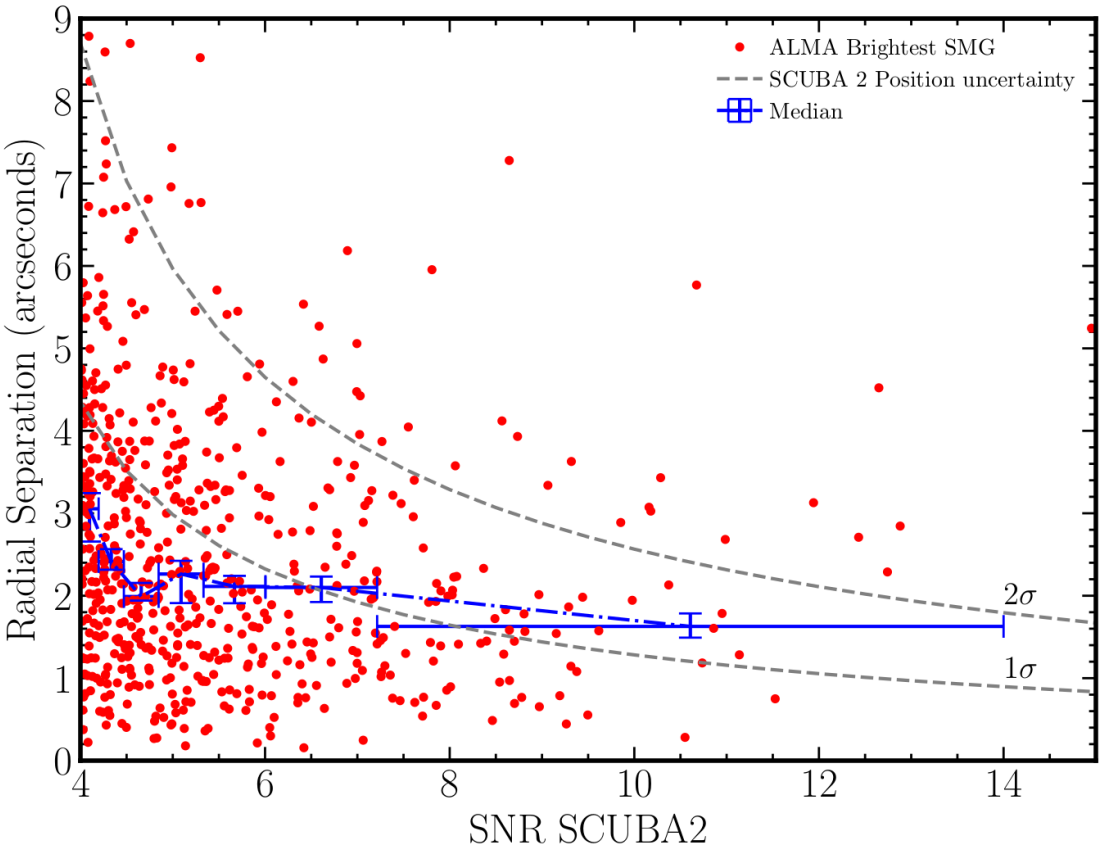

Figure 2.11: The offsets between the field centres (corrected for the astrometric offsets and the brightest sub-millimetre detected galaxies in the AS2UDS catalogue. As shown by Simpson et al. (2015a) based on our ALMA Cycle 1 pilot programme, these separations are consistent with the predicted uncertainties in source positions for SCUBA-2 detections from Ivison et al. (2007) overlaid as the dashed lines. We also plot the median offsets in bins of equal number of brightest sources which show a mostly flat distribution suggesting a fixed search radius for counterparts as opposed to a SNR dependant one would likely be equally effective, most likely due to the influence of secondary components in the maps.

is well within the systematic flux uncertainties for both SCUBA-2 (5–10 %, Dempsey et al., 2013) and ALMA. Therefore we can be confident that all significant contributors to the sub-millimetre fluxes are successfully recovered in this flux regime. However the binned median flux recovery is 87^{+5}_{-8} % for $S_{850} = 2.9$–$3.1\,\mathrm{mJy\,beam^{-1}}$ and 71 ± 6 % at $S_{850} = 2.5$–$2.9\,\mathrm{mJy\,beam^{-1}}$. These medians are biased low by the blank maps with no detected ALMA sources. If we exclude those maps, this results in an 88 ± 6 % flux recovery at $2.5\leq S_{850} \leq 2.9\,\mathrm{mJy\,beam^{-1}}$ and 112 % flux recovery at $2.9\leq S_{850} \leq 3.1\,\mathrm{mJy\,beam^{-1}}$. Therefore only at the faintest SCUBA-2 fluxes do we see the suggestion of decline in the recovered fraction of the SCUBA-2 flux, and in Section 4.4.3 we show that for the majority of cases this is likely due to faint sub-millimetre galaxies just below our $4.3\,\sigma$ threshold being present in the ALMA maps.

2.8.1 AS2UDS Catalogue

The complete AS2UDS catalogue identifies 708 sub-millimetre galaxies brighter than $S_{870} = 0.58\,\mathrm{mJy}$ from the original 716 SCUBA-2 sub-millimetre sources, roughly five times larger than the Miettinen et al. (2017) study in COSMOS or ALESS (Hodge et al., 2013) with the total area of the primary-beam coverage in our ALMA survey equivalent to $47.3\,\mathrm{arcmin^2}$. In Appendix A I present the complete AS2UDS catalogue. From the 716 ALMA maps: one contains four SMG detections, six have three SMG detections, 78 include two, and 530 detect just a single SMG above $4.3\,\sigma$, which leaves 101 maps which returned no detected galaxies. The majority of the maps containing multiple SMGs correspond to the brighter SCUBA-2 sources, as can be seen in Figure 2.13, and as I'll show in the next chapter, the rate of occurrence of multiple counterparts is 26 ± 2 % in SCUBA-2 sources with fluxes brighter than $S_{850} \geq 5\,\mathrm{mJy}$ and 44 ± 16 % at $S_{850} \geq 9\,\mathrm{mJy}$.

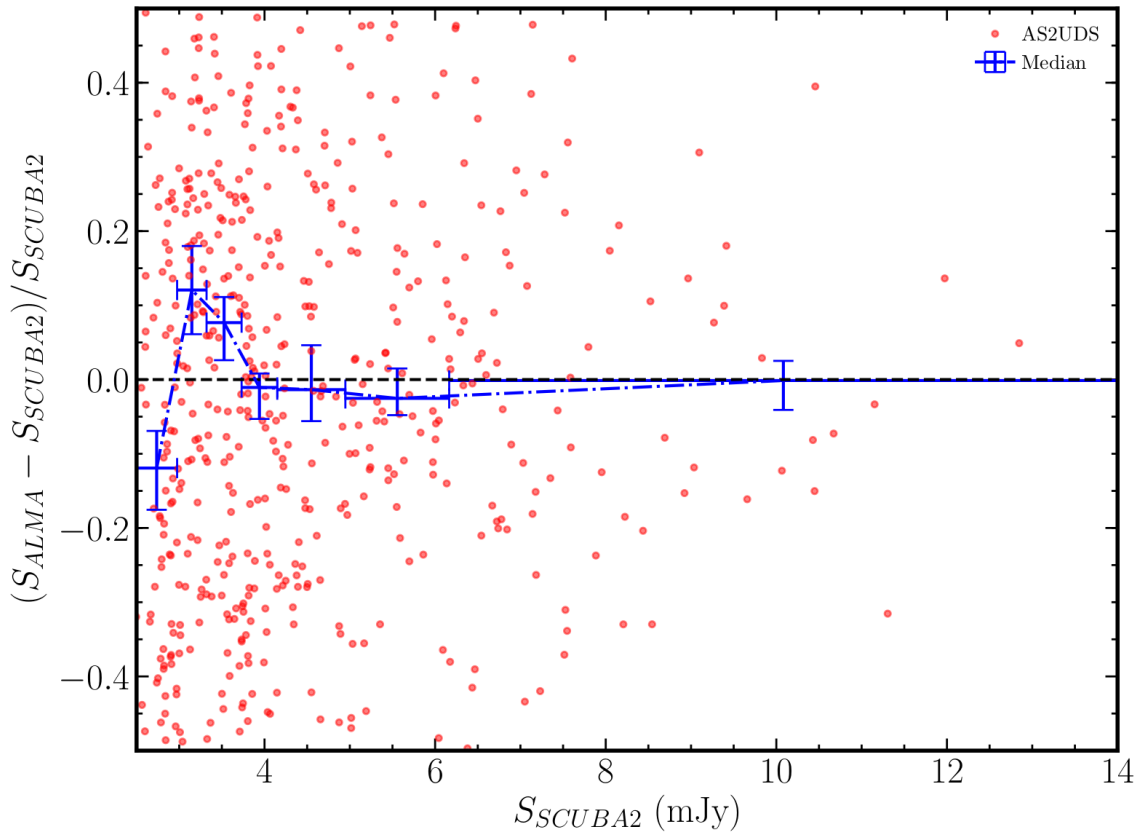

Figure 2.12: The recovered flux fraction as a function of original SCUBA-2 flux. Each point is the integrated flux for all sources detected in a field within the primary beam centred on the original S2CLS position. Points above zero indicate maps where we recover a greater flux than the original S2CLS detection, a result of either noise boosting or sources being detected near the edge of the map thus are primary beam corrected to higher fluxes, and points below zero are maps where we failed to recover all the flux from the parent single-dish source. Overlaid is the median in bins of equal number of ALMA maps that show that for SCUBA-2 sources above $S_{850} \sim 3.5$ mJy we on average recover all the single-dish flux in our ALMA maps.

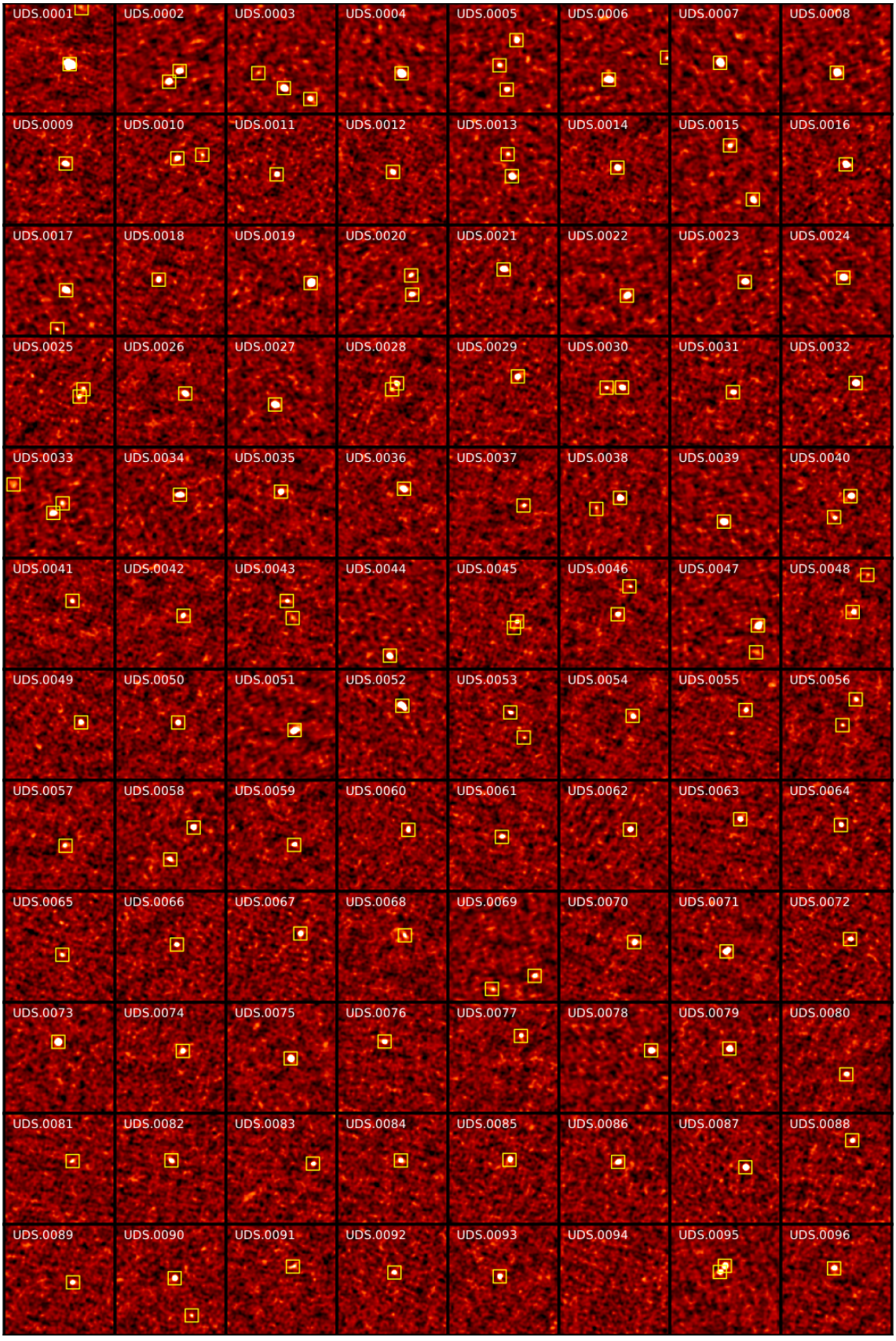

Figure 2.13: Thumbnails for all 716 ALMA maps of the AS2UDS survey. Each thumbnail is 18″ square which covers the ALMA primary beam. Each SMG detected and catalogued is highlighted by a yellow box. The thumbnails are ordered by their S2CLS identifier number shown in the top left of each thumbnail and these are assigned by decreasing S_{850} flux with ascending identifier. A qualitative trend of higher frequency of multiple detections and fewer 'blank' maps can be found at the higher flux density SCUBA-2 source maps.

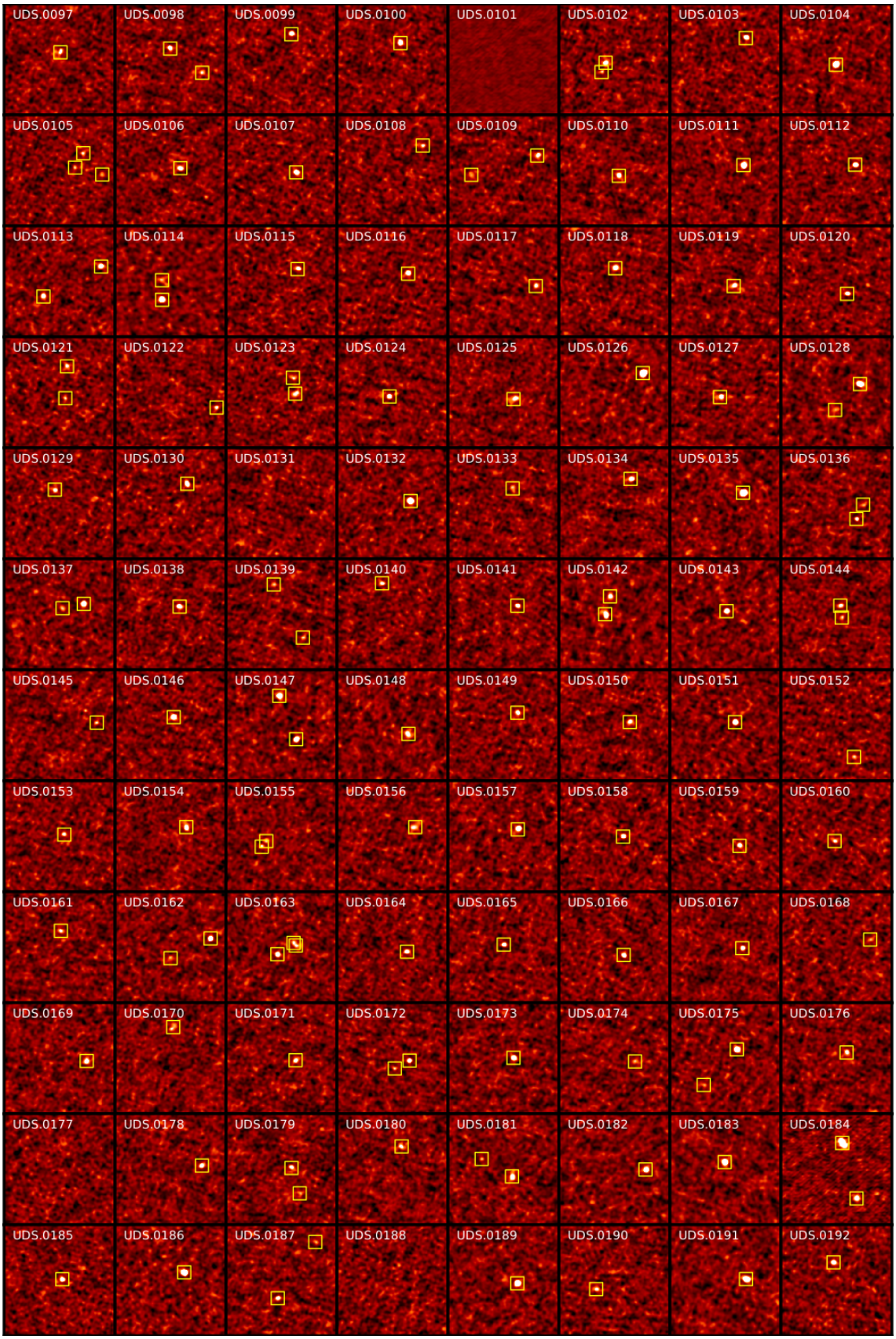

Figure 2.13: continued

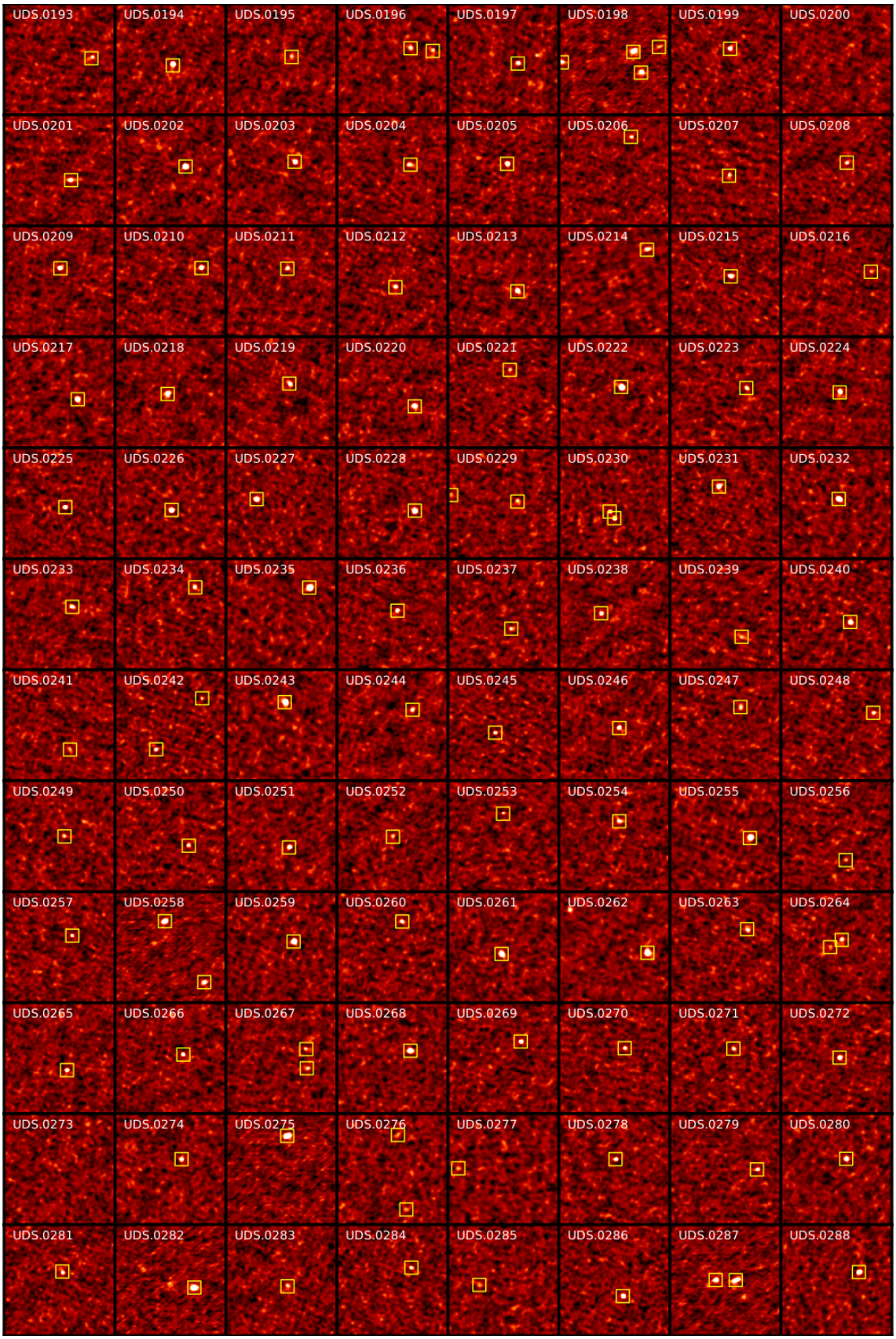

Figure 2.13: continued

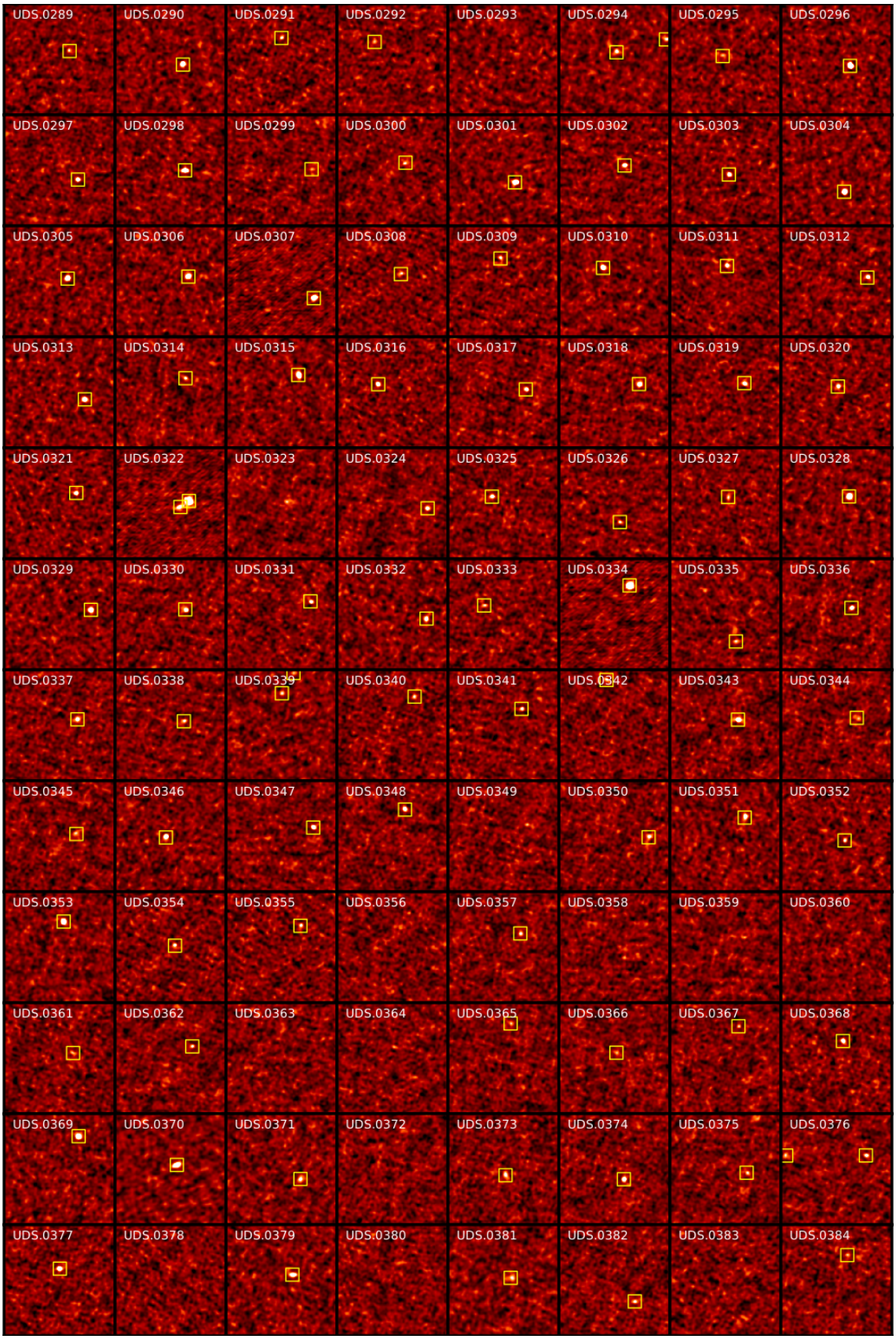

Figure 2.13: continued

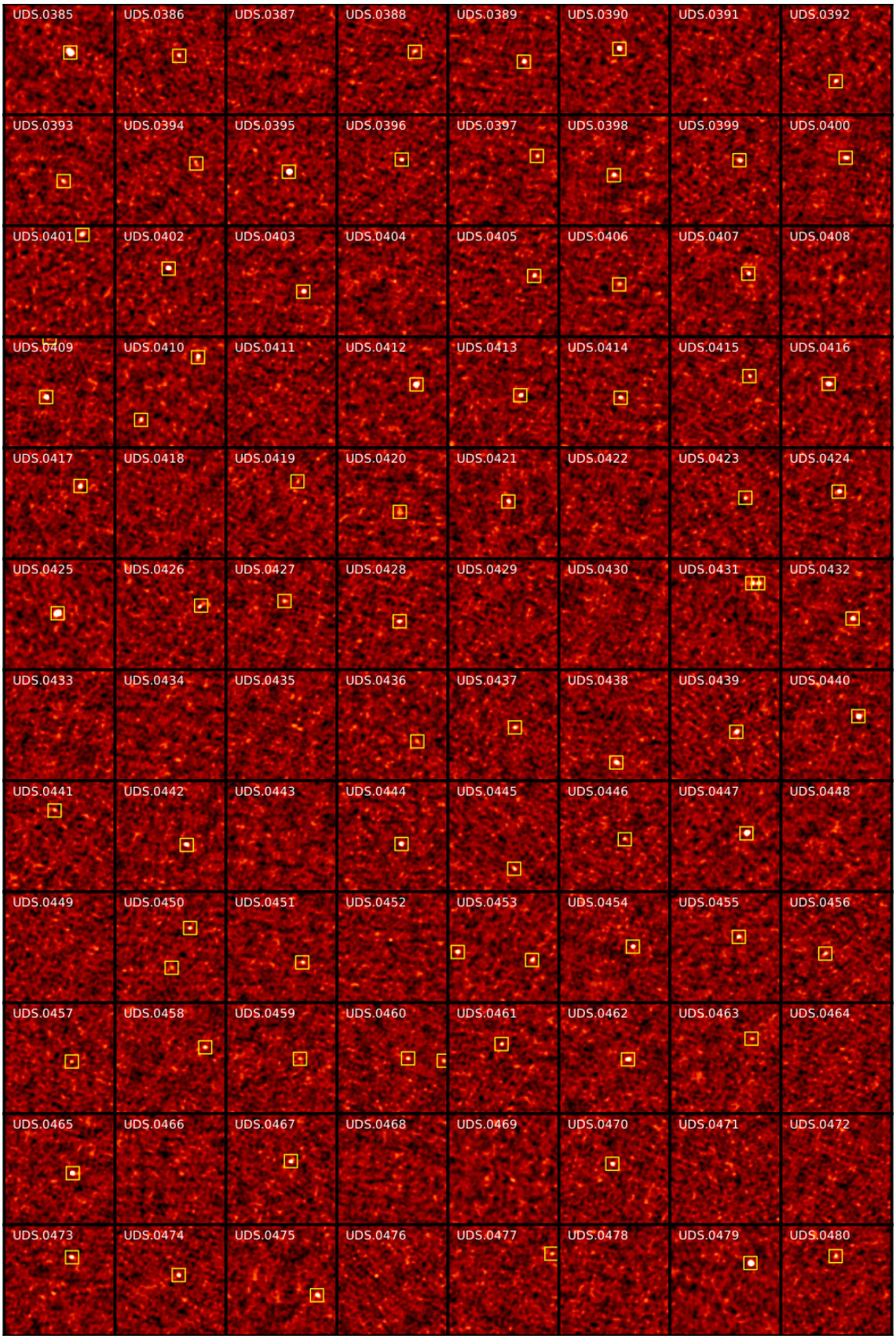

Figure 2.13: continued

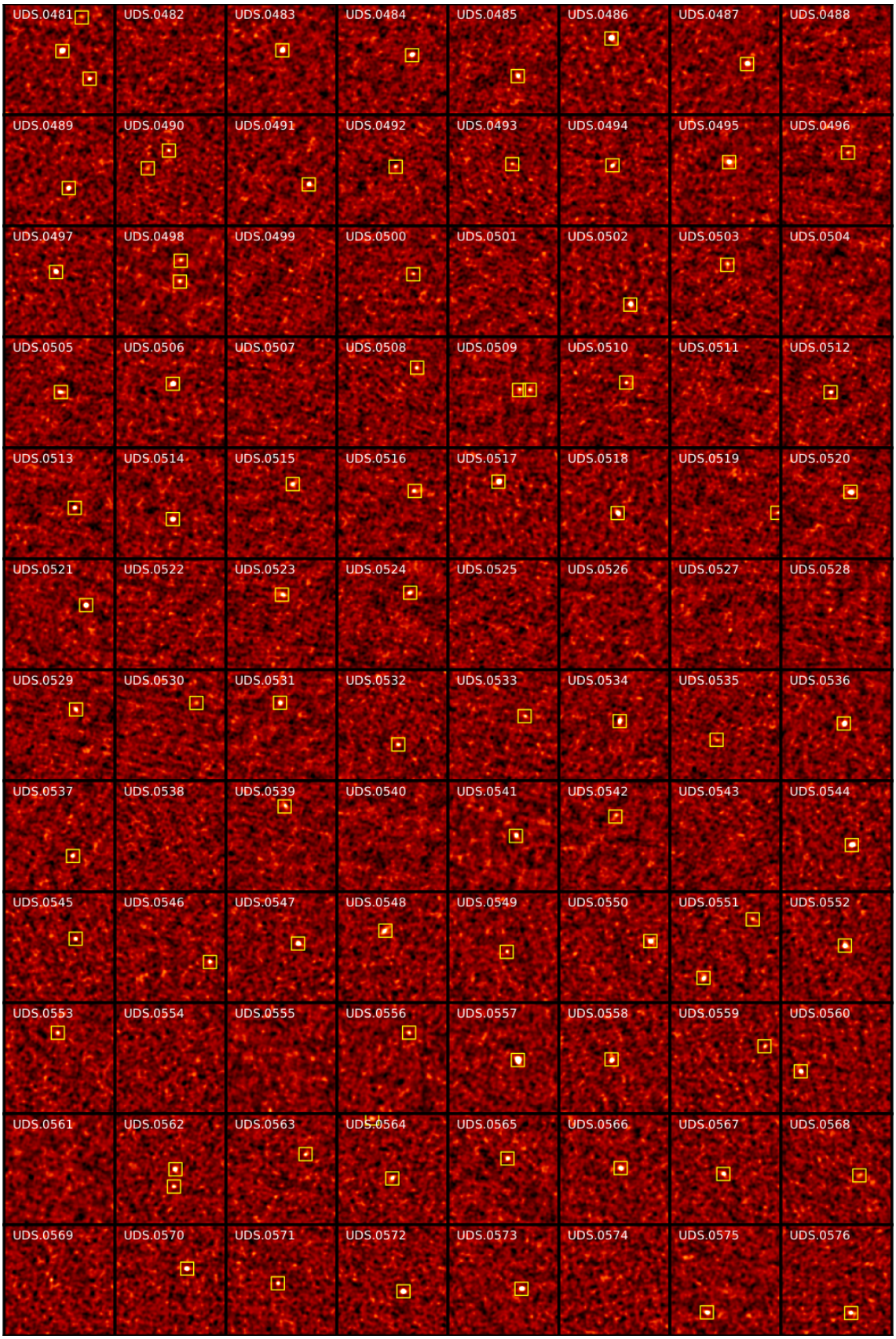

Figure 2.13: continued

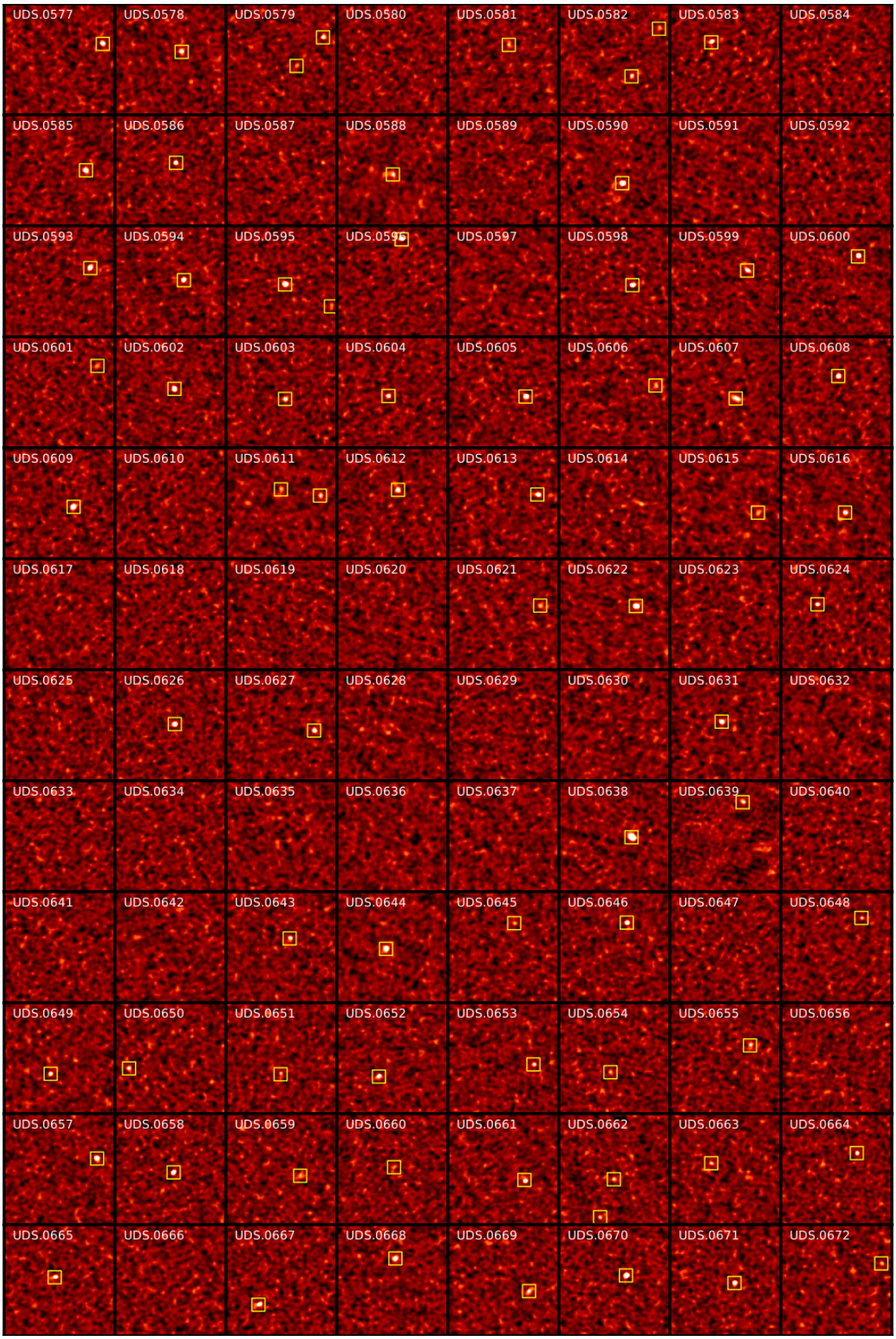

Figure 2.13: continued

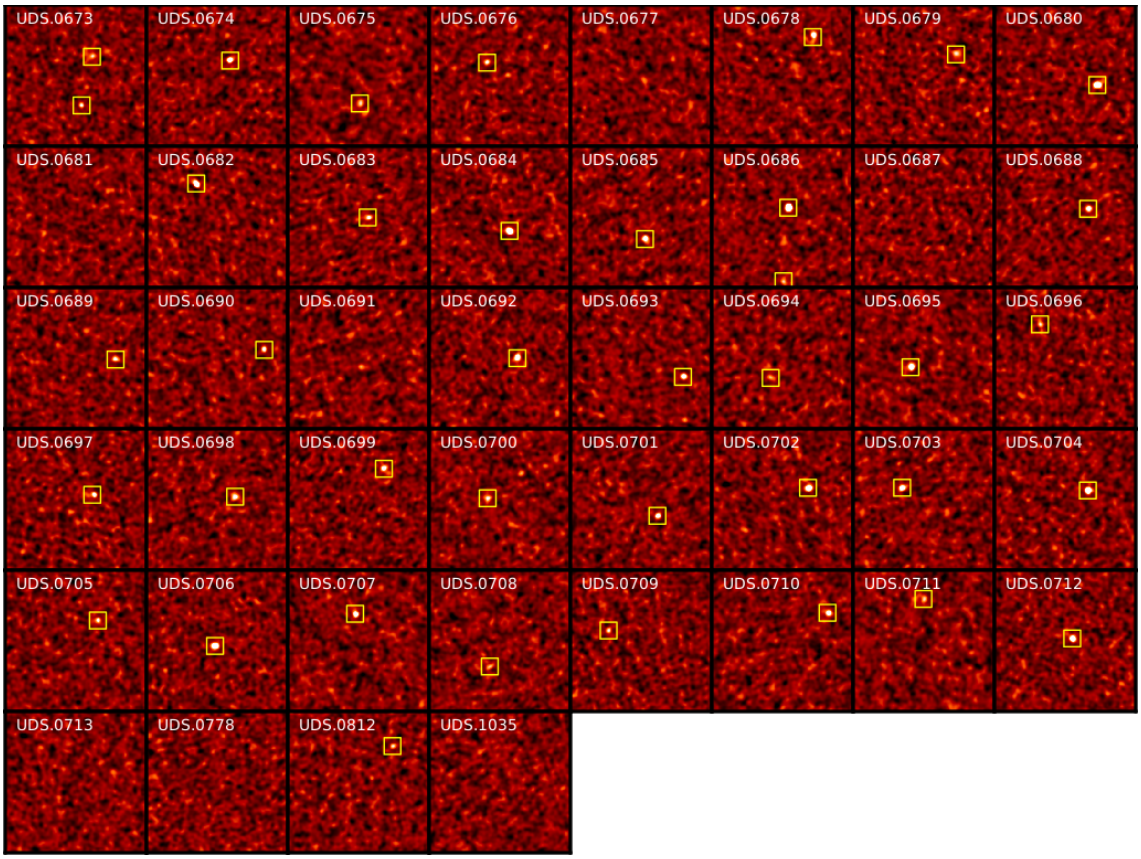

Figure 2.13: continued

CHAPTER 3

An ALMA Survey of the SCUBA-2 Cosmology Legacy Survey UKIDSS/UDS field: Number Counts and Multiplicity of Submillimeter Galaxies

3.1 Summary

Following the description of the creation of the catalogue in the previous chapter, I present some of the first results using this AS2UDS catalogue, which were published in Stach et al. (2018). The most fundamental property of this sub-millimetre sample is the number counts of the SMGs, which provides a key constraint on galaxy formation models (Baugh et al., 2005; Cowley et al., 2018). Prior to the sample presented here, SMG number counts have had to be derived from either; (1) coarse resolution single-dish observations which can suffer from source blending creating an artificially high number of 'bright' SMGs (e.g. Austermann et al., 2009; Weiß et al., 2009; Geach et al., 2017), (2) high-resolution interferometric observations but for sample sizes of $\lesssim$100 SMGs which are insufficient in size to provide differential number counts which can adequately constrain theoretical predictions (e.g. Karim et al., 2013; Dunlop et al., 2016). AS2UDS provides the opportunity for a statistically robust measurement of the SMG number counts which is free from the effects of source blending (with $\sim 0\farcs2$ resolution), and with a near order of magnitude increase in detected galaxies from previous interferometric samples.

In this chapter the AS2UDS catalogue is referred to as having 695 galaxies as opposed

to the final tally of 708 discussed in the previous chapter, as well as referring to 108 blank maps as opposed to the final tally of 101. At the time of the publication of Stach et al. (2018) the ten maps covered in the follow-up, deep, blank map proposal (mentioned in the previous chapter) had not been observed and therefore the earliest AS2UDS papers (An et al., 2018; Stach et al., 2018; Cooke et al., 2018) used an early pre-release catalogue with 695 galaxies. I note that the additional galaxies from the blank map proposals are all, by the nature of the observations, amongst the faintest in the catalogue and below the 870 μm flux density limits that this chapter considers and so do not impact the science results presented here.

This Chapter reports the first results of AS2UDS: an 870 μm continuum survey with the Atacama Large Millimeter/Submillimeter Array (ALMA) of a total area of $\sim 50\,\mathrm{arcmin}^2$ comprising a complete sample of 716 submillimeter sources drawn from the SCUBA-2 Cosmology Legacy Survey (S2CLS) map of the UKIDSS/UDS field. The S2CLS parent sample covers a $0.96\,\mathrm{degree}^2$ field at $\sigma_{850} = 0.90 \pm 0.05\,\mathrm{mJy\,beam}^{-1}$. Our deep, high-resolution ALMA observations with $\sigma_{870} \sim 0.25\,\mathrm{mJy}$ and a $0\farcs15$–$0\farcs30$ FWHM synthesized beam (see Chapter 2), provide precise locations for 695 submillimeter galaxies (SMGs) responsible for the submillimeter emission corresponding to 606 sources in the low resolution, single-dish map. We measure the number counts of SMGs brighter than $S_{870} \geq 4\,\mathrm{mJy}$, free from the effects of blending and show that the normalisation of the counts falls by $28 \pm 2\,\%$ in comparison to the SCUBA-2 parent sample, but that the shape remains unchanged. We determine that $44^{+16}_{-14}\,\%$ of the brighter single-dish sources with $S_{850} \geq 9\,\mathrm{mJy}$ consist of a blend of two or more ALMA-detectable SMGs brighter than $S_{870} \sim 1\,\mathrm{mJy}$ (corresponding to a galaxy with a total-infrared luminosity of $L_{\mathrm{IR}} \gtrsim 10^{12}\,\mathrm{L}_{\odot}$), in comparison to $28 \pm 2\,\%$ for the single-dish sources at $S_{850} \geq 5\,\mathrm{mJy}$. Using the 46 single-dish submillimeter sources that contain two or more ALMA-detected SMGs with photometric redshifts, we show that there is a significant statistical excess of pairs of SMGs with similar redshifts ($< 1\,\%$ probability of occurring by chance), suggesting that *at least* $30\,\%$ of these blends arise from physically associated pairs of SMGs.

3.2 Introduction

It has been two decades since the Submillimeter Common User Bolometer Array (SCUBA) instrument on the James Clerk Maxwell Telescope (JCMT) enabled deep observations of high-redshift submillimeter sources which expanded the number of known high-redshift submillimeter luminous infrared sources up to hundreds (e.g. Hughes et al., 1998). These submillimeter galaxies (SMGs) constitute a population of the most intensely star-forming galaxies, with star-formation rates (SFRs) in the 100s–1000s of $\mathrm{M}_{\odot}\,\mathrm{yr}^{-1}$ (Blain et al., 2002; Magnelli et al., 2012; Swinbank et al., 2013; Casey et al., 2013) at typical redshifts $z \sim 2$–3 (Chapman et al., 2005; Wardlow et al., 2011; Simpson et al., 2014; Chen et al., 2016).

This level of star formation means that in a single starburst event, an SMG would need just a few hundred million years to form the stellar mass of a massive galaxy ($M_* \gtrsim 10^{11}\,\mathrm{M}_{\odot}$). This has led to the suggestion that SMGs have many of the properties expected for the progenitors of the luminous massive elliptical and spheroid galaxies in the local Universe (Lilly et al., 1999; Fu et al., 2013; Simpson et al., 2014) with speculation that they could represent a phase in a single evolutionary path linking SMGs to luminous quasi-stellar objects (QSOs) at $z \sim 2$ and massive, passive galaxies found at $z \sim 1$–2 (Coppin et al., 2008; Cimatti et al., 2008; Whitaker et al., 2012; Toft et al., 2014). Further evidence for this evolutionary path comes from clustering studies from single-dish detections, suggesting they reside in halos of mass $\sim 10^{13}\,\mathrm{M}_{\odot}$, consistent with that of $z \sim 2$ QSOs and with their subsequent evolution into local ellipticals (Farrah et al., 2006; Hickox et al., 2012; Wilkinson et al., 2017).

However, whilst SMGs may play a significant role in the stellar mass growth of massive galaxies, measuring their basic properties have been hampered by the coarse angular resolution of the single-dish telescopes, with beams of $\sim 15''$–$30''$ FWHM. One of the questions raised is whether the (coarse resolution) single-dish detections arises from a single SMG or are blends of multiple SMGs within the single-dish beam. To measure the blending and to accurately identify SMG counterparts at other wavelengths requires high-resolution interferometric studies, which were initially performed via radio counterpart identification (e.g. Smail et al., 2000; Barger et al., 2000; Chapman et al., 2003, 2005;

Ivison et al., 2007), but more recently with submillimeter interferometers. Wang et al. (2011) use deep 850 μm integrations of two bright submillimeter sources in the GOODS-N field to suggest that both sources break into multiple components and suggested that around 30% of 850-μm sources with flux densities $S_{850} \geq 5$ mJy could be composed of blends of more than one SMG. ALMA observations of much larger samples suggested that this rises to $>90\%$ for $S_{850} \sim 8$ mJy sources selected in single-dish surveys (e.g. Simpson et al., 2015a). More recently, Hill et al. (2018) used the Submillimeter Array (SMA) to observe 75 of the brightest S2CLS sources ($S_{850} \gtrsim 8$ mJy) at 870 μm with a resolution of $\sim 2\farcs4$. Combining their SMA data with archival observations they determine a lower multiplicity rate of $\sim$15 %, which is consistent with previous work with the SMA (Chen et al., 2013). However these SMA observations are limited by the sensitivity, with Hill et al. (2018) using maps with an average rms depth of ~ 1.5 mJy. This meant that multiples can only be identified in a bright single-dish source if both components have near equal flux density, which is unlikely to be a frequent occurrence. Therefore, care needs to be taken when comparing such multiplicity studies since they can use different criteria for the brightness ratio of detected sources.

To make definitive progress in understanding the properties of SMGs area requires the improvements in sensitivity and resolution provided by the Atacama Large Millimeter/Submillimeter Array (ALMA). The first such study, comprising Cycle 0 observations of the 122 submillimeter sources detected in the LABOCA survey of the Extended *Chandra* Deep Field South (LESS: Weiß et al., 2009) found that 30 % of LABOCA sources resolved into multiple components with $S_{850} \gtrsim 1.5$ mJy when observed at $1\farcs5$ resolution (Karim et al., 2013; Hodge et al., 2013). Following this result, in ALMA Cycle 1, 30 of the brightest submillimeter sources (median single-dish flux density of $S_{850} \gtrsim 9$ mJy) from the SCUBA-2 Cosmology Legacy Survey (S2CLS: Geach et al., 2017) map of the UKIDSS Ultra Deep Survey (UDS, Lawrence et al. 2007, O. Almaini et al. in prep.) field were observed with ALMA by Simpson et al. (2015a). This suggested that the majority (61^{+19}_{-15} %) of bright, single-dish submillimeter sources are comprised of blends of multiple SMGs brighter than $S_{850} \sim 1.5$ mJy (Simpson et al., 2015a,b). Each of these bright single-dish sources consists of 2–4 SMGs, which themselves are ultraluminous infrared galaxies

(ULIRGs; $L_{\rm IR} \geq 10^{12} L_{\odot}$), seen within a projected diameter of ~ 150 kpc. Simpson et al. (2015a) suggest that such a high over-density of SMGs requires that the majority of such detections result from physical association, as opposed to chance projections along the line of sight.

Several studies have used spectroscopic observations of molecular gas emission to test the origin of blends of SMGs. For example, Zavala et al. (2015) used spectroscopic detections for the components in one blended submillimeter-bright lensed galaxy to show that it split into three distinct galaxies, each at significantly different redshifts. More recently, Wardlow et al. (2018) used ALMA observations to search for CO emission in the fields of six submillimeter sources, which include a total of 14 SMGs, to determine that $\gtrsim 75\%$ of blends of multiple SMGs are not physically associated. Similarly, Hayward et al. (2018) report optical and near-infrared spectroscopy of a sample of seven single-dish sources, where three showed a blending of physically associated SMGs, whilst four contained at least one pair of components that was physically unassociated. This mix of physically associated and unassociated components in the blended single-dish submillimeter sources is consistent with semi-analytic modelling, for example Cowley et al. (2015b) have suggested that most blends of SMGs in single-dish sources arise from projections of unrelated galaxies seen along the line of sight.

The presence of multiple SMG counterparts to individual single-dish submillimeter sources indicates that the number counts derived from low-resolution single-dish surveys do not represent the true number counts of SMGs. Even a small change in the expected form of the counts of SMGs has a potentially significant impact on models that use them as a constraint on the evolution of high-redshift, dust obscured starbursts (e.g. Cowley et al., 2015b; Lacey et al., 2016).

In this chapter we present the first results of the recently completed ALMA survey of the full S2CLS UDS sample, which comprises 870 μm maps of the $716 > 4\,\sigma$ single-dish sources with observed $S_{850} \geq 3.4$ mJy in this 0.96 degree^2 field. Our deep, high-resolution ALMA survey, with rms depths of $\sigma_{870} \sim 0.25$ mJy beam^{-1} at $0\farcs15$–$0\farcs30$ resolution, provides the statistical sample necessary to study the SMG population in detail and supplies us with the largest sample of ALMA-detected SMGs currently available. From this we

construct resolved 870-μm SMG number counts and investigate the multiplicity in single-dish surveys. In §2.4 we describe the sample selection, observations, data reduction and source extraction. §3.3 covers our results and discussions and §3.4 gives our conclusions.

3.3 Analysis, Results and Discussion

As discussed in Chapter 2, the AS2UDS SMG sample is roughly seven times larger than the previous largest sub/millimeter interferometric survey of single-dish submillimeter sources (ALESS: Hodge et al., 2013; Karim et al., 2013) and drawn from a field which is four times larger in terms of contiguous area. As was also found in ALESS, a fraction of our ALMA maps do not contain any detected SMGs (above 4.3 σ significance) – there are 108 of these "blank" maps (15 ± 2 % of the survey). In addition, we have 79 maps (11 ± 1 %) where the single-dish SCUBA-2 source breaks up into multiple SMGs at ALMA resolution. In §3.3.3 we show that the blank maps may in part be a result of similar "multiplicity" effects, as opposed to false positive detections in the original SCUBA-2 catalogue.

With this nearly order-of-magnitude increase in the sample of SMGs, in this Chapter we present number counts of SMGs brighter than $S_{870} \sim 4$ mJy, above the original 4-σ limit of the single-dish SCUBA-2 survey. We also utilise the available multi-wavelength data for the UKIDSS/UDS field to employ photometric redshifts for our SMGs to quantify what fraction of the SCUBA-2 sources corresponding to multiple ALMA SMGs are due to chance projections, rather than physical associations.

3.3.1 Flux Recovery

As discussed in § 2.8 our ALMA observations recover a large fraction of the original SCUBA-2 source fluxes in the corresponding maps from ALMA. In the flux regime that we are interested in this Chaper, $S_{870} \geq 4$ mJy, we find that we recover a median fraction of 97^{+1}_{-2} % of the original SCUBA-2 flux from SMGs detected within the ALMA primary beam pointing of the corresponding SCUBA-2 parent source. In respect to the 108 ALMA maps where we detect no ALMA source at SNR ≥ 4.3 within the primary beam ('blank'

maps) we check that both the noise properties of the SCUBA-2 sources which resulted in 'blank' maps and the noise properties of the ALMA observations of these maps are indistinguishable from those where ALMA detected an SMG. In Figure 3.1 we show the cumulative frequency distributions for the ALMA field rms from the 'blank' maps and the 'non-blank' maps and the equivalent distributions for the errors on the equivalent SCUBA-2 fluxes for these maps. Two sample KS tests for both the ALMA and SCUBA-2 noise properties show p-values (0.09 and 0.56 respectively) which confirms that the 'blank' and 'non-blank' maps are drawn from the same distribution. This suggests that these 'blank' maps are not simply due to variations in the quality of the input catalogue or follow-up observations.

Similarly, it could be that many of the "blank" map sources are due to spurious false positives in the S2CLS parent sample. We test this by stacking *Herschel*/SPIRE maps at the locations of the 108 "blank" map sources, ranked in five bins of their SCUBA-2 flux. We recover emission in all the SPIRE bands (250, 350 and 500 μm) with flux densities between 7–20 mJy for all five flux bins. Even for the faintest 10 % of SCUBA-2 sources with corresponding "blank" ALMA maps, we still recover SPIRE detections at 250 and 350 μm (these maps are further discussed and shown in §4.4.3). Hence we are confident that the majority of the "blank" maps are a result of genuine non-detections in ALMA and not false positive sources in the S2CLS map. However, these "blank" maps do typically correspond to fainter single-dish sources: the median flux of the "blank" maps is $S_{850} = 4.0 \pm 0.1$ mJy, compared to $S_{850} = 4.5 \pm 0.1$ mJy for the whole sample. Thus it is possible that a strong increase in flux boosting in the original S2CLS catalogue at SNR of $\lesssim$4–4.5 σ ($S_{870} \sim 3.6$–4.0 mJy) may play a part in explaining why ALMA detects no SMGs in these maps. To remove this concern, in our analysis we only consider the number counts brighter than $S_{870} \geq 4$ mJy.

We conclude that with the sensitivities of our ALMA maps we can detect $S_{870} = 4$ mJy SMGs in even the shallowest AS2UDS maps across the entirety of the primary beam. In addition, based on our simulated ALMA maps described above, we have shown we have reliably measured flux densities for the complete sample of 299 $S_{870} \geq 4$ mJy SMGs in the AS2UDS catalogue presented here.

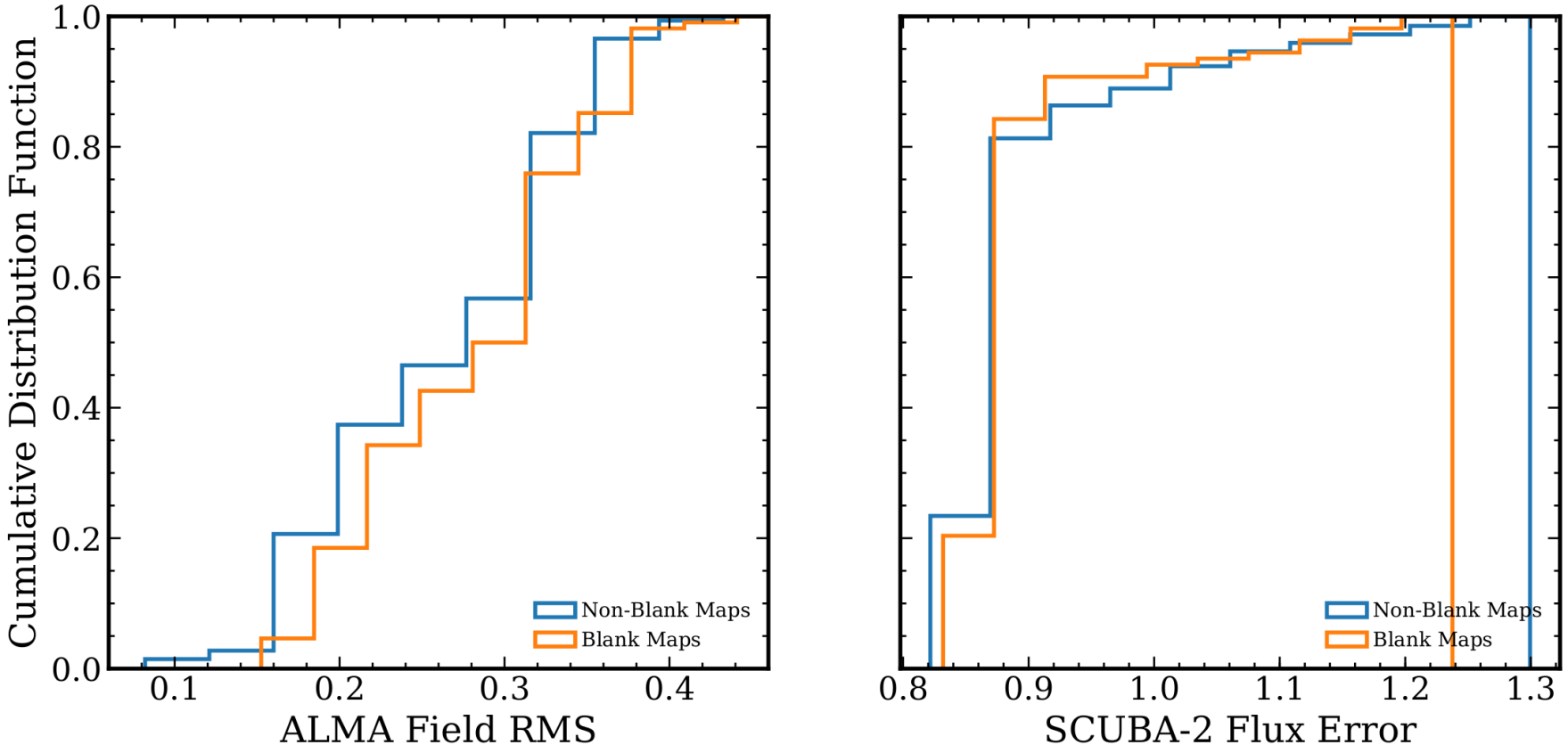

Figure 3.1: *Left:* The cumulative distribution functions for the field rms values of both the fields that returned no ALMA detection, 'blank' maps, and the maps with detected sources. The similarity of these distributions, confirmed from KS tests, suggests that the quality of the ALMA maps are not a significant cause of ALMA maps failing to resolve a galaxy. *Right:* As for the left-hand figure, cumulative distribution functions are plotted for the 'blank' and 'non-blank' maps but for their parent SCUBA-2 flux-errors. The strong similarities in these two distributions suggests that non-detections in the ALMA maps are unlikely to be a result of spurious SCUBA-2 detections resulting from poor regions of the parent SCUBA-2 map. This is unsurprising given the motivation for targeting the UDS field was partially driven by the quality and homogeneity of the SCUBA-2 map.

3.3.2 Number Counts

In Figure 3.2, we show the cumulative and differential number counts of the 299 870 μm-selected SMGs from AS2UDS to a flux limit of $S_{870} = 4$ mJy. Both the cumulative and differential number counts are normalized by the area of the S2CLS UDS map from which the original targets were selected: 0.96 degree^2. Whilst the ALMA completeness factors are minimal for AS2UDS, the number counts do have to be adjusted for the incompleteness of the parent S2CLS survey. We correct our counts by factoring in the estimated incompleteness of the catalogue of the S2CLS UDS map from Geach et al. (2017) who reported that the parent sample is effectively complete at ≥ 5 mJy, dropping to $\sim 88\%$ at ≥ 4.5 mJy and $\sim 83\%$ at ≥ 4 mJy.

As in Karim et al. (2013) the errors are calculated from both the Poissonian error and the individual flux uncertainties added in quadrature, where the flux uncertainty error is the standard deviation of the mean of the counts for each bin based on 1,000 re-samples of the catalogue, assigning random flux densities to each source within their individual error margins, Table 1. We also compare these counts to those from the parent single-dish catalogue of the S2CLS UDS field (Geach et al., 2017), and the earlier ALESS survey (Karim et al., 2013). To convert the S2CLS 850-μm counts to a common S_{870} we use a factor of $S_{870}/S_{850} = 0.95$ derived from a redshifted ($z = 2.5$), composite spectral energy distribution (SED) for SMGs from the ALESS survey (Swinbank et al., 2013), although we note that this correction is smaller than the estimated absolute calibration precision from S2CLS of 15 % (Geach et al., 2017).

Compared to a single power-law fit, the number counts of SMGs show a steepening decline at brighter fluxes. As a result the best fit to the differential number counts is with a double power-law function with the form:

$$\frac{dN}{dS} = \frac{N_0}{S_0}\left[\left(\frac{S}{S_0}\right)^{\alpha} + \left(\frac{S}{S_0}\right)^{\beta}\right]^{-1}, \tag{3.3.1}$$

where N_0 describes the normalisation, S_0 the break flux density, α and β the two power-law slopes. For our AS2UDS data the best-fit parameters found are $N_0 = 1200^{+200}_{-300}$ deg^{-2}, $S_0 = 5.1 \pm 0.7$ mJy, $\alpha = 5.9^{+1.3}_{-0.9}$ and $\beta = 0.4 \pm 0.1$.

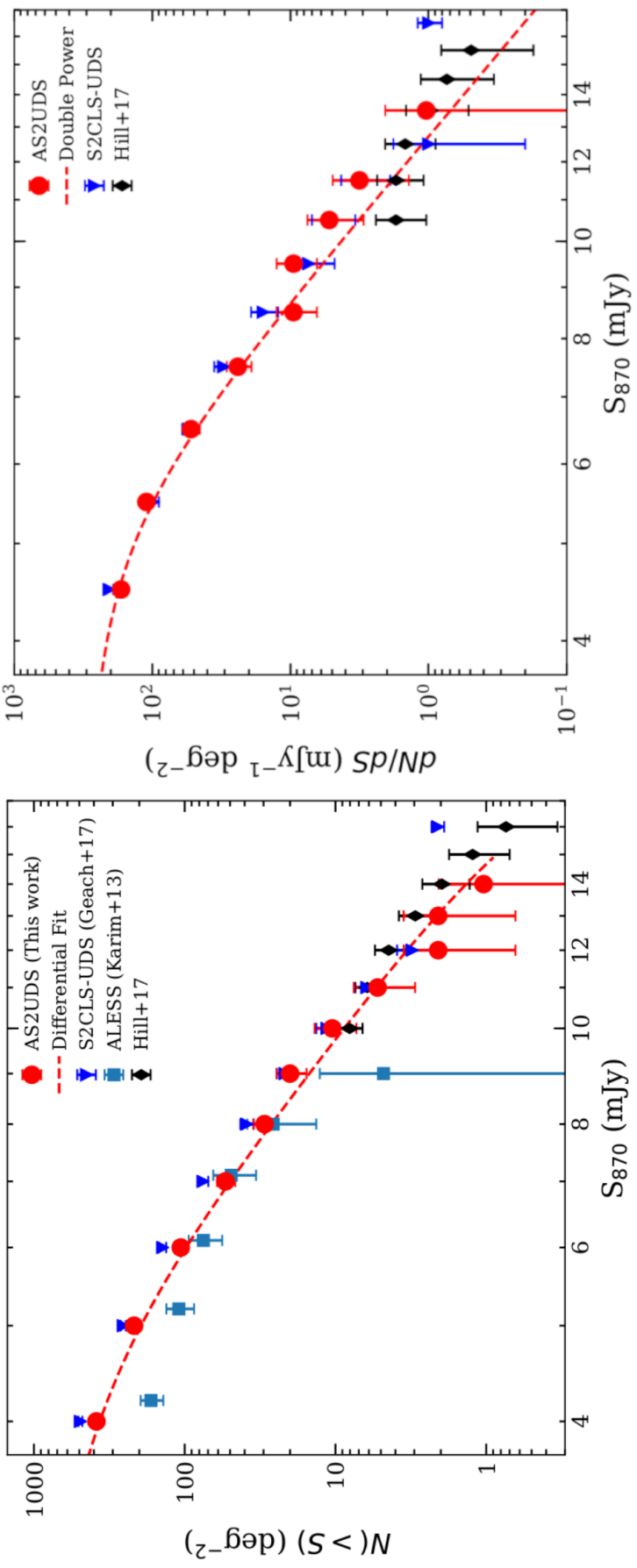

Figure 3.2: *Left:* The 870 μm cumulative number counts of ALMA-identified SMGs from the AS2UDS survey. For comparison we also show the original (deboosted) S2CLS single-dish counts for this field (Geach et al., 2017), the earlier interferometric SMG counts from ALESS survey (Karim et al., 2013), as well as those derived from SMA follow-up counts of the brightest S2CLS sources from (Hill et al., 2018). The AS2UDS counts roughly follow the same shape as the parent single-dish counts from S2CLS, but there is a systematic reduction in the surface density of SMGs of the order 37 ± 3 % (see §3.1). The dashed line is the integral of the double-power law fit to the differential number counts. *Right:* The 870-μm differential number counts for AS2UDS compared to the parent S2CLS-UDS. A double-power law functional fit is overlaid as a dashed line, and the fitting parameters are given in §3.2.

Table 3.1: AS2UDS number counts

S_{870} (mJy)	$N(>S'_{870})$[a] (deg^{-2})	dN/dS[b] ($\mathrm{mJy}^{-1}\,\mathrm{deg}^{-2}$)
4.5	$385.3^{+21.1}_{-7.7}$	$168.5^{+14.8}_{-7.9}$
5.5	$216.7^{+17.3}_{-6.6}$	$110.5^{+12.1}_{-4.1}$
6.5	$106.2^{+11.4}_{-3.5}$	$52.6^{+8.3}_{-2.6}$
7.5	$53.6^{+8.4}_{-2.5}$	$24.1^{+6.0}_{-1.9}$
8.5	$29.6^{+6.5}_{-1.9}$	$9.5^{+4.2}_{-1.1}$
9.5	$20.0^{+5.7}_{-1.8}$	$9.4^{+4.2}_{-1.1}$
10.5	$10.5^{+4.4}_{-1.2}$	$5.2^{+3.5}_{-0.9}$
11.5	$5.3^{+3.5}_{-0.9}$	$3.1^{+3.0}_{-0.7}$
12.5	$2.1^{+2.8}_{-0.6}$	–
13.5	$2.1^{+2.8}_{-0.6}$	$1.0^{+2.4}_{-0.5}$
14.5	$1.0^{+2.4}_{-0.5}$	–

[a] $S'_{870} = S_{870} - 0.5\Delta S$ where ΔS is 1 mJy
[b] "–" denotes fluxes where there is no change in the cumulative counts between the lower flux bin and the current bin

At $S_{870} \geq 4$ mJy we derive a surface density of 390^{+70}_{-80} deg^{-2}, corresponding to one SMG per $\sim$arcmin^2 or one source per ~ 130 ALMA primary beams at this frequency. Figure 3.2 shows a systematic reduction in the surface density of SMGs compared to the single-dish estimate at all fluxes. This reduction from the SCUBA-2 counts to AS2UDS is statistically significant for sources fainter than $S_{870} = 8$ mJy, with a reduction of a factor of 28 ± 2 % at $S_{870} \geq 4$ mJy and 41 ± 8 % at $S_{870} \geq 7$ mJy. At the very bright end ($S_{870} \geq 12$ mJy) the number of SMGs is so low (just two in our ~ 1 deg^2 field) that the reduction in the relative number counts is poorly constrained, 30 ± 20 %. Our bright-end reduction does agree with that seen in Hill et al. (2018) where they found a 24 ± 6 % reduction between $S_{850} = 11$–15 mJy in their SMA follow-up counts compared to the original SCUBA-2 parent sample. This agreement is unsurprising as a large number of their sources are drawn from our ALMA survey of the UDS field. We also note that, as with our earlier pilot ALMA study of UDS in Simpson et al. (2015a), that we do not see an extreme drop-off of the counts above $S_{870} \sim 9$ mJy as was suggested from the smaller-area ALESS survey (Karim et al., 2013). As we discuss below, the main factor which appears to be driving the systematically lower counts of SMGs from interferometric studies, compared to the single-dish surveys, is that a fraction of the brighter single-dish sources break up into multiple fainter sources (with flux densities of $S_{870} \lesssim 1$–4 mJy) in the interferometer maps and thus fall below the single-dish limit adopted for our counts. This effect has been termed 'multiplicity' (Karim et al., 2013; Simpson et al., 2015a). An additional factor is the twelve ALMA 'blank' maps of S2CLS sources brighter than $S^{\rm deb}_{870} \geq 4$ mJy, which also contribute to lowering the normalization of the ALMA number counts. These S2CLS sources, have a mean SNR of 5.8 ± 0.8, and are therefore unlikely to be spurious SCUBA-2 detections and our *Herschel*/SPIRE stacking (described in more details in §4.4.3) confirms this; instead one possible explanation for their ALMA non-detection is 'extreme' multiplicity, where the single-dish source breaks up into several faint SMGs below the detection limit of our ALMA maps. We test this with much deeper observations of ten ALMA maps which returned 'blank' detections in an early version of the catalogue and present these results in §4.4.3. For these brighter SCUBA-2 sources with 'blank' ALMA maps this would require that the single-dish source breaks up into ≥ 4 sources to

result in a non-detection.

3.3.3 Multiplicity

There are differing claims in the literature regarding the influence of multiplicity of SMGs on single-dish submillimeter surveys. This is a result of both the differing depths of the interferometric studies used to investigate this issue and the different definitions of "multiplicity" adopted in these works. Our survey has a relatively uniform sensitivity of $\sigma_{870} \sim 0.25\,\mathrm{mJy\,beam^{-1}}$, and therefore we adopt a fixed S_{870} limit to identify multiple SMGs. We follow Simpson et al. (2015a) and define a multiple map as any field with more than one $S_{870} \geq 1$ mJy SMG within our ALMA Band 7 primary beam (i.e. within $\sim 9''$ of the original SCUBA-2 detection locations). At the redshift of SMGs this corresponds to borderline U/LIRG systems, $L_{\rm IR} \geq 10^{12}\,L_{\odot}$ which have SFRs of the order of $10^2\,\mathrm{M_{\odot}\,yr^{-1}}$ (Swinbank et al., 2013). We also believe this is a more physical choice than, for example, using the *relative* submillimeter brightness of the two sources to decide if they constitute a "multiple", as the relative fluxes may have little relevance to their other physical properties (e.g., mass or redshift) which are essential to understand their significance. This flux limit is also significantly brighter than the expected $S_{870} \approx 0.1$ mJy galaxy in each ALMA pointing that we expect to detect purely by chance, derived from previous faint SMG number counts (Oteo et al., 2016).

In our full sample we have maps with more than one $S_{870} \geq 1$ mJy SMG in 79 of the 716 observations (11 ± 1 %). We note that at 1 mJy our ALMA observations are not complete, therefore this sets the multiplicity as a lower limit. We note, however, that the presence of a secondary source in these maps may act to increase the likelihood of the inclusion of that map into our sample by boosting the apparent SCUBA-2 flux into the S2CLS catalogue. To address this potential bias we estimate the multiplicity rate for the 179 brighter single-dish sources with deboosted SCUBA-2 flux densities of $S_{850}^{\rm deb} \geq 5$ mJy. The rate of multiples in these brighter SCUBA-2 sources is much higher 51/179 (28 ± 2 %), suggesting that the presence of a *detected* secondary SMG in faint single-dish sources does not strongly influence the inclusion of that single-dish source into our parent catalogue. Instead, the influence of multiplicity in faint single-dish sources is more likely to

be seen through the presence of 'blank' maps. Hence we also place an upper limit on the multiplicity in our full survey by assuming that *all* the blank fields are a result of the blending of multiple faint SMGs, giving 187/716 (26 ± 2 %) multiples.

The surface density of $S_{870} \sim 1$ mJy SMGs is ~ 1 arcmin^{-2}, as estimated from unbiased ALMA surveys (Aravena et al., 2016; Dunlop et al., 2016). Hence we expect to find one $S_{870} \sim 1$ mJy SMG per ~ 19 ALMA primary beams or in ~ 5% of the maps, compared to the observed rate of ~ 25–30% (one per 3–4 ALMA maps). As implied above, the multiplicity appears to depend on the single-dish flux: as expected as the inclusion of emission from other SMGs within the beam can only act to increase the apparent flux of the (blended) single-dish source. As described in §3.2, early observations suggested that roughly a third of $S_{850} > 5$ mJy single-dish sources could be blends of multiple SMGs, with this rate increasing to 90 % for $S_{870} > 9$ mJy (e.g. Karim et al., 2013). As shown in Figure 3.3, for AS2UDS we find a frequency of multiplicity (ignoring 'blank' maps) of 28 ± 2 % for $S_{850}^{\rm deb} \geq 5$ mJy rising to 44^{+16}_{-14} % at $S_{850}^{\rm deb} \geq 9$ mJy. This is significantly higher than the 'predicted' multiplicity rates of Cowley et al. (2015b) from semi-analytic models, which predicted 17.2 %.

In Figure 3.3 we also plot the fractional contribution of each secondary and tertiary ALMA SMG (ranked by flux density) to the total recovered ALMA flux density of all the SMGs for each field with multiple SMGs. The mean fraction of the total flux contributed by the secondary component is 34 ± 2 % with no significant variation of this fraction as a function of the original deboosted SCUBA-2 source flux. The 64 ± 2% contribution from the primary components in maps with multiple SMGs is broadly consistent with the semi-analytic model of Cowley et al. (2015b) which suggested that ~ 70 % of the flux density in blended sources would arise from the brightest component.

Physical association of the multiple SMGs

Based on our Cycle 1 pilot study, Simpson et al. (2015a) showed that the number density of secondary SMGs in the maps of the brightest >8 mJy SCUBA-2 sources was 80 ± 30 times that expected from blank-field number counts, suggesting that at least a fraction of these SMGs must be physically associated. However we note that since expanding from

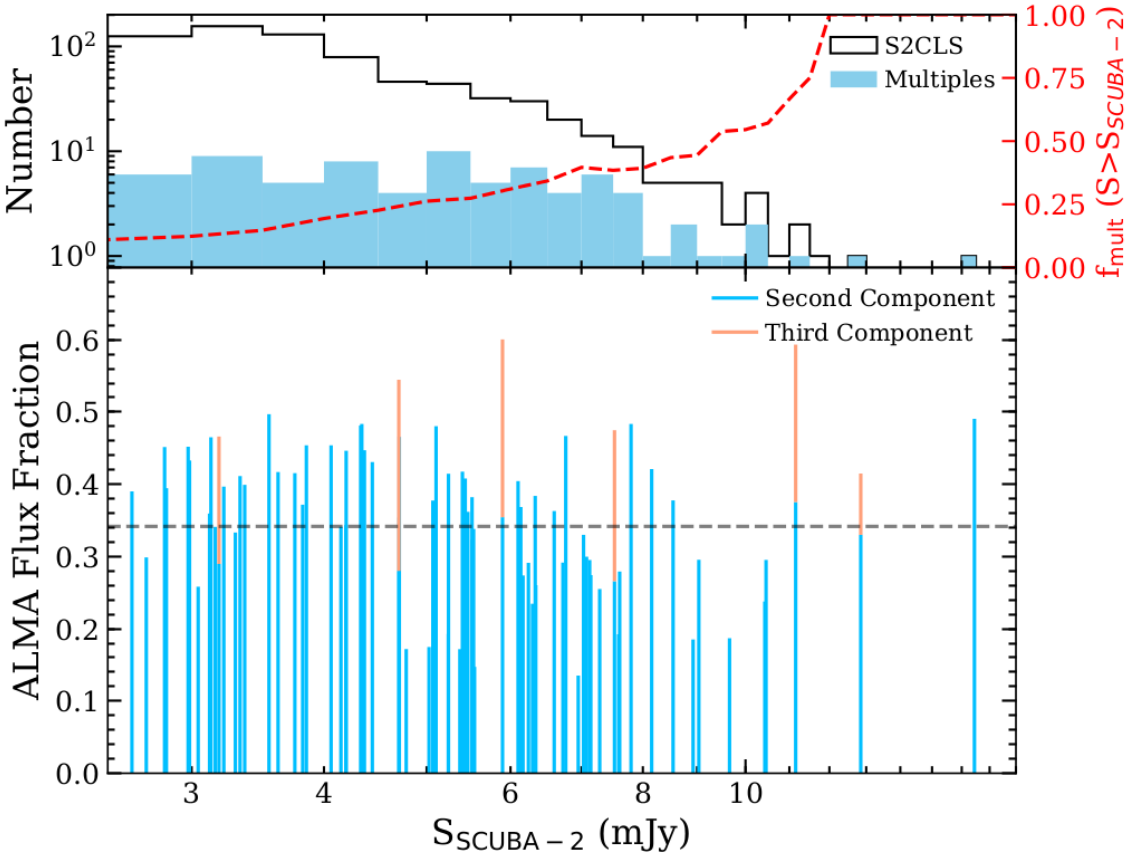

Figure 3.3: *Lower:* The fraction of the integrated ALMA flux of SMGs in each AS2UDS ALMA map that is contributed by secondary and tertiary components (ranked in terms of their relative brightness) as a function of the deboosted flux of the corresponding SCUBA-2 source. The horizontal dashed line shows the median fraction of the total flux contributed by secondary SMGs for these maps, 34 ± 2 %. There is no significant trend in the fractional flux density contributed by the secondary component as a function of the original SCUBA-2 flux density. *Upper:* The filled histogram show the distribution of the deboosted 850-μm fluxes of those SCUBA-2 sources that have multiple SMGs in our ALMA follow-up maps, and the unfilled histogram shows the corresponding SCUBA-2 fluxes of the parent sample of all 716 single-dish sources. We also plot cumulative fraction of the single-dish sources with fluxes greater than $S_{\rm SCUBA-2}$ that break up into multiple components, $f_{\rm mult}(S > S_{\rm SCUBA-2})$. This fraction increases with increasing single-dish flux and reaches $\approx$50 % at $S_{870} \sim$10 mJy.

this pilot sample to the full UDS field we do not replicate such an extreme over-density of secondary sources to our brightest >8 mJy SMGs, instead finding a 6 ± 2 times number of secondary SMGs with $S_{870} > 2$ mJy over the expected number from blank field surveys. Using our large sample we now seek to test this further. The most reliable route to test for physical association between SMGs in the same ALMA map would be to use spectroscopic redshifts for the SMGs (Wardlow et al., 2018; Hayward et al., 2018). However, as the current spectroscopic coverage of SMGs in AS2UDS is sparse, we instead exploit photometric redshifts to undertake this test. We use the photometric redshift catalogue constructed from the UKIDSS DR11 release (Hartley et al. in prep.), where a full description of the DR11 observations will be given in Almaini et al. (in prep.). These photometric redshifts are derived from twelve photometric bands ($U, B, V, R, I, z, Y, J, H, K, [3.6], [4.5]$) and applied to 296,007 K-band-detected sources using EAZY (Brammer et al., 2008); details of the methodology can be found in Simpson et al. (2013). The accuracy of these photometric redshifts is investigated in Hartley et al. (in prep.) from comparison with the $\sim$6,500 sources in the UKIDSS DR11 catalogue which have spectroscopic redshifts, finding $|z_{\rm spec} - z_{\rm phot}|/(1 + z_{\rm spec}) = 0.019 \pm 0.001$ with a median precision of ~ 9 %. Around 85 % of the ALMA maps fall in regions of the UDS with high-quality photometric redshifts and these are considered in the following analysis.

In Figure 3.4 we plot the distribution of the differences in photometric redshifts ($\Delta z_{\rm phot}$) for pairs of SMGs in those single-dish maps with multiple ALMA-detected SMGs. We limit our analysis to SMGs that fall within the region with high-quality photometric redshifts and which have K-band detections within $0\farcs6$ radius from the ALMA positions (497 of the 695 SMGs) for both sources in the map. This yields 46 pairs of SMGs (92 SMGs in total) from the 164 SMGs in the 79 maps with multiple SMGs. We find that 52 % of these pairs (24/46) have $\Delta z_{\rm phot} < 0.25$. We note that $2''$ diameter apertures were employed for the photometry in the DR11 catalog, therefore the $\Delta z_{\rm phot}$ was additionally calculated for only pairs that are separated by greater than $2''$, thus removing the possibility of neighbours contaminating photometry and thus photometric redshifts. This *still* results in 53 % of pairs having $\Delta z_{\rm phot} < 0.25$ (23/43).

To assess the significance of this result we next quantify whether the 24 pairs of mul-

tiple SMGs with $\Delta z_{\rm phot} < 0.25$ is statistically in excess of expectations for 46 randomly selected SMG pairs. To do this we determine the expected distribution of $\Delta z_{\rm phot}$ for pairs of SMGs randomly selected from the 497 SMGs with high-quality photometric redshifts across the full field, and plot this in Figure 3.4. To perform this test we sample the random distribution of our unassociated SMGs 10,000 times, each time drawing 46 pairs, and testing how frequently > 52 % of these are found to have $\Delta z_{\rm phot} < 0.25$. This analysis shows that the median fraction of random pairs with $\Delta z_{\rm phot} < 0.25$ is 20 ± 2 % compared to the 52 % for the actual pairs of SMGs. This strongly suggests that a significant fraction of the single-dish sources that resolve into multiple optically-bright (e.g. those with photometric redshifts) SMGs are in fact physically associated galaxies on projected angular scales of $\sim$10–100 kpc scales. If we assume that all pairs without photometric redshifts for *both* SMGs are physically unassociated, a conservative estimate, then comparing to the total number of ALMA fields with multiple SMGs, we can place a lower limit of at least 30 % (24 pairs out of 79) on the fraction of all multiple-SMG fields arising from closely associated galaxies. This is consistent with previous spectroscopic studies of SMG multiples e.g. $\sim$40 % of SMG pairs physically associated combining the estimates from Wardlow et al. (2018) and Hayward et al. (2018). This rate of physical association however does not return the blank-field counts for $S_{870} > 2$ mJy SMGs (Ono et al., 2014), i.e. if we remove 30 % of the secondary SMGs that we think could be physically associated galaxies to the primary detection we still find $4 \pm 2\times$ more $S_{870} > 2$ mJy secondary SMGs than expected from just random chance projections. Whilst not statistically significant this could indicate we are underestimating the physical association rate or possibly the blank-field counts are slightly underestimated (a likely possibility due to the small number statistics involved in faint SMG counts in blank fields). Of course, to truly test physical association requires a spectroscopic redshift survey of a much larger sample of these multiple-SMG systems.

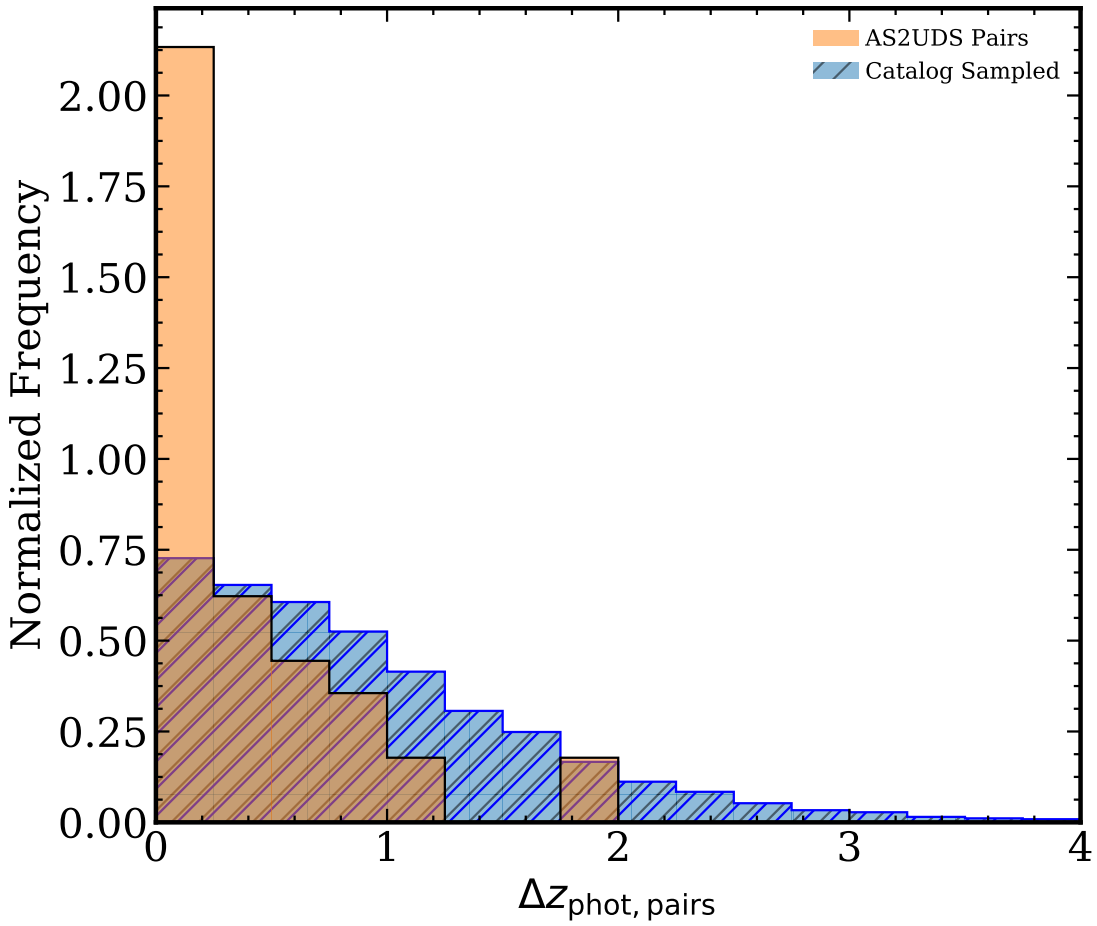

Figure 3.4: The normalized distribution of redshift separation, Δz_{phot}, for pairs of SMGs with reliable photometric redshifts detected in the same ALMA map (separation $\lesssim 9''$), compared to pairs of SMGs randomly selected from the distribution of all isolated AS2UDS SMGs with photometric redshifts. The strong peak at $\Delta z_{\mathrm{phot}} < 0.25$ for the SMGs pairs compared to the random sample, which occurs less than 1 % of the time by chance in our simulations, suggests that a moderate fraction of multiple SMGs (at least those with optically bright counterparts) in single fields arise from physically associated galaxies, rather than chance line of sight projections.

3.4 Conclusions

We have presented the first results from a large ALMA 870-μm continuum survey of 716 single-dish submillimeter sources drawn from the SCUBA-2 Cosmology Legacy Survey map of the UKIDSS UDS field. These sensitive, high-resolution ALMA observations provide the largest sample of interferometrically detected submillimeter galaxies constructed to date, with 695 SMGs above 4.3 σ (corresponding to a false detection rate of 2 %). This sample is seven times larger in terms number of SMGs and drawn from a single-dish survey which has four times the area of the previous largest interferometric SMG survey. The main conclusions of this work are as follows:

- We construct resolved 870 μm differential and cumulative number counts brighter than $S_{870} \geq 4$ mJy (a conservative choice based on the flux limit of the parent single-dish S2CLS survey), which show a similar shape to the number counts from S2CLS, but with a systematically lower normalization at fixed flux density, by a factor of 1.28$\pm$0.02. Much of this reduction in the SMG counts, is due to the influence of multiplicity, i.e. single-dish sources splitting into two or more SMGs detected by ALMA. We fit a double power-law function to our differential number counts to easily facilitate future comparison with observations in other fields and simulations.

- In 11 ± 1 % of our 716 ALMA maps we detect more than one SMG with $S_{870} \geq 1$ mJy corresponding to a $L_{\rm IR} \geq 10^{12}$ L$_\odot$ galaxy in a region with a projected diameter of ~ 100 kpc at $z = 2$. This multiplicity fraction varies from 28 ± 2 % for all single-dish sources with $S_{850}^{\rm deb} \geq 5$ mJy, to 44^{+16}_{-14} % at $S_{850}^{\rm deb} \geq 9$ mJy. The brightest of these multiple-SMG components typically contributes 64 ± 2 % of the total flux of the SCUBA-2 source, with no detectable variation in this fraction with with single-dish source flux, consistent with results from semi-analytic models of blending in single-dish surveys.

- By comparing the photometric redshift differences between pairs of SMGs in ALMA maps with multiple components, we show evidence that a significant fraction of these pairs are likely to be physically associated, with $\gtrsim 30$ % of all multiple-SMG maps arising from physically associated galaxies. This result is consistent

with the results from spectroscopic redshift surveys in Wardlow et al. (2018); Hayward et al. (2018) which find physical associations in $21\pm12\,\%$ and $43^{+39}_{-33}\,\$$ respectively, although their very small sample sizes don't provide particularly strong constraints on the rate of physical association of SMG pairs.

CHAPTER 4

An ALMA survey of the SCUBA-2 Cosmology Legacy Survey UKIDSS/UDS field: Source catalogue and properties

4.1 Summary

We present the catalogue and properties of sources in AS2UDS, an 870-μm continuum survey with the Atacama Large Millimetre/sub-millimetre Array (ALMA) of 716 single-dish sub-millimetre sources detected in the UKIDSS/UDS field by the SCUBA-2 Cosmology Legacy Survey. In our sensitive ALMA follow-up observations we detect 708 sub-millimetre galaxies (SMGs) at $>4.3\sigma$ significance across the $\sim$1-degree diameter field. We combine our precise ALMA positions with the extensive multi-wavelength coverage in the UDS field to fit the spectral energy distributions of our SMGs to derive a median redshift of $z_{\rm phot} = 2.61 \pm 0.09$. This large sample reveals a statistically significant trend of increasing sub-millimetre flux with redshift suggestive of galaxy downsizing. 101 ALMA maps do not show a $>4.3\sigma$ SMG, but we demonstrate from stacking *Herschel* SPIRE observations at these positions, that the vast majority of these blank maps correspond to real single-dish sub-millimetre sources. We further show that these blank maps contain an excess of galaxies at $z_{\rm phot} = 1.5$–4 compared to random fields, similar to the redshift range of the ALMA-detected SMGs. In addition, we combine X-ray and mid-infrared active galaxy nuclei activity (AGN) indicators to yield a likely range for the AGN fraction of 8–28 % in our sample. Finally, we compare the redshifts of this popula-

tion of high-redshift, strongly star-forming galaxies with the inferred formation redshifts of massive, passive galaxies being found out to $z \sim 2$, finding reasonable agreement – in support of an evolutionary connection between these two classes of massive galaxy.

This chapter is adapted from a first-author paper submitted to MNRAS which covered the construction and release of the complete AS2UDS catalogue (the construction is now covered in Chapter 2) combined with the first results from the MAGPHYS SED fitting and AGN selection.

4.2 Introduction

Over twenty years ago the first, deep, sub-millimetre wavelength surveys taken at the James Clerk Maxwell Telescope (JCMT) uncovered a population of sub-millimetre bright galaxies (SMGs – e.g. Barger et al., 1998), which were interpreted as showing some of highest rates of star formation observed in galaxies across the whole history of the Universe. Their sub-millimetre emission originates from the reprocessed ultra-violet starlight that has been absorbed by dust and re-emitted in the restframe far-infrared. This population of highly obscured galaxies are most easily selected at sub-millimetre wavelengths and so are termed 'sub-millimetre galaxies' (SMGs).

The selection of these star-forming galaxies at sub-millimetre wavelengths has both advantages and disadvantages. A major advantage is the strongly negative K-correction at sub-millimetre wavelengths arising from the slope of the Rayleigh-Jeans tail of their far-infrared/sub-millimetre spectral energy distributions (SED). As a result of this negative K-correction, a flux limited sub-millimetre survey provides a uniform selection in terms of far-infrared luminosity (at a *fixed* dust temperature) for sources across a redshift range of $z = 1$–6 (figure 4: Blain et al., 2002). Thus sub-millimetre observations are a very effective means to survey for the most strongly star-forming galaxies in the high redshift Universe. However, a major disadvantage of current single dish observatories operating at sub-millimetre wavelengths is their modest angular resolution, 15–30″ FWHM, which is too coarse to allow the counterpart to the sub-millimetre emission to be easily identified at shorter wavelengths as several candidate galaxies can be encompassed by the single-

dish beam. Hence early attempts to pinpoint the location of SMGs to sub-arcsecond resolutions exploited the FIR–radio correlation (e.g. Ivison et al., 1998; Barger et al., 2000; Ivison et al., 2002; Chapman et al., 2005) to match the sub-millimetre sources to their radio bright counterparts. The limitation of such radio identifications is that the radio waveband does not benefit from a strong negative K-correction, so there is a bias against identifying the highest redshift ($z > 2.5$–3) SMGs in the radio images. The difficulties with reliably identifying sub-millimetre source counterparts contributed in part to the slow advance in our understanding of these galaxies in the years following their discovery.

Not withstanding the challenges described above, the first large-scale spectroscopic redshift surveys of radio-identified SMGs (Chapman et al., 2005), and later sub/millimetre interferometrically-selected samples (Smolčić et al., 2012; Danielson et al., 2017), found that these galaxies are typically located at redshifts of $z \sim 2.5$. At these redshifts, the sub-millimetre flux of the sources corresponds to far-infrared luminosities $> 10^{12}$–$10^{13}\,\mathrm{L}_{\odot}$, i.e. Ultra-Luminous InfraRed Galaxies (ULIRGs). However, SMGs have volume densities three orders of magnitude greater than comparably luminous local ULIRGs (Chapman et al., 2005). Such high infrared luminosities indicate star-formation rates (SFR) of the order 100–1000 $\mathrm{M}_{\odot}\,\mathrm{yr}^{-1}$ (Magnelli et al., 2012; Swinbank et al., 2014), a star-formation rate high enough that within a few dynamical times (a hundred million years) the SMG could form the stellar mass of a massive galaxy $M_{*} \gtrsim 10^{11}\,\mathrm{M}_{\odot}$. Indeed, constraints on the stellar masses of SMGs have suggested $M_{*} \sim 10^{11}$–$10^{12}\,\mathrm{M}_{\odot}$ (Borys et al., 2005; Hainline et al., 2011; Michałowski et al., 2014) making SMGs some of the most massive galaxies at $z \sim 2$. The space density of these sources and their prodigious star-formation rates means that SMGs contribute $\sim 20\%$ of the Universal star-formation density between $z = 1$–4 (Casey et al., 2013; Swinbank et al., 2014). Being both massive and strongly star-forming galaxies in the early Universe, SMGs have been proposed as the progenitors of massive local spheroidal galaxies (e.g. Genzel et al., 2003; Blain et al., 2004; Cimatti et al., 2008; Simpson et al., 2014; Toft et al., 2014; Koprowski et al., 2014; Simpson et al., 2017), potentially following an evolutionary path where, following their ultra-luminous infrared phase, the SMG descendants would display both star-formation and obscured AGN activity, and then appears as a quasi-stellar object (QSO), until the system completely exhausts

its supply of gas (Coppin et al., 2008; Simpson et al., 2012).

The major advance in studies of SMGs came with the development of sensitive sub-millimetre interferometers: initially the Sub-Millimeter Array (SMA) (Younger et al., 2008; Wang et al., 2011; Smolčić et al., 2012) and more recently the Atacama Large Millimetre/sub-millimeter Array (ALMA) (Hodge et al., 2013; Simpson et al., 2015b; Hatsukade et al., 2016; Walter et al., 2016; Franco et al., 2018; Hatsukade et al., 2018; Cowie et al., 2018). Interferometric observations, in particular with ALMA, allow us to observe SMGs in the sub-millimetre at spatial resolutions more than an order of magnitude finer than achievable in single-dish surveys and free from confusion – enabling detections of sources to flux densities more than an order of magnitude fainter than the single-dish limits.

Deep, blank-field surveys utilising these interferometers have successfully recovered faint, serendipitously detected sources across arcmin^2 regions such as in the *Hubble* Ultra-Deep Field and GOODS-South (Aravena et al., 2016; Walter et al., 2016; Dunlop et al., 2016; Franco et al., 2018; Hatsukade et al., 2018). These are effective surveys for detecting the fainter examples of the SMG population free from the potential biases from clustering of sources around bright detections. However, the modest field of view of interferometers means that such surveys can only cover small areas and as a result have so far yielded relatively few (10's) of detected sources, with only very few of the brightest examples having $S_{870} \gtrsim 1$ mJy. To obtain statistically robust samples of the brighter SMGs ($S_{870} \gtrsim 1$–10 mJy), whose properties may be the most distinct from 'normal' star-forming galaxies, we require a hybrid approach – where we exploit the fast mapping speed of single-dish telescopes to identify numbers of these relatively rare sources over the large fields needed to yield large samples – combined with interferometric observations in the same sub-millimetre waveband to allow us to precisely locate the counterparts to the single-dish sources. We first employed this dual-survey approach with the ALMA LABOCA Extended *Chandra* Deep Field South survey (ALESS) (Hodge et al., 2013; Karim et al., 2013). This was an ALMA Cycle 0 survey of the 122 sub-millimetre sources detected in the LABOCA/APEX single-dish survey of the Extended *Chandra* Deep Field South (LESS: Weiß et al., 2009) and yielded detections of 126 single-dish sources with

deboosted 870 μm fluxes $S_{870} > 3.6$ mJy. This survey suggested that some previous single-dish detections were in reality multiple galaxies blended by the coarse resolution of the single-dish telescope (Karim et al., 2013) and previous multiwavelength methods of identification of SMGs, were failing to correctly locate the counterpart to the sub-millimetre emission almost half of the time (Hodge et al., 2013; Simpson et al., 2015b,a).

These initial ALMA studies of flux-limited samples have begun to illuminate the range of characteristics of bright sub-millimetre galaxies, free from the selection biases which influenced earlier radio and mid-infrared based studies. In particular they have highlighted the $\sim$ 10–20% of the population which are effectively undetectable in even the deepest optical/near-infrared (Simpson et al., 2014), which represent either the highest redshift, the least massive or the most obscured examples of this population. However, the first ALMA surveys lacked the sample size to identify statistically significant subsets of the rarest classes of SMGs. For example there are only two $z \sim 4.4$ [CII]-selected sources in the ALESS survey (Swinbank et al., 2012; Gullberg et al., 2018), which provide an insight into the properties of the more distant examples of sub-millimetre galaxies. Similarly, ALESS yielded just ten X-ray detected AGN–SMG systems, which can be used to probe the co-evolution of super-massive black holes in strongly star-forming galaxies (Wang et al., 2013). To improve the statistical strength of the conclusions about these rarer subclasses of sub-millimetre galaxies, larger surveys are needed in extragalactic survey fields with the deepest supporting data necessary to detect the faintest examples of this population.

Driven by this need, we have just completed a larger study, nearly an order-of-magnitude larger than ALESS, which exploits the wide-field sub-millimetre mapping of key extragalactic survey fields undertaken by the SCUBA-2 Cosmology Legacy Survey (S2CLS: Geach et al., 2017). We focus in this project on the S2CLS 850-μm map of the $\sim$ 1 degree diameter UKIDSS Ultra Deep Survey (UDS) Field, which was the largest, uniform area mapped by S2CLS. As discussed in Chapter 2, the S2CLS UDS map has a median sensitivity of $\sigma_{850} = 0.9$ mJy over an area of 0.96 degrees^2, with 716 sources catalogued above a 4-σ detection limit (corresponding to a 2 % false positive rate) of $S_{850} \sim 3.5$ mJy. We began our investigation of this sample with a pilot ALMA study of

a subset of thirty bright SCUBA-2 detected sources in Cycle 1 (Simpson et al., 2015b,a, 2017). We then expanded the study during Cycles 3, 4, and 5 to complete the ALMA 870-μm observations of all 716 $>4\sigma$ sources. This yields AS2UDS – the ALMA SCUBA-2 UDS survey – the largest, homogeneously selected, sample of SMGs to date with 708 detections, a five-fold increase over the previous largest similarly robust sample. The first results from this survey have already been presented: number counts and rates of multiplicity (Stach et al., 2018), the serendipitous detection of high redshift [CII] emitters (Cooke et al., 2018), and the use of this survey as a training set for machine learning algorithms to identify the multiwavelength counterparts to single-dish submillimetre sources (An et al., 2018). We present a full analysis of the multiwavelength properties of this sample in Dudzevičiūtė et al. (in prep.) and in Gullberg et al. (in prep.) we discuss the information available on the sizes and morphologies of the dust continuum in these sources from our highest resolution ALMA observations.

In our analysis we compare results from our new large sample to previous studies. To simplify these comparisons we have limited them in general to flux-limited samples from: 1. larger unbiased blank-field surveys at 850 μm (as there is evidence of differences compared to populations selected in the far-infrared and millimetre, e.g. Smolčić et al., 2012; Koprowski et al., 2014; Scudder et al., 2016; Ikarashi et al., 2017); 2. with deep (<1 mJy rms) interferometric identifications in the same waveband as any initial single-dish selection, if appropriate (c.f. Barger et al., 2014; Umehata et al., 2014; Hill et al., 2018); 3. and which are not explicitly lensed, owing to the potential selection effects and variable flux limits as well as uncertainties from cluster lenses and especially galaxy-scale lensed samples (e.g. Weiß et al., 2013; Fujimoto et al., 2015; Arancibia et al., 2018). Thus most of our comparisons are made to the ALESS survey (Hodge et al., 2013), SuperGOODS (Cowie et al., 2018) and the various ALMA surveys in GOODS-S (Walter et al., 2016; Dunlop et al., 2016; Franco et al., 2018; Hatsukade et al., 2018).

In §4.3 we describe the multiwavelength coverage of the UDS field which we matched to our sample. In §4.4 we present the first results from our MAGPHYS SED fitting (Dudzevičiūtė et al. in prep.): the photometric redshift distribution of our sample and comparisons with previous surveys. In addition we present the selection of active galactic

nuclei (AGNs) from our catalogue through archival X-ray observations of the field and IRAC colour-colour selection. §4.5 presents our main conclusions. We assume a cosmology with $\Omega_{\rm m} = 0.3$, $\Omega_{\Lambda} = 0.7$, and $\rm H_0 = 70\,km\,s^{-1}\,Mpc^{-1}$. All magnitudes are in the AB system and errors are calculated from bootstrap analysis unless otherwise stated.

4.3 Multiwavelength Observations

In this Chapter we present some of the basic properties of our sub-millimetre catalogue, using redshifts derived from spectral energy distribution (SED) fitting with MULTI-WAVELENGTH ANALYSIS OF GALAXY PHYSICAL PROPERTIES (MAGPHYS) (Da Cunha et al., 2008). This analysis exploits the wealth of deep, multi-wavelength observations available in this field (e.g. Figure 2.1). In this section we describe the multi-wavelength observations used in the MAGPHYS analysis, however the full description of the MAGPHYS SED fitting and the resulting constraints on the source properties are given in Dudzevičiūtė et al. (in prep.).

The basis of our multi-wavelength analysis is taken from the UKIRT Infrared Deep Sky Survey (UKIDSS) Ultra Deep Survey data release 11 catalogue (O. Almaini et al. in prep.). This survey contains 296,007 K-band detected sources, extracted with $2''$ diameter apertures corrected to total galaxy magnitudes, detected with SEXTRACTOR with photometry retrieved from J and H maps using SEXTRACTOR dual-image mode. These J,H, and K-band images were observed through a mosaic of four observations, covering a total survey area of $0.77\,\rm deg^2$, with the Wide-Field Camera at UKIRT (Casali et al., 2007), which covers 643 of the 716 pointings of AS2UDS, or $\sim 90\%$. The DR11 maps achieve a $2''$ aperture 3-σ median depth of $J = 26.2$, $H = 25.7$, and $K = 25.9$ mag making this one of the deepest near-infrared surveys on degree scales. The DR11 UDS K-band selected catalogue has been matched with a number of other surveys to broaden the wavelength coverage, with the matching and photometry measurements described in Hartley et al. (in prep.).

Complementary optical data comes from the Subaru/*XMM-Newton* deep survey (SXDS) (Furusawa et al., 2008), this is a survey with B, V, R_c, i' and z'-band magnitudes

with 2″aperture 3-σ depths of $B = 28.4$, $V = 27.8$, $R_c = 27.7$, $i' = 27.7$ and $z' = 26.6$ mag. Additionally there is Y-band data with a 3-σ depth of 25.3 mag supplied from the Visible and Infrared Survey Telescope for Astronomy (VISTA) Deep Extra-galactic Observations (VIDEO) survey (Jarvis et al., 2012).

We use a 0.″6 matching radius to cross-match the DR11 UDS catalogue to our AS2UDS sub-millimetre galaxy catalogue. This matching radius provides a low false match ratio (~ 3.5 %) when matching the two catalogues (see: An et al., 2018).

We include observations in the near-infrared from the *Spitzer* UKIDSS Ultra Deep Survey (SpUDS; PI: J. Dunlop), a $\sim 1\,\mathrm{deg}^2$ IRAC (at 3.6, 4.5, 5.8, and 8.0 μm – corresponding to channels: Ch1, 2, 3 and 4 respectively) survey of the UDS field with 3-σ limiting depths of 23.5, 23.3, 22.3 and 22.4 mag in Ch1–4 respectively. The astrometry of the IRAC images was corrected by stacking the IRAC images on the DR11 UDS K-band locations and corrections of +0.″00 R.A. and +0.″15 Dec. were applied to the Ch1 image, +0.″075 R.A. and +0.″12 Dec. to Ch2, +0.″075 R.A. and +0.″0 Dec. to Ch3, and +.″6 R.A. −0.″075 Dec. to Ch4. At each of the AS2UDS galaxy locations 2.″0 aperture corrected magnitudes were measured, in order to be consistent with the other optical photometric bands. We checked the quality of our photometry by comparing our Ch1 and Ch2 aperture corrected magnitudes to those given in the UKIDSS DR11 catalogue (Ch3 and Ch4 are not supplied in the DR11 catalogue). All sources with a neighbour within 2.″5 were checked for possible contamination. Conservatively, we calculated how K-band aperture corrected magnitudes (or in some cases K-band magnitude limits) of the AS2UDS sources and the near-by sources would change if observed at the resolution of the IRAC Ch1 data. If the flux from a nearby source – as measured in a 2.″0 aperture at the position of AS2UDS source – resulted in contamination of over 50 %, then IRAC magnitudes were set to limits. This reduced the number of detection in each IRAC band by 111.

Far-Infrared

We include photometry at 100, 160, 250, 350 and 500 μm, where available, from the PACS Evolution Probe (PEP: Lutz et al., 2011) and *Herschel* Multi-tiered Extragalactic Survey (HerMES; Oliver et al., 2012). To correct the astrometry of the SPIRE images

the same shifts of $< 1\farcs5$, found in the AS2UDS pilot sample of Simpson et al. (2017), were applied to the *Herschel*/SPIRE and PACS images. This shift was derived from re-centering SPIRE stacked images using VLA radio source positions (see § 4.3). We have confirmed that the radio astrometry aligns with ALMA to $< 0\farcs1$ in both R.A. and Dec. and so no additional correction to the SPIRE astrometry is required. SPIRE has comparatively low angular resolution with 18, 25, and 35″ FWHM at 250, 350 and 500 μm respectively and therefore to deblend the low resolution images we apply the technique described in Swinbank et al. (2014).

This involves initially creating a positional prior catalogue of sources, which consists of combining the $>5\,\sigma$ 24 μm MIPS and 1.4 GHz VLA source catalogue and discarding the lowest signal-to-noise ratio $1\farcs$ matched duplicates. The AS2UDS SMGs are then added to this catalogue with the non-ALMA duplicates removed by matching sources within $1\farcs$ radius of the ALMA positions. Then from the SPIRE map to be deblended, at positions in the field a thumbnail is extracted which is 2.5× the size of the FWHM of the beam for that wavelength. All galaxies in the prior catalogue within this thumbnail are then assigned random flux densities from zero to 1.3× the maximum flux density of SPIRE sources within the thumbnail. These prior-sources are then convolved with the SPIRE point spread function to create a simulated image, the amplitude, residuals and χ^2 comparison between the true SPIRE image and this simulated map is recorded. This is repeated 1000 times to find the flux density distribution amongst the galaxies which creates the best-fitting model (defined as having the lowest χ^2. This process of 1000 models and fittings is repeating but with flux densities assigned to each prior-catalogue galaxy based on the FWHM of the flux density distribution from the previous models. This iterative process is repeated until all 1000 models in the process return a $\chi^2 = 1\,\sigma$ and the best fitting model is selected as the deblended fluxes. To estimate the flux density errors and the upper-limit fluxes for non-detections 10,000 point sources are injected at random positions for each SPIRE map with flux densities drawn randomly from a uniform distribution between 0.5–100 mJy. Then for each source the input flux and recovered flux after source deblending is measured and from this the fractional flux density error can be calculated. The $3\,\sigma$ detection limit is then defined as when 68 % of the distribution is

recovered within a fractional error of 30 %. For the UDS field the detection limits of 5.2, 12.1, 9.2, 10.6, and 12.2 mJy at 100, 160, 250, 350 and 500 μm respectively are derived.

Hubble Space Telescope

A $\sim$202 arcmin^2 sub-region of the UDS field (shown in Figure 2.1) was imaged by the *Hubble Space Telescope* (*HST*) in the Cosmic Assembly Near-infrared Deep Extragalactic Legacy Survey (CANDELS: Galametz et al., 2013). This provides a WFC3 F160W (H_{160}) selected catalogue of sources with a 5-σ limiting magnitude of 27.45 mag for a point source, with SEXTRACTOR dual-mode source photometry in the F814W (I_{814}), and F125W (J_{125}) bands, 47 of our SMGs are covered in the CANDELS region, and we show a random sample of 15 of them in Figure 4.1.

Radio

Imaging at 1.4 GHz is supplied from part of the UDS20 survey (V. Arumugam et al. in prep.) which covers ~ 1.3 deg^2, and as can be seen in Figure 2.1 this mosaic covers the near entirety of the pointings in AS2UDS (714/716 sources). The radio map averages a 1-σ depth of 10 μJy beam^{-1} with the deepest regions of the map reaching 7 μJy beam^{-1} with a synthesised beam size of $\sim 1\farcs8$ FWHM. We employ a $1\farcs6$ matching radius from the AS2UDS sources to the VLA 4-σ catalogue given by Arumuham et al. (in prep.) as this is the radius at which the cumulative number of VLA detections flattens, which yields a false matching rate of 1 %. For our 708 SMGs, 706 are covered by the UDS20 survey. Of those, 273 have a radio counterpart within $1\farcs6$ (29 %) however this includes close pairs in the AS2UDS catalogue which match to a single radio source therefore only 264 unique radio sources are matched to the AS2UDS catalogue.

X-ray

Deep *Chandra* observations of part of the UDS field have been obtained by the X-UDS survey (Kocevski et al., 2018). This survey covers 0.33 deg^2 centred around the *HST*/CANDELS survey region (Figure 2.1). This coverage comprises a deep centre and shallower coverage over a wider area. In the central ~ 100 arcmin^2 of this region, the sur-

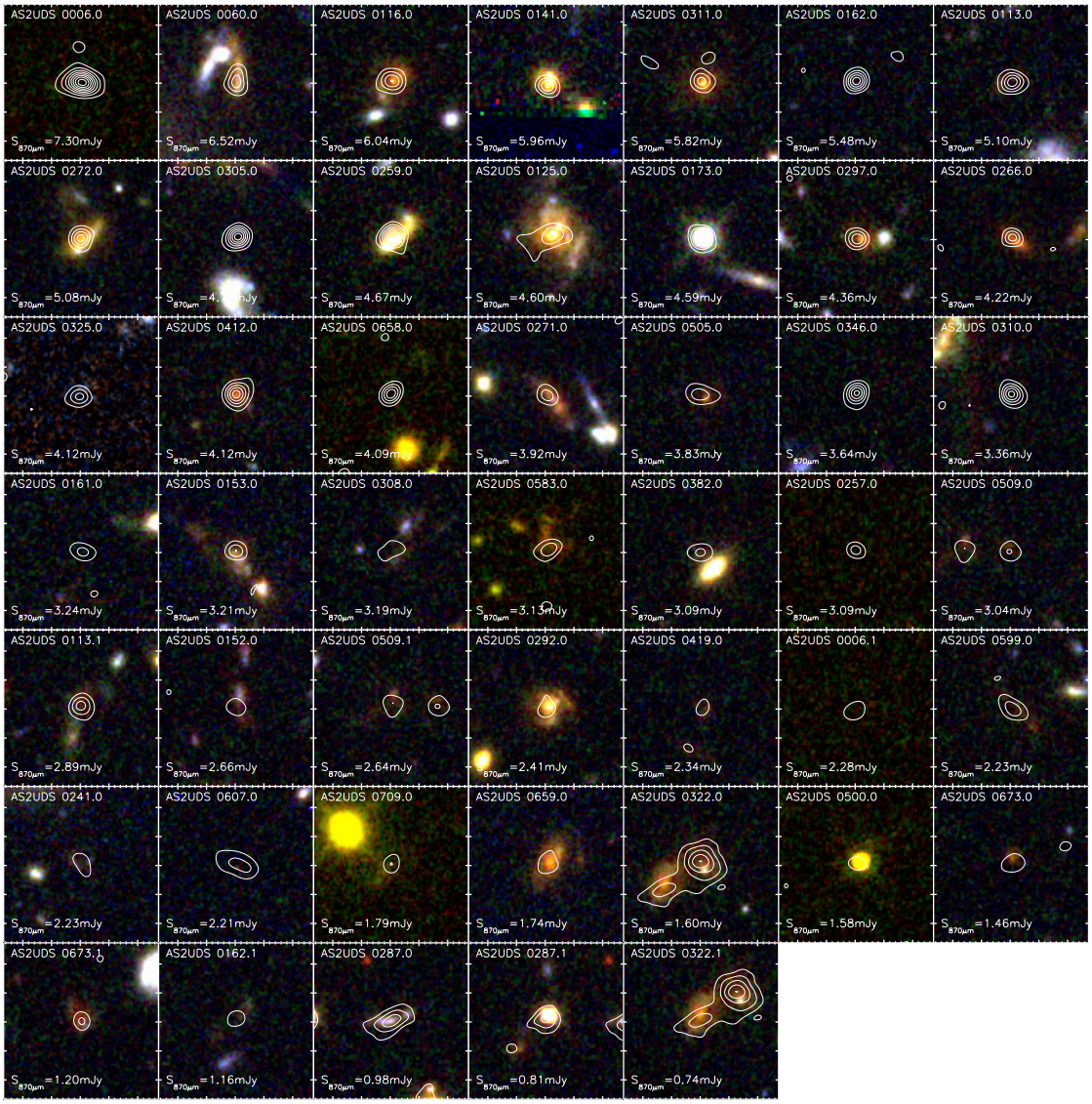

Figure 4.1: *HST* $I_{814}J_{125}H_{160}$-band colour images ($5\farcs4$ square) of the 47 ALMA SMGs in our sample that lie in the CANDELS region. Contours are taken from the tapered ALMA maps, and denote the 870 μm emission, and start at $3\,\sigma$ and are incremented by $3\,\sigma$. The 870 μm flux (in mJy) is given in the lower left corner. The *HST* morphologies of the ALMA SMGs display a range of morphologies, although the majority are morphologically complex. In general the sub-mm emission also appears more compact than the rest-frame optical emission (e.g. Simpson et al., 2015a).

vey has an average exposure time per pixel of 600 ks and outside of this area the survey has an exposure of 200 ks. In total X-UDS catalogue 868 X-ray point sources above a flux limit of 4.4×10^{-16} ergs s^{-1} cm^{-2} in the full band (0.5–10 keV).

We match the X-UDS catalogue to the AS2UDS catalogue using matching radii based on the positional errors radii in the X-UDS survey (median positional error of $0\farcs96$). Over the full X-UDS coverage we have 274 SMGs falling within the *Chandra* footprint, of which 21 are matched to X-ray counterparts. Within the CANDELS *HST* area, where the *Chandra* coverage is deepest, we have 47 SMGs, but only two of these match to X-UDS sources. We also perform a stacking analysis to derive average X-ray fluxes for samples of individually undetected SMGs. This analysis uses the X-UDS *Chandra* soft (0.5–2 keV) and hard (2–8 keV) band observations and the CSTACK stacking software developed by T. Miyaji (Miyaji et al., 2008). For samples of SMGs we use CSTACK to determine the mean stacked, background subtracted, count-rates and uncertainties from which fluxes were derived using the count rate to flux conversion factors given in Kocevski et al. (2018). These fluxes are then converted into X-ray luminosities by assuming a power-law X-ray spectrum with photon index $\Gamma = 1.7$, consistent with the SED shape assumed for the X-ray detections in Kocevski et al. (2018), and the photometric redshifts estimated below.

4.3.1 Photometric Redshifts

With the final AS2UDS catalogue matched to the extensive multiwavelength coverage in the UDS field we derive the multiwavelength properties for our SMGs from SED fitting from a maximum of 22 filters ($U, B, V, R, I, z, Y, J, H, K$, *IRAC* 3.6, 4.5, 5.8, and 8.0 μm, MIPS 24 μm, PACS 100, and 160 μm, SPIRE 250, 350, and 500 μm, S_{870}, and $S_{1.4\,\mathrm{GHz}}$) using MAGPHYS (Da Cunha et al., 2008). MAGPHYS employs the stellar population synthesis models of Bruzual & Charlot (2003) with a Chabrier (2003), combined with a two-component description of the dust attenuation in the ISM and stellar birth clouds Charlot & Fall (2000) in an energy-balance model to ensure consistency between the mid- to far-infrared emission from dust re-processing of the stellar emission and the integrated (dust-attenuated) stellar emission of the galaxy Da Cunha et al. (details in 2008). da Cunha et al. (2015) extended this method to include the computation of photometric redshifts

simultaneously with the constraints on other physical parameters when fitting the SEDs of dusty star-forming galaxies. We use that version of the code in this paper (for a full description of MAGPHYS-photometric redshifts and code release see also Battisti et al, (in prep). To test the reliability of the predicted photometric redshifts, MAGPHYS was fitted to 14 photometric bands of 7316 spectroscopic sources from the UKIDSS UDS DR11 photometric catalogue. The median relative difference, $\Delta z = (z_{\rm spec} - z_{\rm MAGPHYS})/(1+z_{\rm spec})$, was found to be -0.0056 with a standard deviation of 0.30. Similarly, for the 44 AS2UDS SMGs with spectroscopic redshifts we find a median $\Delta z = -0.02$ with a standard deviation of 0.25. The complete description of our MAGPHYS SED fitting and the resulting multiwavelength properties is described in U. Dudzevičiūtė et al (in prep.).

4.4 Results and Discussion

In this section we discuss the trends with redshifts in our sample and the potential causes for maps which lack detected sources. We also study the properties of those in the sample hosting actively accreting super-massive black holes (SMBHs) and the connection of these galaxies to the formation of massive, passive galaxies at high redshifts.

4.4.1 AS2UDS Catalogue

The complete AS2UDS catalogue identifies 708 sub-millimetre galaxies brighter than $S_{870} = 0.58$ mJy from the original 716 SCUBA-2 sub-millimetre sources, roughly five times larger than the Miettinen et al. (2017) study in COSMOS or ALESS (Hodge et al., 2013). In Appendix A.1 we present the AS2UDS catalogue.

From the 716 ALMA maps: one contains four SMG detections, six have three SMG detections, 78 include two, and 530 detect just a single SMG above $4.3\,\sigma$. The majority of the maps containing multiple SMGs correspond to the brighter SCUBA-2 sources so, as Chapter 3 showed, the rate of occurrence of multiple counterparts is 26 ± 2 % in SCUBA-2 sources with fluxes brighter than $S_{850} \geq 5$ mJy and 44 ± 16 % at $S_{850} \geq 9$ mJy. The presence of these multiple strongly star-forming galaxies in close proximity may be hinting at a role for major mergers in driving the enhanced star-formation rates in some of

these systems. Indeed, the small subset of AS2UDS covered by the high-resolution *HST* imaging (see Figure 4.1) indicates that many of the SMGs are morphologically complex, with close companions and/or structured dust obscuration, consistent with the *HST* imaging for the ALESS survey (Chen et al., 2015). From visual inspection, independently carried out by two of the authors, the CANDELS coverage suggests 50 ± 10 % of our SMGs are either clear mergers or are disks with likely companions with similar colours on $<$20 kpc scales, and we group these two visual classifications as 'likely interacting'. The median redshifts for the 'likely interacting' SMGs is $z_{\rm phot} = 2.2 \pm 0.1$, significantly lower than the median redshift for the whole SMG sample (see §4.4.2). Indeed, if we cut our sample to SMGs at redshifts $z_{\rm phot} < 2.75$, the redshift range at which we could reasonably expect to detect interactions in the CANDELS imaging then this 'likely interacting' classification increases to 17/21 or $\sim$80 % of our SMGs, again this is consistent with Chen et al. (2015). This small subset in the CANDELS imaging strongly hints that major mergers are playing a role in driving the enhanced star-formation rates that result in our galaxies being selected in the sub-millimetre maps. Of the 'likely interacting' SMGs roughly half of these are classified as SMGs with close proximity companions and of those 13 SMGs, just four of them are from two pairs where both are ALMA detections in our catalogue with the remaining nine AS2UDS SMG companions being non-detections in ALMA, i.e. 30 ± 20 % of *HST* close companions from visual inspection are ALMA companions. Trying to recover an average flux for the ALMA non-detections by stacking the ALMA maps at the locations of the closest companions in the CANDELS imaging still returns no detections suggesting that if they do lie at similar redshifts to the SMG they have very minimal active star-formation.

In Figure 4.2 we show the apparent magnitude/flux density distributions for the AS2UDS SMGs in V, K, $m_{3.6}$, S_{870}, and 1.4 GHz bands and for comparison the corresponding distributions of the ALESS SMGs (Hodge et al., 2013; Simpson et al., 2014). The median ALMA flux density for the AS2UDS SMGs is $S_{870} = 3.73^{+0.03}_{-0.10}$ mJy, very similar to the $S_{870} = 3.5 \pm 0.3$ mJy for ALESS. Of the 708 SMGs, 529 (75%) have K-band counterparts in the UKIDSS-UDS DR11 catalogue to $K \leq 25.9$ mag. However, excluding ALMA SMGs which fall either outside the DR11 WFCAM K-band image

or in regions which are flagged as being shallower, the detection rate corresponds to 84 ± 4 % (484/577). The median apparent magnitudes for these AS2UDS SMGs are $V = 26.1 \pm 0.1$, $K = 22.8 \pm 0.1$, $m_{3.6} = 21.65^{+0.06}_{-0.03}$. These values are all in good agreement with the equivalent measurements for the ALESS sample of $V = 26.1^{+0.2}_{-0.1}$, $K = 23.0^{+0.3}_{-0.1}$, and $m_{3.6} = 21.8 \pm 0.2$. Hence we conclude that these two ALMA follow-up surveys of single-dish detections find SMGs with multi-wavelength magnitude distributions in excellent agreement with each other. These photometric properties demonstrate the dusty nature of the target populations with an increasing number of non-detections towards the bluer optical wavebands, e.g. only 64 ± 2 % of K-band detected SMGs are detected in the V-band brighter than $V < 27.8$. We note that, unlike in the pilot AS2UDS sample (Simpson et al., 2015a), in the full sample there is no evidence that a lack of a K-band detection is a function of the S_{870}, with a median ALMA flux of $S_{870} = 3.65^{+0.12}_{-0.08}$ mJy for the K-detected SMGs and $S_{870} = 3.5^{+0.2}_{-0.1}$ mJy for the K-undetected SMGs, the same trend was found in Cowie et al. (2018).

With the matched multi-wavelength catalogue we check the effectiveness of the BzK two-colour selection for star-forming galaxies (Daddi et al., 2004) for our SMGs which also tests the reliability of our photometric redshifts. This method selects star-forming galaxies ($sBzK$) within the redshift range $1.4 < z < 2.5$ with selected colours $BzK = (z-K)_{\rm AB} - (B-z)_{\rm AB} > -0.2$, Figure 4.3, with passive galaxies ($pBzK$) within the same redshift range defined as $BzK < -0.2$ and $(z-K) > 2.5$. For our SMGs using the MAGPHYS redshifts, we find within the redshift BzK redshift selection range, that 95 ± 5 % are correctly identified as star-forming galaxies with a single galaxy being mis-identified as a passive galaxy. Of the 13 $z < 1.4$ SMGs with BzK detections, 10 are correctly selected as $z < 1.4$ galaxies in the BzK plane with 3 of them selected as $pBzK$. We also overlay the ALESS composite SED which, as discussed in Simpson et al. (2014), shows that we would expect our SMGs to be successfully classified as star-forming galaxies in the $z \approx 1-4$ redshift range with galaxies above and below that range being classified as $z < 1.4$ galaxies. This is a trend our SMG colours and photometric redshifts agree with, finding 87 ± 5 % of $z = 1-4$ SMGs classified as $sBzK$ and 4 out of 6 SMGs outside that redshift range lying within the $z < 1.4$ galaxy region.

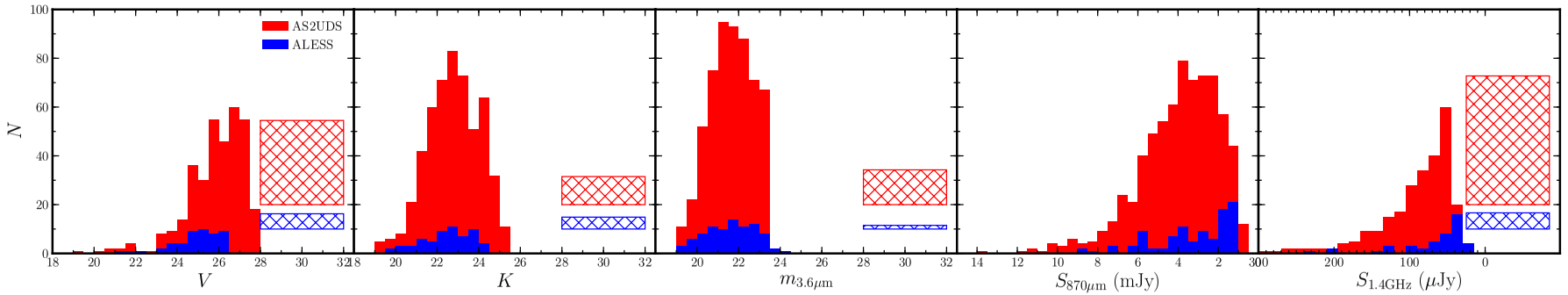

Figure 4.2: Apparent magnitude distributions in the V, K and 3.6 μm wavebands and the flux densities in 870 μm and 1.4 GHz for AS2UDS. For comparison we show the same distributions for the earlier ALESS survey, and in both cases the hatched regions showing the non-detections. The median magnitudes/fluxes for AS2UDS are $V = 26.1 \pm 0.1$, $K = 22.8 \pm 0.1$, $m_{3.6} = 21.65^{+0.06}_{-0.03}$, $S_{870} = 3.73^{+0.03}_{-0.10}$ mJy, and $S_{1.4\,\mathrm{GHz}} = 86^{+2}_{-5}$ μJy, with the estimates for the smaller ALESS survey in good agreement. These illustrate that typical SMGs have red optical-near infrared colours and so are very faint in the optical with a large fraction of the population undetected in the bluest wavebands. In contrast, most of the SMGs are detected at 3.6 μm.

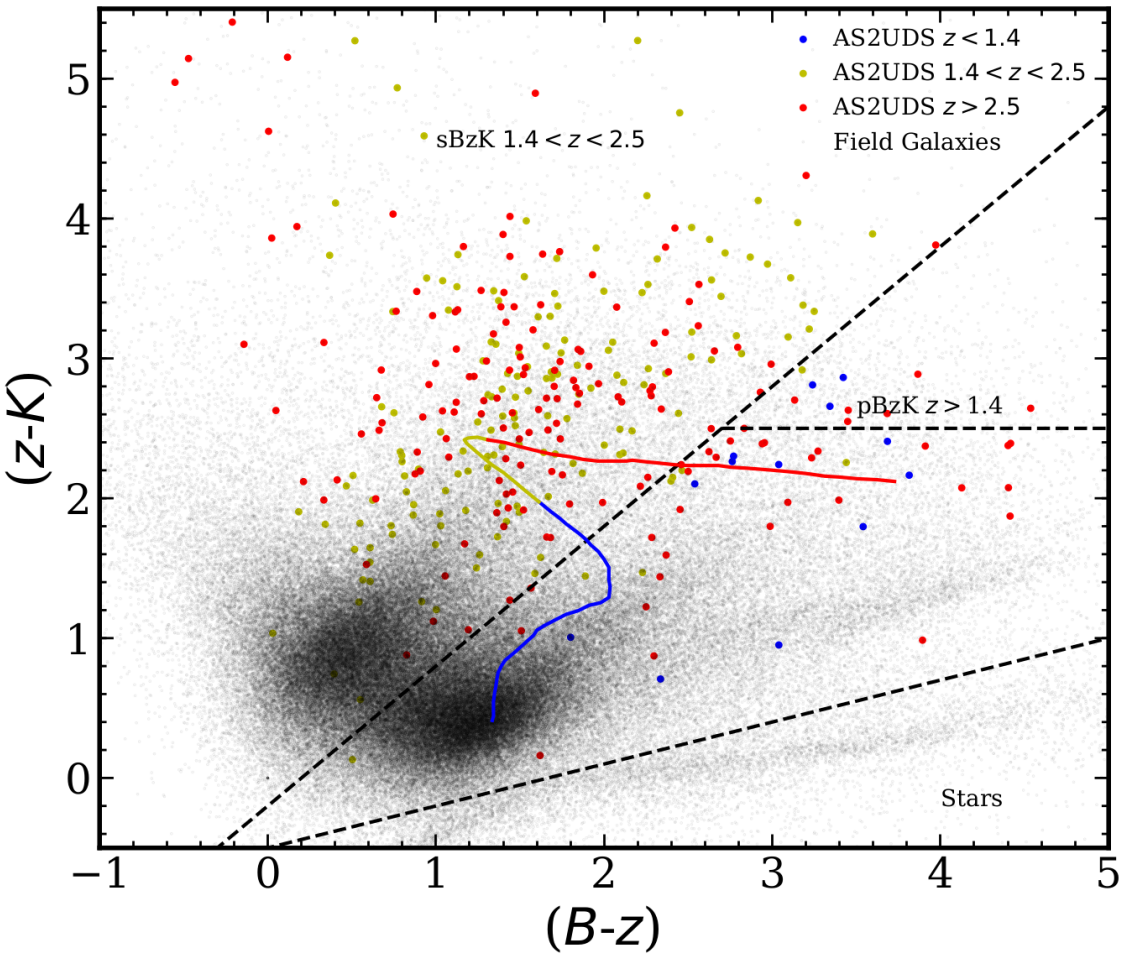

Figure 4.3: The *BzK* colour-colour selection for starforming galaxies applied to our AS2UDS SMGs. We separate the regions for star-forming *sBzK*, passive *pBzK*, and $z < 1.4$ galaxies as defined in Daddi et al. (2004) with black dashed lines. The BzK selection correctly identifies 95±5 % of our SMGs are correctly identified as star-forming galaxies by this selection within the *BzK* $1.4 < z < 2.5$ redshift range. We colour-code our SMGs and the ALESS composite SED by photometric redshift and also show for comparison the field galaxies from the UKIDSS UDS DR11 catalogue.

4.4.2 Redshift Distribution and Trends

The photometric redshift distribution for all 708 SMGs is shown in Figure 4.4. We derive a median redshift of $z_{\rm phot} = 2.61 \pm 0.09$ and a tail at higher redshifts, with 33^{+3}_{-2} % of galaxies at $z_{\rm phot} > 3$. This median redshift is consistent with the Cycle 1 pilot sample of bright SMGs (analysis using HyperZ) from Simpson et al. (2015a) of $z_{\rm phot} = 2.65 \pm 0.13$ (or $z_{\rm phot} = 2.9 \pm 0.2$ including optically faint SMGs without precise photometric redshifts). The more direct comparison to our sample are the MAGPHYS-derived redshift distribution for ALESS from da Cunha et al. (2015) who found a median redshift of $z = 2.7 \pm 0.1$ with a similar fraction of galaxies in the $z_{\rm phot} > 3$ tail of 38^{+7}_{-6}%.

We next compare our photometric redshift distribution with previous spectroscopic redshift surveys selected at 850 μm SMGs. Chapman et al. (2005) found a median redshift for their 73 radio-detected SMGs of $z = 2.2 \pm 0.1$ ($z = 2.3 \pm 0.2$ after statistically correcting for the radio bias). The lower median redshifts is unsurprising given the lack of a negative K-correction at radio wavelengths. We can confirm this by looking at the AS2UDS SMGs with radio bright counterparts where we find a median redshift of $z = 2.4^{+0.3}_{-0.9}$, which is in reasonable agreement with the Chapman et al. (2005) sample. The spectroscopic sample of Danielson et al. (2017), which consisted of 52 ALMA-confirmed SMGs detected in the ALESS catalogue found a median redshift of $z = 2.40 \pm 0.10$, in rough agreement with the photometric redshift distribution of AS2UDS, however, this spectroscopic redshift sample is biased to optically and near-infrared bright counterparts.

There have also been wide-field single-dish surveys at longer wavelengths, $\sim$1–1.2 mm, which are now being similarly followed up with sub/millimetre interferometers (e.g. Smolčić et al., 2012; Miettinen et al., 2017). In particular, Brisbin et al. (2017) obtained ALMA interferometric observations of 129 1.25 mm sources in COSMOS and determined a median redshift (from a heterogeneous mix of spectroscopic, photometric and colour-based estimates or limits) of $z \sim 2.48 \pm 0.05$ for a sample with an equivalent 870-μm flux of $S_{870} \gtrsim 6$ mJy. This is in reasonable agreement with our median redshift, given the different flux and waveband selections.

We can also compare our median redshift with those derived for the typically fainter samples of SMGs from 'blank field' ALMA surveys (e.g. Walter et al., 2016; Dunlop

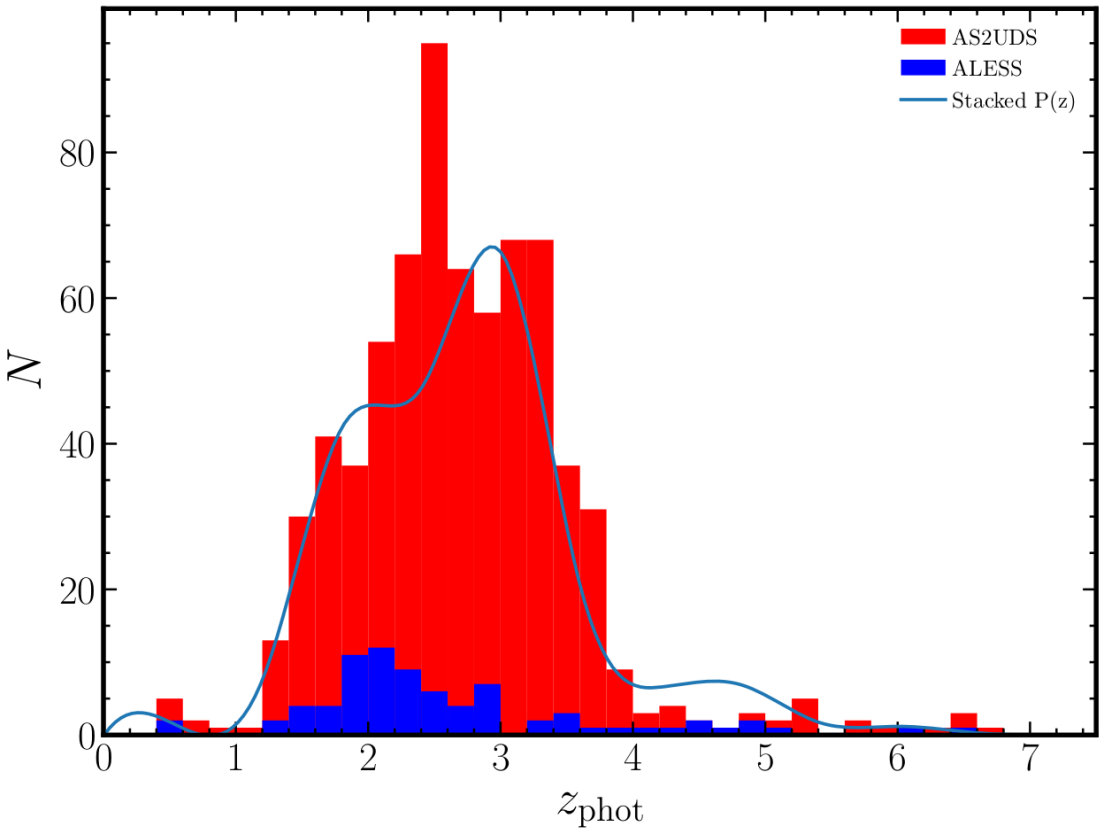

Figure 4.4: The photometric redshift distribution for the AS2UDS SMGs based on MAGPHYS analysis (Dudzevičiūtė et al. in prep). We determine a median redshift of $z_{\rm phot} = 2.61 \pm 0.09$, consistent with the ALESS photometric redshift distribution (da Cunha et al., 2015), which has a median $z_{\rm phot} = 2.7 \pm 0.1$. The ALESS distributions also display a fraction of sources at $z_{\rm phot} > 3$ galaxies, 38^{+7}_{-6}%, that agrees with that derived here for our large AS2UDS sample, 33^{+3}_{-2} %. To illustrate the influence of the asymmetric redshift uncertainties we also overlay the stacked probability distributions for the photometric redshifts of all AS2UDS SMGs from MAGPHYS. This closely resembles the median photometric redshift distribution, suggesting that the full combined photometric redshift is not sensitive to any secondary redshift solutions in individual sources.

et al., 2016). The ALMA 'blank field' surveys are usually undertaken at longer wavelengths than our 870-μm observations, normally in Band 6 at $\sim$1.1–1.3 mm, to exploit the larger ALMA primary beam to increase the area coverage. Three ALMA surveys of blank fields have reported median redshifts for their samples, although we caution that these all study fields in the GOODS-South area and so are not truly independent. Aravena et al. (2016) report a median redshift of $z = 1.7 \pm 0.4$ for a sample of nine galaxies with an 870 μm equivalent flux limit of $S_{870} \gtrsim 0.1$ mJy (median $S_{870} = 0.22^{+0.12}_{-0.06}$ mJy), Dunlop et al. (2016) report $z = 2.0 \pm 0.3$ for 16 sources with optical/near-infrared counterparts and equivalent $S_{870} \gtrsim 0.3$ mJy (median $S_{870} = 0.65^{+0.13}_{-0.09}$ mJy) and Franco et al. (2018) find $z = 2.9 \pm 0.2$ for a sample of 20 galaxies with $S_{870} \gtrsim 1.1$ mJy (median $S_{870} \approx 1.8$ mJy). These studies are challenging and the results from all of them are currently limited by statistics, but there is a hint that the deeper surveys are finding lower median redshifts than from our bright sample, in the same sense as the trend we discuss below.

We next study the variation in median redshift with 870-μm flux density within AS2UDS. It has long been claimed that there is variation in redshift with sub-millimetre flux, in the sense that the more luminous sub-millimetre sources typically lie at higher redshifts. This behaviour was first seen in powerful high-redshift radio galaxies (Archibald et al., 2001), but the existence of a similar trend has been claimed for sub-millimetre galaxies, although these claims have typically suffered from incomplete, heterogeneous or highly uncertain redshift estimates (e.g. Ivison et al., 2002; Pope et al., 2005; Younger et al., 2007; Smolčić et al., 2012; Koprowski et al., 2014; Brisbin et al., 2017). The initial search for a z–S_{870} trend in the ALESS sample (Simpson et al., 2014) and in the initial bright pilot for AS2UDS (Simpson et al., 2015a) both found weak trends. Moreover, these were based on incomplete samples owing to the reliance on optical-near-infrared photometric redshifts. When allowance was made for this incompleteness, they concluded that the trends were not statistically significant.

One benefit of using MAGPHYS for our photometric redshift analysis is that we can obtain more complete and homogeneous redshifts estimates, not only for those sources detected in the optical to near-infrared bands, but also where only longer wavelength constraints are available. So, we begin by determining if the SMGs which are undetected in

the K-band are at higher redshift than those which have a K-band counterpart, as would be required for there to be a trend of z–S_{870}. For galaxies with K-band counterparts we find a median $z_{\rm phot} = 2.6 \pm 0.1$ and for the K-band non-detections we find a median $z_{\rm phot} = 3.0 \pm 0.1$, suggesting that indeed the population of K-faint SMGs, whilst not deviating dramatically in distribution of S_{870} as mentioned above, do represent a higher redshift subset of SMGs.

In Figure 4.5 we show the photometric redshifts as a function of the ALMA 870 μm flux density for AS2UDS using our complete MAGPHYS-derived photometric redshifts. We over plot a linear fit to the median redshifts in bins of equal number of galaxies. This fit shows a trend of median redshift with 870 μm flux density with a highly significant gradient of $0.09 \pm 0.02\,{\rm mJy}^{-1}$. The significance of this result is perhaps surprising given the absence of a strong trend in either ALESS (Simpson et al., 2014) or our Cycle 1 pilot programme (Simpson et al., 2015a). However, the most likely explanation is simply the much smaller sample sizes ($n < 100$) in those studies. To test this we randomly draw samples of 100 galaxies from the complete AS2UDS catalogue 500 times and repeat the same fitting procedure. In this case we recover an average gradient of $0.08 \pm 0.06\,{\rm mJy}^{-1}$ confirming that the smaller samples employed in all previous tests mean that it would be impossible to reliably recover the trend we see at higher than $\sim 1.5\,\sigma$ significance. In addition, to confirm that our detection incompleteness isn't driving this trend we perform the same trend fitting to the galaxies with fluxes $S_{870} > 4$ mJy, again finding a similar gradient of $0.08 \pm 0.03\,{\rm mJy}^{-1}$.

What is the physical process responsible for the z–S_{870} trend we see in AS2UDS? Due to the negative K-correction of the dust SEDs in typical SMGs, across the redshift range ($z \sim 1.5$–5) that we measure this trend, the population have a roughly constant observed flux density at a fixed luminosity (and temperature). Hence the brighter galaxies found at the higher redshifts are intrinsically more luminous. The trend we see then suggests there is a strong luminosity evolution for our SMGs out past $z > 3$, with the most far-infrared luminous galaxies being found in greater numbers in the early Universe. This could be symptomatic of galaxy 'downsizing' (Cowie et al., 1996), i.e. the more massive galaxies are forming at higher redshifts. We will return to the issue of potential evidence

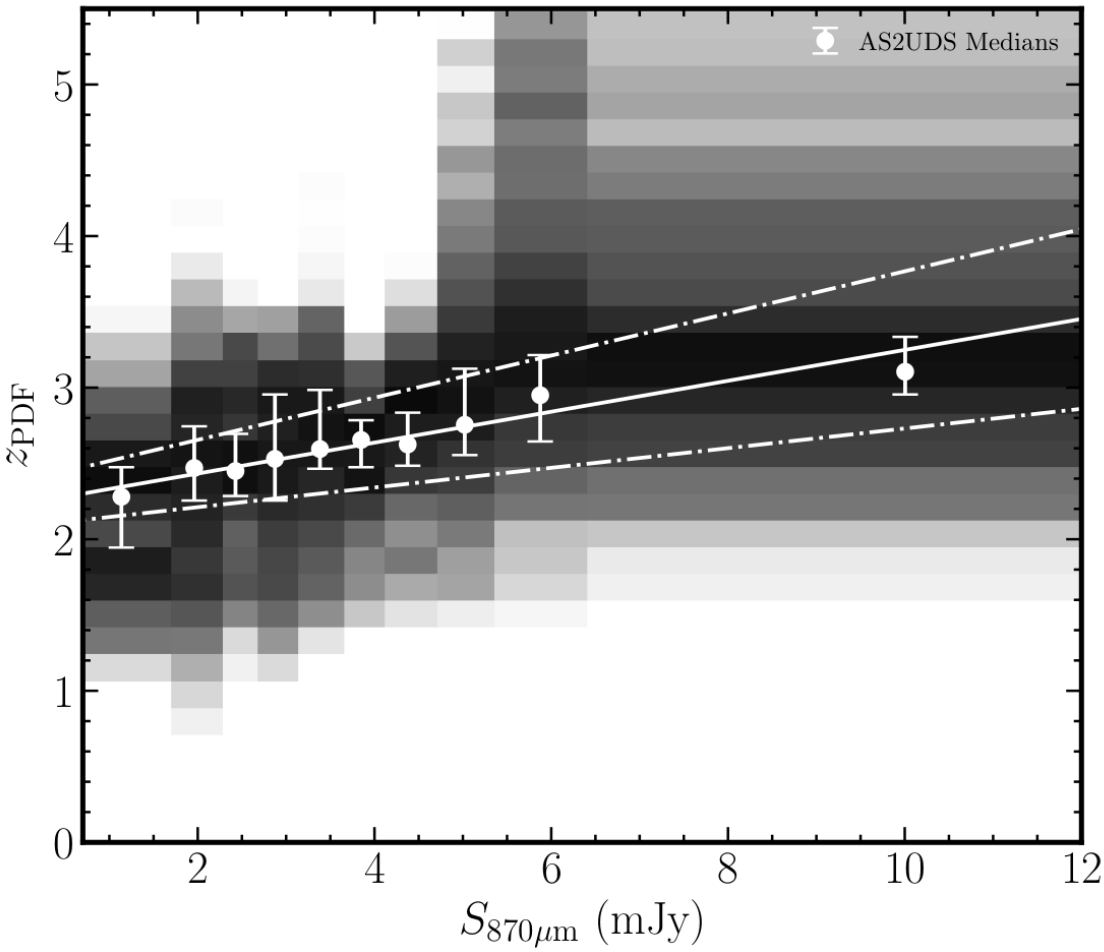

Figure 4.5: The trend between photometric redshifts and ALMA 870 μm flux density for AS2UDS SMGs. We bin the galaxies by ALMA 870 μm flux density with bins of equal galaxy numbers and find that the median redshift and flux of each bin. These show a significant trend of increasing redshift with increase flux. The linear fit to this trend has a gradient of 0.09 ± 0.01 mJy^{-1} and we plot this as the solid line and the 3-σ errors for this fit as the dashed lines. In addition to the medians of the bins, the greyscale background shows the stacks of the redshift probability density functions for each bin, which also display the same flux density evolution.

of 'downsizing' on a forthcoming paper on the clustering of the AS2UDS SMGs in the UDS field (Stach et al. in prep.).

Finally, to attempt to model the variation in median redshifts, we employ the Béthermin et al. (2015) models of SMG number counts and redshift distributions to model the median redshifts of surveys from two variables; the wavelength of selection of the SMGs and the flux density depth of the survey. The Béthermin et al. (2015) model suggests that surveys at longer wavelengths will recover a higher median redshift and that, due to the luminosity evolution, the fainter sources found in deeper surveys will predominantly lie at lower redshifts. Whilst this phenomenological model reproduces the broad trend we see in AS2UDS, as well as the comparatively low median redshifts of Aravena et al. (2016) and Dunlop et al. (2016) due to their fainter flux limits, it does under-predict the median redshift for our survey. For a $S_{870} > 4$ mJy flux limited sample the model predicts $z \sim 2.6$ compared to our $z = 2.8 \pm 0.1$, and this $\Delta z \sim -0.2$ offset between the model and our survey roughly persists across any choice of faint flux limit in our catalogue, indicating that further tuning of this phenomonological model may be needed.

4.4.3 Blank Maps

There are 101 ALMA maps of SCUBA-2 sources in which we find no ALMA detected source above our $4.3\,\sigma$ detection threshold, these are termed 'blank' maps. This rate of non-detection is considerably higher than the expected 2 % false-positive rate predicted from Geach et al. (2017) for the initial SCUBA-2 catalogue. Whilst these 'blank' maps typically correspond to the fainter single-dish sources: the median SCUBA-2 flux of the 'blank' maps is $S_{850} = 4.0 \pm 0.1$ mJy, compared to $S_{850} = 4.5 \pm 0.1$ mJy for the whole sample, the SCUBA-2 noise properties of the 'blank' maps are consistent with those of the maps with detections. To confirm that these are not dominated by false positive detections in the parent SCUBA-2 catalogue we stack the *Herschel*/SPIRE and SCUBA-2 maps at the locations of the 101 'blank' map sources ranked in four bins of their SCUBA-2 flux and further sub-dividing the faintest quartile in SCUBA-2 flux into two independent halves, shown in Figure. 4.6.

For each subsample we detect emission in the *Herschel*/SPIRE at 250 and 350 μm

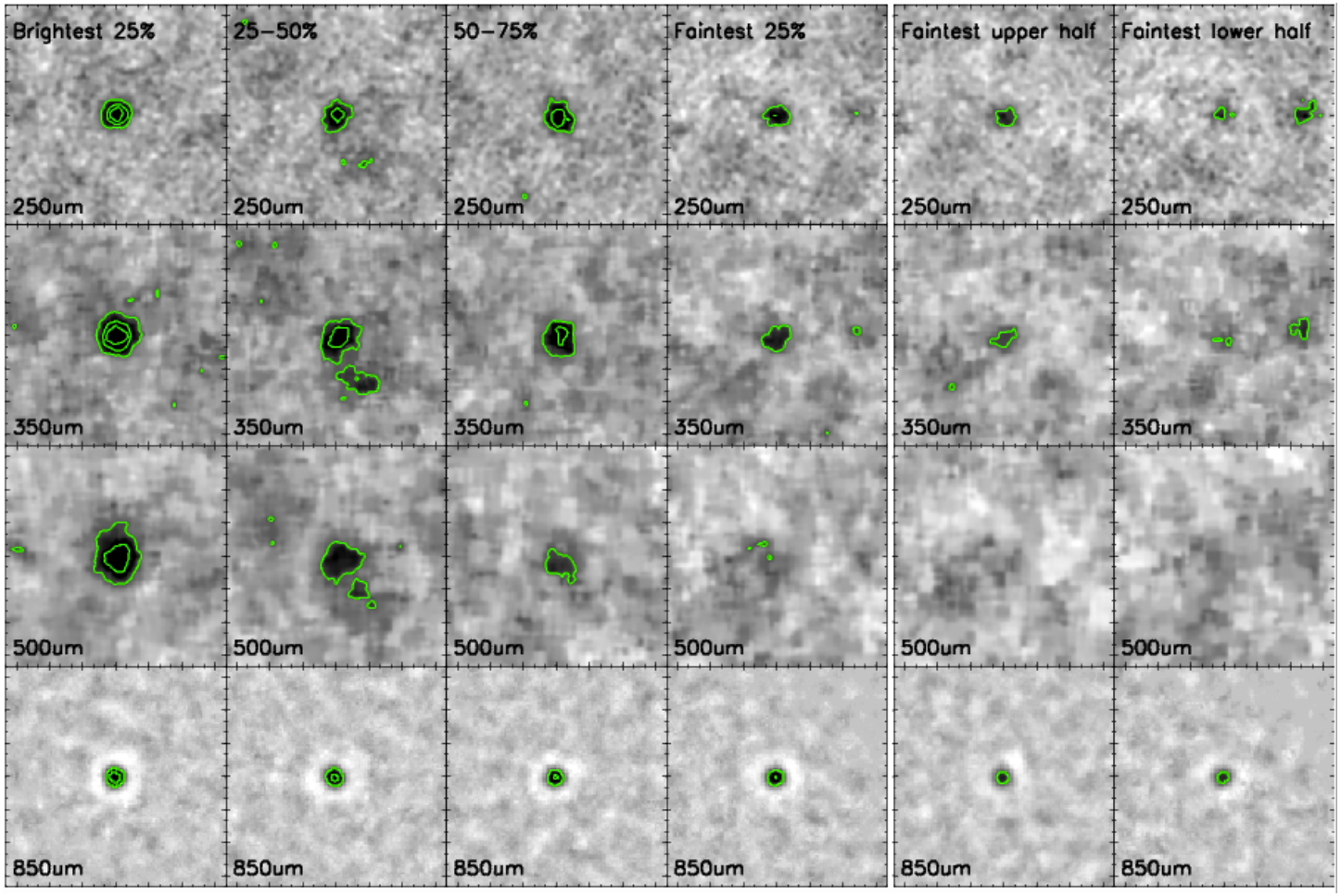

Figure 4.6: *Herschel*/SPIRE and SCUBA-2 stacks on the 101 ALMA 'blank' maps in four bins of original SCUBA-2 flux. Even in the faintest SCUBA-2 bin we detect emission at 250 μm and 350 μm. Further splitting the faintest bin into two results in detected emission strongly suggesting these 'blank' maps are not typically the result of spurious single-dish SCUBA-2 detections. Each map is 120$''$ square and is centred on the SCUBA-2 source position.

and even when further sub-diving the faintest subsample into two there is still emission detected at 250 μm strongly suggesting these ALMA-blank maps are not just the result of spurious single-dish sources. To compare the 850 μm fluxes implied by these SPIRE detections with the original SCUBA-2 measurements, we predict 850 μm flux from the SPIRE stacks by fitting a modified blackbody SED with $z = 2.5$, a dust temperature, $T_d = 35$ K and emissivity $\beta = 1.5$ to each of the 250/350/500 μm stacked fluxes. In Figure 4.7 we show the predicted 850 μm flux from these SED fits against the original detected 850 μm emission from SCUBA-2. Whilst there is significant scatter in these estimates, the 850-μm fluxes predicted from the extrapolation of the stacked *Herschel* fluxes is consistent with that observed by SCUBA-2. We view this as a strong confirmation that the majority of these SCUBA-2 sources with ALMA 'blank' maps are not spurious detections in the original S2CLS catalogue.

We conclude that spurious single-dish detections are not the dominant cause for 'blank' maps, therefore, we next examine possibilities for missing ALMA counterparts in our ALMA maps of these sources. An alternative possibility is multiplicity (e.g. Karim et al., 2013), where a single-dish source splits into more than one, fainter galaxies. The combined flux from these galaxies would recover the single-dish flux, but individually each galaxy is below our detection threshold. To check if this is a possibility we look for over-densities of candidate K-band detected galaxies in our ALMA blank maps in comparison to a 'random' location within the UKIDSS UDS coverage. In Figure 4.8 we show the MAGPHYS photometric redshift distributions for both the K-band detected sources within the primary beams of all 101 'blank' maps and for a 'random' sample covering the same area as the 101 ALMA primary beams, but randomly distributed across the UDS field. We can see an excess of K-selected galaxies in the ALMA-blank maps. The majority of this excess arises from galaxies at redshifts of $z \sim 1.5$–4, corresponding to the redshift range where our detected SMG population peaks, with 153 excess galaxies in this redshift range in the 'blank' map regions compared to the 'random' area (a factor of $1.36^{+0.13}_{-0.12}$ increase). This over-density comprises an average excess in a 'blank' map of 1.5 ± 0.5 K-band sources (within the expected sub-millimetre galaxy redshift range). Stacking the ALMA emission of all of the galaxies at $z = 1.5$–4 in these 'blank' maps re-

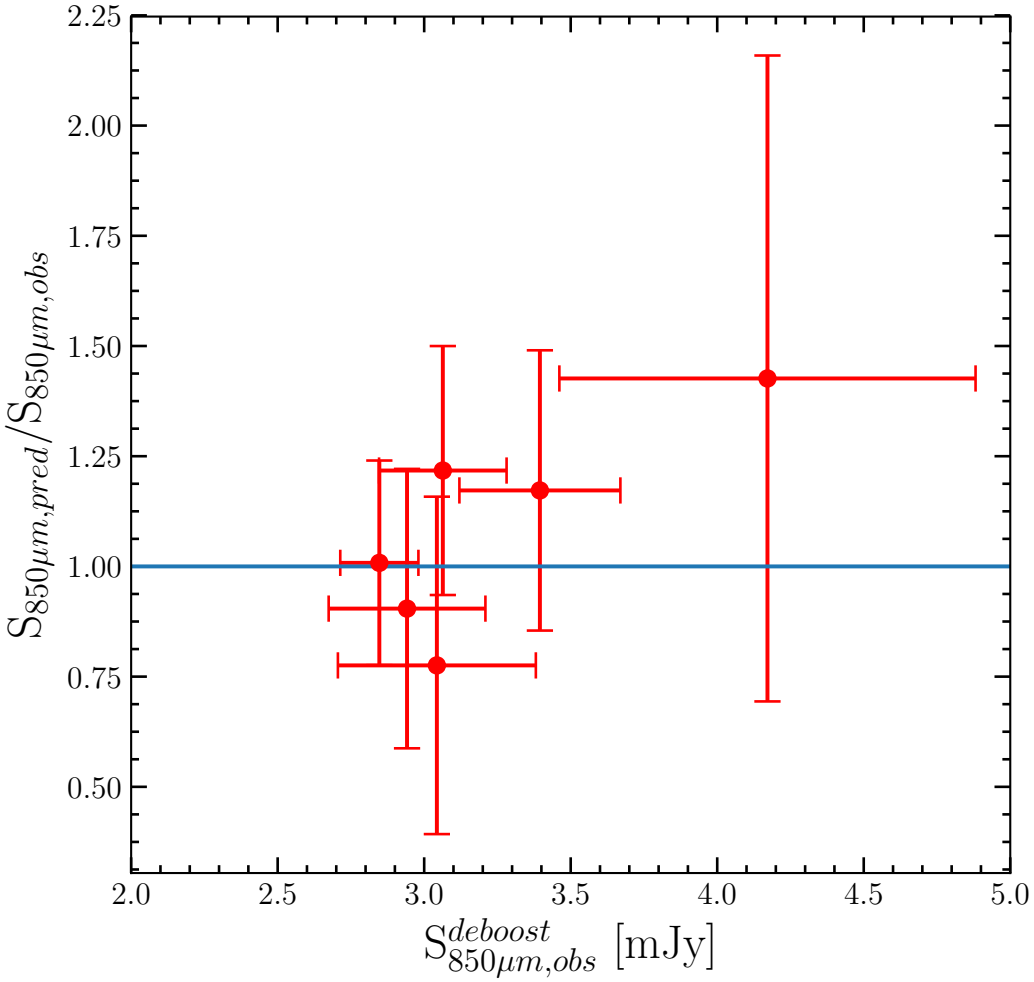

Figure 4.7: Predicted 850 μm flux from fitting SEDs to the stacked *Herschel*/SPIRE fluxes of sub-samples of SCUBA-2 sources, ranked in terms of SCUBA-2 850 μm flux, where our ALMA observations detected no SMGs. These are compared to the observed SCUBA-2 850 μm flux for the equivalent sub-sample. On average we recover the predicted SCUBA-2 fluxes from the SED fitting which strongly suggests that the majority of these SCUBA-2 sources are real, rather than spurious detections in the parent catalogue.

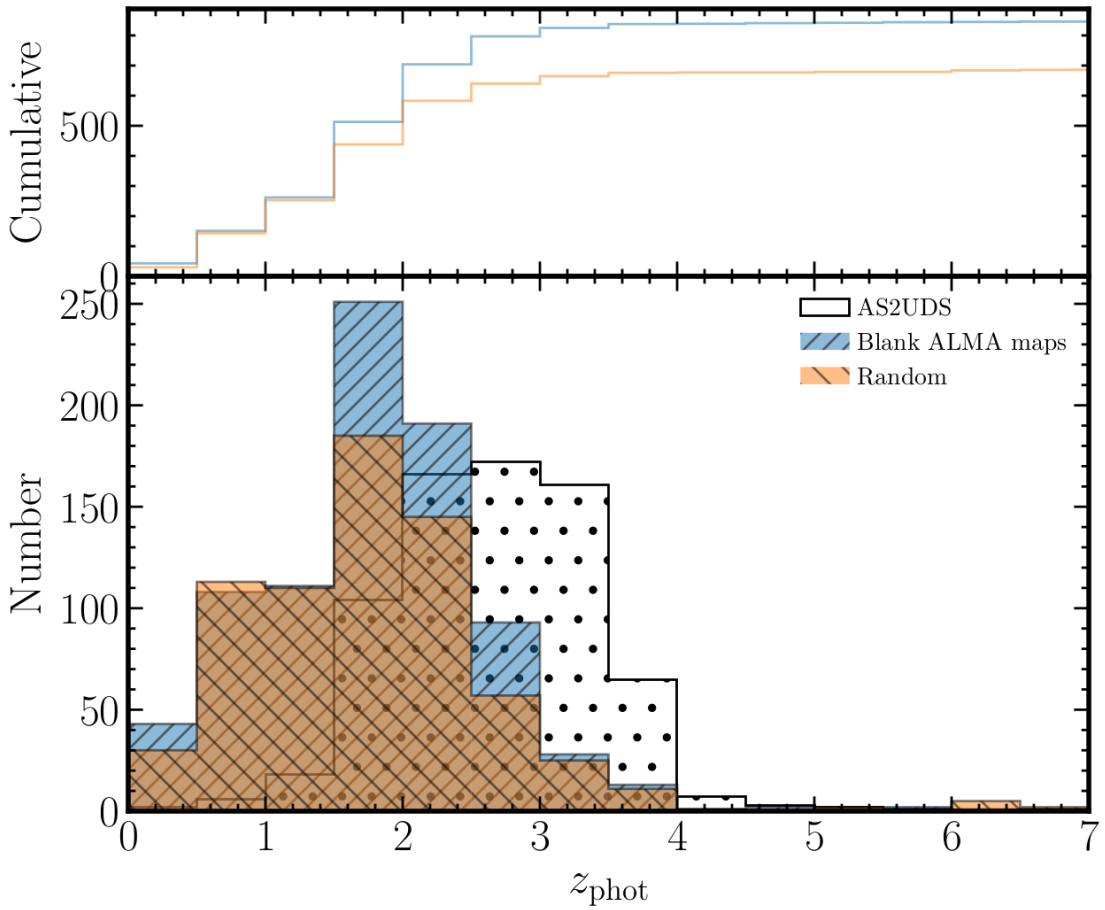

Figure 4.8: The MAGPHYS photometric redshift distribution of the K-band DR11 UKIDSS UDS sources within the primary beam of the ALMA 'blank' maps. This is compared to an identical sized area randomly distributed across the UDS field ('random'). We see a significant excess of galaxies in the 'blank' map regions compared to a random field, corresponding to an excess of 153 galaxies at $z_{\rm phot} = 1.5$–4. This suggests that these apparently 'blank' maps might each contain 1–2 faint SMGs lying at redshifts similar to the distribution of the brighter, detected, SMGs which is also shown.

covers an average flux of $S_{870} = 0.12 \pm 0.02$ mJy corresponding to an average flux per map of $S_{870} = 0.7 \pm 0.1$ mJy to be split between the ~ 1.5 excess sub-millimetre-bright galaxies in these regions, suggesting a typical flux of $S_{870} \sim 0.5$ mJy. This excess of sources and detected sub-millimetre flux is consistent with the interpretation of the 'blank' maps as resulting from the single-dish source comprising flux more than one, faint, sub-millimetre galaxy below our detection threshold.

To test this, in Cycle 5 we re-observed ten of the brightest S2CLS sources which returned no ALMA detections in our Cycle 3 and 4 maps, we show these in Figure 4.9.

To both test for the presence of multiple faint SMGs in these fields and to eliminate the possibility of non-detection due to source flux being resolved out in the interferometric images, these observations were much deeper ($\sigma_{870} = 0.085\,\mathrm{mJy\,beam^{-1}}$) and at much lower resolution than the original maps (synthesised beam: $0\farcs81\times0\farcs54$). From the ten single-dish sources we detect $16 > 4.3\,\sigma$ SMGs. We find four SMGs in the ALMA map of a single SCUBA-2 source which had previously had a 'blank' map, two SMGs in each of a further four maps, four SCUBA-2 sources which have only a single corresponding SMG and just one ALMA 'blank' map which remains blank in these deeper observations (UDS0101, which may be a true false-positive in the S2CLS catalogue). These deeper observations thus confirm that multiplicity is a significant driver of the 'blank' maps and that it remains an issue even for faint SCUBA-2 sources.

The ALMA galaxies in these re-observed 'blank' maps, as expected, are amongst the faintest in the catalogue, with a median deboosted flux of $1.13^{+0.44}_{-0.16}$ mJy. As expected from Figure 4.5, as the median source flux's for these sources are amongst the lowest in our catalogue, they also hint to a lower photometric redshift, with a median $z_{\mathrm{phot}} = 2.37^{+0.21}_{-0.56}$, however the small number of detections makes this an statistically insignificant shift. Even at the $\sim4\times$ depth of these observations, and with the high detection rate of SMG counterparts, we still only recover an average of 52^{+5}_{-3} % of the S2CLS source flux due to flux boosting. Whilst these SMGs are faint, we do not see any evidence from their beam-deconvolved continuum sizes that their 870-μm emission is more spatially extended than the galaxies detected in the higher resolution maps. This suggests that the missing flux, at least in these ten maps, is not a result of flux being resolved out in either our original higher-resolution imaging or the new deeper and lower resolution observations.

4.4.4 AGN Fraction

SMGs have been proposed as the progenitors for the massive spheroid galaxies seen in the local Universe (Lilly et al., 1999; Smail et al., 2004; Simpson et al., 2014). Locally such galaxies exhibit a strong correlation between the mass of their central super-massive black holes (SMBH) and the stellar mass of the host galaxy (Magorrian et al., 1998; Gebhardt et al., 2000; Ferrarese & Merritt, 2000; Gültekin et al., 2009). The existence of

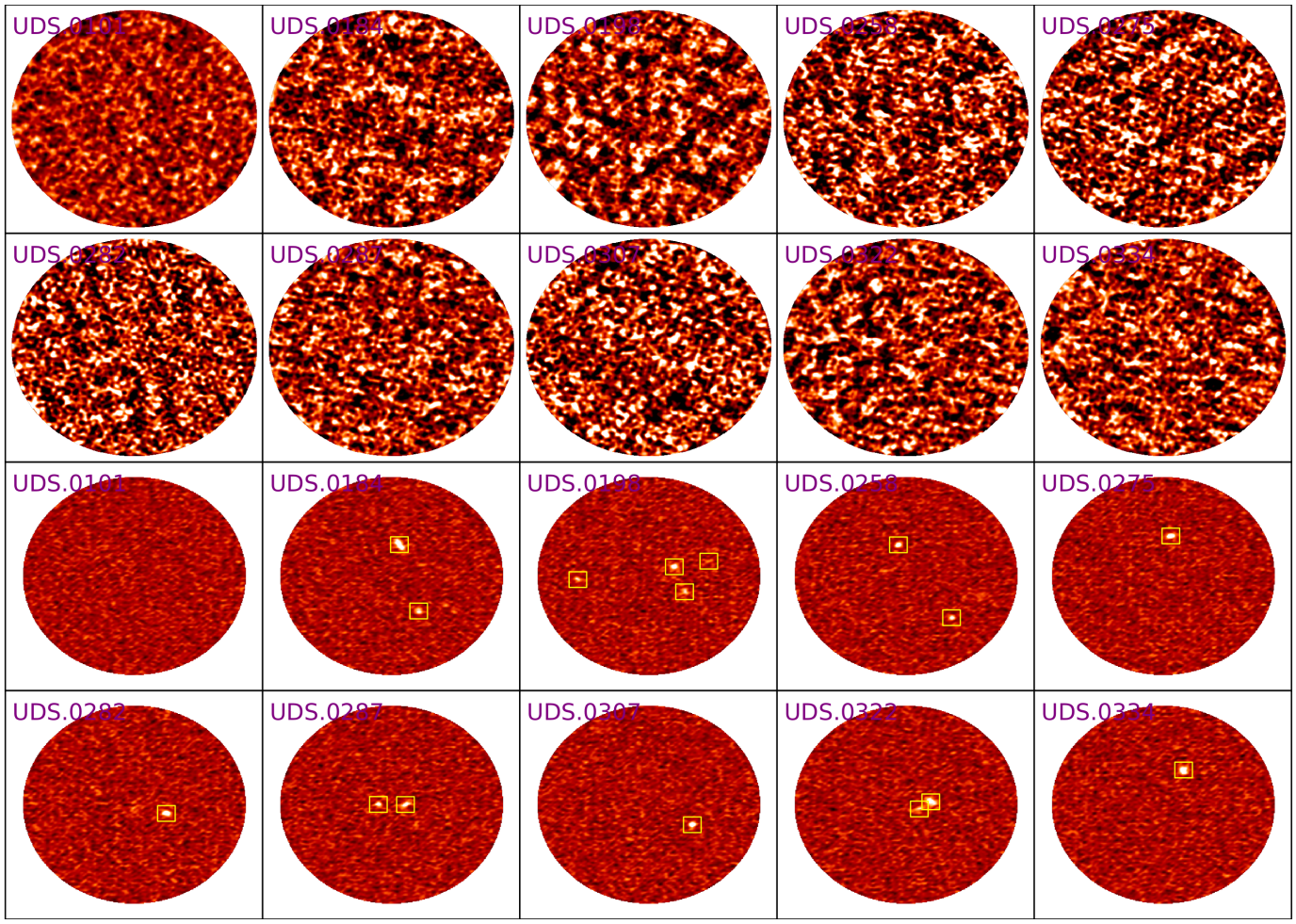

Figure 4.9: AS2UDS Band 7 maps for the 10 'blank' maps from Cycle 3 and 4 which were chosen to be followed up by deeper observations on the top and the resulting followup observations below. These are all set to the same colour-scale and the resulting detections in the follow-up observations are highlighted by the yellow boxes.

this correlation has been used to argue that there is some form of co-evolutionary growth of the SMBH and the surrounding host. This suggestion is supported by observations of the star-formation history and AGN activity of the Universe, which both peak at similar redshifts $z \sim 2$ (Connolly et al., 1997; Merloni, 2004; Hopkins et al., 2007; Cucciati et al., 2012; Kulkarni et al., 2018). Support also comes from simulations of galaxy mergers and AGN activity, which predict that galaxy mergers trigger star formation and then the subsequent fueling of the SMBH creates an AGN which quenches the star formation through feedback winds (Hopkins et al., 2008; Narayanan et al., 2010), consistent with the proposed evolutionary path of Sanders et al. (1988). Hence surveying the AGN activity in the SMG population not only provides insights into SMBH growth, but also potentially the evolutionary cycle of SMGs.

X-ray-selected AGN

The most reliable method to identify AGNs in galaxies is through the detection of luminous X-ray counterparts. As noted earlier, part of the UDS field has been observed in the X-ray band with *Chandra* by the X-UDS survey (Kocevski et al., 2018). X-UDS mapped a total area of 0.33 deg^2, of which the central ~ 100 arcmin^2 (coinciding with the CANDELS footprint) is three times deeper than the remainder. A total of 274 SMGs from AS2UDS are covered by the X-UDS observations, with 47 of these lying in the deeper CANDELS region. Considering the high far-infrared luminosities of our SMGs, which is indicative of high star-formation rates (which contributes to the X-ray emission), we adopt a conservative full-band X-ray luminosity limit of $L_{\rm X} \geq 10^{43}\,{\rm erg\,s^{-1}}$ for classification as an AGN, consistent with Franco et al. (2018). For consistency, we transform the reported $L_{\rm X}$ from the redshifts quoted in the X-UDS catalogue to those derived from our MAGPHYS analysis, where necessary, although this does not significantly change our conclusions.

Of the 274 SMGs covered by the X-ray observations, just 23 (8 ± 2 %) are matched to X-ray counterparts in the X-UDS catalogue based on the positional errors quoted for the X-UDS sources. Within one sigma errors all of these are classed as AGNs with $L_{\rm X} \geq 10^{43}\,{\rm erg\,s^{-1}}$. Of the 47 sources lying within the CANDELS field, only two are

matched to X-UDS X-ray sources: AS2UDS0173.0 and AS2UDS0292.0.

The *Chandra* coverage in the UDS field is relatively shallow for identifying AGN at very high redshifts (c.f. 200–600 ks in UDS, versus 7 Ms in CDF-S). Hence, we also stacked the X-UDS *Chandra* soft (0.5–2 keV) and hard (2–8 keV) bands at the positions of the AS2UDS sources which are individually undetected in X-UDS. To perform this stacking we use the CSTACK stacking software[1]. We excluded the 23 SMGs with X-UDS catalogue matches and stacked the remaining 251 SMGs which are individually undetected from the AS2UDS catalogue in three bins of $L_{8-1000\mu m}$ (derived from MAGPHYS), with the bins chosen to give roughly equal number of sources.

We plot the X-ray and far-infrared luminosities of the 23 individually X-ray detected SMGs and the three composite stacked subsamples in Figure 4.12. We follow Alexander et al. (2005b) by adopting a dividing line between AGN-dominated and star-formation-dominated galaxies at $\mathrm{L_X} \sim 0.004\,\mathrm{L_{FIR}}$ (although we note that the population does not show a sharp division). As expected from the Sanders et al. (1988) model of SMG evolution, the SMGs with X-UDS matches cover the entire range of $L_\mathrm{X}/\,L_\mathrm{FIR}$ from nearly star-formation dominated to the region associated with the AGN-dominated quasars. Nevertheless, the majority of our individually X-ray–detected SMG show $L_\mathrm{FIR}/L_\mathrm{X}$ ratios consistent with AGN dominated systems, as expected from their median $L_\mathrm{X} \sim 10^{44}\,\mathrm{erg\,s^{-1}}$. However, the three stacked subsamples of individually X-ray-undetected SMGs all exhibit ratios of $L_\mathrm{X} = (\,5\pm2\,)\times 10^{-5}\,\mathrm{L_{FIR}}$, more consistent with that expected for star-formation-dominated systems. This indicates that on-average the X-ray-undetected SMGs are likely to be star-formation dominated and hence the bulk of the SMG population is unlikely to host luminous AGN. The stacks however do show an X-ray excess in comparison to a purely star-formation origin suggesting a number of obscured AGNs still present in these stacked samples. Previous X-ray studies of SMGs have found similar X-ray excesses in the X-ray undetected SMGs (Alexander et al., 2005a; Laird et al., 2010; Georgantopoulos et al., 2011; Wang et al., 2013), with the radio-detected SMG samples (with claimed higher AGN fractions Wang et al., 2013) showing a particularly significant ex-

[1]Developed by T. Miyaji. The UDS implementation of CSTACK will be made public a year after the publication of Kocevski et al. (2018)

cess. This highlights the crudeness of the Alexander et al. (2005a) $L_X \sim 0.004\,L_{FIR}$ star-formation/AGN dominated separation, as SMGs can host intrinsically luminous AGNs which are obscured at X-ray wavelengths and thus are detected at significantly fainter fluxes. Therefore for a more complete census of the AGN-dominated population of our SMGs we employ mid-infrared photometry to try to identify these obscured or X-ray faint AGN (§ 4.4.4).

We estimate the black hole mass accretion rates ($\dot{M}_{\rm acc}^{\rm BH}$) for our SMGs by assuming a L_X to $L_{\rm bol}$ bolometric correction factor of 15 (Lusso et al., 2012), an efficiency factor (ε) of 0.1 and using Equation 4.4.1

$$L_{\rm bol} = \varepsilon \dot{M}_{\rm acc}^{\rm BH} c^2. \tag{4.4.1}$$

For our X-ray detected SMGs which we classify as 'AGN dominated' this results in $\dot{M}_{\rm acc}^{\rm BH}$ in the range of 0.1–1.4 $M_\odot\,{\rm yr}^{-1}$, shown in Figure 4.10. For galaxies to evolve along the local relation of spheroid mass-black hole mass, then the ratio of this accretion rate to the star-formation rate must be $\sim 2 \times 10^{-3}$ (Magorrian et al., 1998; Drouart et al., 2014). Taking the MAGPHYS derived star-formation rates, for our AGN dominated SMGs we find a median $\dot{M}_{\rm acc}^{\rm BH}$/SFR ratio of $(1.2\pm0.5)\times10^{-3}$. This is slightly below the expected ratio, which may indicate that these AGN-hosting, but strongly star-forming, SMGs are in a phase where their star-formation rate is exceeding the corresponding SMBH mass growth rate. However, the difference is not statistically significant and moreover, there are significant uncertainties; if the efficiency factor was 0.06 (within the acceptable range of ε e.g. Davis & Laor, 2011) then these systems would comfortably lie on the co-evolutionary track of stellar and black hole mass.

More critically, that is for the relative SMBH and stellar mass growth in the *minority* of SMGs which show AGN signatures. For the bulk of star-formation-dominated SMGs (which lie within the X-UDS coverage) we find $\dot{M}_{\rm acc}^{\rm BH}$/SFR ratios of only $\sim 3.0 \times 10^{-5}$ which is significantly lower than that required for co-evolutionary growth to the local relation. Adopting physically plausible values for the bolometric correction or efficiency factor cannot change this conclusion. Therefore, for the bulk of our SMGs to ultimately follow the local relation in spheroid-black hole mass then there must be some subse-

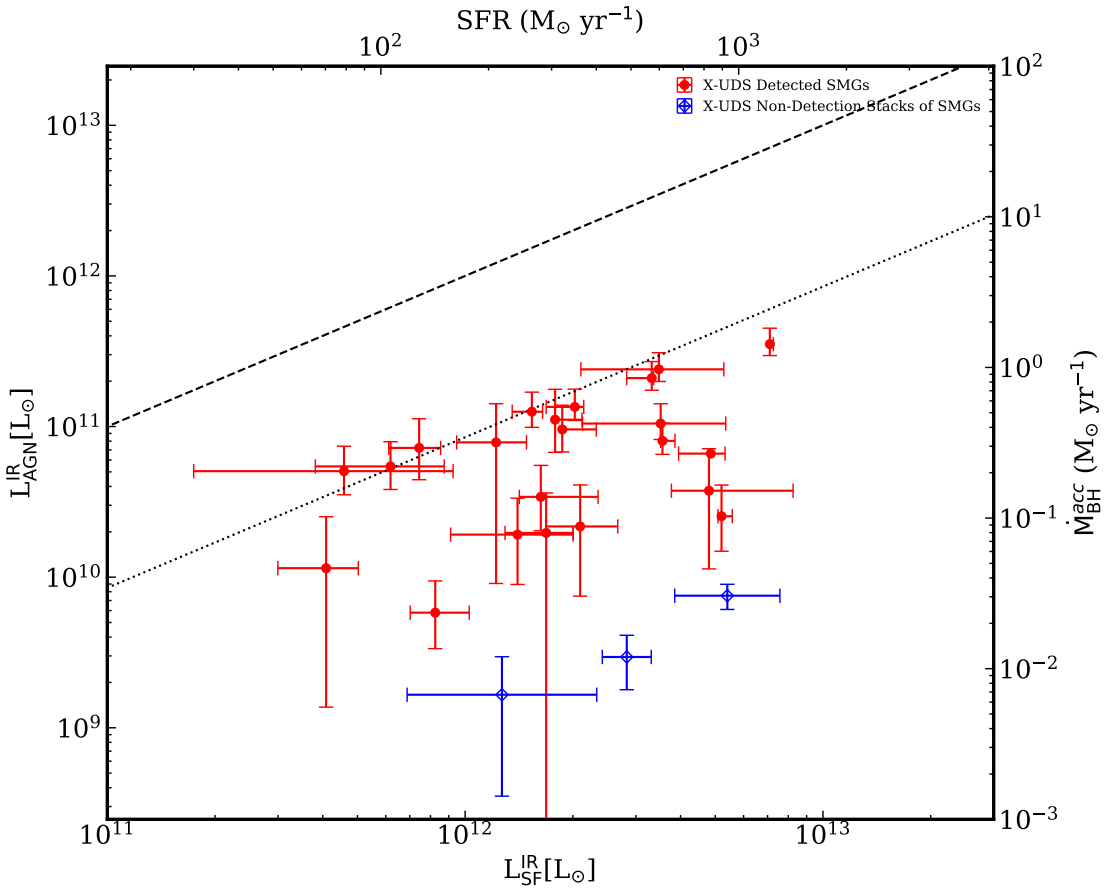

Figure 4.10: The estimated black hole mass accretion rate versus the star-formation rates for both the direct X-ray detected SMGs and the far-infrared luminosity binned stacks of X-ray non-detected SMGs. The dashed black line highlights where $L_{\rm IR}^{\rm AGN} = L_{\rm IR}^{\rm SF}$, and the dotted black line is the predicted line for parallel growth of stellar and black hole masses for galaxies to lie on the local spheroidal-stellar mass relation, $\dot{M}_{\rm BH}^{\rm acc} = 0.002 \times$SFR. Our X-ray detected SMGs which we classify as AGN-dominated show $\dot{M}_{\rm acc}^{\rm BH}$/SFR ratio of $(1.2 \pm 0.5) \times 10^{-3}$ which places them slightly below the local relation however not significantly so when considering the considerable uncertainties in black hole efficiency factors and other systematics. However the stacks for the X-ray non-detections lie significantly below the relation at $\dot{M}_{\rm acc}^{\rm BH}$/SFR$\sim 3.0 \times 10^{-5}$, which suggests that for these galaxies to evolve to the local spheroidal-stellar mass relation they must at some period transition above the dotted line relation and have a phase of significantly increased black hole mass accretion.

quent (-or prior) phase of significant growth of the SMBH with comparatively little star-formation, e.g. high redshift quasars with their SMBH accretion rates of ~ 1–$100\,M_{\odot}\,\mathrm{yr}^{-1}$ (Hao et al., 2008).

Colour-selected AGN

In addition to our X-UDS matching and stacking we also supplement our search for AGN activity in the SMG sample by employing IRAC colour-colour selections (e.g. Donley et al., 2012). These use the IRAC bands to identify galaxies with strong power-law emission in the restframe near-infrared, particularly beyond $2\,\mu$m, which is a good indication of the presence of an AGN, even if it is dust obscured.

Across the whole of the UDS there are 383/708 SMGs with coverage in all four IRAC channels (and with photometry that does not suffer from significant contamination from neighbours, see: §4.3), necessary to apply the colour selection from Donley et al. (2012). We show the distribution of these galaxies in Figure 4.11, but first check that the heavily dust-obscured nature of these sources won't lead to them being misclassified in this colour-colour space. We therefore plot on Figure 4.11 the track of the colours expected from the composite SED for ALESS SMGs from Swinbank et al. (2014). This shows that at the highest redshifts, $z > 3$ the typical colours of SMGs will mimic that of an AGN, while at lower redshifts the colours of these obscured and actively star-forming galaxies will fall outside the region populated by AGN. For this reason we apply the additional selection cut from Donley et al. (2012) to AS2UDS SMGs in independent redshift slices and we also identify the star-formation dominated high-redshift SMGs which display IRAC colours consistent with a redshifted $1.6\,\mu$m stellar 'bump' and $8.0/3.6\,\mu$m flux ratios consistent with the local (Ultra)-luminous infrared galaxies SED templates of Rieke et al. (2009).

We test the efficacy of the Donley et al. (2012) selection by employing CSTACK to derive the average X-ray flux of the 25 SMGs with $z_{\mathrm{phot}} < 3$ that are within both the IRAC AGN selection and X-UDS coverage and are not close to another bright X-ray source, and a control sample of 131 SMGs outside of the colour selection region but similarly lying in the X-ray coverage. We show these in Figure 4.12 and see that the 131

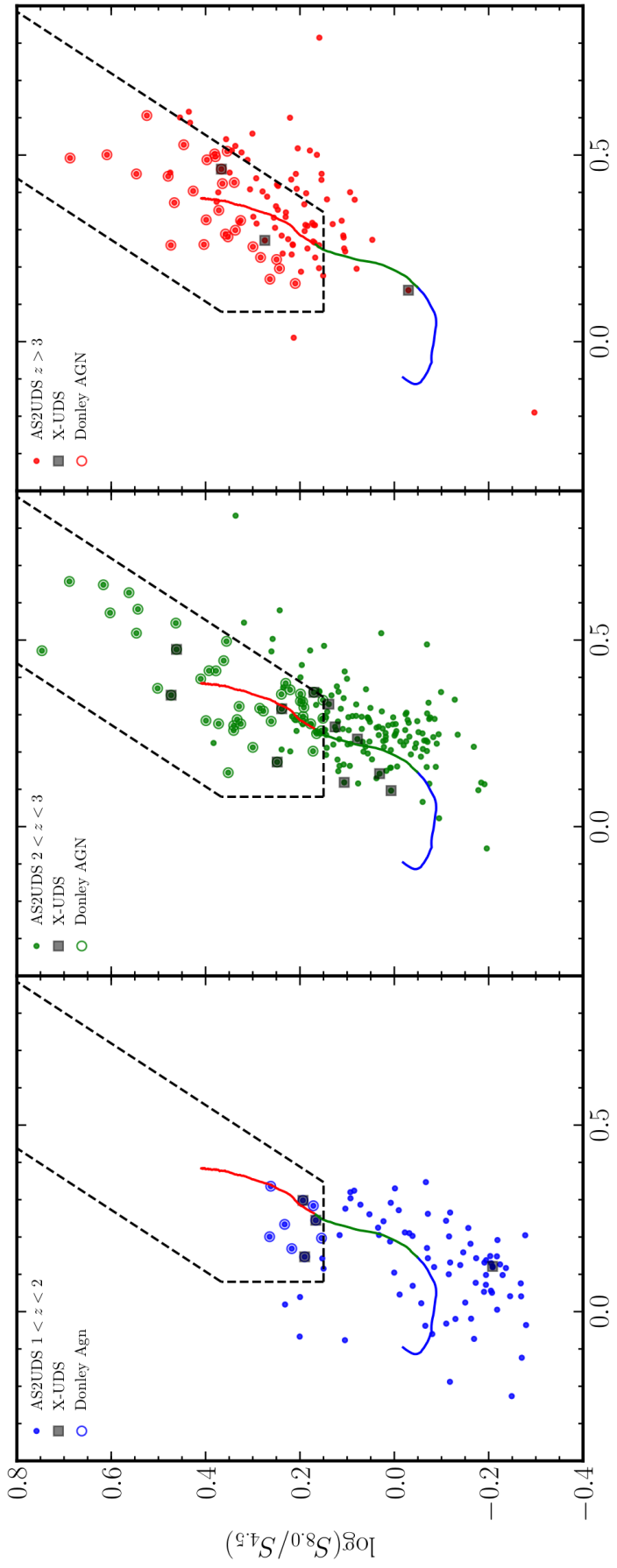

Figure 4.11: We use the IRAC colour–colour selection described in Donley et al. (2012) to select candidate AGN from the AS2UDS SMG sample, shown here in three redshift slices. We overlay the predicted colours for the ALESS composite SED (Swinbank et al., 2014) as a function of redshift, colour coded in blue for $z = 1$–2, green for $z = 2$–3, and red for $z > 3$. The track illustrates how above $z \gtrsim 3$ the AGN colour selection will potentially be contaminated by star-forming galaxies. The final selection of AGNs based on the 'wedge' and the star-formation dominated cut are circled in their respective redshift colours. In total the IRAC-colour selection finds 125 potential AGN candidates across the entire AS2UDS coverage. However, the most reliable estimate of the AGN fraction comes from the sample lying within the X-UDS region and with redshifts of $z < 3$, which yields 37 candidates. The 21 X-UDS X-ray-detected SMGs hosting AGN are marked as black squares.

colour-selected SMGs lying outside the Donley et al. (2012) selection do indeed have a $L_{\rm X}/L_{\rm FIR} = 0.0004 \pm 0.0002$ ratio consistent with those expected from star formation. However, the stacked X-ray properties of the 25 SMGs at $z < 3$ which fall within the Donley et al. (2012) selection provide a more ambiguous value with a $L_{\rm X}/L_{\rm FIR}$ ratio of $0.0015^{+0.0012}_{-0.0003}$, with these sources lying below the threshold ($L_{\rm X}/L_{\rm FIR} \sim 0.004$) to be classified as an AGN. For this reason we choose to view the IRAC-colour selected samples, even at $z < 3$, as providing an *upper limit* on the potential AGN fraction in SMGs.

AGN fraction in SMGs

Due to the limiting flux for the X-UDS survey estimated in Kocevski et al. (2018) of 4.4×10^{-16} erg cm^{-2} s^{-1} for the Full-Band (0.5-10 keV) we expect to be incomplete for even 10^{43} erg s^{-1} X-ray bright AGN in the outer X-UDS survey region. Due to this we derive a *lower* limit on the X-ray detected AGN fraction from SMGs lying with the X-UDS coverage of 23/274 (8 ± 2 %). To estimate an upper limit on the AGN fraction we include the IRAC-colour-selected AGN within this region but employ a $z < 3$ cut off for reasons discussed above. With the IRAC-selected AGN and the redshift cut we estimate an upper limit of 45/162 (28 ± 4 %) AGN in the AS2UDS population.

The range of potential AGN fraction for our flux-limited sample lies inbetween results from earlier work in the literature, e.g. 38^{+12}_{-10} % in Alexander et al. (2005a), (20–29) $\pm$ 7 % in Laird et al. (2010), 18$\pm$7 % in Georgantopoulos et al. (2011) and $\sim$ 28 % in Johnson et al. (2013), as well as the ALMA-based estimate from ALESS: 17^{+16}_{-6} % in Wang et al. (2013).

Recently, working with a 1.1-mm selected ALMA sample of SMGs in the GOODS-South field, Franco et al. (2018) reported a high AGN fraction, $\sim 40 \pm 14$ %. Their SMG sample has an 870-μm equivalent flux range of $S_{870} \sim 0.8$–3.9 mJy. To match to this Franco et al. (2018) selection, we also estimate the AGN fraction for our fainter $S_{870} < 4.0$ mJy SMGs and combine the number of our IRAC-selected candidates at $z < 3$ with the confirmed X-ray bright SMGs from the X-UDS matching to find an upper limit on the AGN fraction of 26 ± 5 % (28/109) within the X-UDS coverage, consistent with our whole sample. This is lower than the estimate from GOODS-South, but given the

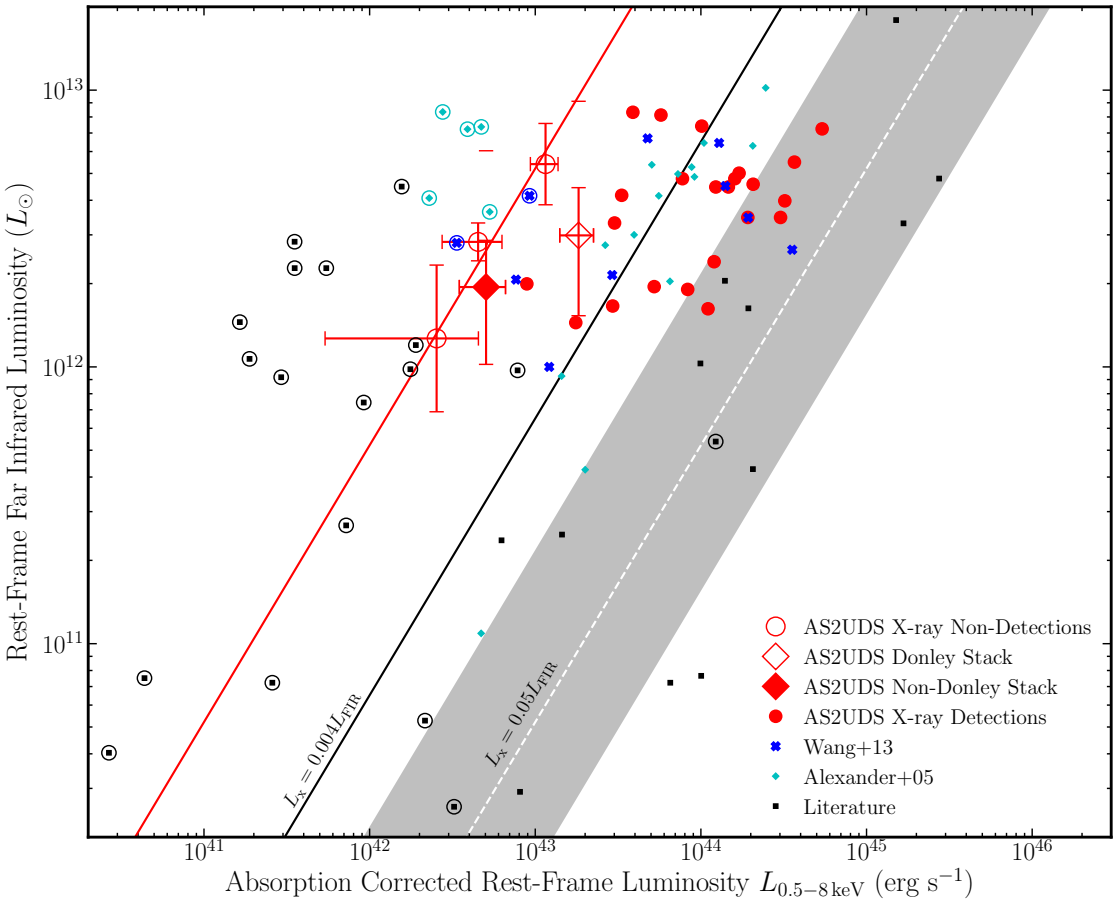

Figure 4.12: We show the relationship between restframe far-infrared (8–1 000 μm) luminosity for the X-ray detected AS2UDS SMGs versus their rest-frame 0.5–8.0 keV absorption-corrected luminosities. The 21 galaxies with X-UDS matches from our catalogue (red points) and lie at $L_\mathrm{x} \gtrsim 0.004\,\mathrm{L_{FIR}}$, the approximate dividing line between starburst and AGN dominated galaxies. We have derived mean X-ray fluxes by stacking, using CSTACK, three sub-samples of individually-X-ray-undetected SMGs – where the sub-samples are ranked on L_FIR – these are plotted as open symbols with error bars. These three samples lie below the line dividing starburst and AGN dominated emission. We conclude that the vast majority of the SMG population, $\gtrsim$90%, do not host luminous AGN. Galaxies from the literature are plotted as blue crosses (Wang et al., 2013), cyan diamonds (Alexander et al., 2005a), and black squares for galaxies from the literature compiled by Alexander et al. (2005a). Starburst dominated galaxies are denoted by a circle. The white dashed line and grey shaded region are the median luminosity ratio and standard deviation for the quasars from Elvis et al. (1994). The filled diamond is the results of the stacking of the galaxies outside of the Donley et al. (2012) selection which show, on average, they are star-formation dominated galaxies whereas the the IRAC selected AGNs in the unfilled diamond appear to be, on average, close to the dividing line between star-formation and AGN dominated.

significant uncertainty on the latter, we do not give too much weight to this disagreement.

4.4.5 Passive Galaxy Progenitors

SMGs, with their extreme star-formation rates and implied high molecular gas content, could form significant stellar masses (M_*) of 10^{10}–$10^{12}\,\mathrm{M}_\odot$ on a timescale of just $\sim 100\,\mathrm{Myrs}$. This rapid formation of a massive system at high redshifts has led to them being proposed as the progenitors of high-redshift compact quiescent galaxies (Simpson et al., 2014; Toft et al., 2014; Ikarashi et al., 2015), which subsequently evolve into local spheroidal galaxies. Observational support for this evolutionary relation has been claimed from comparisons of the stellar masses of SMGs (Swinbank et al., 2006; Hainline et al., 2011; Toft et al., 2014), the spatial clustering of relative to that of local ellipticals (e.g. Hickox et al., 2012; Chen et al., 2016; Wilkinson et al., 2017) and the compact rest-frame far-infrared sizes of SMGs (Simpson et al., 2017; Hodge et al., 2016), as well as from theoretical modelling of SMGs and their descendants (González et al., 2011; McAlpine et al., 2019).

Using our large sample with complete redshift information we can test these claimed connections, especially in light of recent advances in the studies of high-redshift passive galaxies. For example Estrada-Carpenter et al. (2019), using *HST* grism spectroscopy, have constrained the formation redshift and metallicities for a sample of 32 spectroscopically-classified quiescent galaxies at $z = 1$–1.8, which are believed to be massive, $\mathrm{M}_* > 10^{10}\,\mathrm{M}_\odot$. They find that, nearly independent of the observed redshift of the quiescent galaxies, their *formation* redshift (the epoch where $\gtrsim 70\,\%$ of the stellar mass has already formed) is $z_{\mathrm{form}} > 2$–3 ($T_{\mathrm{lookback}} > 10.2$–$11.4\,\mathrm{Gyr}$), with a third of their sample having $z_{\mathrm{form}} > 3$ ($T_{\mathrm{lookback}} > 11.4\,\mathrm{Gyr}$). Constraints on their metallicities suggesting that these star-forming progenitors must have already enriched to approximately Solar metallicities (which is consistent with the high dust masses of the SMGs as well as the crude estimates of their metallicities from Swinbank et al. (2004); Takata et al. (2006)). Morishita et al. (2018), likewise, looked at the mass accumulation and metallicity history for a sample of 24 apparently massive galaxies ($M_* > 10^{11}\,\mathrm{M}_\odot$) at $z = 1.6$–2.5 via SED modelling and inferred that the majority of their sample had formed $> 50\,\%$ of their

mass around ~ 1.5 Gyr prior to their observed redshifts, yielding formation ages similar to Estrada-Carpenter et al. (2019) ($T_{\rm lookback} \sim 10.9$–$12.3$ Gyr).

In Figure 4.13 we plot the age distribution for massive AS2UDS SMGs and the combined Estrada-Carpenter et al. (2019) and Morishita et al. (2018) *formation* redshifts for their samples of quiescent galaxies. We adopt a mass limit of $\mathrm{M}_* > 10^{9.85}\,\mathrm{M}_\odot$, from our MAGPHYS estimated stellar masses to match the passive galaxy samples, this accounts for some continuing star-formation activity and associated stellar mass growth in these systems, although our conclusions are not sensitive to this assumption. For a more accurate comparison of 'formation' ages we derive the mean offset from the observed redshift of our SMGs to the 'age' of their mass-weighted stellar population. This offset is calculated from the inferred gas masses, star-formation rates, and stellar masses from MAGPHYS for the AS2UDS sample. We estimate, and apply, a typical +200 Myr offset to our observed redshifts to correct to a mass-weighted stellar population age which is more representative of the period in which the galaxy was forming the majority of its stellar mass.

Figure 4.13 shows that the AS2UDS age distribution is comparable to the formation ages which are inferred for massive, quiescent galaxies at $z \sim 1$–2.5: both distributions peak at lookback times of 11.5–12.5 Gyr, median ages for the distributions are in agreement with $11.4^{+0.1}_{-0.2}$ Gyr for AS2UDS and 11.5 ± 0.3 Gyr for the comparison sample, and both populations show a younger stellar population < 11 Gyr tail containing $\sim 30\,\%$ of their respective distributions. This provides further support for the claims that the SMG and high-redshift massive quiescent galaxy populations may have an evolutionary link.

We can also ask if the number density of the SMGs and high-redshift passive galaxies are consistent with any likely evolutionary cycle. We can derive a co-moving number densities for the subset of the quiescent population from Estrada-Carpenter et al. (2019) with formation redshifts $z_{\rm form} = 2$–3 (the population where number densities are available), which is $n_{\rm qg} \sim 2.5 \times 10^{-4}\,\mathrm{Mpc}^{-3}$. This compares to a number density of $n_{\rm SMG} = (\,2.8^{+0.2}_{-0.1}) \times 10^{-5}\,\mathrm{Mpc}^{-3}$ for the SMGs in the same redshift range after applying the $M_* > 10^{9.85}\,\mathrm{M}_\odot$ mass cut. The SMG number density is $11^{+3}_{-2}\,\%$ of the quiescent galaxy number density estimated by Estrada-Carpenter et al. (2019). However, we also need to correct the apparent SMG number density for a duty cycle as they are thought

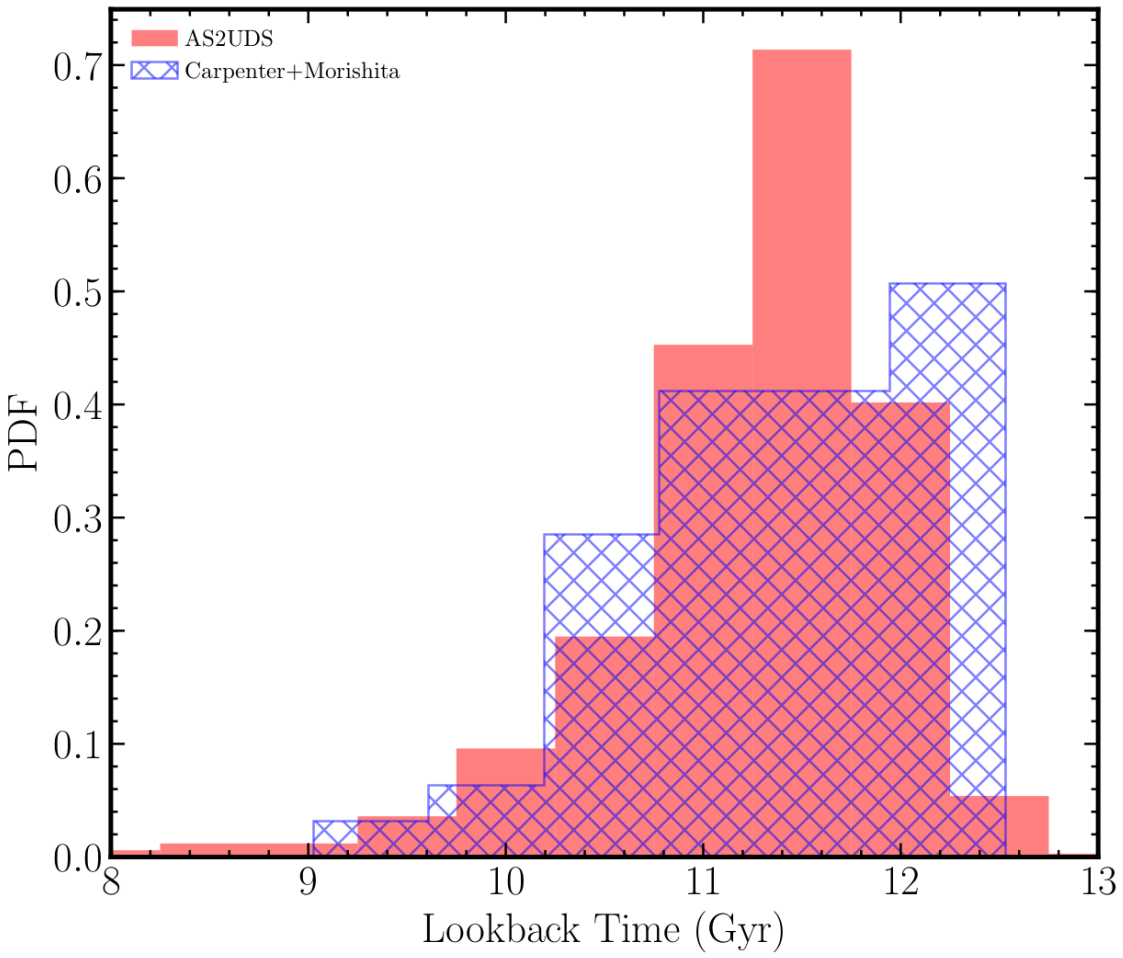

Figure 4.13: The inferred mass-weighted ages of the AS2UDS SMGs compared to the *formation* redshift for $z \sim 1$–2.5 passive galaxies from Estrada-Carpenter et al. (2019) and Morishita et al. (2018). The high-redshift quiescent galaxy population across this broad redshift range are found to have similar *formation* redshifts, which in turn broadly match the redshift distributions for the formation of the SMG galaxy population. This is consistent with the interpretation of the SMGs as likely progenitors for the spectroscopically confirmed quiescent galaxies at $z \sim 1$–2.5.

to attain a high star-formation rate for a comparatively short duration, compared to the redshift range being considered.

The lifetime of the high-star-formation rate phase of SMGs is dependent on either a simple gas depletion timescale, or through some star formation quenching mechanism e.g. active galactic nuclei feedback. Previous estimates of the lifetimes of the SMG-phase based on gas depletion timescales or clustering analysis have suggested durations of $\sim$40–200 Myr (Tacconi et al., 2006; Swinbank et al., 2006; Riechers et al., 2011; Hickox et al., 2012; Bothwell et al., 2013). We can estimate this average duty cycle duration using a simple model of the SMG evolution by making the following assumptions: (i) the $z = 2$–3, $M_* > 10^{9.85} M_\odot$ AS2UDS SMGs are progenitors of the $z = 1$–1.8 quiescent galaxies and likewise all $z = 1$–1.8 quiescent galaxies are the descendants of these SMGs, (ii) each SMG has a single burst of intense star-formation. With these assumptions the burst duration can be estimated by

$$t_{\rm burst} = t_{\rm obs} \times \left(\frac{n_{\rm SMG}}{n_{\rm qg}} \right), \tag{4.4.2}$$

where $t_{\rm burst}$ is the burst duration, $t_{\rm obs}$ is the duration of the epoch we calculated the SMG comoving density ($z = 2$–3), and $n_{\rm SMG}/n_{\rm qg}$ are the co-moving number densities for the SMGs and quiescent galaxies respectively. For our measured number density we find a burst duration of 190^{+50}_{-40} Myr which is consistent with the other estimates derived from observed gas masses and star-formation rates of SMGs within this redshift range in the literature (e.g. Hickox et al., 2012; Bothwell et al., 2013). Therefore the space-density of dusty star-forming galaxies at $z = 2$–3 that form the bulk of the AS2UDS sample, are consistent with that required for them to comprise the progenitors of quiescent galaxy population seen at $z = 1$–1.8.

4.5 Conclusions

We present basic properties of an ALMA 870 μm continuum follow-up survey of 716, $> 4\,\sigma$ single-dish sub-millimetre sources selected from the SCUBA-2 Cosmology Legacy Survey 850-μm map of the UKIDSS UDS field. Our deep, high-resolution ALMA obser-

vations identified 708 $> 4.3\,\sigma$ sources which account for the majority of the flux detected in the parent SCUBA-2 map. The main conclusions of this study are:

- Utilising the extensive multi-wavelength coverage of the UDS field we fit SEDs for our galaxies using MAGPHYS and from these fits derived a median photometric redshift for our galaxies of $z_{\rm phot} = 2.61 \pm 0.09$ with a high-redshift tail comprising 33^{+3}_{-2} % of SMGs with $z_{\rm phot} > 3$.

- From the subset of SMGs with CANDELS imaging we find that 50 ± 10 % show either clear merger morphologies or have likely companions, displaying similar colours, on < 20 kpc scales. These likely interacting systems have a median redshift at $z_{\rm phot} = 2.2 \pm 0.1$, which is significantly lower than the median photometric redshift. When we select SMGs with redshifts $z_{\rm phot} < 2.75$, to account for the redshift at which we reasonably expect to reliable detect interactions in the CANDELS imaging, then this 'likely interacting' fraction accounts for $\sim$80 % of SMGs. This suggests that the elevated star-formation rates in these systems are driven by mergers.

- With our large sample size we see convincing evidence for evolution in the S_{870} flux density of sources with redshift with a best fit trend gradient of $0.09 \pm 0.02\,{\rm mJy}^{-1}$. This evolution was not robustly identified in previous smaller surveys due to their limited statistics and we show how reducing our sample size down to ~ 100 galaxies results in a statistically insignificant result. The consequence of this trend is that on average our most luminous galaxies are found at higher redshifts in comparison to less active galaxies, a strong indication of galaxy downsizing.

- Through stacking *Herschel* observations at the positions of the 101 SCUBA-2 sources for our ALMA maps produced no > 4.3-σ detections, we show that these sources are not dominated by false-positive detections in the parent S2CLS catalogue. We find an overdensity of, on average, ~ 1.5 K-band sources at the locations of these 'blank' ALMA maps at redshifts $z = 1.5$–4 which, combined with the strong evidence from SPIRE-stacking that the original SCUBA-2 flux is real,

suggests that the lack of ALMA counterparts is a result of blending of the sub-millimetre emission from $\gtrsim$1–2 *faint* galaxies at these positions. We confirm that this is the case with deeper repeat Cycle 5 observations of ten examples of these 'blank' maps which yield 16 new ALMA detections below our previous flux limit.

- We identify AGNs associated with our SMG sample by both matching our catalogue to the X-UDS *Chandra* X-ray coverage of the field and also by applying an IRAC colour-colour selection. We estimate a lower limit on our AGN fraction from the X-ray detections of 8 ± 2 % and an upper limit by including our IRAC-colour selected AGNs of 28 ± 4 %. This range is consistent with previous results, although somewhat lower than the most recent results reported for a small sample in the GOODS-S field. We conclude that most sub-millimetre bright galaxies do not host an unobscured or moderately obscured luminous AGN.

- Looking to the most likely candidate descendants for our SMGs we compare the constraints on their redshift and number density (as well as stellar mass and metallicity) to those expected for the progenitors of $z = 1$–2.5 quiescent galaxies from recent studies. We find that the properties of the AS2UDS SMG population are consistent with these constraints, with median mass-weighted ages for the SMGs of $11.4^{+0.1}_{-0.2}$ Gyr, in good agreement with the median formation ages for the quiescent galaxies of 11.5 ± 0.3 Gyr.The number density of the SMGs and high-redshift, high mass passive populations are also consistent with this evolutionary link if the typical star-formation burst duration of the SMGs is $\sim 190^{+50}_{-40}$ Myr, which is similar to previous independent estimates.

CHAPTER 5

ALMA Pinpoints a Strong Overdensity of U/LIRGs in the Massive Cluster XCS J2215 at $z = 1.46$

5.1 Summary

We have surveyed the core regions of the $z = 1.46$ cluster XCS J2215.9−1738 with the Atacama Large Millimeter Array (ALMA) and the MUSE-GALACSI spectrograph on the VLT. We obtained high spatial resolution observations with ALMA of the 1.2 mm dust continuum and molecular gas emission in the central regions of the cluster. These observations detect 14 significant millimetre sources in a region with a projected diameter of just ~ 500 kpc ($\sim 1'$). For six of these galaxies we also obtain ^{12}CO(2–1) and ^{12}CO(5–4) line detections, confirming them as cluster members, and a further five of our millimetre galaxies have archival ^{12}CO(2-1) detections which also place them in the cluster. An additional two millimetre galaxies have photometric redshifts consistent with cluster membership, although neither show strong line emission in the MUSE spectra. This suggests that the bulk ($\geq 11/14$, $\sim 80\%$) of the submillimetre sources in the field are in fact luminous infrared galaxies lying within this young cluster. We then use our sensitive new observations to constrain the dust-obscured star formation activity and cold molecular gas within this cluster. We find hints that the cooler dust and gas components within these galaxies may have been influenced by their environment reducing the gas reservoir available for their subsequent star formation. We also find that these actively

star-forming galaxies have the dynamical masses and stellar population ages expected for the progenitors of massive, early-type galaxies in local clusters potentially linking these populations.

The previous three chapters have dealt with ALMA follow-up of SCUBA-2 sources across the entire UDS field, in this chapter we extend that to ALMA follow-up of SCUBA-2 sources found in the dense core of a $z = 1.46$ galaxy cluster XCS J2215. XCS J2215 was one of ten $z = 0.8$–1.6 clusters that was observed as part of a SCUBA-2 cluster survey (Smail et al., 2014; Ma et al., 2015), and is the cluster which showed the highest density of S_{850} bright sources at its centre. As previous studies have suggested that SMGs could trace the densest structures in the high-redshift Universe (e.g. Blain et al., 2004; Hickox et al., 2012; Wilkinson et al., 2017) our SCUBA-2 survey was partially motivated to study such over-dense regions in the $z \sim 1$ Universe. The work in this chapter is taken from Stach et al. (2017) which looked at the ALMA follow-up of the central 4 SCUBA-2 sources in XCS J2215.

5.2 Introduction

Galaxy clusters present a convenient laboratory for the study of environmental influences on galaxy formation and evolution due to the large variety in environments within a relatively small observable area, from the high-density cores to the low-density outskirts. Observational studies of clusters in the local universe show that their cores are dominated by metal rich, gas-poor early-type (lenticulars, or S0s, and ellipticals) galaxies with little or no current star-formation activity. In contrast, late-type, actively star-forming disk galaxies are found preferentially in the outskirts of clusters and in the surrounding lower-density field, yielding a so-called "morphology–density" relation (Dressler, 1980; Bower et al., 1992; Whitmore et al., 1993; Bamford et al., 2009).

This correlation of galaxy star-formation activity and morphology with environment in the local universe (e.g. Lewis et al., 2002; Gomez et al., 2003; Balogh et al., 2004; Kodama et al., 2004) is suggestive of environmental processes being at least partly responsible for the quenching of star formation in the early-type galaxies in high-density regions.

Potential environmental processes which could drive this include galaxies interacting with the intracluster medium (ICM) causing ram pressure stripping of their interstellar gas (Gunn & Gott III, 1972), or "strangulation," where the continued accretion of gas from their surroundings is cut off (Larson et al., 1980); galaxy mergers leading to dramatic changes in galaxy's structure and the triggering of a starburst which rapidly consumes their gas (Merritt, 1983); and tidal interactions, which can enhance star formation (Aguilar & White, 1985). Ultimately, each of these processes acts to reduce the gas supply and eventually shut off star formation, and all act preferentially on galaxies in higher density regions.

At higher redshift, it has been shown that the fraction of blue star-forming disk galaxies found in clusters increases (Butcher & Oemler Jr, 1978; Aragón-Salamanca et al., 1993). A similar behaviour has also been seen in these clusters using star-formation tracers that are less sensitive to dust extinction, such as mid-infrared emission. Indeed, 24 μm surveys of actively star-forming galaxies using the MIPS instrument on the *Spitzer Space Telescope* have found increasing numbers of starbursts in clusters out to $z \sim 0.5$–1, although these clusters still typically contained a core of passive galaxies (e.g. Geach et al., 2006; Fadda et al., 2007; Saintonge et al., 2008; Haines et al., 2009; Finn et al., 2010; Biviano et al., 2011). The mass-normalized integrated star-formation rate (SFR) for these systems increases with redshift as $\propto (1+z)^{\gamma}$ with $\gamma \sim 7$ (Geach et al., 2006), an accelerated evolution in comparison to the field where $\gamma \sim 4$ (Cowie et al., 2004).

Although these clusters are growing at $z \sim 0.5$–1, through the infall and accretion of star-forming galaxies from their environment, the cores still contain a population of massive, passive galaxies which suggests that at least some of their galaxies must have formed their stars at much earlier epochs potentially suggesting a link to the early intense star-formation in SMGs discussed in Chapter 4. At higher redshifts, it has been shown that cluster cores show star-formation rate densities equivalent to that of the field (Brodwin et al., 2013; Darvish et al., 2016) and in some $z \gtrsim 1$ cluster cores there are even claims of a reversal of the star-formation–density relation (e.g. Tran et al., 2010).

However, one issue with these studies is that for clusters at $z > 1$ the observed 24 μm emission, which is often used as a star-formation tracer, becomes increasingly problematic

due to the presence of strong, redshifted emission from polycyclic aromatic hydrocarbon (PAH) and silicate absorption features which fall in the band. As a result, studies of more distant clusters have focused on the far-infrared/submillimetre wavebands and have uncovered evidence of a continued rise with redshift in the activity in overdense regions at $z > 1$, as traced by an increasing population of the most strongly star-forming, dusty (Ultra-)Luminous InfraRed Galaxies (U/LIRGs) (e.g. Webb et al., 2005, 2013; Tran et al., 2010; Popesso et al., 2012; Smail et al., 2014; Noble et al., 2016). These studies have uncovered mixed evidence of a reversal in the star-formation–density relation in cluster cores at high redshift. For example, a "reversal" has been claimed in some massive clusters at $z \gtrsim 1.5$ such as XDCP J0044.0−2033 (Santos et al., 2015) and Cl J1001+0220 (Wang et al., 2016), but this is not ubiquitous. Smail et al. (2014) identify 31 probable cluster U/LIRGs within Cl J0218.3−0510 at $z = 1.62$. However, these highly star-forming galaxies did not reside in the densest regions of the cluster and instead the core was already populated with passive red galaxies, a trend also seen by Newman et al. (2014) in a $z = 1.8$ cluster, which has a cluster core dominated by a quiescent galaxy population. These results suggest that a massive quiescent population in some $z \sim 1.5$ cluster cores is already in place well before this epoch.

Some of the disagreement between the conclusions of these various studies may result from the uncertainties in reliably identifying the counterparts of far-infrared/submillimetre sources at other wavelengths, due to the typically poor spatial resolution of the long-wavelength data from single-dish facilities. To make progress on these issues, we took high-spatial resolution millimetre imaging of one of the well-studied high-redshift cluster which appears to exhibit a very significant overdensity of submillimetre sources in its core: XCS J2215.9−1738 (Stanford et al., 2006). This cluster has been claimed to exhibit enhanced star-formation activity in its core regions (Hayashi et al., 2010), including a striking overdensity of submillimetre sources in single-dish 450/850 μm maps obtained by Ma et al. (2015).

In this paper, we present Atacama Large Millimeter/submillimeter Array (ALMA) interferometric observations of dust continuum and CO emission of galaxies in the central region of XCS J2215. Our observations include a 1.2 mm mosaic of a 500 kpc di-

ameter region encompassing the central four SCUBA-2 850 μm sources detected by Ma et al. (2015) (hereafter, Ma15). Our ALMA data provide us with the means to study the U/LIRG population in this cluster in the millimetre at resolutions an order of magnitude higher than that provided from current single-dish bolometer cameras and with much greater sensitivity. We use our ALMA continuum observations to robustly identify the 850 μm counterparts. We then searched for emission lines arising from molecular gas in cluster members. At the cluster redshift, our ALMA observations in Band 3 and Band 6 cover two transitions commonly seen in star-forming galaxies: ^{12}CO(2–1) and ^{12}CO(5–4). We employ these detections to confirm the cluster membership of U/LIRGs seen toward the cluster core and to estimate their molecular gas content and physical properties.

This chapter is structured as follows: §5.3 covers the target selection, the ALMA observations and data reduction, with the resultant continuum and CO line detections reported in §5.4. We then discuss these in §5.5 and give our main conclusions in §5.6. We assume a ΛCDM cosmology with $\Omega_M = 0.3$, $\Omega_\Lambda = 0.7$ and $H_0 = 70\,\mathrm{km\,s^{-1}\,Mpc^{-1}}$, which gives an angular scale of $8.5\,\mathrm{kpc\,arcsec^{-1}}$ at $z = 1.46$. We adopt a Chabrier initial mass function (IMF) (Chabrier, 2003) and any magnitudes are quoted in the AB system.

5.3 Observations and Data Reduction

5.3.1 XCS J2215.9-1738

XCS J2215 provides an excellent opportunity to study the nature of star-formation activity in the central regions of a high-redshift cluster. At $z = 1.46$ it is one of the most distant clusters discovered in X-rays (Stanford et al., 2006), with extensive multiwavelength follow-up (Hilton et al., 2007, 2009, 2010; Hayashi et al., 2010, 2014). Of particular relevance here is the SCUBA-2 survey of the clusters by Ma15 which discovered an overdensity of submillimetre galaxies (SMGs) in its core. Unlike other (proto-)clusters studied at high redshifts (e.g. CLG J0218 Rudnick et al., 2012; Lotz et al., 2013; Hatch et al., 2016), XCS J2215 appears structurally well-developed. By combining *XMM-Newton* and *Chandra* observations, Hilton et al. (2010) (hereafter H10) derived an X-ray luminosity

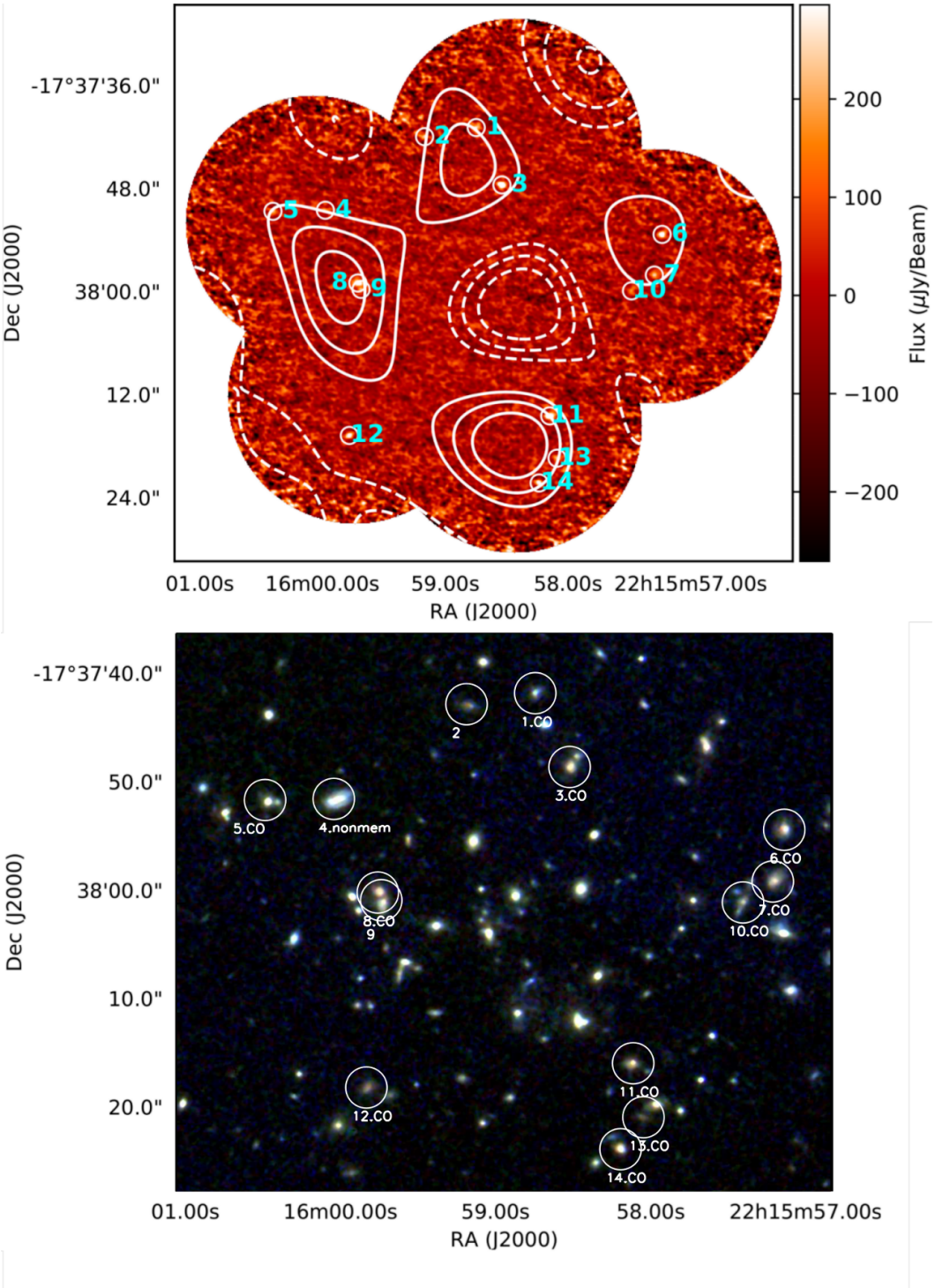

Figure 5.1: *Upper panel*: the ALMA 1.25 mm (Band 6) mosaic of XCS J2215 taken from six overlapping pointings covering a 500 kpc diameter region in the cluster core. We detect 14 $>4\,\sigma$ continuum detections, demonstrating a very significant overdensity of millimetre sources in this region marked by circles and numbered. We list their properties in Table 5.1. We also overlay the SCUBA-2 850 μm S/N contours from Ma15 starting at $2\,\sigma$ and increasing in steps of $1\,\sigma$ (dashed lines showing the equivalent negative contours). *Lower panel*: a slightly zoomed three-colour *HST* image (F125W, F140W, and F160W), with our ALMA detections labelled, showing the rest-frame V-band morphologies of the millimetre sources. We highlight source #4 as "nonmem" as this is a known interloper from its spectroscopic redshift; all the other sources have either ^{12}CO (labelled "CO") detections from this study or archival ^{12}CO(2-1) which confirm cluster membership (eleven sources) or photometric redshifts suggesting possible membership (IDs 2, 9)

of $L_X = 2.9^{+0.2}_{-0.4} \times 10^{44}\,\mathrm{erg\,s^{-1}}$ and an ICM temperature $T = 4.1^{+0.6}_{-0.9}\,\mathrm{keV}$. Employing the R_{200}–velocity dispersion relation of Carlberg et al. (1997); where R_{200} is the radius from the cluster centre within which the mean density is 200 times the critical density at the redshift of the cluster, H10 used an iterative method to estimate a line-of-sight velocity dispersion of $\sigma_v = 720 \pm 110\,\mathrm{km\,s^{-1}}$ from the 31 galaxies with spectroscopic redshifts within $R_{200} = 0.8 \pm 0.1\,\mathrm{Mpc}$ or $100''$. The velocity distribution of the galaxies, however, did show signs of bimodality, suggesting that the cluster may not be a completely relaxed and virialized system. This bimodality is unsurprising given the estimated characteristic timescales for the relaxation of this cluster (t_{relax}), estimated by:

$$t_{\mathrm{relax}} = \left(\frac{R^3}{GM}\right)^{1/2} \frac{N}{8 \ln N} \tag{5.3.1}$$

where R is an estimation of the 'radius' of the cluster, M the mass enclosed, G the gravitational constant, and N the number of cluster galaxies. A simple order-of-magnitude estimation of t_{relax} for XCS 2215, by assuming $N \sim 10^3$, gives relaxation times on the order of 10^{11} years, considerably longer than the age of the universe and thus this bimodality is expected.

Within the central 0.25 Mpc of the cluster Hayashi et al. (2010, 2014) found 20 [OII] emitters with dust-free star-formation rates (SFR) $> 2.6\,M_\odot\,\mathrm{yr^{-1}}$. Using *Spitzer*/MIPS, H10 found a further three bright 24-μm sources with estimated SFRs of $\sim 100\,M_\odot\,\mathrm{yr^{-1}}$ within the central 0.25 Mpc. However, as noted earlier, at $z = 1.46$ the broad PAH feature at 8.6 μm and potential silicate absorption features are redshifted into the 24 μm MIPS band, complicating the measurements of SFRs from this mid-infrared band. To provide a more robust census of luminous dusty galaxies Ma15 obtained sensitive, longer wavelength observations with SCUBA-2 at 850/450 μm of XCS J2215. These observations were combined with JVLA observations at 1.4 GHz and archival images and photometry from *Hubble Space Telescope* (*HST*), Subaru, and *Spitzer* (respectively: Dawson et al., 2009; Hilton et al., 2009, 2010) to study the U/LIRGs in the cluster. Ma15 detected seven submillimetre sources above a 4-σ significance cut within R_{200} ($100''$ radius), an order of magnitude above the expected blank-field counts. A further four fainter ($> 3\sigma$) 850 μm sources were detected which were confirmed through counterparts in *Herschel*/PACS

70μm, 160μm and MIPS 24μm. The probabilistic identification of counterparts to these submillimetre sources in the mid-IR and radio associated 9 of the 11 with galaxies that had spectroscopic or photometric redshifts that suggested that they are cluster members. The total SFR from these potential U/LIRG cluster members yields an integrated SFR within R_{200} of $> 1400\,M_{\odot}\,\mathrm{yr}^{-1}$, this suggests that XCS J2215 is one of the highest SFR clusters known at high redshifts (Ma et al., 2015).

We note that after submission of this paper Hayashi et al. (2017) published an ALMA Band 3 ^{12}CO(2-1) study of XCS J2215 which overlaps with our observations. Their concentration on just ^{12}CO(2-1) enabled them to take deeper integrations over a slightly wider field and hence allowed them to detect fainter sources; however, where our observations overlap we obtain similar results.

5.3.2 ALMA Band 6 Observations

We obtained 1.25 mm continuum and simultaneous ^{12}CO($J = 5$–4) observations of the core of the XCS J2215 cluster using ALMA covering the core of the cluster including four of the SCUBA-2 sources identified by Ma15. These Band 6 observations were carried out on 2016 June 19 (project ID: 2015.1.00575.S). To cover the ^{12}CO(5–4) emission lines we set two spectral windows (SPWs) to cover the observed frequencies from 232.7 to 236.4 GHz or $\Delta \mathrm{V} \sim 4800\,\mathrm{km\,s^{-1}}$ which comfortably covers the expected $720 \pm 110\,\mathrm{km\,s^{-1}}$ velocity dispersion of the cluster. A further two SPWs were centred at 248.9 and 251.4 GHz, where no visible emission lines are expected, for continuum imaging. Each SPW had a bandwidth of 1.875 GHz with a spectral resolution of 3.904 MHz for the emission-line SPWs (corresponding to a velocity resolution of 4.97–5.01 $\mathrm{km\,s^{-1}}$) and a spectral resolution of 31.250 MHz for the continuum SPWs (37.3–37.6 $\mathrm{km\,s^{-1}}$). At these frequencies the full-width-half-maximum (FWHM) of the primary beam is $\sim 25''$; therefore, a mosaic of six pointings was required to map the central 500 kpc diameter covering the cluster core (Fig. 5.1). The observations were conducted with forty-two 12 m antennae where the bandpass calibration was obtained from J2258$-$2758, the flux calibrator used was Titan, and the phase calibrator was J2206$-$1835 with an on-source integration time of 244 s for each pointing.

Calibration and imaging was carried out with the COMMON ASTRONOMY SOFTWARE APPLICATION (CASA v4.6.0 (McMullin et al., 2007)). The observation used a configuration which yielded a synthesised beam in Band 6 for the six pointings of $\sim 0\farcs66 \times 0\farcs47$ (PA ~ 78 deg.). The resulting continuum maps were created with the CLEAN algorithm using multi-frequency synthesis mode with a natural weighting to maximise sensitivity. We initially created a dirty image from the combined SPWs for each field and calculated the rms noise values. The fields are then initially cleaned to 3σ and then masking boxes are placed on sources $> 4\sigma$ and the sources cleaned to 1.5σ. The six fields were then combined to create a final image for source detection with an rms $\sigma_{1.25\mathrm{mm}} = 48\,\mu\mathrm{Jy\,beam^{-1}}$ at its deepest point, shown in Fig. 5.1.

5.3.3 ALMA Band 3 Observations

As well as the Band 6 mosaic, we also obtained a single pointing in Band 3 centered on the cluster to cover ^{12}CO(2–1) emission from gas-rich cluster members. These observations were carried out on 2015 August 7 using thirty-nine 12 m antennae (project ID:2013.1.01213.S), using J2258−2758 as the bandpass calibrator, Ceres as the flux calibrations, and the phase calibrator was J2206−1835 with an on-science target integration time of 37.5 minutes. Two spectral windows were used centred at observed frequencies 93.246 GHz and 95.121 GHz, with spectral bandwidths of 1.875 GHz and a resolution of 1.938 MHz for both SPWs (corresponding to 6.1–6.2 km s^{-1}). At this observing frequency, the FWHM of the primary beam is $\sim 61''$ and therefore the central ~ 500 kpc of the cluster (Fig. 5.1) could be covered in a single pointing. The same reduction approach was taken for the Band 3 observations as used for the Band 6 data, to create channel maps with a velocity resolution of 50 km s^{-1} and a noise level in each channel of 0.3–0.8 mJy beam^{-1}.

5.3.4 Source Detection

To search for sources in the 1.25 mm continuum map we used AEGEAN (Hancock et al., 2012) to identify $> 4\sigma$ detections. As we expected the galaxies to be unresolved in our

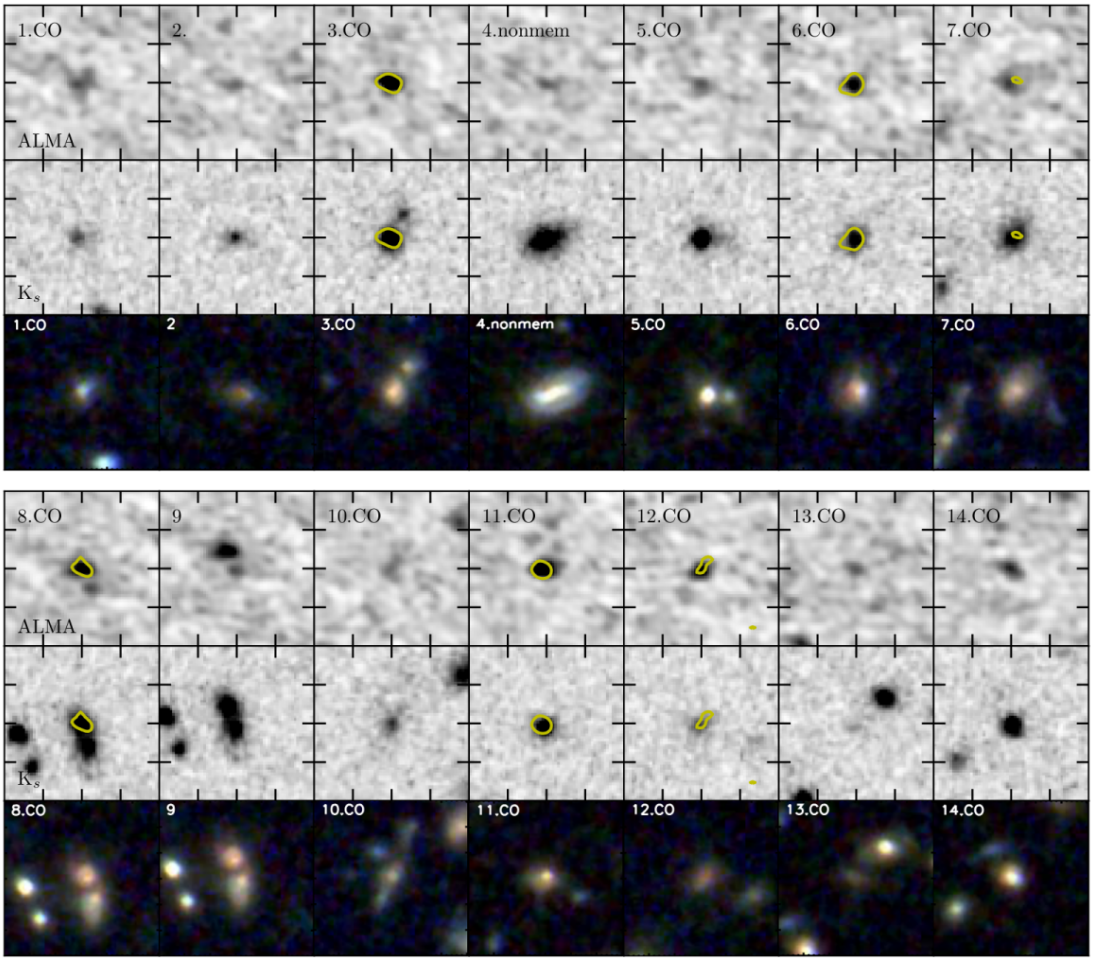

Figure 5.2: Thumbnails showing the ALMA Band 6 continuum (top row of each panel), K_s (middle row of each panel) and three-colour *HST* WFC3 images (1.25, 1.40, and 1.60 μm, lower row of each panel), of the S/N $>$ 4 millimetre continuum sources detected in our map. Several sources display disturbed morphologies or very close neighbours (although these are typically faint in K_s and hence likely to be low mass), suggesting that dynamical interactions may be triggering the strong star formation in these galaxies. Each of these thumbnails is centred on the positions given in Table 5.1. Six of the brightest sources in the ALMA continuum map: IDs 3, 6, 7, 8, 11, 12 additionally yield ^{12}CO(2–1) and ^{12}CO(5–4) emission-line detections, while IDs 1, 5, 10, 13, 15 have archival ^{12}CO(2–1) detections from Hayashi et al. (2017) confirming that these are members of the cluster. Each thumbnail is $6''\times 6''$with major ticks every $1\farcs5$ and with north up and east left. The yellow contours show the $3\,\sigma$ contour for the integrated ^{12}CO(5–4) map across the FWHM of the detected lines, showing the high-J ^{12}CO emission is aligned with the dust continuum.

continuum image, we also experimented with a peak pixel signal-to-noise ratio source extraction method as in Chapter 2, however for this work AEGEAN returned more detections at our detection threshold. As part of this source extraction, we constructed a noise map for the mosaic by deriving standard deviations of the flux density in a box around each pixel with a size comparable to the synthesised beam. Bright pixels are rejected in each box using a 3σ clipping to avoid real sources contaminating the noise map. The outside edge of the ALMA mosaic was then trimmed to the half-width half-maximum radius of the primary beams and source extraction was performed within this region which had a maximum noise of $\sigma_{\rm rms} = 0.09\,{\rm mJy\,beam^{-1}}$. Based on this noise map we detect 14 S/N $> 4.0\sigma$ candidate sources from the Band 6 continuum map shown in Fig. 5.1 and listed in Table 5.1. All continuum sources have corresponding K_s, i_{850}, r_{775} and H_{160} band counterparts within $0\farcs5$, (Fig. 5.1 & 5.2) and to estimate the reliability of these detections we perform the same detection routine in the negative source map which yields zero detections at $> 4\sigma$.

We compare this number of detections with the blank-field 1.2 mm number counts from the *Hubble* Ultra Deep Field (Aravena et al., 2016; Dunlop et al., 2016) (see also Oteo et al. (2016)). For sources brighter than a flux limit of ~ 0.18 mJy, we would expect $\sim 2 \pm 1$ sources in the area of our continuum map. Therefore, we appear to be detecting a $\sim 7\times$ overdensity of millimetre sources in the central projected 500 kpc of XCS J2215 seen in Fig. 5.1.

Line Detection

To search for ^{12}CO emission lines we first adopted a targeted search by extracting spectra from the Band 3 and 6 datacubes at the positions of the fourteen 1.25 mm continuum detections. In addition, we extract spectra at the positions of the 25 spectroscopic members from H10, the 46 sources from H09 with photometric redshifts indicating possible cluster membership and the 20 [OII] emitters from Hayashi et al. (2014) that are within the footprint of the ALMA observations.

We detect six significant emission lines in the Band 3 data, all corresponding to bright dust continuum sources (IDs: 3, 6, 7, 8, 11, 12 in Fig. 5.1). One of these sources, ID 6,

also has a redshift from H10: $z = 1.454$, consistent with our ^{12}CO-derived measurement, Hayashi et al. (2017) also report ^{12}CO(2–1) detections for all six of these sources with redshifts consistent with our own. We identify all of these lines as ^{12}CO(2–1) from cluster members and plot the spectra for these in Fig. 5.3. Applying the same procedure on the Band 6 cube yielded significant detections of ^{12}CO(5–4) from just the same six sources and these are also shown in Fig. 5.3 and the line emission is contoured over the continuum in Fig. 5.2 showing the high-J gas is colocated with the rest-frame 500 μm dust emission. For the ^{12}CO(5–4) emission lines, we subtracted the continuum emission in the uv data using the UVCONSTSUB task in CASA and, by averaging data across channels, created continuum-subtracted channel maps at a velocity resolution of 50 km s^{-1} with an rms of 0.3–0.4 mJy beam^{-1}. We find no individually detected ^{12}CO(2–1) or ^{12}CO(5–4) emission from any of the other sources in the spectroscopic or photometric samples.

For the galaxies where ^{12}CO emission lines were detected, we calculated the intensity-weighted redshift. This was calculated for both the ^{12}CO(5–4) and ^{12}CO(2–1) lines, and for both lines for all six sources the derived redshifts were in excellent agreement, as can be seen in Fig. 5.3. The redshift values reported in Table 5.2 are the means of the redshifts derived from the two transitions. Line widths are derived from fitting Gaussian profiles to the binned spectra using scipy.curve_fit in PYTHON weighted by the uncertainty in the spectra.

We attempted a blind search for CO emission lines in the Band 3 and 6 cubes by collapsing them in 300 km s^{-1} wide bins (similar to the observed FWHM of the targeted detections) and stepping the bins in 100 km s^{-1} increments across a velocity range $-2\sigma_v < v < +2\sigma_v$ where σ was the given velocity dispersion of the cluster from H10. AEGEAN was used to detect peaks in these collapsed channel maps looking for $>4\sigma$ detections. This procedure recovered the six previously identified line emitters but did not uncover any additional blind detections. We do see hints ($< 3.5\,\sigma$) of further ^{12}CO(5–4) detections at the locations and redshifts of two of the ^{12}CO(2–1) detections from Hayashi et al. (2017) (ALMA.B3.04 and ALMA.B3.08) however these are all faint and none of them make our selection cut and so they are not considered for the rest of the paper.

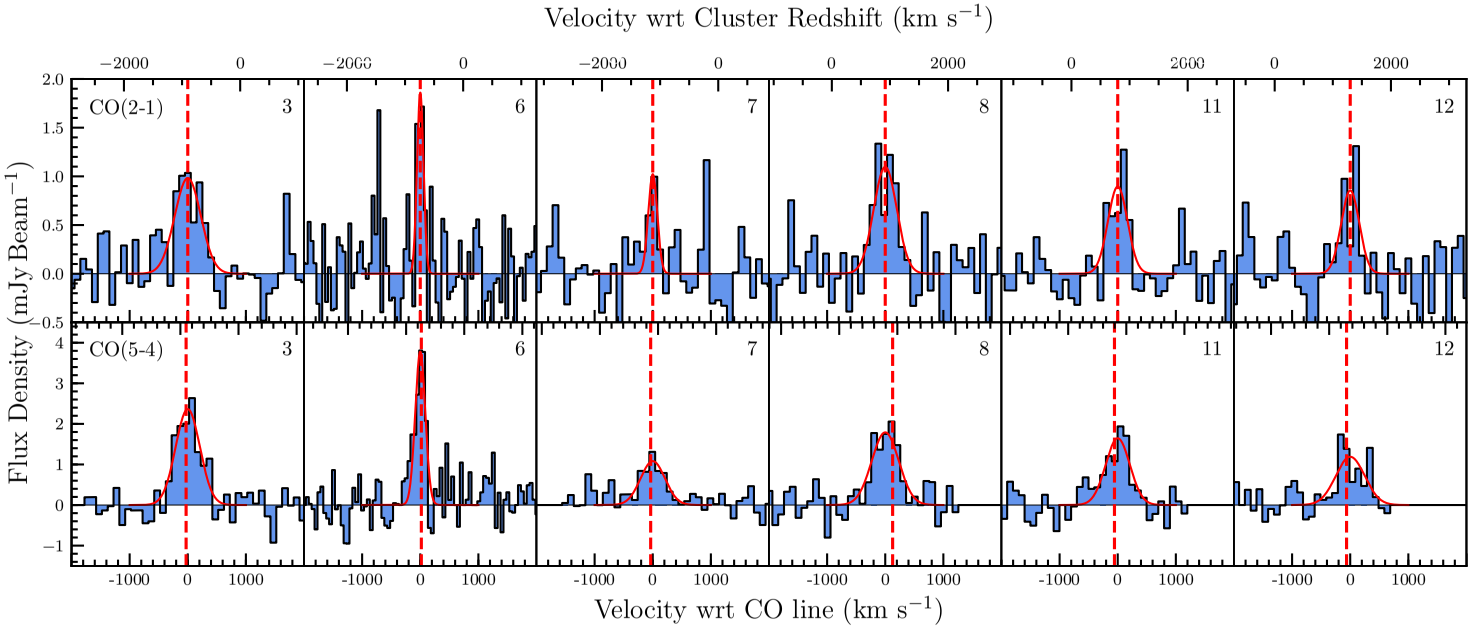

Figure 5.3: Spectra of the six ^{12}CO detected cluster members with the top row showing the ^{12}CO(2–1) emission in Band 3 and the bottom row the ^{12}CO(5–4) lines which fall in Band 6. In each case the best-fitting single Gaussian profiles are overlaid. We see detections of lines in both transitions in all six sources, confirming these millimetre sources as gas-rich cluster members. The lower velocity axis is centered on the peak velocity of the Gaussian fit to the ^{12}CO(2–1) line whilst the upper velocity axis shows a velocity scale relative to the nominal cluster redshift of $z = 1.460$. The spectra for IDs 3, 7, 8, 11, 12 are binned to 100 km s^{-1} resolution however for ID 6 the data was binned at 50 km s^{-1} due to their narrow line width. The lack of spectral coverage at velocities > 1000 km s^{-1} for ^{12}CO(5–4) IDs 8, 11 and 12 is due to the edge of the spectral window. The dashed red vertical lines show the velocity at which the ^{12}CO(2–1) Gaussian's peak for each of our six detections.

5.3.5 MUSE AO Observations

Observations of the central 1×1 arcmin of XCS J2215 were taken with the MUSE IFU during the science verification of the wide-field adaptive optics (WFM-AO) mode on 2017 August 15. In this mode, the GALACSI AO system is used to increase the Strehl ratio of the observations by employing four laser guide stars (and a deformable secondary mirror) to correct for the turbulent atmospheric ground layer. An $R = 16.1$ mag star located $95''$ from the field center was used to correct for the remaining atmospheric tip-tilt. In total, we observed the cluster core for 3.5 ks, which was split into four 860 s exposures, each of which was spatially dithered by $\sim 5''$. Between exposures, the IFU was also rotated through 90 degrees to improve the flat-fielding along slices in the final datacube. We used the standard spectral range, which covers 4770–9300 Å and has a spectral resolution of $R = \lambda / \Delta\lambda = 4000$ at $\lambda = 9200$Å (the wavelength of the [OII] at the redshift of the cluster sample) – sufficient to resolve the [OII]$\lambda\lambda$3726.2,3728.9 emission-line doublet.

To reduce the data, we use the MUSE ESOREX pipeline which extracts, wavelength-calibrates, flat-fields the spectra, and forms each datacube. Each observation was interspersed with a flat-field to improve the slice-by-slice flat field (illumination) effects. Sky subtraction was performed on each sub-exposure by identifying and subtracting the sky emission using blank areas of sky at each wavelength slice, and the final mosaics were then constructed using an average with a $3\,\sigma$ clip to reject cosmic rays, using point sources in each (wavelength collapsed) image to register the cubes.

For each source in our 1.2 mm catalog, we extract a spectrum by integrating the datacube within a $0\farcs5$ aperture and search for the [OII] emission at the cluster redshift. For all the galaxies with CO detections, we detect the [OII] emission line with signal-to-noise ranging from 5 to 100. We fit the [OII] emission doublet and derive redshifts that agree with the CO (within their $1\,\sigma$ error) in all cases. We report the [OII] emission-line redshifts in Table 1.

5.4 Analysis and Results

Our ALMA survey of the central regions of XCS J2215 has resolved the overdensity of four submillimetre sources in the core of the cluster into 14 separate 1.25 mm continuum sources (Fig. 5.1). The four brightest 1.25 mm continuum components each correspond to one of the SCUBA-2 sources discovered by Ma15: our ID 11 corresponds to SCUBA-2 source #4 from Ma15, ID 3 is #11, ID 8 is #6 and ID 6 is #13. Our ALMA-detected millimetre sources also confirm the primary IDs proposed by Ma15 for these single-dish sources, but their analysis did not identify any of the other 10 sources detected by ALMA in this region, which contribute to the sub/millimetre flux seen by SCUBA-2.

As noted above, the five brightest millimetre continuum sources (plus the seventh) also exhibit ^{12}CO(2–1) and ^{12}CO(5–4) emission with redshifts that place them within the cluster. In addition, we match the remaining fainter continuum sources to the Hayashi et al. (2017) ^{12}CO(2–1) catalog, finding five further matches: IDs 1, 5, 10, 13, 14. Matching to the H10 redshift catalogue finds that a further continuum source, ID 4, has a spectroscopic redshift of $z = 1.301$ making it an interloper in the foreground of the cluster and we do not consider it a cluster member in the following analysis. In the remaining two continuum-selected ALMA sources (ID 2 and 9) we do not detect any emission lines in the MUSE spectra, which covers 4770–9300 Å (which corresponds to $z = 0.28$–1.50 for [OII] emission). However, we note that both of these two galaxies in the H09 photometric redshift catalogue have redshifts that are consistent with being possible cluster members, although the absence of lines in the MUSE spectra either suggests they are highly obscured, or they lie at higher redshift than $z = 1.50$. For the 11 spectroscopically confirmed millimetre-selected cluster members we derive a rest-frame velocity dispersion of $\sigma = 1040 \pm 100\,\mathrm{km\,s^{-1}}$. This is marginally higher than the $\sigma = 720 \pm 110\,\mathrm{km\,s^{-1}}$ determined by H10 for the cluster members within the cluster core. This difference is not statistically significant ($\sim 2\,\sigma$), but the sense of the difference is consistent with the expectation that the millimetre-selected sources are likely to be relatively recently accreted galaxies which have yet to fully virialise.

Our ALMA observations provide precise positions for the sub/millimetre emission and so unambiguously identify the counterparts in the optical and near-infrared wave-

bands, as shown in Fig. 5.1 and Fig. 5.2. Over half of these sources have companions on scales of $\sim 2''$–$3''$, although more than half of these are faint or undetected in the K_s band, suggesting they have relatively modest stellar masses. Nevertheless, this is some indication that close tidal interactions or minor mergers may be the trigger for the starburst activity seen in this population.

5.4.1 SED Fitting

We estimate the far-infrared luminosities for each of our continuum sources by fitting their far-infrared and submillimetre photometry using a library of galaxy template SEDs from Chary & Elbaz (2001); Draine et al. (2007); Rieke et al. (2009). We use our 1.25 mm continuum fluxes along with fluxes from the lower resolution single-dish observations from SCUBA-2 at 450 and 850 μm (Ma et al., 2015) and archival *Herschel* PACS data at 100 and 160 μm (see Santos et al., 2013). Due to the low resolution for the single-dish observations, the fluxes for the individual sources were estimated by deblending these maps using the method detailed in Swinbank et al. (2013) using the ALMA detections as positional priors as described in Ma15. We calculate the infrared luminosity from integrating the best-fitting SEDs for each galaxy in the wavelength range 8–1000 μm and from this derived the far-infrared luminosity assuming the sources lie at the cluster redshift (Table 5.1). The far-infrared luminosities show a $\sim 50\%$ dispersion at a fixed 1.25 mm flux, but the formal error bars are consistent with a single ratio, and hence there is no strong evidence for a variation in SED shape within our small sample. In particular, we note that we obtained ^{12}CO detections for six of the brightest 1.25 mm continuum sources, only three of which fall in the top five brightest sources based on the far-infrared luminosities. This may indicate that the far-infrared luminosities may be less reliable than adopting a single representative SED model and fitting this just to the 1.25 mm continuum flux. We also caution that if there are systematic differences in the dust SEDs of galaxies in high-density environments, e.g., due to stripping of diffuse cold gas and dust components (Rawle et al., 2012), then this will not be captured by the templates in our library.

We next estimate the star-formation rate from the far-infrared luminosities using the Kennicutt (1998) relation and assuming a Chabrier IMF. For the 14 ALMA

Table 5.1: Properties of the ALMA 1.25 mm continuum detections in XCS J2215

ID	R.A.	Dec.	$S_{1.25\mathrm{mm}}$	L_{FIR}	SFR	z_p	z_s^*	z_{MUSE}
	(J2000)		(mJy)	($10^{11}\,\mathrm{L}_\odot$)	($M_\odot\,\mathrm{yr}^{-1}$)	(H09)		
1	22 15 58.75	−17 37 40.9	0.46±0.09	$3.5^{+1.9}_{-2.2}$	50^{+30}_{-30}	$1.44^{+1.10}_{-1.10}$	1.451†	1.451 (1.464)††
2	22 15 59.17	−17 37 41.9	0.49±0.08	$2.8^{+1.3}_{-1.4}$	40^{+20}_{-20}	$1.15^{+2.80}_{-0.20}$	...	...
3	22 15 58.54	−17 37 47.6	0.93±0.05	$8.8^{+4.4}_{-2.2}$	130^{+60}_{-30}	$1.99^{+0.39}_{-0.57}$	**1.453**	1.454
4	22 15 59.98	−17 37 50.5	0.21±0.04	$3.6^{+2.1}_{-1.2}$	50^{+30}_{-20}	$1.25^{+0.11}_{-0.36}$	*1.301*	1.302
5	22 16 00.40	−17 37 50.6	0.37±0.07	$1.7^{+0.6}_{-0.8}$	20^{+10}_{-10}	$1.33^{+0.69}_{-0.19}$	1.451†	1.452
6	22 15 57.23	−17 37 53.3	0.68±0.08	$9.4^{+2.7}_{-1.7}$	140^{+40}_{-30}	$1.30^{+0.92}_{-0.48}$	**1.454**	1.454
7	22 15 57.30	−17 37 58.0	0.46±0.09	$3.6^{+1.9}_{-2.0}$	50^{+30}_{-30}	$1.35^{+1.00}_{-0.18}$	**1.450**	1.453
8	22 15 59.71	−17 37 59.0	0.88±0.08	$3.3^{+0.9}_{-1.1}$	50^{+10}_{-20}	$1.32^{+1.10}_{-0.35}$	**1.466**	1.468
9	22 15 59.69	−17 37 59.7	0.28±0.05	$6.7^{+2.5}_{-1.7}$	100^{+40}_{-20}	$1.50^{+0.81}_{-0.22}$	...	...
10	22 15 57.48	−17 37 59.9	0.18±0.04	$1.8^{+0.8}_{-1.3}$	30^{+10}_{-20}	$1.97^{+0.37}_{-0.61}$	1.450†	1.451
11	22 15 58.15	−17 38 14.5	0.98±0.06	$5.5^{+1.6}_{-2.8}$	80^{+20}_{-40}	$1.73^{+0.52}_{-0.36}$	**1.467**	1.467
12	22 15 59.78	−17 38 16.7	0.60±0.09	$2.4^{+1.4}_{-1.0}$	40^{+20}_{-10}	$1.54^{+0.86}_{-0.47}$	**1.472**	1.472
13	22 15 58.09	−17 38 19.4	0.30±0.07	$3.9^{+1.2}_{-0.6}$	60^{+20}_{-10}	$1.34^{+1.70}_{-0.66}$	1.467†	1.469
14	22 15 58.23	−17 38 22.3	0.56±0.08	$3.6^{+2.0}_{-1.9}$	50^{+30}_{-30}	$1.46^{+0.99}_{-0.32}$	1.457†	1.457

* Spectroscopic redshifts in **bold** are from ^{12}CO emission described in this paper, confirmed non-members are in *italics*.

† ^{12}CO spectroscopic redshifts from Hayashi et al. (2017). †† There are two galaxies separated by $<0\farcs5$ and $\sim 1500\,\mathrm{km\,s^{-1}}$, both of which are detetced in CO and [OII].

continuum sources we derive $L_{\rm IR}$ in the range of (1.7–9.1) $\times 10^{11}\,L_{\odot}$ and a median $(3.6^{+2.1}_{-1.2}) \times 10^{11}\,L_{\odot}$ which corresponds to SFRs of $\sim$20–140 $M_{\odot}\,{\rm yr}^{-1}$ (Table 5.1). The derived luminosities of $L_{\rm IR} = 10^{11}$–$10^{12}\,L_{\odot}$ classify these cluster galaxies as LIRGs with the brightest on the ULIRG boundary.

Integrating the ongoing star formation in the spectroscopically confirmed millimetre-selected cluster members we derive a total SFR in the central $\sim$500 kpc of the cluster of $\gtrsim 700\,M_{\odot}\,{\rm yr}^{-1}$. Including the photometrically identified members (but excluding ID 4), this increases to $\gtrsim 840\,M_{\odot}\,{\rm yr}^{-1}$. This is comparable to the total SFR estimated by Ma15 within $R_{200} = 0.8$ Mpc ($\sim 100''$), even though that region is much larger than the extent of our current ALMA survey of the central $R \leq 0.25$ Mpc (Fig. 5.1). Thus, our results reinforces the claims that XCS J2215 demonstrates a very rapid increase in the SFR density in the central regions of clusters out to $z \sim 1.5$ and beyond.

5.4.2 CO Line Properties

To derive ^{12}CO line properties we fit single Gaussians to each of the Band 3 and 6 emission spectra, which appear to provide adequate descriptions of the observed line profiles (Fig. 5.3). Estimates of the line widths were taken from the FWHM of the Gaussian fits, and the flux density of the ^{12}CO lines were determined by integrating the ^{12}CO spectrum,

$$I_{\rm CO} = \int_{-2\sigma}^{+2\sigma} I(v)dv, \tag{5.4.2}$$

where σ was taken from the Gaussian fits. Then, the ^{12}CO luminosities were calculated using the relation given in Solomon & Vanden Bout (2005):

$$L'_{\rm CO} = 3.25 \times 10^7 S_{\rm CO}\Delta v \nu_{\rm obs}^{-2} D_L^2 (1+z)^{-3}, \tag{5.4.3}$$

where $L'_{\rm CO}$ is the line luminosity in K km s^{-1} pc^2, $S_{\rm CO}\Delta v$ is the observed velocity-integrated flux density in Jy km s^{-1}, ν is the observed frequency of the emission line in GHz and D_L is the luminosity distance in Mpc. The FWHM and ^{12}CO flux densities for both transitions are given in Table 5.2. For simplicity in comparing to the literature we adopted the same values for the constants $\alpha_{\rm CO} = 1$, radius of galaxy $R_{kpc} = 7$ kpc

and the $L_{CO(2\text{-}1)}/L_{CO(1\text{-}0)}$ ratio of 0.84 ± 0.13 from Bothwell et al. (2013) when deriving M_{gas} and M_{dyn}. We then list the estimated gas masses (M_{gas}) for the galaxies based on their ^{12}CO(2–1) luminosities and adopting $\alpha_{CO} = 1$ (following Bothwell et al. 2013). We also list the dynamical masses (M_{dyn}) for a disk-like dynamical model with a 7 kpc radius and the average inclination for a population of randomly orientated disks (again following Bothwell et al. 2013). We note that the derived values are highly dependant on the value of α_{CO} and due to the SFRs being lower than the ULIRG sources in Bothwell et al. (2013), a more Milky Way-like $\alpha_{CO} \sim 4.4$ which has been claimed to be appropriate for less active high-redshift galaxy populations might be more applicable (Tacconi et al., 2013) however a Milky Way-like α_{CO} results in gas masses for two out of our six detections being greater than our calculated dynamical masses. We note that our dynamical masses, whilst consistent with independent stellar mass estimations shown below, are based on adopting a mean inclination angle for populations of randomly oriented disks and an adopted value for the galaxy radius of $R_{kpc} = 7$ kpc however the two galaxies with gas fractions >1 adopting $\alpha_{CO} \sim 4.4$ are ID 6 and ID 7 (see Fig. 5.2) and from their HST morphologies do not appear "edge-on;" therefore, the inclination angle assumption will not create an underestimation of their dynamical masses. To reconcile the unphysical gas fractions would require dynamical masses estimated with galaxies of radii >35 kpc which is again unphysical and an order of magnitude greater than previous size estimators of ^{12}CO-emitting regions (Engel et al., 2010). This suggests, that for at least these two galaxies, that a Milky Way-like $\alpha_{CO} \sim 4.4$ is an inappropriate conversion factor to use and a lower value more typical for local ULIRGs is more appropriate.

The median gas mass for the six galaxies is $M_{gas} = 1.6 \pm 0.2 \times 10^{10}\, M_{\odot}$ (or M_{gas}=4.3–10.5 $\times 10^{10}\, M_{\odot}$ for $\alpha_{CO} = 4.36$), the median dynamical mass is $M_{dyn} = 0.9^{+0.3}_{-0.6} \times 10^{10}\, R_{kpc}\, M_{\odot}$ ($M_{dyn} = 6^{+2}_{-4} \times 10^{10}\, M_{\odot}$ for $R_{kpc} = 7$ kpc) and the median gas fraction is relatively low at $f_{gas} = 0.3 \pm 0.3$. We estimate stellar masses for our 1.2 mm continuum-selected galaxies using their *Spitzer* imaging. In particular, we exploit the archival IRAC imaging of XCS J2215 to measure IRAC 3.6 μm magnitudes for our sources, deriving a median magnitude of 21.1 $^{+0.1}_{-0.2}$. At $z = 1.45$, this corresponds to rest-frame H-band, which is sensitive to the underlying stellar mass of a galaxy. We exploit the MAGPHYS-derived

stellar masses of comparably luminous submillimeter-selected galaxies in the Extended Chandra Deep Field South from da Cunha et al. (2015) and apply their median rest-frame H-band mass-to-light ratio to our sample. We derive a median stellar mass of $M_* = 4^{+2}_{-2} \times 10^{10}\,M_\odot$ which suggests a median gas fraction for our six sources with CO detections of $f_{\rm gas} = 0.3 \pm 0.4$ for $\alpha_{\rm CO} = 1.0$, which is in excellent agreement with the gas fractions derived from the dynamical masses, suggesting our choice of $R_{kpc} = 7$ kpc is appropriate.

Combining these gas masses with the SFRs, we estimate a median gas consumption timescale of 200±100 Myrs which is comparable to the crossing-time of the cluster core. However, as noted above, this is highly dependent on the choice of $\alpha_{\rm CO}$, scaling linearly, therefore if a more Milky Way-like $\alpha_{\rm CO}$ is appropriate, then the consumption timescale increases to ~ 800 Myrs, which is comparable to timescales expected for similar main-sequence galaxies at this redshift ($\sim 1.1 \pm 0.2$ Gyrs, Genzel et al. 2015). We note that the fainter ^{12}CO detections for the remaining millimetre sources with archival ^{12}CO detections indicate gas masses of $\lesssim 1 \times 10^{10}$ M$_\odot$ and this may reduce the median gas consumption timescale for the whole population (although these fainter members also tend to have lower SFRs, Table 5.1).

For the two continuum sources without spectroscopic redshifts, from their calculated $L_{\rm IR}$ and based on the scatter in the $L'_{\rm CO}$-$L_{\rm IR}$ relation shown in Figure 5.4 it is plausible that we might not detect ^{12}CO(5-4) for ID 9. For ID 2, on the other hand, the combination of its faint continuum detection and location close to the edge of the ALMA primary beam (see Fig. 5.1) points to a non-detection possibly being a result of insufficient sensitivity.

As we have observations of two ^{12}CO transitions for our ALMA-identified cluster U/LIRGs, we can determine the ratio of the line brightness temperatures between the ^{12}CO(5–4) and ^{12}CO(2–1) transitions. We show in Fig. 5.5 the spectral line distributions (SLEDs) for our sources compared to other populations and models from the literature. This shows that the cool interstellar medium within our cluster LIRGs is less excited than comparably luminous local galaxies, although it has very similar properties to that seen in high-redshift, submillimetre-selected ULIRGs and *BzK* galaxies. To quantify this further, we determine a median value of the ^{12}CO(5–4) and ^{12}CO(2–1) line brightness ratio for our

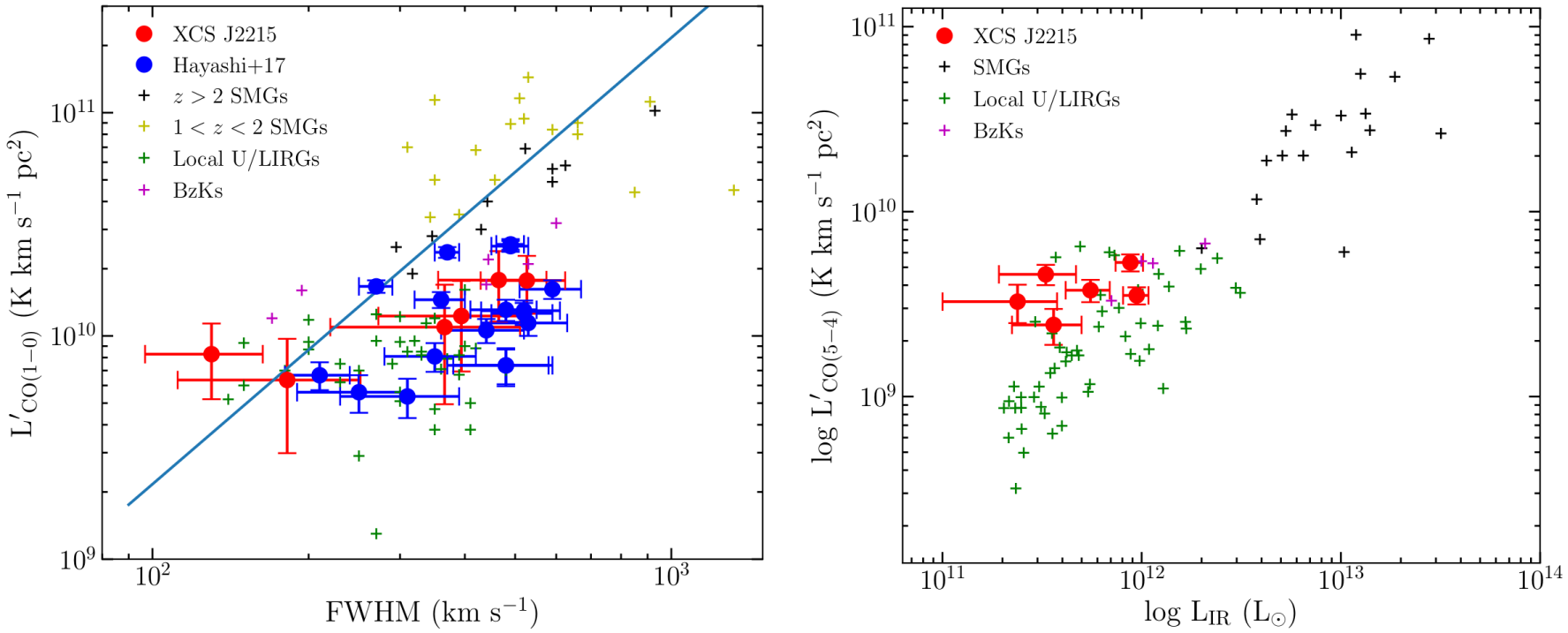

Figure 5.4: (a) Variation of $L'_{CO(1-0)}$ with FWHM of the line for the cluster LIRGs in this work (converting the ^{12}CO(2–1) line luminosity and FWHM) compared to: the Hayashi et al. (2017) detections from the same cluster, local U/LIRGs (Downes & Solomon, 1998), field SMGs from Genzel et al. (2010); Bothwell et al. (2013) and *BzK*s from Daddi et al. (2010). The solid line is the relation for $L'_{CO(1-0)}$ given in Eq. 5.5.4. Our cluster LIRGs overlap with the local U/LIRG sample, although they appear to have slightly lower inferred $L'_{CO(1-0)}$ luminosities, at a fixed line width, compared to submillimetre-selected field SMGs and BzKs at a similar redshift. (b) The observed trend of $L'_{CO(5-4)}$ with L_{IR} for our six ^{12}CO-detected cluster LIRGs and comparison samples of local U/LIRGs, SMGs, and *BzK*s compiled by Daddi et al. (2015). Our cluster LIRGs show $L_{CO(5-4)}/L_{IR}$ ratios consistent within the spread of the local U/LIRG population.

Table 5.2: Emission-line properties for ^{12}CO(2–1) and ^{12}CO(5–4) detections in XCS J2215 member galaxies

ID	$I_{\mathrm{CO(2-1)}}$ (J km s^{-1})	FWHM$_{\mathrm{CO(2-1)}}$ (km s^{-1})	$I_{\mathrm{CO(5-4)}}$ (J km s^{-1})	FWHM$_{\mathrm{CO(5-4)}}$ (km s^{-1})	M$_{\mathrm{gas}}$ (10^{10} M$_\odot$)	M$_{\mathrm{dyn}}$ (10^{10} M$_\odot$)
3	0.5±0.1	530±90	1.2±0.1	490±40	2.4±0.7	11±4
6	0.25±0.08	130±30	0.80±0.09	200±20	1.0±0.2	0.6±0.3
7	0.19±0.09	190±120	0.6±0.1	490±60	1.3±0.2	9±5
8	0.6±0.1	460±90	1.0±0.1	550±50	2.2±0.6	9±4
11	0.4±0.1	390±90	0.8±0.1	490±50	1.6±0.5	6±3
12	0.3±0.1	370±90	0.7±0.2	580±100	1.5±0.7	5±3

six sources of $r_{54/21} = 0.37 \pm 0.06$. We can compare this to the value derived for statistical samples of high-redshift, submillimetre-selected ULIRGs from (Bothwell et al., 2013) and *BzK*s from Daddi et al. (2015): $r_{54/10} = 0.32 \pm 0.05$, $r_{21/10} = 0.84 \pm 0.13$, which yield $r_{54/21} = 0.38 \pm 0.08$ for SMGs and $r_{54/10} = 0.23 \pm 0.04$, $r_{21/10} = 0.76 \pm 0.09$, which yield $r_{54/21} = 0.32 \pm 0.06$ for *BzK*s. As expected from Fig. 5.5, these are in agreement to the values we derive and suggests comparable gas excitation in our sample of $z = 1.46$ cluster LIRGs to the more luminous and typically higher-redshift field SMGs studied by Bothwell et al. (2013), as well as the less luminous *BzK*s. This in turn suggests that the $r_{21/10}$ values for the Bothwell et al. (2013) sample should be broadly applicable to our sources.

5.5 Discussion

Our high-resolution continuum observations with ALMA have confirmed and significantly expanded the overdensity of luminous, dusty star-forming galaxies known in XCS J2215. Our data also enable us to survey the cluster for massive gas reservoirs, and we find six gas-rich systems, associated with the typically brighter dust continuum sources. These ^{12}CO detections, along with five sources that have archival ^{12}CO detections, unambiguously demonstrate that the majority of these galaxies are members of the cluster, while photometric redshifts suggest that two of the remaining continuum sources

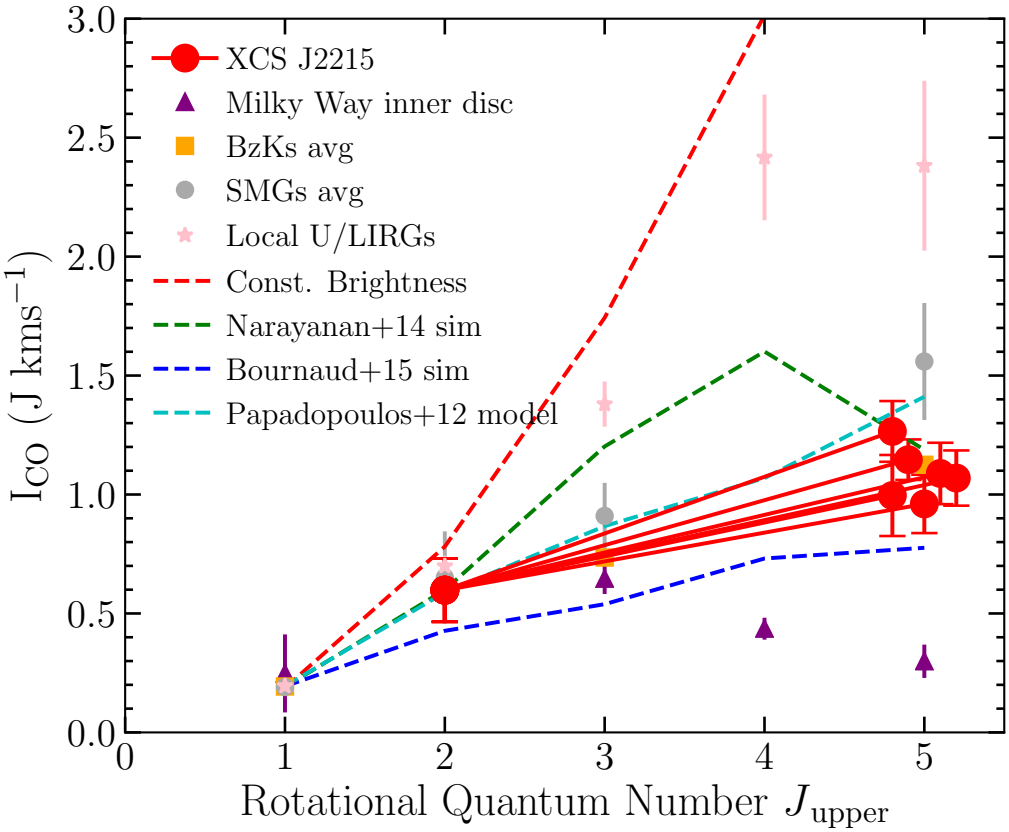

Figure 5.5: ^{12}CO SLEDs for the six XCS J2215 LIRGs compared to SLEDs for other populations from the compilation of Daddi et al. (2015). We see that our cluster LIRGs have SLEDs that peak at higher-J than the Milky Way (Fixsen et al., 1999), indicating that the interstellar medium in these galaxies is more excited, although less excited than local U/LIRGs (Papadopoulos et al., 2012). Our sources appear to be similar to the submillimetre-selected field ULIRGs studied by Bothwell et al. (2013) and the less luminous BzK from Daddi et al. (2015). We also show model SLEDs from the simulations of Narayanan et al. (2012) and Bournaud et al. (2015), and the toy model of Papadopoulos et al. (2012). The latter implies that the interstellar medium is a two-phase mix of star-forming and non-star-forming gas, with 10% of its gas in the star-forming phase. All the SLEDs are normalised to the average $J = 1$ transition for Daddi et al. (2015) *BzK* average except for the Milky Way and XCS J2215 SLEDs which are normalised to the *BzK* average $J = 2$ transition. We note that if environmental processing has preferentially removed cool material from these galaxies, then their measured SLED will appear to be more "active" than it initially started off with.

are also possible members.

We can use the CO line properties for our sources to compare to similar observations of other galaxy populations at high and low redshift to understand their physical properties. Hence, while $L'_{\rm CO}$ provides a tracer for the molecular gas content in these galaxies, the FWHM of the emission lines provides us with a degenerate tracer of both the dynamical mass of the galaxy (narrower FWHM suggests lower mass) and inclination of the galaxy (narrower FWHM suggests a more "face-on" galaxy). In Fig. 5.4(a) we compare the $L'_{\rm CO(1-0)}$ (converted from our $L'_{\rm CO(2-1)}$ detections, adopting $r_{21/10} = 0.84$) versus FWHM for our six ^{12}CO-detected galaxies against a sample of local and high-redshift U/LIRGs. As in Bothwell et al. (2013) we overlay the functional form given in Eq. 5.5.4

$$L'_{\rm CO(1-0)} = \frac{(V/2.35)^2 R}{1.36 \alpha G}, \tag{5.5.4}$$

where V is the FWHM of the line, 1.36α is the ^{12}CO to gas mass conversion factor, R is the radius of the ^{12}CO(2–1) emission region and G is the gravitational constant. We, again, adopt the values of $\alpha = 1$ and $R = 7$ kpc (Bothwell et al., 2013). We see that LIRGs identified with ALMA in XCS J2215 fall within the scatter of the properties of local U/LIRGs, but slightly below the *BzK*s population seen at similar redshifts. They may also show a marginally shallower trend than the functional form given in Eq. 5.5.4, although the latter provides a good fit for the higher redshift and higher luminosity SMGs in Bothwell et al. (2013). We stress that the conversion of the line luminosities to ^{12}CO(1–0) may result in systematic uncertainties between samples and individual sources in Fig. 5.4.

Comparing the line widths for ^{12}CO(2–1) and ^{12}CO(5–4) emission lines for individual galaxies in our sample, we derive a median ratio of $\rm FWHM_{21}/FWHM_{54} = 0.7 \pm 0.2$. If both transitions are tracing the rising part of the rotation curve in these galaxies, this marginal difference suggests that the ^{12}CO(5–4) emission may be more extended than ^{12}CO(2–1). This is the opposite behaviour to that expected if transitions with lower excitation temperatures have larger contributions from cool gas on the outskirts of galaxies (Papadopoulos et al., 2001; Ivison et al., 2011; Bolatto et al., 2013). This could reflect environmental influences on the gas disks in these cluster LIRGs, with the removal of the

more diffuse cool interstellar medium from their extended disks. Similar environmentally driven stripping of cooler material was invoked by Rawle et al. (2012) to explain the apparently higher dust temperatures seen in the SEDs of star-forming galaxies in $z \sim 0.3$ clusters. We note that this would imply that before material was removed, the galaxies would have had a lower $r_{54/21}$ ratio than is currently observed, implying that originally they had a lower excitation SLED and a higher cold gas and dust mass and gas fraction.

As the far-infrared luminosity traces a galaxy's SFR and $L'_{\rm CO}$ traces its gas content we show the ratio of these two observables for the ALMA-detected population in XCS J2215 in comparison to similar galaxies in the low- and high-redshift field in Fig. 5.4b. To try to limit the effect of potential systematic errors we plot the line luminosities derived directly from our higher-S/N ^{12}CO(5–4) detections, $L'_{\rm CO(5-4)}$, and compare to similar high-J observations of the other populations (following Daddi et al. (2015)). Again, we see that our sources lie within the scatter of the local U/LIRG population, although they lie on the high side of the distribution. In comparison to the linear fit of the local U/LIRG population, our cluster galaxies show a median increase in $L'_{\rm CO(5-4)}$ for their detected $L_{\rm IR}$ of 48 %$\pm$12 % (or conversely a deficit in $L_{\rm IR}$ at a fixed $L'_{\rm CO(5-4)}$). One possible explanation for this trend would be if the far-infrared luminosities of these sources are underestimated due to a relative paucity of cold dust (a consequence of the estimates of their far-infrared luminosities being driven primarily by the 1.25 mm flux measurements due to their comparatively small errors in the SED fitting), due to environmental processing, compared to the template populations used to fit their SEDs (see §3.1).

5.5.1 Phase space diagram

In Figure 5.6 we plot the the line-of-sight velocity against cluster centric radius for the galaxies of XCS J2215 which have spectroscopic redshifts. This phase-space diagram is a frequently used tool to classify member galaxies as virialized galaxies or those most recently accreted. Virialized galaxies in a cluster will tend to have larger dispersions closer to the centre of the cluster with smaller dispersions at larger radii. We show in the grey region in Figure 5.6 the virialized region as defined by Jaffé et al. (2015) which is derived from cosmological simulations. Galaxies within this region are predicted to

have experienced multiple pericentric passages across the cluster (and thus potentially stripped of gas through ram pressure stripping) whilst galaxies on the edge or outside of this region are more recent additions to the cluster. We also show the Noble et al. (2016) phase-space classification for how recently a galaxy has been accreted onto a cluster. Noble et al. (2016) defines four regions in the phase-space separated by lines of constant $v \times R$ with a 'central' region at smallest velocity dispersions, to an 'intermediate' region, at higher $v \times R$, where the majority of our CO emitters lie, then an 'recently accreted' region to 'infalling' galaxies at the largest $v \times R$. Our actively star-forming CO emitters are preferentially found at the edge or outside of the Jaffé et al. (2015) defined region, and within the 'intermediate' $v \times R$ region suggesting they are more recently accreted galaxies. In comparison the red quiescent galaxies of Hilton et al. (2010) are preferentially found within the 'central' virialized bin. Thus the potential environmental effects on our CO emitters has had a relatively short duration of effect in comparison to the gas depleted 'central' galaxies and thus we are observing the galaxies that are beginning to undergo the cluster's environment effects.

5.5.2 Environmental affects on the gas and dust in cluster U/LIRGs

Looking at the gas and dust properties of our CO-detected galaxies in XCS J2215 we see several hints which all may be pointing to a relative paucity of cool gas and dust in these systems: (i) the galaxies typically have low ^{12}CO(2–1) luminosities at a fixed FWHM, compared to field galaxies; (ii) the line width measured from the ^{12}CO(2–1) is typically smaller than that measured for ^{12}CO(5–4); (iii) at a fixed ^{12}CO(5–4) line luminosity, these galaxies have lower inferred far-infrared luminosities (which is driven primarily by 1.25 μm – rest-frame $\sim$500 μm – flux) than comparable field galaxies. To isolate these trends in Fig. 5.7a we plot $L'_{\rm CO}$/FWHM^2, a proxy of gas fraction, as a function of redshift. The XCS 2215 galaxies possess similar $L'_{\rm CO}$/FWHM^2 for both the ^{12}CO(2–1) and ^{12}CO(5–4) transitions in comparison to similar U/LIRGs in the field taken from literature (Bothwell et al., 2013; Carilli & Walter, 2013; Zavala et al., 2015; Decarli et al., 2016). While in Fig. 6(b), we consider the CO luminosity and FWHM *ratio* for these two transitions for the cluster galaxies and a sample of similar redshift field galaxies. We limit

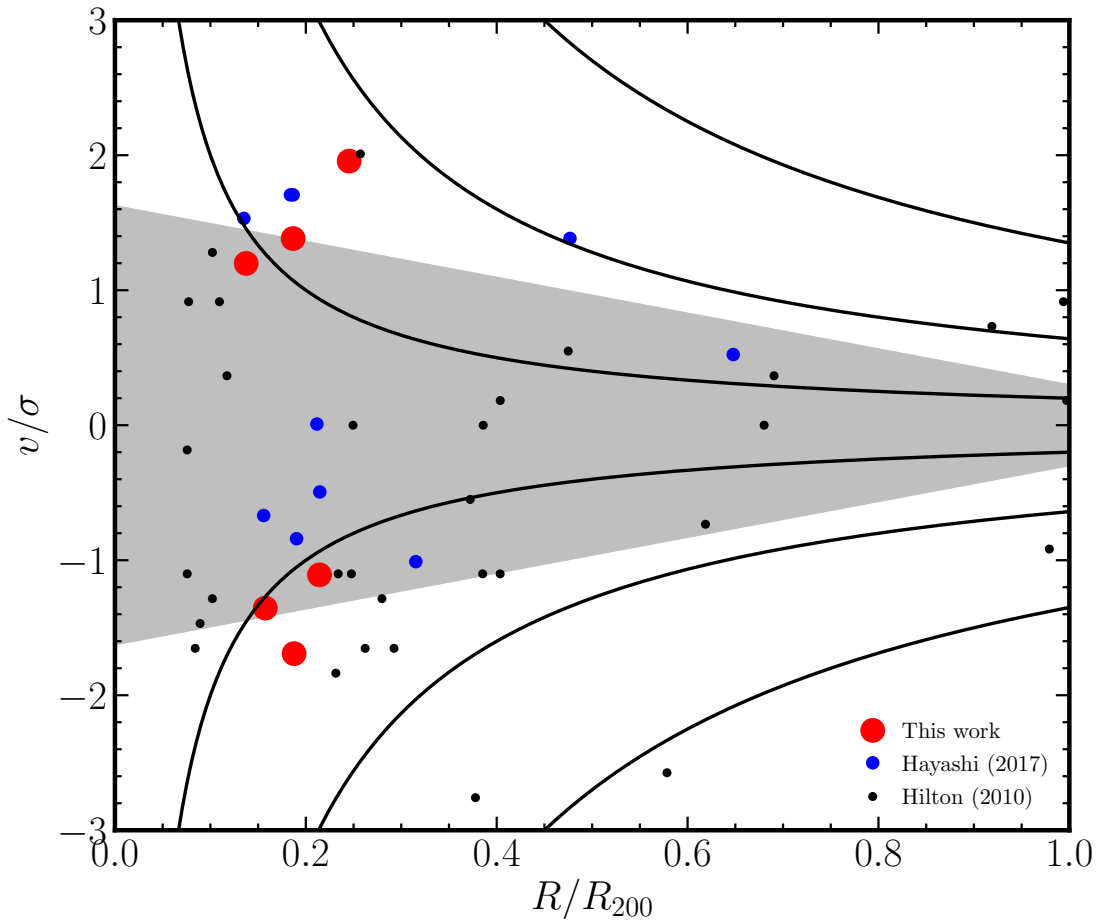

Figure 5.6: Line of sight velocities against cluster centric radii for the XCS J2215 galaxies with spectroscopic redshifts. We show the CO(2-1) actively star-forming galaxies of this work in red, the additional Hayashi et al. (2017) CO(2-1) detections in blue, and the other confirm members from Hilton et al. (2010) in black. Our cluster members lie on the edge and outside of the 'virialized' grey region as defined from Jaffé et al. (2015) suggesting that in comparison to the more passive galaxies of Hilton et al. (2010) the CO emitters tend to lie on the edge of the virialized region and thus are more recently accreted galaxies into the cluster. We also show the lines of constant $v \times R$ as defined from Noble et al. (2016) which also classify cluster member galaxies between central galaxies to infalling galaxies with our CO emitters lying in the intermediate range between these two classes, again suggesting these are more recently accreted galaxies in the cluster.

the redshift range for the field comparison sample to $z = 1$–2 to try to remove evolutionary behaviour such as the increasing size of star-forming galaxies at lower redshifts (van der Wel et al., 2014) which might otherwise produce a spurious trend in $L'_{CO}/FWHM^2$ with redshift. Unfortunately, this leaves us with very few appropriate comparison sources as we are constrained by field galaxies in our redshift range that have observations in both high- and low-J CO transitions. The CO luminosity and FWHM ratios both show a tentative trend that the cluster galaxies are comparatively poorer in the lower-density, cool ^{12}CO(2–1) gas and also show a smaller ^{12}CO(2–1) FWHM, suggesting that any deficit may be occurring on the outskirts of these galaxies. This would be consistent with the stripping of the cool, lower-density gas and dust from the gas disks as a result of an environment process (e.g. ram pressure stripping) that leaves the more tightly bound, denser ^{12}CO(5–4) material relatively untouched (Rawle et al., 2012). However, further observations of low- and high-J CO are needed of larger samples of high-redshift cluster and field galaxies are needed to test this suggestion.

5.5.3 Present descendants of cluster U/LIRGs

The final issue we wish to address is, what are the likely properties of the present-day descendants of these galaxies? They are bound in the cluster potential and so their stellar remnants will reside in a massive cluster of galaxies at the present day. As we have noted, while these galaxies are rapidly forming stars at $z = 1.46$ and ~ 200–800 Myrs later ($z \sim 1.2$–1.4, depending upon the choice of α_{CO}) this activity is likely to have declined substantially as their gas reservoirs are exhausted (this process will be even quicker if outflows or the further action of environmental processes suggested above accelerate to the removal of gas). These star-formation events may form a significant fraction of the stellar mass of these systems, up to $\sim 10^{11}\,M_{\odot}$ (Ma15), although these estimates are highly uncertain. Hence, we can conclude that the galaxies are likely to be massive at the present day and if their star formation terminates at $z \sim 1.2$–1.4 then their stellar populations will appear old today as this corresponds to a lookback time of ~ 9 Gyrs.

Clusters of galaxies have long been known to house some of the oldest and most massive galaxies seen at the present day, but we can use our (relatively obscuration-free)

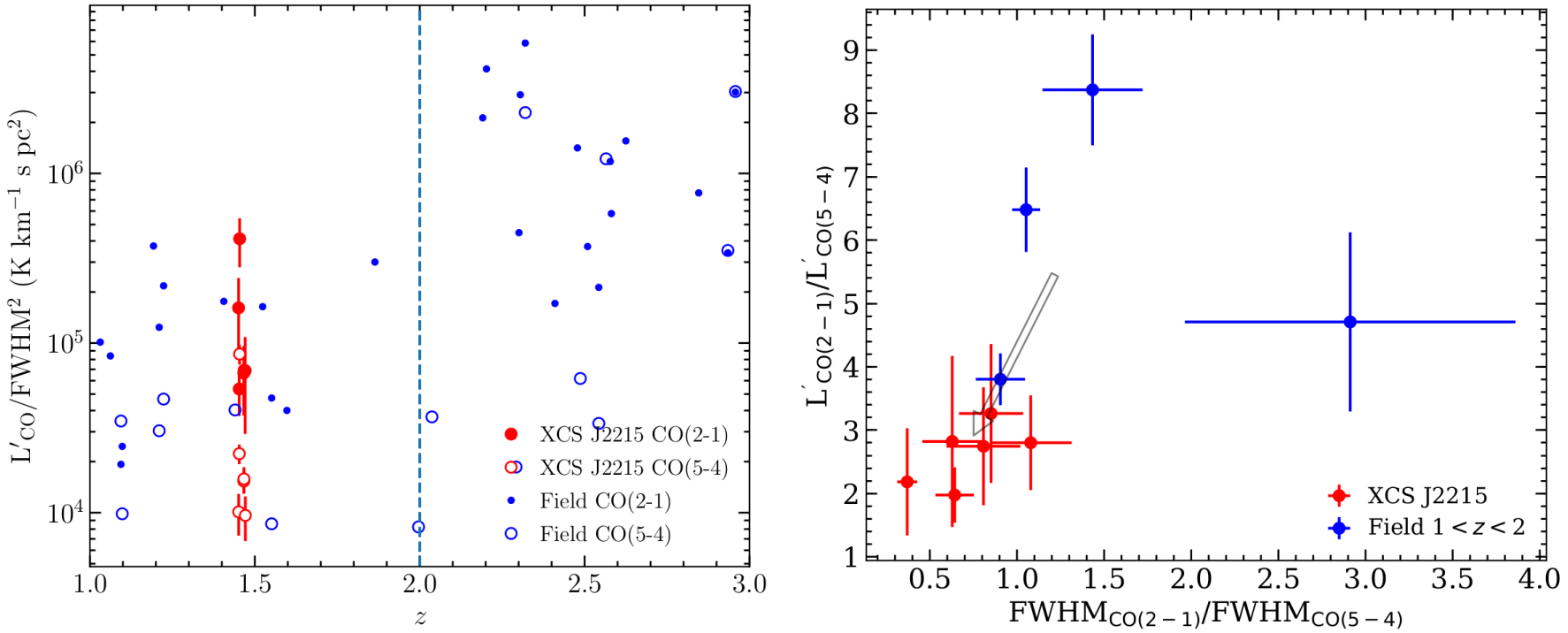

Figure 5.7: (a) Variation of $L'_{CO}/FWHM^2$ as a function of redshift. We take XCS J2215 cluster members and compare them to a field sample from the literature with published ^{12}CO(2–1) and ^{12}CO(5-4) observations. At the cluster's redshift, the galaxies with line detections show similar $L'_{CO}/FWHM^2$ ratios, within errors, to the field samples at their comparable redshift ($z \sim 1$–2) for each CO transition. In the right panel, we show that it is not until you consider the ratio of L' and FWHM for the two transitions that the differences become clear. The dashed line represents our redshift cut for sample field galaxies used in the right-hand plot. (b) Plot of the ratios of the CO line luminosities against the corresponding FWHM of the two CO transitions. As in the left panel we plot the cluster members from XCS J2215 and comparison field sources at a similar redshift from the literature which have both low-J CO detections ((2–1) or (1–0)) and high-J CO detections ((7–6), (6–5), (5–4), or (4–3)) converted to ^{12}CO(2–1) and ^{12}CO(5–4), respectively, using the brightness ratios from Bothwell et al. (2013). We see that the cluster galaxies inhabit the lower left of the plot compared to the small sample of field sources with the relevant observations, suggesting that these galaxies may be comparatively poor in lower-density, cool gas in comparison to the field sample. One possible explanation for this trend is environmental processes stripping of the cooler, less-bound gas from the outskirts of the galaxies. We overlay an arrow indicating the difference in the median values of the field sample to the cluster galaxies to highlight the possible transition of a field galaxy to a cluster galaxy and the resulting effect on the low-J CO line properties.

measures of the dynamical masses of these galaxies to compare them more directly to local early-type galaxies. The lookback time to $z = 1.46$ is 9.3 Gyr, and our expectation is that the galaxies will rapidly exhaust their current gas supplies (and are unlikely to accrete substantial amounts of cold gas from their surroundings). Hence, the stellar populations in their descendants at the present day are likely to have inferred ages of *at least* 9 Gyr. In addition, if we assume the dynamical mass of the galaxies do not change significantly during the 9 Gyr then the width of our Gaussian fits ($\sigma_{\rm Gauss}$) can be converted into an expected velocity dispersion (σ) by comparing the ratio of our mass estimator for disks with a simple virial equation estimator for a spherical mass distribution, giving us a conversion factor of $\sigma \sim 0.3\sigma_{\rm Gauss}$. We compare the expected properties of these galaxies to those of samples of early-type galaxies in local clusters in Fig. 5.8. We see that most (five out of six) of the ^{12}CO-detected LIRGs in XCS J2215 have characteristics similar to those expected for the progenitors of relatively massive early-type galaxies at the present day.

5.6 Conclusions

We have analysed ALMA 1.25 mm and 3 mm and MUSE-GALACSI observations of a ~ 500 kpc diameter region in the core of the $z = 1.46$ cluster, XCS J2215. Our ALMA observations detect 14 luminous 1.25 mm dust continuum sources within this region (Fig. 5.1), representing a $\sim 7\times$ over-density of sources compared to a blank field. We detect line emission from six of the brightest of these sources in the 1.25 mm and 3 mm datacubes and associate these lines with redshifted ^{12}CO(5–4) and ^{12}CO(2–1) transitions (Fig. 5.3). These lines unambiguously identify the millimetre sources as members of the clusters, while five other continuum sources have archival ^{12}CO(2–1) detections that also place them in the cluster. A further two sources have photometric redshifts compatible with them being cluster members, but lack spectroscopic redshifts from either ALMA or MUSE (consistent with the expected field contamination in this map of $\sim$ 1–2 sources).

Together, these results indicate that the vast majority of the millimetre sources are cluster members, and they confirm the intense obscured star formation occurring in the cluster core: $\gtrsim 1000\,M_{\odot}\,{\rm yr}^{-1}$ in a ~ 500 kpc region, suggested by Ma15's earlier

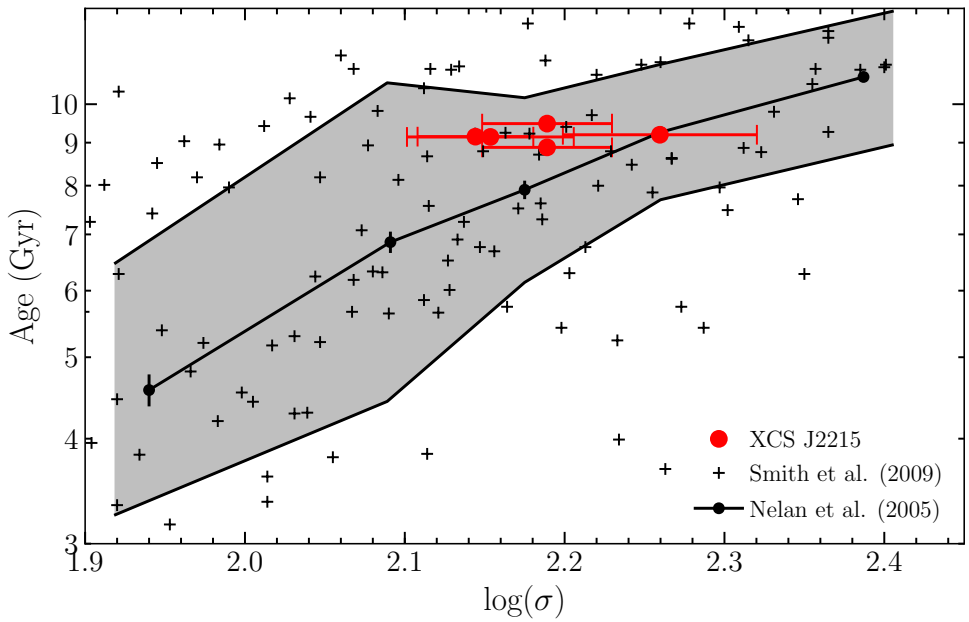

Figure 5.8: A plot of the velocity dispersion of local early-type galaxies to their luminosity-weighted stellar ages, adapted from Nelan et al. (2005). We show the median trend line and dispersion derived by Nelan et al. (2005) and overplot measurements for individual galaxies in the Shapley Supercluster from Smith et al. (2009) to illustrate the scatter. We plot the velocity dispersions derived from the Gaussian fits to the ^{12}CO lines for the six CO-detected millimetre members in the core of XCS J2215, where their adopted age is the lookback time to $z = 1.46$, 9.3 Gyrs. These points therefore lie where they would appear today if the bulk of their stars were formed in the starburst event we are currently witnessing.

SCUBA-2 study. Combining our precise ALMA positions with high-resolution *HST* imaging, we see a high fraction of millimetre continuum-selected galaxies with close companions on $\lesssim 2''$–$3''$scales (Fig. 5.2), suggesting that galaxy–galaxy interactions may be a trigger for their activity, although most of these companions are faint in the K_s band, indicating these are likely to be minor mergers/interactions.

We combine the ^{12}CO(5–4) and ^{12}CO(2–1) line fluxes for the cluster LIRGs to derive a median line brightness ratio, $r_{54/21} = L'_{\rm CO(5-4)}/L'_{\rm CO(2-1)} = 0.37 \pm 0.06$. This is comparable to the median ratio estimated for SMGs and BzK populations at similar and higher redshifts, indicating broadly similar gas excitation in our sample of $z = 1.46$ cluster LIRGs to these high-redshift star-forming populations (Fig. 5.5). We estimate gas masses (assuming $\alpha_{\rm CO} = 1$) of ~ 1–$2.5 \times 10^{10}\,M_{\odot}$ and a median gas consumption time-scale of ~ 200 Myrs. This time-scale is comparable to the time for a galaxy to cross the cluster core and so we anticipate that most of these galaxies will deplete their reservoirs before they exit the region they are currently seen in.

From considering the line-of-sight velocities and cluster centric radii we classify our CO emitters as recently accreted galaxies onto the cluster which has just start undergoing the potential environmental effects from entering the dense cluster environment. We also see a possible trend in terms of the gas and dust properties of the millimetre sources compared to $z \sim 1$–2 field galaxies, which may be pointing to a relative paucity of cool gas and dust in the cluster population: (i) our XCS J2215 galaxies typically have lower ^{12}CO(2–1) luminosities compared to their FWHM than comparable field galaxies, (ii) the line width measured from the ^{12}CO(2–1) is typically smaller than that measured for ^{12}CO(5–4), (iii) at a fixed ^{12}CO(5–4) line luminosity, these galaxies have lower far-infrared luminosities than comparable field galaxies, and (iv) the ratio of the ^{12}CO(2–1) and ^{12}CO(5–4) CO line luminosities and the FWHM suggest that the cluster galaxies contain a larger fraction of warmer, denser ^{12}CO(5–4) gas compared to field galaxies. These trends could be caused by the preferential removal of cooler, lower-density material as a result of an environmental process (possibly ram pressure stripping; Rawle et al. (2012)). Larger samples of cluster galaxies are needed to confirm the reality of this trend.

Finally, we have demonstrated that these galaxies have some of the properties of the

expected progenitors of the massive, early-type galaxies which dominate the high-density regions of rich clusters of galaxies at the present day. Specifically, their dynamical masses and stellar ages roughly match those seen in early-type galaxies in local clusters.

CHAPTER 6

Conclusions and Future Work

This thesis presented the results of investigations into the actively star-forming population in both the field and dense cluster environments in the high redshift Universe. This was achieved through high-resolution ALMA follow-up of SCUBA-2 surveys combined with archival multi-wavelength and spectroscopic surveys of our targets. In this final chapter I summarise the key results from the previous four chapters and the ongoing and future follow-up projects that will contribute to answering the major questions about the sub-millimetre bright population that remain unanswered.

6.1 Summary of the Presented Work

6.1.1 AS2UDS: Data Reduction and Catalogue Creation

Chapter 2 covered the creation of the AS2UDS catalogue, the ALMA detected galaxies in the 716 maps from the high-resolution follow-up of the $>4\,\sigma$ sources in the S2CLS UDS map (Geach et al., 2017). These ALMA maps provided a nearly two orders of magnitude improvement in resolution from the parent SCUBA-2 images ($\sim$15″ to $\sim$0.″2 – 0.″8) which allowed us to accurately identify the individual galaxies contributing to the single-dish source flux. The 716 SCUBA-2 sources were observed with ALMA across four Cycles, with a resulting 708 sub-millimetre galaxy detections and these ALMA maps are presented at the end of the Chapter.

The data reduction for all the maps using CASA and the justification for our *uv*-tapering to create 'detection' maps, which would be more sensitive to the more extended emission

we might expect from previous studies of SMG sizes (Simpson et al., 2015b; Hodge et al., 2016; Ikarashi et al., 2017), was also presented. As well as the data reduction the source extraction method was given in detail: a $> 4.3\,\sigma$ $0\farcs5$ aperture selection based on maximising the number of 'positive' galaxies detected whilst maintaining a 2 % purity threshold.

With the final catalogue we checked whether the positional offset of our AS2UDS SMGs from the parent SCUBA-2 positions were consistent with theoretical expressions given in Ivison et al. (2007). We found that our radial offsets as a function of SCUBA-2 SNR showed a flatter trend than the theoretical expression suggesting that previous attempts to alter the search radii for identifying single-dish counterparts based on the single-dish SNR could potentially result in mis-identifications (e.g. Biggs et al., 2011).

6.1.2 AS2UDS: Number Counts and Multiplicity

Chapter 3 covered the first published results for the AS2UDS survey from an early version of the catalogue. With an order of magnitude increase in the number of detected galaxies in comparison to the previous largest interferometric study (ALESS: Hodge et al., 2013) we better constrained the 870 μm SMG number counts. The differential number counts for galaxies with $S_{870} > 4.0$ (the flux limit to where our survey is complete) were fit with a double power law with a systematically lower normalization by a factor of 1.28 ± 0.02 in comparison to the parent S2CLS sample. A significant contributor to this reduction in the normalization factor is the multiplicity, i.e. where single-dish sources, particularly at the bright end of the S2CLS sample, break up into multiple SMG detections in ALMA.

Across the entire AS2UDS sample 11 ± 1 % of the ALMA maps have multiple SMG detections with $S_{870} \geq 1$ mJy in a region with a projected diameter of ~ 100 kpc at $z = 2$. This rate of multiplicity varies with single-dish flux with 28 ± 2 % of all $S_{850}^{\rm deb} \geq 5$ mJy SCUBA-2 sources breaking into multiples, which increases to 44^{+16}_{-14} % for sources with $S_{850}^{\rm deb} \geq 9$ mJy.

Finally we investigate whether these multiples are physically associated or just chance associations seen in projection. The photometric redshifts of our multiples suggest $\gtrsim 30$ % of our SMG-pairs are physically associated consistent with spectoscopic redshift surveys

of smaller samples of SMG pairs (Wardlow et al., 2018; Hayward et al., 2018). This suggests a significant fraction of our SMGs have elevated star-formation rates due to recent or on-going galaxy merger activity.

6.1.3 AS2UDS: Basic Source Properties

Chapter 4 covers the basic source properties for the final, complete AS2UDS catalogue and introduces the first results from our multi-wavelength SED fitting. To complement the result from Chapter 3 which found that a significant percentage of our SMG pairs are physically associated, we investigate the subset of our SMGs which were covered by CANDELS *HST* imaging. We found that 50 ± 10 % of our SMGs show either a disturbed morphology or have companion galaxies which display similar colours, further suggesting that mergers are a significant driver for the intense star-formation we observe in our SMGs.

Combining our catalogue with the extensive multi-wavelength coverage in the field, allows us to use MAGPHYS to derive photometric redshifts. For our sample we derive a median photometric redshift of $z_{\rm phot} = 2.61 \pm 0.09$ with a high-redshift tail comprising 33^{+3}_{-2} % of SMGs with $z_{\rm phot} > 3$. The significant increase in sample size also provides the most convincing evidence yet for a S_{870} flux density evolution with redshift, which previously could not be identified in the smaller Cycle 1 AS2UDS pilot (Simpson et al., 2015a) or ALESS (Simpson et al., 2014). This trend suggests that our higher redshift SMGs are preferentially more massive, which is possible evidence of 'galaxy downsizing' and this is something we will return to in future work (see: §6.2).

From the high-redshift interpretation of the Sanders et al. (1988) ULIRG evolutionary model we expect a number of our SMGs to exhibit varying levels of AGN activity before their transition into a QSO phase. Therefore we identify AGNs within our catalogue through X-ray detections and IRAC colour-colour selection. The majority of our SMGs do not host an un/moderately-obscured luminous AGN, finding an upper-limit of 28 ± 4 % of our SMGs hosting significant AGNs through IRAC colour selection, a result consistent with previous such studies (Alexander et al., 2005a; Blain et al., 2002; Georgantopoulos et al., 2011; Wang et al., 2013; Franco et al., 2018).

To examine what population the SMGs evolve in to we compare the redshift, stellar mass distribution, and number density of the expected progenitors of $z = 1$–2.5 quiescent galaxies from recent studies (Estrada-Carpenter et al., 2019; Morishita et al., 2018). We find our SMGs are consistent with these constraints with the median mass-weighted ages for our SMGs of $11.4^{+0.1}_{-0.2}$ Gyr compared to the median formation ages for the $z = 1$–2.5 quiescent galaxies of 11.5 ± 0.3 Gyr.

6.1.4 ALMA Survey of XCS J2215

In Chapter 5 we focus on SMGs in dense environments and present the ALMA and MUSE observations in the central ~ 500 kpc diameter region of XCS J2215, a $z = 1.46$ cluster. These observations were targeting four SCUBA-2 sources which, from the high resolution $S_{1.25\,\mathrm{mm}}$ ALMA observations, split into 14 sub-millimetre bright galaxies which is a $\sim 7\times$ over-density of sub-millimetre galaxies in comparison to a 'blank' field. We also detected ^{12}CO(2–1) and ^{12}CO(5–4) for six of these SMGs with a further five galaxies being spectroscopically confirmed as cluster members from our MUSE observations.

As with the AS2UDS SMGs, a significant fraction of these star-forming galaxies either show disturbed morphologies or very close companions galaxies suggesting, again, that galaxy mergers are a likely significant driver for the enhanced star-formation rates observed. The integrated star-formation rate from these galaxies makes the core of XCS J2215 one of the most active cluster cores discovered to date.

From the ^{12}CO line fluxes we estimate gas masses of ~ 1–$2.5 \times 10^{10}\,M_{\odot}$ which, combined with the estimated star-formation rates, results in median gas consumption timescales of ~ 200 Myrs, in agreement with the values derived in Chapter 4 for SMGs. The line fluxes also suggest that these cluster galaxies contain larger fractions of warmer, denser ^{12}CO(5-4) gas than field galaxies at similar redshifts. As the line-of-sight velocities of these galaxies suggest they are recent accretors into the cluster this relative paucity of cooler ^{12}CO(2–1) gas could be a result of ram pressure stripping beginning to preferentially strip the more weakly bound cool gas content of these galaxies as suggested in Rawle et al. (2012).

6.2 Ongoing and Future Work

6.2.1 High Redshift Sub-Millimetre Galaxies

Chapters 2–4, alongside other published work (An et al., 2018; Cooke et al., 2018), present some of the earliest science results from the AS2UDS survey. This catalogue, combined with the deep multi-wavelength coverage in the UKIDSS UDS field, provides us with the most statistically robust sample of SMGs to date. In this section I will briefly cover some of the work that is currently being done with this catalogue and a couple of the follow-up projects that have been allocated telescope time and how they will improve our understanding of these galaxies.

Spatial Clustering of SMGs

One of the primary goals of the AS2UDS survey was to test the proposed evolutionary path between SMGs, QSOs, and the lower redshift massive quiescent galaxies. Evidence for this link has been found from matching photometric redshift distributions and formation ages (as seen in Chapter 4), and black hole and gas masses (e.g. Coppin et al., 2008; Simpson et al., 2012). Another powerful test is to see if these populations match in halo masses, derived through their three-dimensional clustering strength. Previous attempts to measure the clustering of SMGs (e.g. Blain et al., 2004; Williams et al., 2011; Hickox et al., 2012; Wilkinson et al., 2017) have relied on radio/mid-infrared counterpart identification to single-dish sub-millimetre sources, which are known to be incomplete and suffer from mis-identifications. For example, Hickox et al. (2012) measured the clustering strength for SMGs from the radio/mid-infrared SMG counterparts identified in Biggs et al. (2011), however follow-up ALMA observations of the single-dish sources in Hodge et al. (2013) found that the radio/mid-infrared selection was only 55 % complete. Therefore in an upcoming paper we can apply the method used in Hickox et al. (2012), which utilises the probability distribution functions (PDFs) for the photometric redshifts of our galaxies, to provide the most robust clustering measurements for SMGs yet using our AS2UDS catalogue which has accurate SMG positions across a survey area and sample size that are each a factor > 100 larger than before. From this we can test whether

this clustering strength is consistent with that of $z \sim 2$ QSOs and the quiescent massive galaxies at $z \sim$1–3, a requirement for the proposed evolutionary path.

Spectroscopic Follow-up of AS2UDS SMGs

The MAGPHYS photometric redshifts are effective for constraining overall trends within the AS2UDS catalogue even though the uncertainties for each individual source may be large. However for accurate constraints and the detailed study of individual galaxy properties then spectroscopic redshifts are required. Therefore with the sub-arcsecond positional accuracy of our catalogue combined with the photometric redshift estimators a number of follow-up telescope proposals have been allocated observing time to obtain spectroscopic redshifts.

One such recent follow-up has been NOEMA observations of the 10 brightest *unlensed* AS2UDS SMGs to search for ^{12}CO transition lines. Millimetre interferometers, such as NOEMA, are particularly well-suited for this task as traditional optical/near-infrared spectroscopy have been found to return poor yields of redshifts for the brightest SMGs (Danielson et al., 2017) as the dust content responsible for their far-infrared brightness also results in these galaxies being extremely faint in the optical bands. Obtaining spectroscopic redshifts for our brightest galaxies (and faintest) is particularly important because as we showed in Figure 4.5, from our photometric redshifts we observe a trend of increasing redshift for our brighter sources. To truly test the validity of this trend requires reducing the largest sources of errors in that trend, which is the photometric redshift errors for brightest and faintest galaxies.

In addition these ^{12}CO detections provide not only spectroscopic redshifts but, as shown in Chapter 5, the line properties can also be used to estimate molecular and dynamical masses which can be combined with star-formation rate estimators to return gas depletion timescales. The bandwidth coverage with NOEMA for these observations is also wide enough (32 GHz) that the galaxies with redshifts $z > 3$ should return multiple ^{12}CO (and/or [CI]) transition lines from which the CO excitation can be estimated as in Figure 5.5 for our cluster ULIRGs. The results of these NOEMA observation will be published in J. Birkin et al. (in prep.).

More recently we have been allocated a large program of 245 hours of observations with KMOS (KAOSS, ID: 1103.A-0182 PI: I. Smail) to obtain spectroscopic redshifts for 545 ALMA-identified SMGs. The bulk of the targeted SMGs will be from our AS2UDS catalogue with additional KMOS pointings targeting the brightest sources of the pilot AS2COSMOS survey (similar to the AS2UDS pilot except for the 160 brightest sources from the latest SCUBA-2 COSMOS field map, J. Simpson et al. submitted) and ALESS sources. This will increase the total number of SMGs with spectroscopic redshifts by $\sim 3\times$ and is an order of magnitude increase in size to previous spectroscopic surveys of homogeneously selected SMGs (e.g. Danielson et al., 2017).

These KMOS observations will significantly improve the precision of our clustering measurements by providing accurate redshifts for roughly half of our SMGs in the UDS field, thus reducing the increase in the uncertainties added from using the photometric redshift PDFs. The near-infrared spectroscopy will also supplement our X-ray and IRAC colour-colour selection of AGNs described in §4.4.4, by identifying AGN activity through the redshifted restframe-optical line ratios of Hα, [OIII], Hβ, and [NII] (e.g. Harrison et al., 2016). These spectra will provide significantly more insight into the relative contributions of the starbursting and AGN activity of the galaxies than the sub-millimetre continuum detections alone could, as described in Chapter 4, by providing further constraints on the physical properties of the SMGs such as their gas masses. Their should be a significant number of galaxies covered by the survey, both *with* significant AGN activity and without, that potential trends in these derived properties can be found.

As KMOS is an integral field unit (IFU) we expect that, for the brightest of our SMGs with the most significant detections in the near-infrared, we can derive the dynamics of their gas. There is a wealth of information that can be derived from this but I will list a couple of examples relevant to work in the previous chapters. Firstly we can separate galaxies between those that are rotationally supported and those with disturbed morphologies, beyond the region of the UDS field covered by CANDELS (see §4.4) which has implications for what is triggering the SMG phase in these galaxies. Secondly it can provide a measurement for the total mass of the galaxies, and with a statistically significant sample size the trends of this mass with redshift could potentially be found and compared

to the results from Chapter 4 of potential 'galaxy downsizing' in our SMGs.

6.2.2 Cluster ULIRGs

Following our survey of XCS J2215 the most obvious continuation of this work was to increase our sample size of $z \sim 1-1.6$ clusters observed with ALMA. In Cycle 5 we targeted the millimetre continuum and ^{12}CO(5-4) for an additional 12 SCUBA-2 sources in two additional clusters from our SCUBA-2 cluster survey (Cooke et al. submitted), RXJ 0152.7-1357 at $z = 0.83$ and XDCPJ 0044.0-2033 at $z = 1.58$. These two clusters were selected due to being both observable with ALMA, and that their SCUBA-2 maps showed extensive star-formation activity (as with XCS J2215). The aim of these observations were to precisely identify the individual SMGs and from their ^{12}CO(5-4) detections confirm their membership to the cluster. As in Chapter 5 the CO line profiles allow us to determine the dynamics and dynamical masses for these cluster galaxies. We can compare these to our larger AS2UDS population for further evidence of 'galaxy downsizing', as we expect the higher-redshift SMGs could be progenitors to the most massive ellipticals in clusters. This data has been reduced and from early source-finding we see $\sim$21 millimetre continuum detections with ^{12}CO detections in six galaxies, which approximately doubles our sample size from Chapter 5, this work will be presented in Stach et al. (in prep.).

We have also begun to complement our ALMA observation of cluster ULIRGs with KMOS near-infrared IFU observations. Recently we have obtained KMOS follow-up of the ALMA detected galaxies in XCS J2215 from Chapter 5 with the aim to measure the dynamics and distribution of this star-forming population from the Hα emission lines. Also, as we noted above, we expect these galaxies to be stripped of material during their interactions with the dense cluster core gas and these Hα maps can further test this by comparing our cluster Hα sizes at fixed circular velocities against the wealth of similar IFU observations at these redshifts for field galaxies (e.g. Tiley et al., 2016). With ALMA observations of a further two clusters mentioned above we hope to extend the KMOS follow-up to their newly detected star-forming populations.

6.2.3 Next Generation Instruments

In the future, complimenting ALMA, will be a number of new telescopes operating at wavelengths suitable for follow-up observations of dusty star-forming galaxies, e.g.:

- For ground-based single-dish observations, the Cerro Chajnantor Atacama Telescope-prime telescope (CCAT-p) is set for first light in 2021 operating at millimetre/sub-millimetre wavelengths, 220–860 GHz (1.4 mm–350 μm). This will be a 6 m aperture telescope designed for very wide field-of-view observations ($\sim$1.3° diameter FoV) but limited in resolution due to the modest sized aperture. CCAT-p will therefore map sub-millimetre emission on scales impractical for ALMA and to depths greater than the confusion-limited *Herschel* surveys. One of the primary goals of CCAT-p is to provide an extensive survey of the dust-obscured star-formation activity of the distant universe through planned 350 μm micron surveys covering $\sim$100 deg^2 which will be combined with optical surveys to detect a predicted $\sim$600,000 galaxies with robust measurements of their infra-red emission sampled close to the peak of their dust emission SED.

- Longer wavelength radio interferometry is set for a radical improvement over current arrays with the Square-Kilometre Array (SKA). The deployment of SKA will be phased, with the first phase consisting of 197 dishes operating at 350 MHz–15.3 GHz in the southern hemisphere with maximum baselines of 150 km to provide sub-arcsecond resolutions with fields of view with diameter $\sim$10–100 arcmin and a lower frequency companion operating at 50–350 MHz consisting of $\sim$131,000 antennae with maximum baselines of 65 km. There is a myriad of potential science goals with the SKA (e.g. Takeuchi et al., 2016; Keane, 2017; De Zotti et al., 2018; Paragi et al., 2019) and with just a basic increase in the depths obtainable with this array there will be an opening up of direct detections of higher redshift SMGs that were undetected by the JVLA (Chapman et al., 2005). Whilst the longer wavelength observations of the SKA do not benefit from a negative K-correction they are also not biased against detection of galaxies with higher dust temperatures, which we know ALMA 870 μm surveys are insensitive to (Chapman et al., 2005). Therefore

SKA can efficiently map regions in combination with ALMA to provide a more complete picture of the sub-millimetre bright population.

- The James Webb Space Telescope (JWST) will be the flagship infrared space observatory when it is set to launch in 2021. It will be equipped with a 6.5 m primary mirror with four instruments: Mid-Infrared Instrument (MIRI) which is both a mid-infrared camera and spectrometer operating at 5–27 μm, Near-infrared Camera (NIRCam) an infrared imager for 0.6–5.0 μm, NIRSpec which is a multi-object spectrometer able to image up to 100 objects in a 9 square-arcminute field of view and the Near InfraRed Imager and Slitless Spectrograph (NIRISS) which compliments NIRSpec as a low resolution but wide field spectrometer operating at 0.8–5.0 μm. JWST will enable sub-arcsecond resolution near-infrared observations of SMGs at rest-frame optical-NIR wavelengths from which the resolved structure of the dust emission in SMGs can be measured out to high redshifts where current *HST* observations return non-detections.

6.3 Concluding Remarks

In the last 20 years, the samples of sub-millimetre galaxies has grown from the first detections of several gravitationally-lensed, high redshift galaxies in clusters to extensive multi-wavelength coverage of thousands of galaxies across entire galactic fields, and from images of blended 15″ sources to galaxies with sub-arcsecond resolved continuum. Advances in instrumentation have created an effective combination of large field-of-view, but poor resolution, single-dish surveys in the sub-millimetre which can then be followed up by sub-millimetre interferometers, which suffer from small primary beam areas but which can achieve high angular resolutions.

These surveys have confirmed SMGs as a population of some of the most actively star-forming galaxies discovered, with star-formation rates that can reach $>1000\,M_{\odot}$ yr^{-1}, and with a redshift distribution that peaks between $z = 2-3$, therefore they are significant contributors to the era of peak stellar mass assembly in the Universe. However there are still a number of key questions about core properties of the SMG population that have yet

to be answered. For instance, we still don't completely understand the physical triggers for the high luminosities/star-formation rates in SMGs. In Chapters 3 and 4 we show a significant percentage of SMGs appear to have close companions and/or show disturbed morphologies that indicate merger-driven triggering and other studies have found markers for mergers from the majority of their sample to an almost negligent percentage of their samples. Progress on this can be made through future IFU surveys of ALMA detected SMGs to determine their spatially resolved kinematics and in the future the James Webb Space Telescope (*JWST*) could potentially be an effective instrument for efficiently determining the morphologies of large samples of SMGs and thus better constrain the merger-driven fraction of SMGs.

Developments in instrumentation have made it viable to recover spectroscopic redshifts for SMGs in large samples, a traditionally inefficient task. With KMOS currently and *JWST* in the future we can start to obtain larger samples for our SMGs. These will be required for determining the most accurate clustering measurements to check their role in the evolution of local elliptical galaxies. In addition NIR spectroscopy can provide another measure of the AGN contributions to our SMGs, aiding our understanding of the co-evolution of the black-hole and host spheroid mass.

Since their initial discovery, considerable observing time has been invested to create larger samples of SMGs with each successive generation of instrument. In the last few years ALMA has provided us with the most detailed imaging of robustly identified SMGs from which their multi-wavelength properties can be derived. Using ALMA, the work in this thesis is just the first steps to fully characterise the properties of both the largest single sample of robustly identified SMGs to date and the actively star-forming population of high redshift clusters. A necessary contribution to the field and the stepping stone to future detailed studies and follow-up observations which will improve our understanding of these dusty star-forming galaxies.

Appendix A

A.1 AS2UDS Catalogue

Table A.1: The AS2UDS Catalogue. The ALMA_ID comprises a 4-digit numbers giving the field identifier from the parent S2CLS survey and a final digit which identifies the individual galaxies detected from each S2CLS source with ascending numbers for descending flux. The source co-ordinates are the source centroids from SEXTRACTOR from the *uv*-tapered detection maps. Field rms is the sigma-clipped rms across the entire map and are plotted in Figure 2.5. PB Correction gives the primary beam-correction factor at each source location, a higher number indicating galaxies further away from the ALMA phase centre. The S2CLS Flux columns lists the flux-deboosted 850 μm flux from Geach et al. (2017). The Aper SNR column is the $0\farcs5$ diameter aperture flux SNR used to select of galaxies in the catalogue and the Final Flux is the $1\farcs0$ diameter aperture flux of the galaxy with the primary beam, aperture, and flux boosting corrections applied. The complete catalogue also contains information on which ALMA cycles the galaxies were observed, the individual flux corrections and the restoring beam properties of the maps.

ALMA ID	Field RMS	SMG RA	SMG Dec	SNR	PB Corr	Flux	Flux Err
	mJy	(J2000)	(J2000)			mJy	mJy
0001.0	0.38	34.6277	-5.5254	35.7	1.01	30.2	0.86
0001.1	0.38	34.6272	-5.5230	4.46	1.91	5.23	1.24
0002.0	0.32	34.6005	-5.3820	18.7	1.03	7.73	0.48
0002.1	0.32	34.6010	-5.3824	17.5	1.10	7.44	0.51
0003.0	0.23	34.8381	-4.9475	24.8	1.18	7.88	0.36
0003.1	0.23	34.8369	-4.9480	9.84	1.68	4.44	0.49
0003.2	0.23	34.8391	-4.9469	4.72	1.15	1.14	0.28
0004.0	0.24	34.1996	-5.0249	22.3	1.05	7.73	0.36
0005.0	0.28	34.3567	-5.4260	11.4	1.10	4.38	0.42
0005.1	0.28	34.3571	-5.4281	10.4	1.20	4.04	0.45
0005.2	0.28	34.3575	-5.4270	7.42	1.00	2.35	0.36
0006.0	0.22	34.5235	-5.1804	26.7	1.08	7.30	0.30
0006.1	0.22	34.5210	-5.1795	4.99	1.81	2.27	0.42
0007.0	0.26	34.3768	-5.3229	29.7	1.00	9.89	0.38
0008.0	0.29	34.5125	-5.4783	22.8	1.02	8.87	0.41
0009.0	0.33	34.1821	-5.2982	19.1	1.00	10.1	0.64
0010.0	0.38	33.9831	-4.9190	14.8	1.02	10.2	0.82
0010.1	0.38	33.9821	-4.9188	5.50	1.28	4.30	0.91

Continued on next page

Table A.1 – continued from previous page

ALMA ID	Field RMS	SMG RA	SMG Dec	SNR	PB Corr	Flux	Flux Err
0011.0	0.36	34.1284	-5.4009	21.8	1.00	11.1	0.65
0012.0	0.39	34.5148	-4.9242	17.0	1.00	10.3	0.73
0013.0	0.22	34.8523	-4.8833	24.8	1.01	6.15	0.28
0013.1	0.22	34.8525	-4.8824	6.35	1.04	1.39	0.25
0014.0	0.34	34.4344	-5.3357	23.0	1.00	11.8	0.64
0015.0	0.23	34.7086	-5.4570	13.8	1.40	5.61	0.45
0015.1	0.23	34.7095	-5.4547	7.84	1.12	2.35	0.34
0016.0	0.17	34.0488	-5.0149	37.9	1.01	9.42	0.30
0017.0	0.22	34.3211	-5.5573	26.4	1.01	6.58	0.29
0017.1	0.22	34.3215	-5.5590	5.43	1.62	1.51	0.41
0018.0	0.34	34.3776	-4.9935	14.5	1.01	8.01	0.70
0019.0	0.18	33.9796	-5.4157	39.5	1.18	13.6	0.41
0020.0	0.24	34.5299	-4.7371	12.4	1.11	3.56	0.33
0020.1	0.24	34.5299	-4.7363	8.62	1.07	2.16	0.30
0021.0	0.16	34.8594	-4.8702	21.4	1.01	5.49	0.27
0022.0	0.28	34.5988	-5.1940	17.9	1.07	6.71	0.44
0023.0	0.26	34.7010	-5.3014	22.5	1.07	6.70	0.35
0024.0	0.23	34.1712	-5.0642	26.0	1.00	6.95	0.31
0025.0	0.31	34.4794	-4.7899	8.07	1.08	4.20	0.57
0025.1	0.31	34.4792	-4.7895	7.80	1.11	3.93	0.58
0026.0	0.32	34.7587	-5.4824	19.5	1.03	9.97	0.65
0027.0	0.22	34.7914	-5.0023	22.6	1.02	6.01	0.28
0028.0	0.32	34.4254	-4.9410	15.5	1.00	7.85	0.68
0028.1	0.32	34.4256	-4.9412	6.21	1.00	3.04	0.62
0029.0	0.34	34.8631	-4.7517	17.1	1.08	10.1	0.65
0030.0	0.17	34.1681	-5.2272	25.2	1.00	5.57	0.27
0030.1	0.17	34.1687	-5.2272	6.96	1.00	1.32	0.25
0031.0	0.35	34.4158	-5.4885	16.9	1.00	9.44	0.73
0032.0	0.16	34.2999	-4.7215	40.2	1.09	9.96	0.30
0033.0	0.27	34.5850	-5.5286	14.9	1.01	4.83	0.36
0033.1	0.27	34.5867	-5.5274	4.51	1.67	2.44	0.47
0033.2	0.27	34.5846	-5.5282	6.15	1.00	1.92	0.31
0034.0	0.17	34.1597	-5.0226	20.8	1.02	5.19	0.28
0035.0	0.19	34.1690	-5.1830	17.0	1.01	4.99	0.34
0036.0	0.17	34.3638	-5.1118	16.3	1.06	4.72	0.31
0037.0	0.36	34.1911	-5.0630	8.28	1.08	4.19	0.73

Continued on next page

Table A.1 – continued from previous page

ALMA ID	Field RMS	SMG RA	SMG Dec	SNR	PB Corr	Flux	Flux Err
0038.0	0.19	34.7780	-5.3660	32.7	1.00	7.70	0.29
0038.1	0.19	34.7790	-5.3665	5.33	1.06	1.20	0.25
0039.0	0.23	34.7905	-5.2584	20.8	1.06	5.84	0.30
0040.0	0.21	34.1326	-5.4393	25.1	1.04	6.92	0.35
0040.1	0.21	34.1333	-5.4402	8.12	1.03	2.37	0.32
0041.0	0.32	34.7302	-5.2357	7.70	1.06	3.99	0.64
0042.0	0.33	34.4607	-5.5164	12.0	1.02	6.09	0.68
0043.0	0.34	34.8058	-5.3129	8.70	1.02	4.22	0.65
0043.1	0.34	34.8056	-5.3136	4.41	1.01	2.40	0.55
0044.0	0.20	34.4783	-5.3897	16.6	1.42	5.29	0.34
0045.0	0.32	34.7430	-5.3688	8.77	1.04	4.18	0.58
0045.1	0.32	34.7432	-5.3691	4.38	1.05	2.05	0.48
0046.0	0.33	34.2206	-5.3524	16.1	1.00	7.66	0.63
0046.1	0.33	34.2201	-5.3512	6.06	1.21	2.89	0.69
0047.0	0.25	34.0927	-5.1854	17.2	1.26	6.91	0.42
0047.1	0.25	34.0928	-5.1866	4.47	1.66	1.89	0.43
0048.0	0.31	34.1252	-5.3695	14.1	1.04	6.95	0.65
0048.1	0.31	34.1246	-5.3679	4.47	1.69	2.91	0.87
0049.0	0.31	34.5927	-5.4973	12.7	1.09	6.37	0.62
0050.0	0.31	34.6473	-5.2717	19.0	1.00	8.00	0.60
0051.0	0.28	34.8534	-5.1557	16.1	1.03	6.28	0.41
0052.0	0.20	34.4118	-4.5594	28.1	1.09	8.82	0.32
0053.0	0.38	34.1278	-5.4413	10.5	1.03	5.58	0.71
0053.1	0.38	34.1272	-5.4423	5.03	1.11	2.38	0.67
0054.0	0.32	34.8866	-5.0763	13.5	1.08	6.78	0.63
0055.0	0.31	34.3740	-5.0551	12.1	1.12	5.53	0.55
0056.0	0.31	34.7572	-5.1863	8.62	1.22	4.87	0.73
0056.1	0.31	34.7578	-5.1874	5.50	1.00	2.00	0.56
0057.0	0.31	34.8181	-5.3005	6.94	1.01	3.94	0.64
0058.0	0.17	34.0856	-4.8481	25.1	1.12	6.51	0.33
0058.1	0.17	34.0866	-4.8494	10.1	1.11	2.67	0.31
0059.0	0.35	34.8404	-4.8516	13.5	1.04	6.72	0.68
0060.0	0.36	34.2475	-5.1821	11.3	1.05	6.52	0.61
0061.0	0.35	34.2136	-5.2502	10.9	1.00	5.50	0.63
0062.0	0.20	34.1922	-5.4671	20.3	1.04	5.38	0.35
0063.0	0.33	34.1294	-4.9222	14.2	1.09	8.07	0.67

Continued on next page

Table A.1 – continued from previous page

ALMA ID	Field RMS	SMG RA	SMG Dec	SNR	PB Corr	Flux	Flux Err
0064.0	0.37	34.7869	-5.2319	13.5	1.01	7.39	0.75
0065.0	0.31	34.7181	-4.7127	7.15	1.00	3.20	0.48
0066.0	0.37	34.9269	-5.3010	14.9	1.00	7.60	0.72
0067.0	0.37	34.5686	-4.9191	16.4	1.10	10.8	0.80
0068.0	0.32	34.6158	-4.9769	6.59	1.05	3.76	0.65
0069.0	0.26	34.3397	-5.3188	9.35	1.45	3.86	0.49
0069.1	0.26	34.3415	-5.3193	5.76	1.47	2.41	0.45
0070.0	0.30	34.7582	-4.9610	12.2	1.08	6.68	0.62
0071.0	0.19	34.3653	-5.2943	20.4	1.00	6.03	0.31
0072.0	0.37	34.6537	-5.2982	14.3	1.04	8.19	0.76
0073.0	0.17	34.4000	-5.3429	35.1	1.04	8.78	0.30
0074.0	0.31	34.1853	-5.0393	14.3	1.03	6.40	0.55
0075.0	0.17	34.8175	-5.4357	29.6	1.00	7.12	0.29
0076.0	0.33	34.8075	-5.3300	12.0	1.06	6.56	0.63
0077.0	0.32	34.3055	-4.9826	9.52	1.16	5.16	0.74
0078.0	0.23	34.0838	-5.2906	17.3	1.33	5.71	0.36
0079.0	0.17	34.5576	-4.9620	31.0	1.01	6.94	0.27
0080.0	0.32	34.5312	-5.4953	11.6	1.07	5.65	0.62
0081.0	0.32	34.6542	-4.9287	6.63	1.03	2.98	0.50
0082.0	0.32	34.8032	-5.2125	11.0	1.00	5.21	0.54
0083.0	0.32	34.1877	-5.2388	10.4	1.22	5.52	0.76
0084.0	0.33	34.3366	-4.8304	10.3	1.01	5.30	0.57
0085.0	0.31	34.9062	-5.2241	14.1	1.01	6.77	0.55
0086.0	0.16	34.3323	-4.8155	16.7	1.00	3.87	0.27
0087.0	0.16	34.1710	-5.0201	29.2	1.07	6.28	0.27
0088.0	0.34	34.6819	-4.6512	11.0	1.23	7.29	0.86
0089.0	0.34	34.9103	-5.1474	13.0	1.02	6.40	0.60
0090.0	0.20	34.1452	-5.5017	19.4	1.00	4.60	0.30
0090.1	0.20	34.1445	-5.5033	6.09	1.42	1.73	0.38
0091.0	0.32	34.2080	-5.4496	6.51	1.05	3.12	0.55
0092.0	0.36	34.6905	-5.2221	13.5	1.00	7.12	0.69
0093.0	0.40	33.9838	-5.3515	13.6	1.00	9.08	0.90
0095.0	0.22	34.8922	-4.7439	19.1	1.03	5.70	0.35
0095.1	0.22	34.8924	-4.7442	15.2	1.00	4.14	0.34
0096.0	0.34	34.5785	-4.8414	15.6	1.01	8.30	0.69
0097.0	0.38	34.8679	-5.2059	8.41	1.00	5.01	0.74

Continued on next page

Table A.1 – continued from previous page

ALMA ID	Field RMS	SMG RA	SMG Dec	SNR	PB Corr	Flux	Flux Err
0098.0	0.33	34.3560	-4.6453	11.3	1.01	5.13	0.59
0098.1	0.33	34.3546	-4.6463	5.98	1.26	3.48	0.67
0099.0	0.30	34.4051	-4.7980	12.9	1.15	5.72	0.61
0100.0	0.29	34.6595	-5.0550	13.6	1.06	6.26	0.53
0102.0	0.31	34.9261	-4.9052	9.63	1.00	5.12	0.60
0102.1	0.31	34.9263	-4.9056	4.54	1.05	1.57	0.54
0103.0	0.38	34.3528	-4.6743	14.5	1.19	9.40	0.86
0104.0	0.18	34.0947	-5.4148	21.1	1.00	5.58	0.31
0105.0	0.36	34.6511	-5.1694	5.77	1.18	3.58	0.73
0105.1	0.36	34.6503	-5.1703	4.58	1.46	3.18	0.81
0105.2	0.36	34.6514	-5.1701	4.89	1.04	2.21	0.62
0106.0	0.37	34.4971	-5.0845	11.4	1.01	7.23	0.79
0107.0	0.36	34.3547	-5.1097	17.5	1.03	9.38	0.70
0108.0	0.37	34.8458	-4.9007	6.31	1.37	4.71	0.99
0109.0	0.32	34.0765	-5.3722	8.86	1.32	5.52	0.74
0109.1	0.32	34.0793	-5.3731	4.40	1.23	2.63	0.56
0110.0	0.33	34.3779	-5.5421	10.5	1.00	5.41	0.68
0111.0	0.17	34.4120	-5.0911	17.8	1.06	4.47	0.29
0112.0	0.32	33.9205	-5.2225	18.0	1.07	7.92	0.61
0113.0	0.20	34.4188	-5.2196	13.7	1.50	5.09	0.46
0113.1	0.20	34.4213	-5.2208	10.4	1.09	2.88	0.32
0114.0	0.21	34.8049	-4.7855	16.0	1.07	3.77	0.26
0114.1	0.21	34.8049	-4.7847	5.04	1.00	1.02	0.20
0115.0	0.36	34.5119	-5.0086	9.73	1.07	5.53	0.73
0116.0	0.32	34.3334	-5.2182	12.0	1.05	6.04	0.56
0117.0	0.20	34.7861	-4.9898	7.22	1.23	2.48	0.40
0118.0	0.31	33.9803	-5.3533	10.9	1.02	5.43	0.53
0119.0	0.32	34.2630	-4.7215	8.23	1.00	4.39	0.63
0120.0	0.37	34.4257	-5.4296	10.5	1.04	5.45	0.69
0121.0	0.36	34.5457	-4.8296	7.43	1.15	5.04	0.80
0121.1	0.36	34.5458	-4.8310	5.22	1.00	2.57	0.65
0122.0	0.30	34.5402	-5.3120	7.34	1.64	4.30	0.85
0123.0	0.35	34.3247	-4.7036	7.60	1.03	5.04	0.62
0123.1	0.35	34.3248	-4.7029	5.64	1.06	3.47	0.62
0124.0	0.33	34.5903	-5.3770	11.0	1.00	5.32	0.65
0125.0	0.29	34.3632	-5.1994	9.95	1.01	4.59	0.51

Continued on next page

Table A.1 – continued from previous page

ALMA ID	Field RMS	SMG RA	SMG Dec	SNR	PB Corr	Flux	Flux Err
0126.0	0.15	33.9445	-5.3136	38.1	1.27	11.2	0.35
0127.0	0.35	34.2293	-5.4954	10.7	1.00	5.66	0.62
0128.0	0.15	34.3142	-4.9654	20.6	1.13	5.41	0.31
0128.1	0.15	34.3152	-4.9665	4.30	1.05	0.93	0.22
0129.0	0.36	34.6976	-5.4690	8.48	1.03	5.15	0.71
0130.0	0.20	34.0728	-5.3470	11.5	1.13	3.58	0.37
0132.0	0.15	34.6948	-5.0373	31.1	1.06	6.54	0.25
0133.0	0.32	34.3677	-5.4273	4.87	1.05	2.56	0.53
0134.0	0.31	34.1856	-5.0341	11.6	1.18	6.59	0.75
0135.0	0.17	34.2353	-4.6747	33.1	1.08	8.81	0.32
0136.0	0.31	34.3973	-5.4770	7.55	1.12	2.97	0.64
0136.1	0.31	34.3971	-5.4764	4.35	1.15	2.12	0.56
0137.0	0.20	34.8172	-5.0130	21.6	1.14	5.90	0.35
0137.1	0.20	34.8181	-5.0132	5.37	1.00	1.22	0.25
0138.0	0.32	34.6830	-5.4437	10.5	1.01	5.21	0.62
0139.0	0.32	34.8916	-4.9755	4.63	1.21	2.48	0.69
0139.1	0.32	34.8903	-4.9777	4.50	1.21	2.30	0.69
0140.0	0.36	34.9200	-4.7887	8.01	1.24	5.46	0.88
0141.0	0.38	34.2654	-5.2776	10.8	1.04	5.95	0.80
0142.0	0.18	34.6123	-5.4163	12.1	1.00	3.79	0.34
0142.1	0.18	34.6121	-5.4155	8.06	1.06	2.29	0.34
0143.0	0.17	34.1472	-5.1122	14.5	1.00	3.33	0.31
0144.0	0.30	34.7229	-5.4859	7.41	1.00	2.97	0.50
0144.1	0.30	34.7228	-5.4864	5.52	1.00	1.83	0.46
0145.0	0.32	34.0426	-4.8950	5.18	1.33	2.72	0.77
0146.0	0.35	34.5443	-5.5815	19.1	1.00	9.22	0.60
0147.0	0.17	34.0934	-5.5151	16.9	1.07	4.42	0.34
0147.1	0.17	34.0941	-5.5133	11.6	1.19	3.87	0.37
0148.0	0.18	34.8080	-5.0149	7.83	1.05	2.46	0.29
0149.0	0.33	34.5929	-5.1269	11.5	1.06	5.11	0.54
0150.0	0.30	34.9655	-5.1754	7.98	1.04	3.82	0.56
0151.0	0.19	34.1629	-5.4483	19.7	1.01	4.56	0.29
0152.0	0.31	34.2959	-5.2126	5.18	1.29	2.66	0.60
0153.0	0.32	34.4081	-5.2640	8.11	1.00	3.21	0.51
0154.0	0.40	34.1455	-5.0992	9.03	1.06	7.24	0.84
0155.0	0.20	34.5462	-5.3665	5.80	1.04	1.43	0.27

Continued on next page

Table A.1 – continued from previous page

ALMA ID	Field RMS	SMG RA	SMG Dec	SNR	PB Corr	Flux	Flux Err
0155.1	0.20	34.5464	-5.3667	6.44	1.09	1.44	0.30
0156.0	0.35	34.6567	-5.2709	5.46	1.12	4.11	0.65
0157.0	0.21	34.0135	-4.9120	20.6	1.04	5.34	0.35
0158.0	0.32	34.1480	-5.1518	11.8	1.00	5.19	0.60
0159.0	0.37	34.6727	-5.2261	9.59	1.05	6.32	0.84
0160.0	0.38	34.7229	-5.0470	6.80	1.00	4.35	0.74
0161.0	0.34	34.3865	-5.2751	5.96	1.04	3.24	0.67
0162.0	0.21	34.2643	-5.2642	15.9	1.42	5.47	0.47
0162.1	0.21	34.2660	-5.2651	4.97	1.01	1.15	0.27
0163.0	0.18	34.8797	-4.9743	11.9	1.00	2.85	0.30
0163.1	0.18	34.8789	-4.9739	6.14	1.03	1.75	0.28
0163.2	0.18	34.8790	-4.9738	6.07	1.02	1.66	0.27
0164.0	0.38	34.4824	-5.5043	10.1	1.03	5.88	0.76
0165.0	0.33	34.8158	-4.7356	11.4	1.00	4.59	0.58
0166.0	0.38	34.6778	-4.9922	11.3	1.01	7.11	0.82
0167.0	0.32	34.1410	-5.0452	11.8	1.04	4.87	0.57
0168.0	0.38	33.9655	-5.3725	4.65	1.27	3.06	0.77
0169.0	0.31	34.5327	-5.4303	10.6	1.15	5.93	0.64
0170.0	0.31	34.5119	-4.9450	5.38	1.21	3.64	0.59
0171.0	0.30	34.4423	-4.7964	8.60	1.03	4.06	0.56
0172.0	0.32	34.3657	-5.6197	11.6	1.05	5.05	0.63
0172.1	0.32	34.3663	-5.6201	4.79	1.01	1.77	0.53
0173.0	0.21	34.3850	-5.2141	16.2	1.01	4.59	0.38
0174.0	0.33	34.3019	-5.3325	4.55	1.08	2.39	0.57
0175.0	0.18	34.3079	-5.3215	20.1	1.03	4.90	0.28
0175.1	0.18	34.3093	-5.3230	4.41	1.26	1.01	0.27
0176.0	0.32	34.7479	-4.7166	9.14	1.01	4.04	0.54
0178.0	0.32	33.9289	-5.1721	10.3	1.22	5.61	0.66
0179.0	0.30	34.1339	-5.3773	9.19	1.01	3.84	0.55
0179.1	0.30	34.1335	-5.3784	4.62	1.19	2.10	0.54
0180.0	0.35	34.6114	-4.6542	6.91	1.12	4.49	0.68
0181.0	0.21	34.4040	-5.5699	11.9	1.01	3.73	0.35
0181.1	0.21	34.4053	-5.5692	4.37	1.11	0.89	0.33
0182.0	0.17	34.0477	-5.1329	15.3	1.21	4.50	0.34
0183.0	0.18	34.5076	-5.0866	19.4	1.00	4.97	0.33
0184.0	0.08	34.5213	-5.0813	13.2	1.15	1.57	0.12

Continued on next page

Table A.1 – continued from previous page

ALMA ID	Field RMS	SMG RA	SMG Dec	SNR	PB Corr	Flux	Flux Err
0184.1	0.08	34.5207	-5.0837	8.53	1.28	0.99	0.13
0185.0	0.36	34.6100	-4.7435	13.2	1.00	7.04	0.71
0186.0	0.16	34.2008	-4.9832	22.6	1.04	5.49	0.26
0187.0	0.33	34.0440	-5.4286	9.83	1.05	4.53	0.66
0187.1	0.33	34.0424	-5.4262	4.31	1.74	3.21	0.93
0189.0	0.17	34.0814	-5.1658	19.0	1.03	4.91	0.30
0190.0	0.31	34.4325	-5.4456	6.65	1.07	3.26	0.55
0191.0	0.16	34.2824	-5.5357	17.8	1.08	4.60	0.29
0192.0	0.33	34.5255	-4.6583	13.1	1.06	6.18	0.58
0193.0	0.34	34.1435	-5.4034	5.97	1.22	3.73	0.72
0194.0	0.31	34.3490	-5.6060	14.8	1.00	7.10	0.64
0195.0	0.31	34.1324	-4.9478	5.13	1.01	2.52	0.57
0196.0	0.21	34.3087	-5.3636	7.50	1.09	2.30	0.38
0196.1	0.21	34.3078	-5.3637	5.66	1.41	2.00	0.46
0197.0	0.17	34.8739	-4.9775	8.58	1.03	1.82	0.28
0198.0	0.08	34.1766	-5.1352	11.7	1.56	0.58	0.16
0198.1	0.08	34.1777	-5.1354	7.13	1.08	1.13	0.11
0198.2	0.08	34.1807	-5.1358	8.27	1.79	1.08	0.19
0198.3	0.08	34.1774	-5.1363	4.72	1.18	0.91	0.12
0199.0	0.38	34.8455	-5.2496	9.49	1.01	5.78	0.75
0201.0	0.31	34.1747	-5.1178	8.99	1.03	4.72	0.62
0202.0	0.20	34.3820	-4.8389	17.6	1.04	5.43	0.39
0203.0	0.32	34.4111	-5.0609	11.4	1.04	5.75	0.66
0204.0	0.37	34.3317	-4.7961	7.42	1.06	5.02	0.73
0205.0	0.31	34.3439	-5.4782	14.9	1.00	6.27	0.60
0206.0	0.30	34.4985	-4.7804	7.62	1.33	3.24	0.62
0207.0	0.32	34.2635	-5.4771	5.75	1.00	2.63	0.54
0208.0	0.39	34.7620	-4.9948	7.44	1.02	4.04	0.74
0209.0	0.32	34.7830	-4.9001	10.8	1.02	5.05	0.58
0210.0	0.30	34.2515	-4.7268	13.4	1.25	6.83	0.72
0211.0	0.32	34.8904	-4.9562	8.64	1.03	3.62	0.52
0212.0	0.38	34.3524	-4.9782	9.29	1.00	5.11	0.73
0213.0	0.32	34.0351	-5.0966	11.2	1.05	5.92	0.68
0214.0	0.27	34.2603	-4.9555	7.46	1.54	3.22	0.49
0215.0	0.35	34.1844	-5.0499	11.8	1.00	6.49	0.65
0216.0	0.31	34.3554	-5.5548	4.65	1.30	2.35	0.58

Continued on next page

Table A.1 – continued from previous page

ALMA ID	Field RMS	SMG RA	SMG Dec	SNR	PB Corr	Flux	Flux Err
0217.0	0.17	34.8627	-5.1643	15.0	1.07	3.70	0.33
0218.0	0.32	34.6387	-4.9686	12.5	1.00	6.08	0.58
0219.0	0.39	34.0711	-5.0053	8.20	1.01	5.79	0.86
0220.0	0.31	34.1955	-4.7524	14.1	1.14	7.26	0.64
0221.0	0.37	34.3310	-5.3848	5.56	1.11	3.04	0.78
0222.0	0.16	34.9753	-5.1914	30.1	1.00	5.98	0.26
0223.0	0.32	34.7628	-5.4460	6.80	1.09	3.39	0.63
0224.0	0.31	34.3601	-5.5257	12.2	1.00	5.65	0.60
0225.0	0.32	34.7696	-5.4319	10.6	1.00	4.18	0.53
0226.0	0.20	34.4334	-4.7194	15.3	1.00	3.74	0.31
0227.0	0.16	34.8488	-5.0310	14.5	1.12	3.43	0.26
0228.0	0.18	34.2697	-4.6611	16.8	1.11	4.64	0.34
0229.0	0.32	34.7649	-5.4225	4.39	1.80	3.07	0.76
0229.1	0.32	34.7620	-5.4228	6.26	1.03	2.84	0.49
0230.0	0.25	34.9238	-5.3512	11.1	1.03	3.33	0.40
0230.1	0.25	34.9240	-5.3509	7.05	1.00	1.94	0.37
0231.0	0.36	34.7202	-4.6400	12.1	1.05	7.58	0.73
0232.0	0.17	33.9777	-4.9571	21.3	1.00	4.55	0.27
0233.0	0.31	34.7893	-5.1637	8.94	1.03	3.90	0.57
0234.0	0.37	34.1947	-5.1051	7.42	1.31	5.88	0.97
0235.0	0.15	33.9475	-5.1328	21.1	1.35	6.74	0.38
0236.0	0.38	34.3858	-4.8406	9.18	1.00	4.82	0.74
0237.0	0.33	34.3321	-5.2880	5.71	1.04	2.97	0.58
0238.0	0.31	34.7436	-5.2329	9.06	1.02	4.01	0.62
0239.0	0.33	34.6816	-5.4667	4.84	1.16	3.09	0.65
0240.0	0.20	34.4629	-4.8028	10.7	1.04	3.00	0.32
0241.0	0.30	34.4876	-5.1846	5.10	1.14	2.22	0.53
0242.0	0.35	34.6922	-5.0701	8.18	1.16	4.61	0.75
0242.1	0.35	34.6903	-5.0679	4.75	1.42	2.41	0.83
0243.0	0.15	34.0746	-5.1219	17.2	1.11	4.29	0.30
0244.0	0.33	34.5871	-5.4323	6.60	1.13	3.72	0.72
0245.0	0.38	34.7863	-5.3265	7.06	1.01	3.36	0.67
0246.0	0.32	34.2837	-4.9353	10.6	1.00	4.43	0.57
0247.0	0.32	34.1309	-5.1977	7.33	1.11	3.76	0.56
0248.0	0.39	33.9081	-5.0839	7.59	1.36	5.60	1.05
0249.0	0.16	34.4103	-5.5519	5.31	1.00	0.94	0.23

Continued on next page

Table A.1 – continued from previous page

ALMA ID	Field RMS	SMG RA	SMG Dec	SNR	PB Corr	Flux	Flux Err
0250.0	0.32	34.2028	-5.1211	7.36	1.08	3.27	0.58
0251.0	0.17	34.5792	-5.0240	11.6	1.02	2.39	0.28
0252.0	0.40	34.8823	-5.0201	5.56	1.00	2.77	0.68
0253.0	0.33	34.1775	-4.8164	4.61	1.10	1.17	0.57
0254.0	0.38	34.7683	-4.9539	7.82	1.04	5.37	0.73
0255.0	0.19	34.1763	-5.2608	16.5	1.12	4.95	0.35
0256.0	0.33	34.3727	-5.5973	4.47	1.13	1.91	0.58
0257.0	0.38	34.5695	-5.2625	6.21	1.05	3.08	0.78
0258.0	0.08	34.2417	-5.2796	12.8	1.14	1.22	0.12
0258.1	0.08	34.2400	-5.2822	8.29	1.63	1.12	0.18
0259.0	0.18	34.4005	-5.2555	19.1	1.02	4.66	0.30
0260.0	0.32	34.0532	-4.9223	7.75	1.16	3.87	0.63
0261.0	0.19	34.5278	-5.4649	13.6	1.00	3.58	0.29
0262.0	0.18	33.9948	-4.9781	12.8	1.25	4.61	0.37
0263.0	0.38	34.2691	-4.7389	6.69	1.17	5.63	0.81
0264.0	0.32	34.5536	-4.9560	7.75	1.00	3.27	0.54
0264.1	0.32	34.5541	-4.9563	4.66	1.00	1.69	0.46
0265.0	0.30	34.6680	-5.3223	9.92	1.03	3.73	0.58
0266.0	0.36	34.4657	-5.1639	9.35	1.02	4.22	0.71
0267.0	0.32	34.0088	-5.3621	6.31	1.15	3.16	0.61
0267.1	0.32	34.0088	-5.3613	4.67	1.14	2.55	0.60
0268.0	0.21	34.6407	-5.1721	15.8	1.07	4.49	0.33
0269.0	0.32	34.3440	-4.6750	10.0	1.11	4.76	0.65
0270.0	0.32	34.6259	-5.0225	7.73	1.03	3.16	0.55
0271.0	0.36	34.4693	-5.2009	6.76	1.02	3.92	0.71
0272.0	0.31	34.4611	-5.2013	11.8	1.00	5.08	0.53
0274.0	0.21	34.1196	-4.8636	9.78	1.03	2.65	0.35
0275.0	0.08	34.4030	-5.4004	18.3	1.26	1.85	0.13
0276.0	0.20	34.5996	-5.1397	4.47	1.44	1.50	0.38
0276.1	0.20	34.5999	-5.1365	4.81	1.27	1.40	0.34
0277.0	0.21	34.2400	-5.3440	4.61	1.52	1.37	0.34
0278.0	0.31	34.3982	-4.7164	11.2	1.01	3.92	0.55
0279.0	0.31	34.1182	-4.7946	8.48	1.22	3.85	0.61
0280.0	0.19	34.4692	-5.3625	11.5	1.03	2.91	0.31
0281.0	0.37	34.3975	-5.2976	5.87	1.00	3.73	0.67
0282.0	0.08	34.2004	-4.9332	14.6	1.12	1.45	0.12

Continued on next page

Table A.1 – continued from previous page

ALMA ID	Field RMS	SMG RA	SMG Dec	SNR	PB Corr	Flux	Flux Err
0283.0	0.39	34.8096	-4.9959	6.46	1.00	3.92	0.72
0284.0	0.37	34.8866	-5.1312	7.74	1.10	3.95	0.76
0285.0	0.20	34.4428	-4.9110	4.58	1.11	1.30	0.30
0286.0	0.38	34.6618	-5.3547	10.5	1.05	6.86	0.81
0287.0	0.08	34.3643	-5.2508	9.98	1.01	0.97	0.12
0287.1	0.08	34.3652	-5.2507	8.86	1.00	0.81	0.12
0288.0	0.27	33.9117	-4.9285	13.0	1.11	5.16	0.46
0289.0	0.32	34.4464	-4.9404	5.07	1.02	2.23	0.51
0290.0	0.24	33.9998	-5.4430	17.3	1.02	5.01	0.35
0291.0	0.35	34.5895	-4.7087	5.59	1.09	3.06	0.72
0292.0	0.33	34.3226	-5.2300	4.78	1.12	2.41	0.56
0294.0	0.18	34.1207	-4.7643	5.88	1.93	3.07	0.56
0294.1	0.18	34.1228	-4.7648	7.16	1.00	1.81	0.30
0295.0	0.18	34.8335	-5.2094	4.52	1.00	0.96	0.26
0296.0	0.20	34.9138	-5.3870	27.7	1.03	6.82	0.31
0297.0	0.30	34.3857	-5.1989	10.8	1.08	4.35	0.56
0298.0	0.18	34.4339	-4.9302	16.0	1.03	4.05	0.29
0299.0	0.31	33.9965	-5.1055	4.36	1.19	2.08	0.57
0300.0	0.39	34.0821	-4.8448	5.31	1.03	3.80	0.75
0301.0	0.16	34.4641	-5.1085	18.7	1.04	4.03	0.24
0302.0	0.32	34.9623	-5.1109	11.6	1.01	4.92	0.58
0303.0	0.20	34.9073	-5.0869	9.89	1.00	2.35	0.30
0304.0	0.19	34.8516	-5.4487	19.1	1.10	4.75	0.30
0305.0	0.20	34.4609	-5.1956	18.8	1.00	4.70	0.32
0306.0	0.16	34.4393	-5.0311	16.4	1.06	3.61	0.25
0307.0	0.08	34.3634	-5.3648	14.8	1.30	1.46	0.12
0308.0	0.36	34.3410	-5.2404	5.78	1.01	3.18	0.61
0309.0	0.31	34.1402	-4.8653	6.42	1.10	2.78	0.55
0310.0	0.17	34.4740	-5.1830	14.2	1.05	3.36	0.30
0311.0	0.38	34.4685	-5.1823	9.59	1.04	5.82	0.75
0312.0	0.33	34.6166	-4.7289	7.87	1.21	4.53	0.75
0313.0	0.16	34.8893	-5.3903	14.1	1.14	3.25	0.28
0314.0	0.32	34.0574	-5.0745	6.34	1.08	2.57	0.62
0315.0	0.20	34.4918	-4.9884	17.6	1.11	5.25	0.35
0316.0	0.36	34.2146	-5.5109	10.6	1.04	5.95	0.64
0317.0	0.31	34.1642	-5.0645	8.36	1.10	3.79	0.64

Continued on next page

Table A.1 – continued from previous page

ALMA ID	Field RMS	SMG RA	SMG Dec	SNR	PB Corr	Flux	Flux Err
0318.0	0.30	33.9321	-5.0135	11.0	1.14	5.78	0.58
0319.0	0.32	34.5129	-5.4592	8.87	1.08	4.69	0.53
0320.0	0.36	34.0168	-4.9315	9.60	1.00	5.06	0.63
0321.0	0.38	34.5559	-4.6359	10.7	1.07	6.42	0.74
0322.0	0.08	34.2797	-5.1667	15.9	1.06	1.60	0.11
0322.1	0.08	34.2801	-5.1670	8.32	1.01	0.73	0.10
0324.0	0.32	34.7348	-5.1637	8.20	1.29	5.06	0.79
0325.0	0.32	34.5031	-5.1266	9.41	1.02	4.12	0.57
0326.0	0.32	34.8243	-5.2781	5.58	1.06	2.22	0.55
0327.0	0.31	34.8422	-5.2398	5.75	1.00	2.39	0.46
0328.0	0.20	34.4077	-5.6277	21.2	1.03	5.88	0.32
0329.0	0.17	34.1743	-5.2266	15.5	1.22	4.04	0.32
0330.0	0.31	34.1404	-5.2632	9.26	1.04	4.69	0.57
0331.0	0.39	34.2553	-5.3657	8.04	1.22	5.87	0.97
0332.0	0.17	34.5306	-4.8276	9.05	1.26	2.58	0.32
0333.0	0.37	34.5285	-4.9882	5.20	1.08	2.76	0.70
0334.0	0.08	34.0898	-4.9311	14.8	1.23	1.76	0.13
0335.0	0.33	34.8865	-5.2690	5.52	1.17	2.93	0.63
0336.0	0.30	34.0631	-4.8259	10.3	1.04	4.53	0.63
0337.0	0.31	34.5620	-4.9011	9.50	1.06	4.55	0.55
0338.0	0.33	34.0932	-5.0805	6.62	1.03	2.74	0.52
0339.0	0.17	34.4190	-4.6319	4.69	1.85	1.66	0.42
0339.1	0.17	34.4195	-4.6327	5.68	1.22	1.38	0.29
0340.0	0.36	34.1875	-5.2217	5.98	1.31	4.07	0.84
0341.0	0.31	34.5096	-5.6189	7.12	1.12	2.62	0.57
0342.0	0.39	33.9897	-5.1120	5.75	1.55	5.00	1.06
0343.0	0.32	34.3742	-5.5844	13.6	1.03	6.92	0.65
0344.0	0.31	34.1275	-4.8548	4.45	1.09	2.42	0.50
0345.0	0.31	34.5152	-4.9918	5.21	1.05	2.59	0.56
0346.0	0.20	34.2735	-5.2513	14.5	1.00	3.64	0.33
0347.0	0.33	33.9583	-5.2930	9.41	1.24	5.62	0.77
0348.0	0.33	34.2590	-4.6707	9.95	1.19	5.16	0.70
0350.0	0.30	34.0003	-4.9940	7.39	1.27	4.13	0.62
0351.0	0.17	33.9695	-5.2453	10.5	1.15	2.69	0.31
0352.0	0.38	34.9143	-4.9702	5.60	1.00	3.07	0.73
0353.0	0.15	34.7745	-4.9385	17.2	1.14	4.14	0.30

Continued on next page

Table A.1 – continued from previous page

ALMA ID	Field RMS	SMG RA	SMG Dec	SNR	PB Corr	Flux	Flux Err
0354.0	0.36	34.6574	-4.9807	6.80	1.00	3.65	0.69
0355.0	0.37	34.3061	-4.7876	7.05	1.17	4.25	0.82
0357.0	0.31	34.1745	-4.9329	6.50	1.09	2.96	0.59
0361.0	0.39	34.4322	-5.0539	4.76	1.03	2.70	0.64
0362.0	0.31	34.6962	-4.8902	6.09	1.12	2.27	0.61
0365.0	0.31	34.0483	-5.0014	5.24	1.29	2.59	0.61
0366.0	0.33	34.6920	-4.7155	4.71	1.00	2.15	0.55
0367.0	0.39	34.3269	-4.7155	4.63	1.27	2.42	0.86
0368.0	0.38	34.1921	-5.1839	10.3	1.06	6.69	0.85
0369.0	0.17	34.3390	-4.6682	16.0	1.35	5.19	0.35
0370.0	0.26	34.4863	-4.8774	13.7	1.00	4.05	0.32
0371.0	0.17	34.4097	-5.3767	6.97	1.08	1.95	0.28
0373.0	0.30	34.8797	-5.3009	7.53	1.00	3.41	0.48
0374.0	0.31	34.8794	-5.3660	12.6	1.02	5.52	0.58
0375.0	0.32	34.0976	-5.4630	5.61	1.09	2.47	0.54
0376.0	0.33	34.0006	-4.9384	5.57	1.77	4.81	0.90
0376.1	0.33	33.9972	-4.9383	7.97	1.24	4.00	0.69
0377.0	0.32	33.9341	-5.1951	11.7	1.01	6.06	0.58
0379.0	0.17	34.0161	-5.3381	10.6	1.02	2.62	0.27
0381.0	0.19	34.3511	-4.8823	5.99	1.00	1.69	0.27
0382.0	0.30	34.3382	-5.2539	6.05	1.18	3.09	0.61
0384.0	0.30	34.4820	-5.5558	4.90	1.16	2.11	0.55
0385.0	0.15	34.7540	-4.6854	14.7	1.02	3.92	0.27
0386.0	0.37	34.5932	-5.3078	5.98	1.00	3.13	0.67
0388.0	0.33	34.2472	-5.4082	6.21	1.11	3.07	0.55
0389.0	0.32	34.8105	-4.7269	10.0	1.08	4.81	0.60
0390.0	0.16	34.4215	-4.7475	12.7	1.01	2.69	0.25
0392.0	0.39	34.7781	-5.0205	6.64	1.09	4.24	0.83
0393.0	0.35	34.0822	-5.3722	5.54	1.01	2.95	0.60
0394.0	0.41	34.0873	-5.5020	4.32	1.14	3.22	0.79
0395.0	0.16	34.3523	-4.7586	24.6	1.00	4.87	0.24
0396.0	0.38	34.8615	-5.2735	8.74	1.03	4.39	0.68
0397.0	0.32	34.9255	-4.9589	6.42	1.31	3.21	0.63
0398.0	0.33	34.1856	-5.4670	6.89	1.00	3.62	0.66
0399.0	0.37	34.5611	-5.5175	7.36	1.05	4.98	0.75
0400.0	0.31	34.3426	-5.5435	9.08	1.04	4.07	0.57

Continued on next page

Table A.1 – continued from previous page

ALMA ID	Field RMS	SMG RA	SMG Dec	SNR	PB Corr	Flux	Flux Err
0401.0	0.26	33.9231	-5.2769	7.94	1.77	4.72	0.61
0402.0	0.20	34.8127	-5.0362	13.4	1.02	3.22	0.32
0403.0	0.31	34.4219	-5.5373	9.51	1.11	4.47	0.65
0405.0	0.31	34.2464	-4.8949	7.78	1.21	4.01	0.61
0406.0	0.33	34.0050	-4.8791	5.56	1.00	2.47	0.51
0407.0	0.31	34.6807	-5.3365	6.40	1.12	3.30	0.66
0409.0	0.30	34.1066	-5.0736	11.6	1.03	5.16	0.54
0409.1	0.30	34.1064	-5.0711	4.54	1.94	3.43	0.82
0410.0	0.16	34.6921	-5.1026	7.83	1.51	2.55	0.39
0410.1	0.16	34.6946	-5.1052	6.67	1.39	1.83	0.35
0412.0	0.16	34.4223	-5.1810	15.3	1.13	4.11	0.31
0413.0	0.30	34.2554	-4.9553	9.84	1.05	3.81	0.56
0414.0	0.32	34.4744	-5.4432	8.69	1.00	3.43	0.51
0415.0	0.38	34.0566	-4.7838	6.43	1.18	3.28	0.81
0416.0	0.20	34.5993	-4.8598	10.9	1.01	2.96	0.31
0417.0	0.32	34.0326	-5.1282	8.64	1.15	4.65	0.66
0419.0	0.37	34.4104	-5.1820	4.34	1.15	2.33	0.69
0420.0	0.31	34.4141	-5.5700	4.42	1.01	2.47	0.52
0421.0	0.31	34.4560	-5.5023	7.73	1.00	3.27	0.58
0423.0	0.39	34.2818	-5.5194	5.92	1.08	3.89	0.76
0424.0	0.38	34.4801	-5.1125	11.2	1.01	6.07	0.70
0425.0	0.15	34.2716	-5.4707	25.5	1.00	5.46	0.25
0426.0	0.20	34.9229	-5.0258	4.93	1.22	1.71	0.35
0427.0	0.31	34.3010	-5.2880	5.19	1.02	2.43	0.54
0428.0	0.39	34.7961	-4.9426	8.15	1.01	4.67	0.76
0431.0	0.19	34.3490	-4.5872	8.49	1.53	3.23	0.44
0431.1	0.19	34.3492	-4.5872	7.14	1.42	2.60	0.39
0432.0	0.35	34.1723	-4.7920	9.41	1.05	4.87	0.65
0436.0	0.17	34.0398	-4.9308	4.38	1.19	0.98	0.25
0437.0	0.40	34.7420	-5.3313	7.15	1.01	4.12	0.66
0438.0	0.33	34.6024	-5.5301	10.2	1.31	6.47	0.76
0439.0	0.38	34.5998	-5.5355	11.1	1.02	6.57	0.74
0440.0	0.32	34.4034	-5.3920	12.9	1.11	7.11	0.67
0441.0	0.38	34.4905	-5.1102	4.68	1.14	2.48	0.79
0442.0	0.30	34.2669	-5.5528	9.06	1.06	3.94	0.56
0444.0	0.33	34.4503	-5.4261	10.3	1.01	4.81	0.56

Continued on next page

Table A.1 – continued from previous page

ALMA ID	Field RMS	SMG RA	SMG Dec	SNR	PB Corr	Flux	Flux Err
0445.0	0.39	34.4759	-5.0255	6.39	1.26	4.44	0.84
0446.0	0.37	34.8725	-5.1774	4.93	1.01	2.51	0.67
0447.0	0.18	34.9067	-5.2866	19.2	1.08	4.48	0.30
0450.0	0.33	34.4515	-5.5910	6.31	1.16	2.73	0.58
0450.1	0.33	34.4523	-5.5927	4.69	1.07	1.94	0.48
0451.0	0.32	34.7816	-5.0052	5.87	1.13	2.68	0.58
0453.0	0.17	34.4354	-4.8493	8.18	1.54	2.61	0.39
0453.1	0.17	34.4322	-4.8496	7.11	1.21	1.82	0.30
0454.0	0.32	34.4410	-5.0157	9.08	1.06	3.95	0.65
0455.0	0.31	34.8556	-5.1319	7.51	1.05	3.39	0.55
0456.0	0.38	34.8861	-4.9814	5.94	1.02	3.51	0.73
0457.0	0.38	34.8675	-5.3674	4.46	1.02	1.95	0.66
0458.0	0.31	34.7304	-5.3758	7.21	1.31	3.57	0.66
0459.0	0.31	34.1235	-5.2479	4.33	1.06	1.80	0.51
0460.0	0.37	34.7308	-5.3158	5.61	1.74	4.74	1.08
0460.1	0.37	34.7323	-5.3157	6.03	1.04	3.12	0.67
0461.0	0.31	34.8562	-4.9967	6.37	1.03	2.35	0.57
0462.0	0.31	34.5132	-5.3191	10.2	1.02	4.77	0.57
0463.0	0.29	34.8812	-5.0020	4.63	1.23	1.97	0.57
0465.0	0.32	34.4718	-4.8309	12.8	1.02	5.81	0.64
0467.0	0.39	34.3839	-4.7637	6.53	1.02	4.52	0.77
0470.0	0.36	34.5707	-5.3811	9.78	1.00	4.87	0.72
0473.0	0.33	34.7578	-4.6653	7.44	1.14	4.07	0.69
0474.0	0.38	34.1074	-4.9571	7.91	1.00	4.31	0.71
0475.0	0.31	34.1511	-5.5463	7.69	1.35	5.34	0.89
0477.0	0.33	34.5318	-5.5941	5.31	1.91	3.75	0.94
0479.0	0.16	34.4178	-4.9572	16.7	1.20	4.45	0.33
0480.0	0.30	34.4005	-4.9308	6.00	1.11	2.60	0.48
0481.0	0.17	34.3904	-4.7887	17.4	1.00	3.97	0.28
0481.1	0.17	34.3892	-4.7899	7.98	1.29	2.15	0.34
0481.2	0.17	34.3895	-4.7873	4.46	1.61	1.31	0.36
0483.0	0.17	34.6795	-5.4731	12.9	1.00	3.11	0.29
0484.0	0.33	34.1853	-5.5755	11.6	1.08	5.58	0.63
0485.0	0.39	34.5338	-5.5237	8.69	1.09	5.82	0.81
0486.0	0.16	34.1473	-5.3365	15.3	1.08	3.92	0.29
0487.0	0.21	34.0522	-4.9886	11.4	1.09	3.58	0.36

Continued on next page

Table A.1 – continued from previous page

ALMA ID	Field RMS	SMG RA	SMG Dec	SNR	PB Corr	Flux	Flux Err
0489.0	0.21	34.8364	-5.3764	11.3	1.07	2.94	0.32
0490.0	0.38	34.4260	-5.3073	4.71	1.10	2.72	0.60
0490.1	0.38	34.4251	-5.3066	6.30	1.07	2.98	0.66
0491.0	0.20	34.0049	-5.2751	9.13	1.20	3.01	0.43
0492.0	0.38	34.5398	-5.0334	5.77	1.00	2.76	0.68
0493.0	0.37	34.8740	-4.7715	4.75	1.01	2.25	0.63
0494.0	0.31	34.8952	-4.9082	8.48	1.00	3.65	0.53
0495.0	0.17	34.4137	-4.8998	9.54	1.00	2.32	0.25
0496.0	0.31	34.6643	-4.9972	4.91	1.09	2.17	0.57
0497.0	0.16	34.5836	-5.3653	12.4	1.01	2.37	0.23
0498.0	0.19	34.5808	-5.3582	5.40	1.10	1.39	0.34
0498.1	0.19	34.5808	-5.3591	5.63	1.00	1.37	0.32
0500.0	0.31	34.5357	-5.2121	5.19	1.09	1.57	0.50
0502.0	0.22	33.9567	-5.3688	8.39	1.16	3.90	0.55
0503.0	0.38	34.1595	-5.1294	5.52	1.05	3.54	0.74
0505.0	0.33	34.4456	-5.2280	7.88	1.00	3.82	0.55
0506.0	0.21	34.0637	-4.7697	16.7	1.00	4.26	0.33
0508.0	0.39	34.7401	-4.7385	6.01	1.28	4.63	0.83
0509.0	0.32	34.2421	-5.1473	5.54	1.14	3.03	0.62
0509.1	0.32	34.2425	-5.1473	5.69	1.04	2.63	0.56
0510.0	0.34	34.0129	-5.0435	5.65	1.04	2.73	0.62
0512.0	0.38	33.9254	-5.2111	7.91	1.00	4.10	0.76
0513.0	0.32	34.5181	-5.5676	8.54	1.04	3.64	0.62
0514.0	0.19	34.5426	-5.3653	12.1	1.04	2.96	0.31
0515.0	0.31	34.1953	-5.2277	7.87	1.10	3.89	0.53
0516.0	0.33	34.2846	-5.1202	6.65	1.13	3.90	0.64
0517.0	0.19	34.3640	-4.5687	13.8	1.09	3.76	0.30
0518.0	0.22	34.9585	-4.8599	10.1	1.01	3.75	0.42
0519.0	0.30	34.4273	-5.4834	5.16	1.81	3.55	0.88
0520.0	0.31	34.4512	-4.6075	11.3	1.06	6.05	0.62
0521.0	0.21	34.1686	-4.8470	15.7	1.16	4.47	0.38
0523.0	0.33	34.7218	-5.1871	7.35	1.07	4.03	0.58
0524.0	0.31	34.4778	-4.7365	7.86	1.16	4.12	0.65
0529.0	0.45	34.9085	-5.1071	7.27	1.10	5.05	0.79
0530.0	0.44	34.8366	-4.9164	4.64	1.26	3.14	0.76
0531.0	0.33	34.8023	-5.4547	9.26	1.10	4.91	0.69

Continued on next page

Table A.1 – continued from previous page

ALMA ID	Field RMS	SMG RA	SMG Dec	SNR	PB Corr	Flux	Flux Err
0532.0	0.38	34.8020	-5.4620	7.22	1.07	4.07	0.68
0533.0	0.47	34.0890	-4.9725	5.18	1.10	3.09	0.79
0534.0	0.21	34.3423	-4.9400	9.69	1.00	2.60	0.29
0535.0	0.40	34.5554	-5.5080	4.41	1.04	2.41	0.54
0536.0	0.19	34.2338	-5.5412	15.0	1.00	3.45	0.28
0537.0	0.40	34.9816	-5.0864	8.57	1.11	5.62	0.93
0539.0	0.46	34.2101	-5.1711	6.36	1.19	4.71	0.85
0541.0	0.19	34.8734	-4.9134	7.53	1.02	2.16	0.36
0542.0	0.32	34.7829	-4.7232	5.01	1.07	2.42	0.60
0544.0	0.18	34.3491	-4.9111	15.9	1.05	3.93	0.29
0545.0	0.20	34.2181	-4.9104	6.66	1.06	1.49	0.30
0546.0	0.20	34.2237	-4.9575	7.31	1.44	2.55	0.47
0547.0	0.25	34.3986	-5.6056	13.8	1.05	4.36	0.37
0548.0	0.19	34.0152	-5.3421	6.85	1.06	1.93	0.27
0549.0	0.20	34.9407	-4.9386	5.60	1.00	0.93	0.25
0550.0	0.26	34.8044	-5.0565	11.2	1.31	4.85	0.46
0551.0	0.25	34.6838	-5.4859	7.69	1.33	3.32	0.45
0551.1	0.25	34.6817	-5.4834	4.50	1.37	1.72	0.41
0552.0	0.23	34.0534	-4.7761	8.33	1.00	3.46	0.43
0553.0	0.26	34.6232	-5.3519	6.56	1.13	2.01	0.39
0556.0	0.19	34.7189	-5.2207	5.54	1.20	1.42	0.32
0557.0	0.22	34.4897	-4.8497	15.3	1.03	5.23	0.35
0558.0	0.26	34.1702	-5.2585	10.5	1.00	4.21	0.44
0559.0	0.20	34.7000	-4.9086	5.25	1.41	1.47	0.34
0560.0	0.25	34.5772	-5.5763	10.0	1.34	3.74	0.46
0562.0	0.19	34.7097	-4.7763	9.94	1.00	2.53	0.28
0562.1	0.19	34.7098	-4.7770	6.48	1.05	1.42	0.27
0563.0	0.19	34.0363	-5.2183	5.33	1.17	1.62	0.34
0564.0	0.26	34.7242	-4.9897	4.87	1.89	3.48	0.69
0564.1	0.26	34.7234	-4.9922	6.76	1.00	2.66	0.40
0565.0	0.20	34.7187	-4.9897	6.90	1.01	2.05	0.36
0566.0	0.23	34.8022	-4.7923	9.49	1.00	3.46	0.42
0567.0	0.21	34.5138	-5.4715	10.1	1.00	2.62	0.34
0568.0	0.20	34.6668	-5.3349	4.54	1.11	1.19	0.28
0570.0	0.20	34.1996	-4.9947	11.3	1.08	2.93	0.32
0571.0	0.20	34.4860	-4.8392	7.56	1.00	1.32	0.25

Continued on next page

Table A.1 – continued from previous page

ALMA ID	Field RMS	SMG RA	SMG Dec	SNR	PB Corr	Flux	Flux Err
0572.0	0.19	34.6594	-5.1445	15.9	1.03	3.65	0.29
0573.0	0.20	34.0700	-5.2149	11.9	1.07	3.10	0.32
0575.0	0.17	34.6725	-5.4960	8.40	1.32	2.47	0.34
0576.0	0.26	34.0442	-4.8448	7.66	1.29	3.70	0.51
0577.0	0.20	33.9509	-4.8705	11.5	1.56	4.38	0.49
0578.0	0.18	34.2176	-5.1265	7.93	1.02	1.98	0.28
0579.0	0.22	34.9135	-5.0041	6.75	1.59	3.44	0.54
0579.1	0.22	34.9146	-5.0053	4.74	1.04	1.20	0.32
0581.0	0.26	34.4058	-5.5351	4.66	1.04	1.70	0.38
0582.0	0.19	34.1636	-5.4238	4.80	1.87	1.68	0.41
0582.1	0.19	34.1648	-5.4259	6.27	1.11	1.39	0.27
0583.0	0.26	34.5160	-5.2111	8.44	1.09	3.12	0.43
0585.0	0.20	34.6967	-5.2096	11.2	1.14	3.25	0.33
0586.0	0.22	34.2072	-5.2432	8.19	1.00	2.44	0.36
0588.0	0.23	34.4166	-5.0209	5.91	1.00	1.89	0.33
0590.0	0.17	34.7282	-5.2851	12.7	1.03	3.32	0.32
0593.0	0.25	33.9434	-5.1789	12.7	1.25	5.12	0.43
0594.0	0.20	34.1634	-5.1401	11.0	1.02	2.58	0.30
0595.0	0.19	34.4209	-5.6064	13.5	1.00	3.50	0.28
0595.1	0.19	34.4190	-5.6074	4.34	1.93	1.75	0.42
0596.0	0.19	34.2601	-4.8762	9.74	1.47	2.91	0.37
0598.0	0.22	34.9759	-5.1562	9.76	1.06	3.65	0.42
0599.0	0.20	34.4151	-5.2364	8.24	1.12	2.22	0.28
0600.0	0.19	34.2385	-4.7130	13.6	1.24	3.76	0.38
0601.0	0.19	34.8178	-5.2795	4.90	1.56	1.57	0.31
0602.0	0.19	34.5961	-5.2367	13.6	1.00	3.04	0.26
0603.0	0.22	34.8120	-5.2893	6.91	1.00	2.25	0.34
0604.0	0.25	34.0496	-5.4891	7.01	1.00	2.01	0.34
0605.0	0.20	34.8649	-5.3958	10.8	1.10	2.92	0.31
0606.0	0.17	34.8799	-4.8448	4.70	1.43	1.55	0.36
0607.0	0.20	34.3097	-5.1293	7.30	1.01	2.21	0.29
0608.0	0.22	34.8755	-4.9344	10.6	1.04	3.52	0.41
0609.0	0.27	34.5573	-5.6242	11.9	1.03	4.24	0.38
0611.0	0.22	34.7145	-4.9231	5.82	1.37	2.11	0.43
0611.1	0.22	34.7161	-4.9229	5.13	1.03	1.35	0.31
0612.0	0.19	34.7259	-4.9701	8.08	1.03	2.27	0.30

Continued on next page

Table A.1 – continued from previous page

ALMA ID	Field RMS	SMG RA	SMG Dec	SNR	PB Corr	Flux	Flux Err
0613.0	0.23	33.9781	-4.8935	8.53	1.28	3.76	0.50
0615.0	0.23	34.0020	-5.1160	4.79	1.25	1.79	0.39
0616.0	0.17	34.6595	-5.3695	7.54	1.02	1.71	0.26
0621.0	0.19	34.2638	-5.5248	5.03	1.33	1.55	0.30
0622.0	0.20	34.1387	-5.1997	15.1	1.10	3.21	0.24
0624.0	0.26	34.1012	-5.2102	7.76	1.08	2.61	0.42
0626.0	0.24	34.9987	-5.0088	13.0	1.00	4.00	0.35
0627.0	0.20	34.4231	-4.9032	9.79	1.24	2.77	0.34
0631.0	0.20	34.7904	-4.8483	8.22	1.00	2.11	0.27
0638.0	0.16	34.4109	-5.4230	17.3	1.05	4.73	0.27
0639.0	0.32	34.4165	-5.4226	5.53	1.34	3.76	0.78
0643.0	0.27	34.2138	-5.2603	7.46	1.01	2.20	0.36
0644.0	0.19	34.2361	-5.4652	10.9	1.00	3.01	0.31
0645.0	0.23	34.4904	-4.6781	4.57	1.14	1.46	0.38
0646.0	0.26	34.2745	-5.0591	10.6	1.16	3.85	0.46
0648.0	0.27	34.4625	-5.3840	5.00	1.35	1.79	0.54
0649.0	0.28	34.3830	-4.9898	7.55	1.05	2.41	0.40
0650.0	0.22	34.7801	-5.4767	6.52	1.44	2.80	0.51
0651.0	0.22	34.4033	-5.0770	4.60	1.04	1.16	0.31
0652.0	0.27	34.5416	-5.0788	9.47	1.09	3.62	0.47
0653.0	0.27	34.3523	-5.3799	7.16	1.20	2.08	0.40
0654.0	0.25	34.3181	-4.9569	4.51	1.03	1.36	0.35
0655.0	0.24	34.8916	-5.3812	5.96	1.16	2.38	0.44
0657.0	0.23	34.8714	-5.2207	10.2	1.36	5.00	0.55
0658.0	0.26	34.5465	-5.2431	12.7	1.00	4.09	0.42
0659.0	0.26	34.4454	-5.1305	5.25	1.07	1.73	0.32
0660.0	0.26	34.6860	-4.9929	4.55	1.00	1.30	0.31
0661.0	0.28	34.1132	-5.5267	7.96	1.11	3.75	0.49
0662.0	0.21	34.4033	-5.4906	4.98	1.68	2.03	0.49
0662.1	0.21	34.4027	-5.4890	5.46	1.00	1.32	0.29
0663.0	0.27	34.5411	-5.3555	5.19	1.03	1.49	0.34
0664.0	0.27	34.5419	-5.3506	7.64	1.14	2.70	0.45
0665.0	0.26	34.6618	-5.2628	8.15	1.00	2.26	0.34
0667.0	0.27	34.6167	-4.9379	8.25	1.24	3.94	0.50
0668.0	0.19	34.1633	-5.0498	9.04	1.09	2.73	0.33
0669.0	0.27	34.5578	-5.0879	6.48	1.16	2.53	0.38

Continued on next page

Table A.1 – continued from previous page

ALMA ID	Field RMS	SMG RA	SMG Dec	SNR	PB Corr	Flux	Flux Err
0670.0	0.19	34.8991	-4.9421	16.8	1.02	3.72	0.27
0671.0	0.26	34.7304	-5.4042	12.2	1.00	3.02	0.30
0672.0	0.25	34.7298	-5.0055	4.49	1.62	1.82	0.53
0673.0	0.20	34.2622	-5.2034	5.99	1.07	1.46	0.26
0673.1	0.20	34.2625	-5.2051	5.98	1.11	1.20	0.28
0674.0	0.18	33.9906	-5.2251	11.0	1.04	2.52	0.29
0675.0	0.23	34.9982	-4.9876	5.21	1.09	1.71	0.37
0676.0	0.27	34.0863	-5.2263	7.07	1.03	1.95	0.34
0678.0	0.26	34.0109	-4.8282	8.64	1.35	3.86	0.52
0679.0	0.19	34.0245	-5.3144	5.75	1.20	1.81	0.30
0680.0	0.23	34.6192	-5.4577	10.8	1.14	4.97	0.49
0682.0	0.20	34.6114	-4.8252	11.9	1.21	3.61	0.38
0683.0	0.26	34.1534	-5.5201	6.70	1.00	2.29	0.41
0684.0	0.21	34.5229	-5.5962	16.2	1.02	4.31	0.33
0685.0	0.27	34.4723	-5.4537	8.96	1.05	3.39	0.45
0686.0	0.21	34.5603	-4.6449	19.7	1.00	4.92	0.31
0686.1	0.21	34.5605	-4.6473	4.90	1.69	2.09	0.44
0688.0	0.27	34.1539	-4.7710	9.39	1.07	3.43	0.45
0689.0	0.25	34.1511	-4.7630	6.51	1.21	2.21	0.38
0690.0	0.27	34.3460	-4.9583	7.95	1.33	2.71	0.48
0692.0	0.24	34.3202	-5.0663	9.90	1.03	3.56	0.44
0693.0	0.23	34.7404	-5.0024	9.03	1.29	3.33	0.47
0694.0	0.20	34.2603	-5.0547	4.31	1.05	1.06	0.26
0695.0	0.17	34.8412	-5.4548	10.6	1.02	2.53	0.28
0696.0	0.18	34.1388	-4.8468	4.99	1.25	1.43	0.31
0697.0	0.19	34.2428	-4.7300	6.22	1.02	1.64	0.27
0698.0	0.20	34.4735	-4.9690	7.41	1.03	1.95	0.28
0699.0	0.19	34.0746	-4.9485	7.99	1.21	2.52	0.33
0700.0	0.20	34.3445	-5.3052	6.68	1.00	1.61	0.26
0701.0	0.20	34.9294	-5.2839	7.70	1.05	1.73	0.29
0702.0	0.20	33.9261	-5.0474	12.1	1.09	3.55	0.35
0703.0	0.20	34.1341	-5.0586	9.91	1.06	2.52	0.31
0704.0	0.19	34.6257	-5.4365	13.9	1.07	3.89	0.33
0705.0	0.26	34.0919	-5.0017	6.10	1.11	1.82	0.38
0706.0	0.19	34.5919	-5.1093	13.8	1.00	3.38	0.28
0707.0	0.17	34.7984	-5.2525	9.66	1.09	2.23	0.29

Continued on next page

Table A.1 – continued from previous page

ALMA ID	Field RMS	SMG RA	SMG Dec	SNR	PB Corr	Flux	Flux Err
0708.0	0.20	34.0209	-5.2709	4.40	1.08	1.06	0.29
0709.0	0.26	34.5182	-5.1404	5.40	1.14	1.78	0.44
0710.0	0.20	34.8620	-5.2452	8.72	1.43	2.92	0.42
0711.0	0.22	34.0447	-5.0392	4.94	1.24	1.69	0.41
0712.0	0.19	34.5961	-5.4101	13.5	1.00	2.97	0.27
0812.0	0.26	34.0637	-4.9133	4.95	1.37	1.73	0.45

Bibliography

Aguilar, L. A., & White, S. 1985, ApJ, 295, 374

Alexander, D., Bauer, F., Chapman, S., et al. 2005a, ApJ, 632, 736

Alexander, D., Smail, I., Bauer, F., et al. 2005b, Nature, 434, 738

Alexander, D. M., Brandt, W. N., Smail, I., et al. 2008, AJ, 135, 1968

An, F. X., Stach, S., Smail, I., et al. 2018, ApJ, 862, 101

Aragón-Salamanca, A., Ellis, R. S., Couch, W. J., & Carter, D. 1993, MNRAS, 262, 764

Arancibia, A. M., González-López, J., Ibar, E., et al. 2018, A&A, 620, A125

Aravena, M., Decarli, R., Walter, F., et al. 2016, ApJ, 833, 68

Archibald, E. N., Dunlop, J., Hughes, D., et al. 2001, MNRAS, 323, 417

Austermann, J., Dunlop, J., Perera, T. A., et al. 2009, MNRAS, 401, 160

Balogh, M., Eke, V., Miller, C., et al. 2004, MNRAS, 348, 1355

Bamford, S. P., Nichol, R. C., Baldry, I. K., et al. 2009, MNRAS, 393, 1324

Barger, A., Cowie, L., & Richards, E. 2000, ApJ, 119, 2092

Barger, A., Cowie, L., Sanders, D., et al. 1998, Nature, 394, 248

Barger, A., Cowie, L., Chen, C.-C., et al. 2014, ApJ, 784, 9

Baugh, C. M., Lacey, C. G., Frenk, C., et al. 2005, MNRAS, 356, 1191

Berta, S., Magnelli, B., Nordon, R., et al. 2011, A&A, 532, A49

Bertoldi, F., Carilli, C., Aravena, M., et al. 2007, ApJS, 172, 132

Béthermin, M., De Breuck, C., Sargent, M., & Daddi, E. 2015, A&A, 576, L9

Biggs, A., Ivison, R., Ibar, E., et al. 2011, MNRAS, 413, 2314

Biviano, A., Fadda, D., Durret, F., Edwards, L., & Marleau, F. 2011, A&A, 532, A77

Blain, A., & Phillips, T. 2002, MNRAS, 333, 222

Blain, A. W., Chapman, S. C., Smail, I., & Ivison, R. 2004, ApJ, 611, 52

Blain, A. W., Smail, I., Ivison, R., Kneib, J.-P., & Frayer, D. T. 2002, Phys. Reports, 369, 111

Bolatto, A. D., Wolfire, M., & Leroy, A. K. 2013, ARAA, 51, 207

Bond, N. A., Benford, D. J., Gardner, J. P., et al. 2012, ApJL, 750, L18

Borys, C., Smail, I., Chapman, S., et al. 2005, ApJ, 635, 853

Bothwell, M., Smail, I., Chapman, S., et al. 2013, MNRAS, 429, 3047

Bournaud, F., Daddi, E., Weiß, A., et al. 2015, A&A, 575, A56

Bourne, N., Dunlop, J., Merlin, E., et al. 2017, MNRAS, 467, 1360

Bower, R. G., Lucey, J., & Ellis, R. S. 1992, MNRAS, 254, 589

Brammer, G. B., van Dokkum, P. G., & Coppi, P. 2008, ApJ, 686, 1503

Brisbin, D., Miettinen, O., Aravena, M., et al. 2017, A&A, 608, A15

Brodwin, M., Stanford, S., Gonzalez, A. H., et al. 2013, ApJ, 779, 138

Bruzual, G., & Charlot, S. 2003, MNRAS, 344, 1000

Butcher, H., & Oemler Jr, A. 1978, ApJ, 226, 559

Carilli, C., & Walter, F. 2013, ARAA, 51, 105

Carlberg, R., Yee, H., & Ellingson, E. 1997, ApJ, 478, 462

Casali, M., Adamson, A., de Oliveira, C. A., et al. 2007, A&A, 467, 777

Casey, C. M., Narayanan, D., & Cooray, A. 2014, Physics Reports, 541, 45

Casey, C. M., Chen, C.-C., Cowie, L. L., et al. 2013, MNRAS, 436, 1919

Chabrier, G. 2003, PASP, 115, 763

Chapin, E. L., Pope, A., Scott, D., et al. 2009, MNRAS, 398, 1793

Chapman, S., Barger, A., Cowie, L., et al. 2003, AJ, 585, 57

Chapman, S. C., Blain, A., Smail, I., & Ivison, R. 2005, ApJ, 622, 772

Charlot, S., & Fall, S. M. 2000, ApJ, 539, 718

Chary, R., & Elbaz, D. 2001, ApJ, 556, 562

Chen, C.-C., Cowie, L. L., Barger, A. J., et al. 2013, ApJ, 776, 131

Chen, C.-C., Smail, I., Swinbank, A., et al. 2015, ApJ, 799, 194

Chen, C.-C., Smail, I., Ivison, R. J., et al. 2016, ApJ, 820, 82

Cimatti, A., Cassata, P., Pozzetti, L., et al. 2008, A&A, 482, 21

Condon, J. 1992, ARA&A, 30, 575

—. 1997, PASP, 109, 166

Condon, J. J., Cotton, W., Greisen, E., et al. 1998, ApJ, 115, 1693

Connolly, A., Szalay, A., Dickinson, M., Subbarao, M., & Brunner, R. 1997, ApJL, 486, L11

Cooke, E., Smail, I., Swinbank, A., et al. 2018, ApJ, 861, 100

Coppin, K., Chapin, E. L., Mortier, A. M., et al. 2006, MNRAS, 372, 1621

Coppin, K., Swinbank, A., Neri, R., et al. 2008, MNRAS, 389, 45

Coppin, K. E., Geach, J., Almaini, O., et al. 2015, MNRAS, 446, 1293

Cowie, L. L., Barger, A., Fomalont, E., & Capak, P. 2004, ApJL, 603, L69

Cowie, L. L., Gonzalez-Lopez, J., Barger, A. J., et al. 2018, ApJ, 865, 106

Cowie, L. L., Songaila, A., Hu, E. M., & Cohen, J. 1996, ApJ, 112, 839

Cowley, W., Lacey, C. G., Baugh, C. M., et al. 2018, arXiv preprint arXiv:1808.05208

Cowley, W. I., Lacey, C. G., Baugh, C. M., & Cole, S. 2015a, MNRAS, 446, 1784

—. 2015b, MNRAS, 446, 1784

Cucciati, O., Tresse, L., Ilbert, O., et al. 2012, A&A, 539, A31

Da Cunha, E., Charlot, S., & Elbaz, D. 2008, MNRAS, 388, 1595

da Cunha, E., Walter, F., Smail, I., et al. 2015, ApJ, 806, 110

Daddi, E., Cimatti, A., Renzini, A., et al. 2004, ApJ, 617, 746

Daddi, E., Dickinson, M., Morrison, G., et al. 2007, ApJ, 670, 156

Daddi, E., Bournaud, F., Walter, F., et al. 2010, ApJ, 713, 686

Daddi, E., Dannerbauer, H., Liu, D., et al. 2015, A&A, 577, A46

Danielson, A., Swinbank, A., Smail, I., et al. 2017, ApJ, 840, 78

Darvish, B., Mobasher, B., Sobral, D., et al. 2016, ApJ, 825, 113

Davis, S. W., & Laor, A. 2011, ApJ, 728, 98

Dawson, K., Aldering, G., Amanullah, R., et al. 2009, AJ, 138, 1271

De Zotti, G., Bonato, M., & Cai, Z.-Y. 2018, arXiv preprint arXiv:1802.06561

Decarli, R., Walter, F., Aravena, M., et al. 2016, ApJ, 833, 69

Dempsey, J. T., Friberg, P., Jenness, T., et al. 2013, MNRAS, 430, 2534

Donley, J., Koekemoer, A., Brusa, M., et al. 2012, ApJ, 748, 142

Downes, D., & Solomon, P. 1998, ApJ, 507, 615

Draine, B., Dale, D., Bendo, G., et al. 2007, ApJ, 663, 866

Dressler, A. 1980, ApJ, 236, 351

Driver, S. P., Andrews, S. K., Davies, L. J., et al. 2016, ApJ, 827, 108

Drouart, G., De Breuck, C., Vernet, J., et al. 2014, A&A, 566, A53

Dunlop, J. S., McLure, R., Biggs, A., et al. 2016, MNRAS, 466, 861

Dunne, L., & Eales, S. A. 2001, MNRAS, 327, 697

Eales, S., Dunne, L., Clements, D., et al. 2010, PASP, 122, 499

Elbaz, D., Dickinson, M., Hwang, H., et al. 2011, A&A, 533, A119

Elvis, M., Wilkes, B. J., McDowell, J. C., et al. 1994, ApJS, 95, 1

Engel, H., Tacconi, L., Davies, R., et al. 2010, ApJ, 724, 233

Estrada-Carpenter, V., Papovich, C., Momcheva, I., et al. 2019, ApJ, 870, 133

Fadda, D., Biviano, A., Marleau, F. R., Storrie-Lombardi, L. J., & Durret, F. 2007, ApJL, 672, L9

Farrah, D., Lonsdale, C., Borys, C., et al. 2006, ApJL, 641, L17

Ferrarese, L., & Merritt, D. 2000, ApJL, 539, L9

Finn, R. A., Desai, V., Rudnick, G., et al. 2010, ApJ, 720, 87

Fixsen, D. J., Bennett, C., & Mather, J. C. 1999, ApJ, 526, 207

Franceschini, A. 2003, Galaxies at High Redshift, 69

Franco, M., Elbaz, D., Bethermin, M., et al. 2018, A&A, 620, A152

Fu, H., Cooray, A., Feruglio, C., et al. 2013, Nature, 498, 338

Fujimoto, S., Ouchi, M., Ono, Y., et al. 2015, ApJ Supp., 222, 1

Furusawa, H., Kosugi, G., Akiyama, M., et al. 2008, ApJS, 176, 1

Galametz, A., Grazian, A., Fontana, A., et al. 2013, ApJS, 206, 10

Geach, J., Dunlop, J., Halpern, M., et al. 2017, MNRAS, 465, 1789

Geach, J. E., Smail, I., Ellis, R., et al. 2006, ApJ, 649, 661

Geach, J. E., Chapin, E., Coppin, K., et al. 2013, MNRAS, 432, 53

Gebhardt, K., Bender, R., Bower, G., et al. 2000, ApJL, 539, L13

Genzel, R., Baker, A. J., Tacconi, L. J., et al. 2003, ApJ, 584, 633

Genzel, R., Tacconi, L., Gracia-Carpio, J., et al. 2010, MNRAS, 407, 2091

Genzel, R., Tacconi, L., Lutz, D., et al. 2015, ApJ, 800, 20

Georgantopoulos, I., Rovilos, E., & Comastri, A. 2011, A&A, 526, A46

Gomez, P. L., Nichol, R. C., Miller, C. J., et al. 2003, ApJ, 584, 210

González, J. E., Lacey, C., Baugh, C., & Frenk, C. 2011, MNRAS, 413, 749

Greve, T., Ivison, R., Bertoldi, F., et al. 2004, MNRAS, 354, 779

Greve, T. R., Pope, A., Scott, D., et al. 2008, MNRAS, 389, 1489

Gullberg, B., Swinbank, A., Smail, I., et al. 2018, ApJ, 859, 12

Gültekin, K., Richstone, D. O., Gebhardt, K., et al. 2009, ApJ, 698, 198

Gunn, J. E., & Gott III, J. R. 1972, ApJ, 176, 1

Haines, C., Smith, G., Egami, E., et al. 2009, ApJ, 704, 126

Hainline, L. J., Blain, A., Smail, I., et al. 2011, ApJ, 740, 96

Hancock, P. J., Murphy, T., Gaensler, B. M., Hopkins, A., & Curran, J. R. 2012, MNRAS, 422, 1812

Hancock, P. J., Trott, C. M., & Hurley-Walker, N. 2018, PASA, 35

Hao, C.-N., Xia, X.-Y., Mao, S.-D., Deng, Z.-G., & Wu, H. 2008, CJAA, 8, 12

Harrison, C., Alexander, D., Mullaney, J., et al. 2016, MNRAS, 456, 1195

Hatch, N. A., Cooke, E. A., Muldrew, S. I., et al. 2016, MNRAS, 464, 876

Hatsukade, B., Kohno, K., Umehata, H., et al. 2016, PASJ, 68

Hatsukade, B., Kohno, K., Yamaguchi, Y., et al. 2018, PASJ, 70, 105

Hayashi, M., Kodama, T., Koyama, Y., et al. 2010, MNRAS, 402, 1980

—. 2014, MNRAS, 439, 2571

Hayashi, M., Kodama, T., Kohno, K., et al. 2017, ApJL, 841, L21

Hayward, C. C., Chapman, S. C., Steidel, C. C., et al. 2018, MNRAS, 476, 2278

Helou, G., Soifer, B., & Rowan-Robinson, M. 1985, ApJ, 298, L7

Hickox, R. C., Wardlow, J., Smail, I., et al. 2012, MNRAS, 421, 284

Hill, R., Chapman, S. C., Scott, D., et al. 2018, MNRAS, 477, 2042

Hilton, M., Collins, C. A., Stanford, S. A., et al. 2007, ApJ, 670, 1000

Hilton, M., Stanford, S. A., Stott, J. P., et al. 2009, ApJ, 697, 436

Hilton, M., Lloyd-Davies, E., Stanford, S. A., et al. 2010, ApJ, 718, 133

Ho, P. T. P., Moran, J. M., & Lo, K. Y. 2004, ApJL, 616, L1

Hodge, J., Karim, A., Smail, I., et al. 2013, ApJ, 768, 91

Hodge, J., Swinbank, A., Simpson, J., et al. 2016, ApJ, 833, 103

Hopkins, P. F., Hernquist, L., Cox, T. J., & Kereš, D. 2008, ApJS, 175, 356

Hopkins, P. F., Richards, G. T., & Hernquist, L. 2007, ApJ, 654, 731

Hubble, E., & Rosseland, S. 1936, Science, 84, 509

Hubble, E. P. 1925, ApJ, 62

—. 1926, ApJ, 64

Hughes, D. H., Serjeant, S., Dunlop, J., et al. 1998, Nature, 394, 241

Ikarashi, S., Kohno, K., Aguirre, J., et al. 2011, MNRAS, 415, 3081

Ikarashi, S., Ivison, R., Caputi, K. I., et al. 2015, ApJ, 810, 133

Ikarashi, S., Caputi, K. I., Ohta, K., et al. 2017, ApJL, 849, L36

Iono, D., Peck, A. B., Pope, A., et al. 2006, ApJ, 640, L1

Ivison, R., Papadopoulos, P., Smail, I., et al. 2011, MNRAS, 412, 1913

Ivison, R., Smail, I., Le Borgne, J.-F., et al. 1998, MNRAS, 298, 583

Ivison, R. J., Greve, T. R., Smail, I., et al. 2002, MNRAS, 337, 1

Ivison, R. J., Greve, T., Dunlop, J., et al. 2007, MNRAS, 380, 199

Ivison, R. J., Alexander, D. M., Biggs, A. D., et al. 2010a, MNRAS, 402, 245

Ivison, R. J., Magnelli, B., Ibar, E., et al. 2010b, A&A, 518, L31

Jaffé, Y. L., Smith, R., Candlish, G. N., et al. 2015, MNRAS, 448, 1715

Jarvis, M. J., Bonfield, D. G., Bruce, V., et al. 2012, MNRAS, 428, 1281

Johnson, S. P., Wilson, G. W., Wang, Q., et al. 2013, MNRAS, 431, 662

Kant, I. 1755, Theoretical philosophy, 1770, 373

Karim, A., Swinbank, A., Hodge, J., et al. 2013, MNRAS, 196

Keane, E. F. 2017, Proceedings of the International Astronomical Union, 13, 158

Kennicutt, R. 1998, ARAA, 36, 189

Kocevski, D. D., Hasinger, G., Brightman, M., et al. 2018, APJS, 236, 48

Kodama, T., Yamada, T., Akiyama, M., et al. 2004, MNRAS, 350, 1005

Komatsu, E., Dunkley, J., Nolta, M., et al. 2009, ApJS, 180, 330

Koprowski, M., Dunlop, J., Michałowski, M., Cirasuolo, M., & Bowler, R. 2014, MNRAS, 444, 117

Kulkarni, G., Worseck, G., & Hennawi, J. F. 2018, arXiv preprint arXiv:1807.09774

Lacey, C. G., Baugh, C. M., Frenk, C. S., et al. 2016, MNRAS, 462, 3854

Lagache, G., Puget, J.-L., & Dole, H. 2005, ARA&A, 43, 727

Laird, E. S., Nandra, K., Pope, A., & Scott, D. 2010, MNRAS, 401, 2763

Larson, R., Tinsley, B., & Caldwell, C. 1980, ApJ, 237, 692

Lawrence, A., Warren, S., Almaini, O., et al. 2007, MNRAS, 379, 1599

Lewis, I., Balogh, M., De Propris, R., et al. 2002, MNRAS, 334, 673

Lilly, S. J., Eales, S. A., Gear, W. K., et al. 1999, ApJ, 518, 641

Lilly, S. J., Le Fevre, O., Hammer, F., & Crampton, D. 1996, ApJL, 460, L1

Lindner, R. R., Baker, A. J., Omont, A., et al. 2011, ApJ, 737, 83

Lotz, J. M., Papovich, C., Faber, S., et al. 2013, ApJ, 773, 154

Lusso, E., Comastri, A., Simmons, B., et al. 2012, MNRAS, 425, 623

Lutz, D., Poglitsch, A., Altieri, B., et al. 2011, A&A, 532, A90

Ma, C.-J., Smail, I., Swinbank, A., et al. 2015, ApJ, 806, 257

Madau, P., & Dickinson, M. 2014, ARA&A, 52, 415

Madau, P., Ferguson, H. C., Dickinson, M. E., et al. 1996, MNRAS, 283, 1388

Magnelli, B., Lutz, D., Santini, P., et al. 2012, A&A, 539, A155

Magorrian, J., Tremaine, S., Richstone, D., et al. 1998, ApJ, 115, 2285

McAlpine, S., Smail, I., Bower, R. G., et al. 2019, arXiv preprint arXiv:1901.05467

McMullin, J., Waters, B., Schiebel, D., Young, W., & Golap, K. 2007, in Astronomical data analysis software and systems XVI, Vol. 376, 127

Merloni, A. 2004, MNRAS, 353, 1035

Merritt, D. 1983, ApJ, 264, 24

Messier, C. 1781, Connoissance des Temps ou des Mouvements Célestes, for 1784, p. 227-267, 227

Michałowski, M. J., Hayward, C. C., Dunlop, J. S., et al. 2014, A&A, 571, A75

Miettinen, O., Delvecchio, I., Smolčić, V., et al. 2017, A&A, 606, A17

Miyaji, T., Griffiths, R., et al. 2008, in AAS/High Energy Astrophysics Division# 10, Vol. 10

Morishita, T., Abramson, L., Treu, T., et al. 2018, arXiv preprint arXiv:1812.06980

Murphy, E. J. 2009, ApJ, 706, 482

Narayanan, D., Hayward, C. C., Cox, T. J., et al. 2010, MNRAS, 401, 1613

Narayanan, D., Krumholz, M. R., Ostriker, E. C., & Hernquist, L. 2012, MNRAS, 421, 3127

Nelan, J. E., Smith, R. J., Hudson, M. J., et al. 2005, ApJ, 632, 137

Newman, A. B., Ellis, R. S., Andreon, S., et al. 2014, ApJL, 788, 51

Noble, A., Webb, T., Yee, H., et al. 2016, ApJ, 816, 48

Oliver, S., Bock, J., Altieri, B., et al. 2012, MNRAS, 424, 1614

Ono, Y., Ouchi, M., Kurono, Y., & Momose, R. 2014, The Astrophysical Journal, 795, 5

Oteo, I., Zwaan, M., Ivison, R., Smail, I., & Biggs, A. 2016, ApJ, 822, 36

Papadopoulos, P., Ivison, R., Carilli, C., & Lewis, G. 2001, Nature, 409, 58

Papadopoulos, P. P., van der Werf, P. P., Xilouris, E., et al. 2012, MNRAS, 426, 2601

Paragi, Z., Chrysostomou, A., & Garcia-Miro, C. 2019, arXiv preprint arXiv:1901.10361

Pope, A., Borys, C., Scott, D., et al. 2005, MNRAS, 358, 149

Pope, A., Chary, R.-R., Alexander, D. M., et al. 2008, ApJ, 675, 1171

Popesso, P., Biviano, A., Rodighiero, G., et al. 2012, A&A, 537, A58

Puget, J.-L., Abergel, A., Bernard, J.-P., et al. 1996, A&A, 308, L5

Rawle, T., Rex, M., Egami, E., et al. 2012, ApJ, 756, 106

Riechers, D. A., Cooray, A., Omont, A., et al. 2011, ApJL, 733, L12

Riechers, D. A., Bradford, C., Clements, D., et al. 2013, Nature, 496, 329

Rieke, G. H., Alonso-Herrero, A., Weiner, B., et al. 2009, ApJ, 692, 556

Rudnick, G. H., Tran, K.-V., Papovich, C., Momcheva, I., & Willmer, C. 2012, ApJ, 755, 14

Saintonge, A., Tran, K.-V. H., & Holden, B. P. 2008, ApJL., 685, L113

Sanders, D., Soifer, B., Elias, J., et al. 1988, ApJ, 325, 74

Sanders, D. B., & Mirabel, I. F. 1996, ARAA, 34, 749

Santos, J., Altieri, B., Popesso, P., et al. 2013, MNRAS, 433, 1287

Santos, J. S., Altieri, B., Valtchanov, I., et al. 2015, MNRAS Lett., 447, L65

Sargent, M. T., Schinnerer, E., Murphy, E., et al. 2010, ApJS, 186, 341

Scudder, J. M., Oliver, S., Hurley, P. D., et al. 2016, MNRAS, 460, 1119

Simpson, C., Westoby, P., Arumugam, V., et al. 2013, MNRAS, 433, 2647

Simpson, J., Smail, I., Swinbank, A., et al. 2012, MNRAS, 426, 3201

—. 2015a, ApJ, 807, 128

—. 2015b, ApJ, 799, 81

—. 2017, ApJ, 839, 58

Simpson, J. M., Swinbank, A., Smail, I., et al. 2014, ApJ, 788, 125

Slipher, V. M. 1915, Popular astronomy, 23, 21

Smail, I., Chapman, S., Blain, A., & Ivison, R. 2004, ApJ, 616, 71

Smail, I., Ivison, R., & Blain, A. 1997, ApJL, 490, L5

Smail, I., Ivison, R., Blain, A., & Kneib, J.-P. 2002, MNRAS, 331, 495

Smail, I., Ivison, R., Owen, F., Blain, A., & Kneib, J.-P. 2000, ApJ, 528, 612

Smail, I., Geach, J., Swinbank, A., et al. 2014, ApJ, 782, 19

Smith, D. J. B., Dunne, L., Maddox, S. J., et al. 2011, MNRAS, 416, 857

Smith, R. J., Lucey, J. R., & Hudson, M. J. 2009, MNRAS, 400, 1690

Smolčić, V., Aravena, M., Navarrete, F., et al. 2012, A&A, 548, A4

Solomon, P., & Vanden Bout, P. 2005, ARAA, 43, 677

Stach, S. M., Swinbank, A., Smail, I., et al. 2017, ApJ, 849, 154

Stach, S. M., Smail, I., Swinbank, A., et al. 2018, ApJ, 860, 161

Stanford, S., Romer, A. K., Sabirli, K., et al. 2006, ApJL, 646, L13

Sutherland, W., & Saunders, W. 1992, MNRAS, 259, 413

Swinbank, A., Chapman, S., Smail, I., et al. 2006, MNRAS, 371, 465

Swinbank, A., Smail, I., Chapman, S., et al. 2004, ApJ, 617, 64

Swinbank, A., Karim, A., Smail, I., et al. 2012, MNRAS, 427, 1066

Swinbank, A., Simpson, J., Smail, I., et al. 2013, MNRAS, 438, 1267

—. 2014, MNRAS, 438, 1267

Tacconi, L., Neri, R., Genzel, R., et al. 2013, ApJ, 768, 74

Tacconi, L. J., Neri, R., Chapman, S., et al. 2006, ApJ, 640, 228

Takata, T., Sekiguchi, K., Smail, I., et al. 2006, ApJ, 651, 713

Takeuchi, T. T., Morokuma-Matsui, K., Iono, D., et al. 2016, arXiv preprint arXiv:1603.01938

Thomas, D., Maraston, C., Bender, R., & De Oliveira, C. M. 2005, ApJ, 621, 673

Thompson, A. R., Moran, J. M., Swenson, G. W., et al. 1986, Interferometry and synthesis in radio astronomy (Wiley New York et al.)

Thomson, A. P., Ivison, R. J., Simpson, J. M., et al. 2014, MNRAS, 442, 577

Tiley, A. L., Stott, J. P., Swinbank, A., et al. 2016, MNRAS, 460, 103

Toft, S., Smolčić, V., Magnelli, B., et al. 2014, ApJ, 782, 68

Tran, K.-V. H., Papovich, C., Saintonge, A., et al. 2010, ApJL, 719, L126

Umehata, H., Tamura, Y., Kohno, K., et al. 2014, MNRAS, 440, 3462

van der Wel, A., Franx, M., Van Dokkum, P., et al. 2014, ApJ, 788, 28

Walter, F., Decarli, R., Aravena, M., et al. 2016, ApJ, 833, 67

Wang, S., Brandt, W., Luo, B., et al. 2013, ApJ, 778, 179

Wang, T., Elbaz, D., Daddi, E., et al. 2016, ApJ, 828, 56

Wang, W.-H., Cowie, L. L., Barger, A. J., & Williams, J. P. 2011, ApJL, 726, L18

Wardlow, J., Smail, I., Coppin, K., et al. 2011, MNRAS, 415, 1479

Wardlow, J. L., Simpson, J., Smail, I., et al. 2018, MNRAS, 479, 3879

Webb, T., Yee, H., Ivison, R., et al. 2005, ApJ, 631, 187

Webb, T., O'Donnell, D., Yee, H. K., et al. 2013, ApJ, 146, 84

Weiß, A., Kovács, A., Coppin, K., et al. 2009, ApJ, 707, 1201

Weiß, A., De Breuck, C., Marrone, D. P., et al. 2013, ApJ, 767, 88

Whitaker, K. E., Kriek, M., Van Dokkum, P. G., et al. 2012, ApJ, 745, 179

White, S. D., & Rees, M. J. 1978, MNRAS, 183, 341

Whitmore, B. C., Gilmore, D. M., & Jones, C. 1993, ApJ, 407, 489

Wilkinson, A., Almaini, O., Chen, C.-C., et al. 2017, MNRAS, 464, 1380

Williams, C. C., Giavalisco, M., Porciani, C., et al. 2011, ApJ, 733, 92

Xu, C., Klein, U., Meinert, D., Wielebinski, R., & Haynes, R. F. 1992, A&A, 257, 47

Younger, J., Dunlop, J., Peck, A., et al. 2008, MNRAS, 387, 707

Younger, J. D., Fazio, G. G., Huang, J.-S., et al. 2007, ApJ, 671, 1531

Younger, J. D., Fazio, G. G., Huang, J.-S., et al. 2007, ApJ, 671, 1531

Zavala, J., Yun, M., Aretxaga, I., et al. 2015, MNRAS, 452, 1140